Numerical modelling of a masonry farmhouse retrofitted with bed joint reinforced repointing

by

Jarno Frankenmolen

TU Delft

Numerical modelling of a masonry farmhouse retrofitted with bed joint reinforced repointing

by

Jarno Frankenmolen

in partial fulfilment of the requirements for the degree of

Master of Science

in Civil Engineering

at the Delft University of Technology,

to be defended publicly on Thursday August 8, 2024 at 14:00

Student number:	4315626	
Thesis committee:	Prof.dr.ir. J.G. Rots,	TU Delft, Chair of the Committee
	Dr. R. Esposito,	TU Delft, Daily Supervisor
	Ir. S. Pasterkamp,	TU Delft, Supervisor

Summary

In the 1960s a large natural gas field was discovered in the Dutch province of Groningen, in the northern part of the Netherlands. Due to gas extraction, localised earthquakes started occurring in the 1990s. In this part of the country large numbers of buildings are constructed using unreinforced masonry (URM). Damage due to seismic activity in the region poses a threat to the structural integrity of existing masonry structures, as these buildings were never designed to withstand seismic loading. A strengthening measure was deemed necessary, to reduce damage due to seismic loading. Among others, an intervention method that was considered was retrofitting with bed joint reinforced repointing, often done in combination with foundation strengthening. This is an attractive solution, as it is already often used in strengthening of masonry structures against settlement-induced damage, especially for heritage structures, as it does not affect the aesthetics of the structure. Furthermore, since this reinforcing technique is already applied to limit damage due to ground settlements, it is an attractive potential solution to counter damage due to seismic loading, as it does not require additional funding. However, not much research is available on the performance of existing masonry structures retrofitted with bed joint reinforced repointing, considering both the effect of ground settlements and seismic loading conditions.

To investigate the added benefit of bed joint reinforcement, used to counteract seismic-induced damage, nonlinear finite element analyses, of a case study of a typical masonry farmhouse in the Groningen region, were performed. In this research, an orthotropic continuum model called the engineering masonry model (EMM) was adopted.

The used numerical modelling approach was first validated against in-plane experimental tests of unstrengthened and strengthened masonry walls, performed at TU Delft. A sensitivity study on the head-joint failure type, analysis procedure settings, iterative method and interpolation scheme was performed, to see which analysis settings provided optimal results in terms of initial stiffness, peak load, crack patterns and crack widths. It was found that optimal results, in terms of the above-mentioned quantities, were obtained when using the head-joint failure type ‘tensile strength head-joint defined by friction’, the secant method with BFGS and quadratic elements. These results were used in analysis of the masonry farmhouse. Furthermore, a sensitivity analysis with regards to various material parameters was performed on the masonry walls.

Considering that the type of strengthening measure applied acts mainly on the in-plane resistance of the structural elements, only the farmhouse façade was modelled, meaning it was assumed no out-of-plane failure could occur. The façade of the masonry farmhouse, subject to settlement and seismic loading was modelled leveraging on a previous study performed at TU Delft. Various cases were analysed: an unstrengthened façade, strengthened façades, using various peak ground velocities (namely the expected load and two models including an amplified seismic load by a factor of 1.5 and 2), where bed joint reinforced repointing was applied *after* the settlement loading phase, and a partially reinforced masonry façade, where the bed joint reinforcement was applied *before* the settlement loading phase. The results were analysed in terms of crack widths, crack patterns and a damage values (ψ_D). The damage value parameter was previously developed by others for analysing progressive damage in masonry.

For each analysis two important points of interest were identified. The first is the point where the total damage value is at its maximum value ($\psi_{D,total,max}$) during analysis. This is the damage value that quantifies the damage in the façade due to *all* the cracks found at any given point. The second point of interest is at the end of analysis, when the seismic motion has passed completely.

The numerical results of the façade strengthened with bed joint reinforcement showed that, compared to the unstrengthened façade, the added benefit on the structural performance of the structure, under seismic loading, is minimal. Due to the limited damage caused by an earthquake with the expected seismic load (PGV of 64mm/s), application of bed joint reinforced repointing after the settlement has already occurred, does not greatly increase the structural performance of this type of farmhouse façade as most of the damage is already formed at the end of the settlement loading phase. When the maximum total damage value, during seismic loading, was reached, a reduction in the maximum crack width of -4.7% was found, compared to the unstrengthened façade. Furthermore, a reduction in the maximum total damage value of -5.5% was found. At the end of analysis, a minor increase in the maximum crack width, of +7.5%, was found, relative to the unstrengthened façade, due to the steel reinforcement resisting closing of cracks that were already formed after

the settlement loading phase. However, when all crack are considered, a reduction of the total damage value of -2.0% was found, compared to the unstrengthened façade. Amplification of the seismic load by a factor 1.5 showed that the increase in crack widths and damage values, at any point during seismic loading, is minor compared to the numerical models where the expected seismic load has been used, while, relatively, the reinforcement is significantly more activated. However, damage quickly ramps up when the seismic load in amplified by a factor 2. In this numerical model failure of the masonry façade is even observed.

The numerical results of the façade with partially reinforced masonry showed that, compared to the unstrengthened façade, the added benefit on the structural performance of the structure, under seismic loading, is quite significant. Only very minor cracking was now observed after the settlement loading phase. When the maximum total damage value, during seismic loading, was reached, a reduction in the maximum crack width of -58.1% was found, as well as a reduction of -23.6% of the maximum total damage value, compared to the unstrengthened façade. At the end of analysis, a reduction of the maximum crack width of -60.3% is found, as well as a reduction of the total damage value of -23.7%, compared to the unstrengthened façade.

When retrofitting with bed joint reinforcement, the steel reinforcement is applied after the ground settlement has occurred, meaning large damage values are already present in the façade. Due to the limited damage caused by seismic loading, when using the expected seismic load, application of bed joint reinforcement after the settlement has occurred, results in only a minor decrease in damage values at the end of analysis, compared to the unstrengthened façade. Since the damage due to seismic loading is so small, it was therefore not recommended to strengthen this type of façade with bed joint reinforcement purely against seismic-induced damage, as the added benefit is small. However, since this strengthening technique is often applied already for strengthening against only ground settlements, it could provide a minor benefit during seismic loading, as a side effect. When looking at the results of the partially reinforced masonry façade, a sharp reduction in crack widths and damage values is observed at the end of analysis, compared to the unstrengthened façade, since the steel reinforcement now also resists the ground settlements (most sensitive parameter). Thus, when this type of façade is subjected to combined settlement and seismic loading, the added benefit of bed joint reinforced repointing in partially reinforced masonry is very significant. Since this numerical model simulates the case in which the bed joint reinforcement is applied during the construction phase, use of bed joint reinforcement would be beneficial for future masonry constructions. To make conclusive statements on the benefit of existing masonry structures, more in-depth numerical modelling of foundation strengthening measures is necessary, since this numerical model can be seen as a slimmed down form of foundation strengthening.

There are various limitations to the work done in this report. From this follow several recommendations for further research, such as extension of the numerical model in the out-of-plane direction, a more elaborate soil-structure interaction modelling approach, a full implementation of foundation strengthening, the type of façade considered, the used settlement profile as well as the the seismic load, the bed joint reinforcement layout and amount and an in-depth material sensitivity analysis.

Acknowledgement

I would hereby like to express my gratitude to everyone who has helped and supported me during my MSc degree in structural engineering at the Delft University of Technology.

First of all, I would like to thank all the members of my thesis committee, Prof. Dr. Ir. Jan Rots, Dr. Rita Esposito and Ir. Sander Pasterkamp, for their help and valuable feedback over the course of my MSc thesis. Without their feedback I would never have been able to produce something I am so proud of. I would like to thank in particular my daily supervisor, Rita, who was always there for me if I was running into problems or had any question. Especially during some difficult times I encountered while writing my thesis. Furthermore, I would like to thank Michele Longo for his help with the numerical analyses. Whenever I was stuck, he would make time to help me out and I will be forever grateful for that. I would also like to extend my gratitude towards Marten de Jong of TotalWall and Michiel van Hunen from the Agency of Cultural Heritage, who provided valuable assistance for practical information on bed joint reinforced repointing in existing historical structures.

I would like to express my gratitude and love for my mother, who has always been there for me through thick and thin. You are my biggest supporter and without you I would never have been able to be where I am now. I am so happy we can finally celebrate this moment together.

Lastly, I would like to thank my girlfriend Emilia, who has always supported me, as well as my friends who have helped me immensely during my MSc degree.

Jarno Frankenmolen
The Hague, August 2024

Table of Contents

List of Figures

List of Tables

1 Introduction

This chapter will show the basis of the research carried out in this report. First, the background problem and gaps are presented. After this, the main research objectives are discussed, and, following from this, the main research question, and sub-questions, are presented. Finally, the adopted research methodology and report outline is discussed.

1.1 Background problem

The Netherlands has, historically, never been a country with large tectonic earthquakes. In the 1960s a large natural gas field was discovered in the Dutch province of Groningen, in the northern part of the Netherlands. Earthquakes started occurring in the in this area in the 1990s. These localised earthquakes were not due to tectonic activity but, instead, induced due to gas extraction. A correlation between the volume of gas extraction and the number of earthquakes in the Groningen area was reported (Bakema et al., 2017), shown in Figure 1.1.

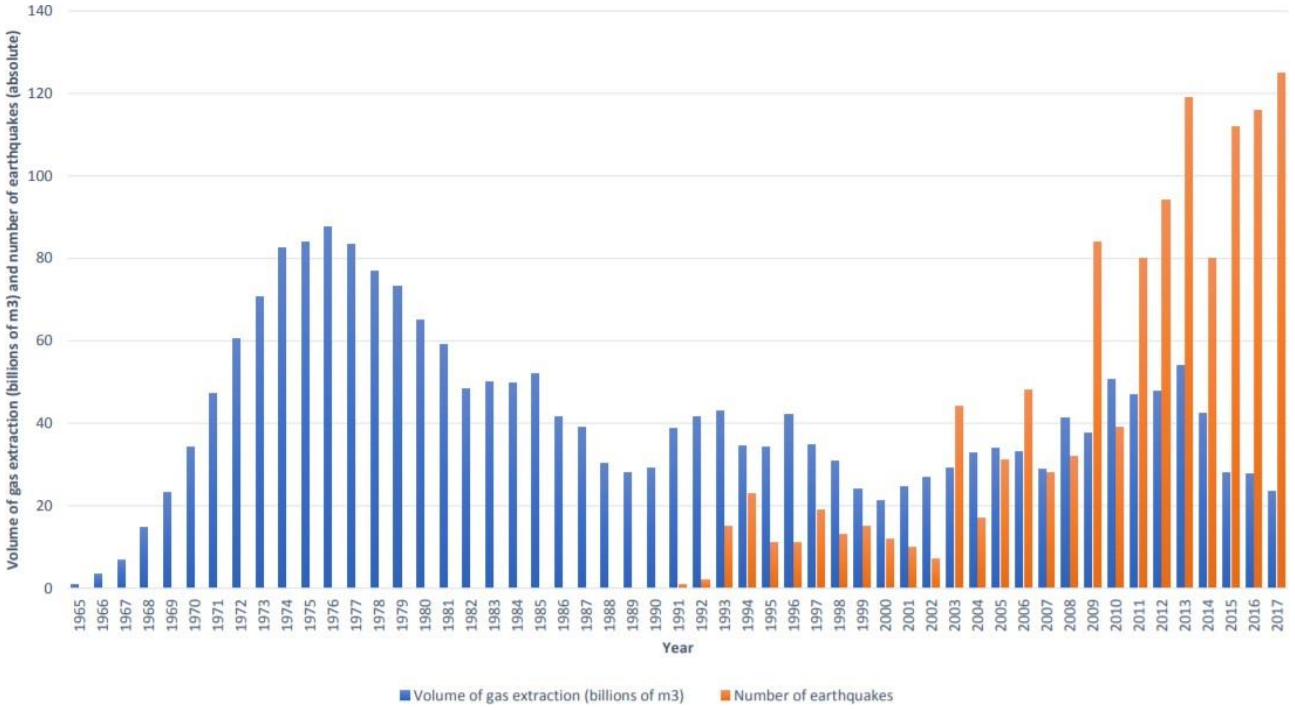

Figure 1.1 volume of gas extraction and number of earthquakes in Groningen (Bakema et al., 2018)

Between 1991 and 2018 the Groningen area experienced more than 320 earthquakes with magnitude $M \geq 1.5$ (on the scale of Richter), of which 38 were $M \geq 2.5$. The most critical event occurred in August 2012 having a magnitude of 3.6. Emergency assistance planners take a maximum possible event of magnitude 5.0 into account (Vlek, 2018).

The buildings in Groningen are mainly constructed using unreinforced masonry (URM). The seismic activity in the region over the last few decades, in combination with ground settlement, has resulted in damaging of URM buildings. This is obviously unwanted from an aesthetical viewpoint, but also gives residents a feeling that the structural safety has been compromised, which may not actually be the case.

Different strengthening measures have been considered to tackle this problem. One of these retrofitting techniques is the use of bed joint reinforced repointing, often done in combination with foundation strengthening. Bed joint reinforced repointing has already been used in the Netherlands for some time, but mainly to counter damage due to ground settlement. Its limited impact on building aesthetics makes it an attractive solution for strengthening of historical buildings. Furthermore, this potential solution does not require additional funding, as it is already often used to counter settlement-induced damage.

Since this reinforcing technique is already present in several buildings, applicability to prevent damage due to low magnitude induced earthquakes has been recently studied. Over the last few years, the applicability of this strengthening measure against seismic action has been researched at Delft University of Technology. Experiments on small-scale wallets and full-scale masonry walls have been performed to evaluate the effectiveness of the strengthening method under combined action of settlement and earthquake loading (Licciardello & Esposito, 2019). Additionally, nonlinear finite element analyses have been performed to better understand the response of the full-scale wall test (Drougkas et al., 2020; Mahmoudimotlagh, 2020).

In this research, the effectiveness of the bed joint reinforced repointing strengthening method will be studied at building level by means of nonlinear finite element analysis, since not much research is available on this. With reference to application in practice, the case study of a farmhouse will be considered. The combined effect of settlement and earthquake loading will be studied. Furthermore, a partially reinforced masonry façade will be studied to assess the added benefit of this strengthening technique during the construction stage of the building. In Figure 1.2 an image of a typical farmhouse in the Groningen region is shown.

Figure 1.2 typical farmhouse in Groningen (van Galen, 2008)

1.2 Research objectives and questions

The main objective of this research is to accurately predict the structural performance of a masonry farmhouse retrofitted with bed joint reinforced repointing by means of nonlinear finite element analyses. Modelling choices and assumptions are elaborated further in the literature study (chapter 2), numerical modelling approach (chapter 3) and model validation (chapter 4) chapters. The main research question is formulated as:

What is the added benefit of bed joint reinforced repointing, used as a repair method against settlement, for masonry farmhouses subjected to settlement and seismic loading?

Different sub-questions can be formulated that, by answering them, will lead to easier-to-understand and more logical conclusions to the main research question posed. Three main aspects, that are of importance, are considered here: the most appropriate modelling approach for the posed problem, the added benefit of only bed joint reinforced repointing, under settlement and seismic loading, and the added benefit of bed joint reinforced repointing in partially reinforced masonry, under settlement and seismic loading.

These aspects are made more explicit trough formulation of the research sub-questions, and are formulated as follows:

1. Which modelling approach is most appropriate to simulate progressive damage in masonry strengthened with bed joint reinforced repointing?
2. What is the contribution of bed joint reinforced repointing on the performance of a farmhouse in the Groningen region, subjected to settlement and seismic loading?
3. What is the contribution of bed joint reinforced repointing in partially reinforced masonry on the performance of a farmhouse in the Groningen region, subjected to settlement and seismic loading?

1.3 Research methodology

Answering of the previously posed research questions was done through nonlinear finite elements analysis of a typical farmhouse façade, situated in the Groningen region. Considering that the type of strengthening measure applied acts mainly on the in-plane resistance of the structural elements, only the farmhouse façade was modelled, meaning it was assumed no out-of-plane failure could occur. Analysis was done using the finite element package DIANA (version 10.6).

Before work was started on the typical farmhouse façade, the most appropriate modelling approach, and corresponding modelling assumptions, was validated. This was done through numerical modelling of masonry walls that were experimentally tested at TU Delft previously (Licciardello, Esposito, 2019). Numerical models of the unstrengthened and strengthened wall, retrofitted with bed joint reinforced repointing, were developed. The numerical and experimentally obtained results were compared and discussed. This resulted in a modelling approach that was used in finite element analysis of the large-scale masonry façade.

A series of numerical models of typical unstrengthened façades, found in the Groningen region, were developed and analysed previously at TU Delft (Korswagen et al., 2019). To answer the research questions posed in section 1.2, one of the numerical models investigated, was chosen as a starting point. The numerical model of the chosen unstrengthened façade was refined and extended upon and was used for comparing and assessing the performance of the considered strengthening techniques. In this model, ground settlements, that were present prior to application of the strengthening measures, were simulated by applying a differential settlement profile along the length of the façade. The seismic load was implemented using a nonlinear time history analysis, since this most accurately simulates the structural response of the farmhouse façade as it would be in-field. Soil-structure interaction was modelled according to the Gazetas approach, where the interaction is simulated through a series of distributed springs and dashpots along the foundation of the façade. Based on the characteristics of the facade an orthotropic continuum smeared cracking model called the engineering masonry model was adopted, to accurately simulate the structural behaviour of the masonry façade.

Several numerical models, of the façade, were developed to assess the performance of the strengthening technique considered. First, the unstrengthened model was taken and retrofitted with bed joint reinforcement, where the location of the steel reinforcements was based on the crack patterns obtained after settlement loading. For this model various load levels (peak ground velocities) were considered to see the effect of this parameter on the performance of the applied bed joint reinforcement. Furthermore, a model with partially reinforced masonry was developed, where the bed joint reinforcement was applied prior to settlement loading. This simulates the case where the strengthening technique is applied during the construction stage of the considered façade. A more in-depth description of this process is given in section 5.4. The numerical model of the farmhouse façade considered is shown in Figure 1.3.

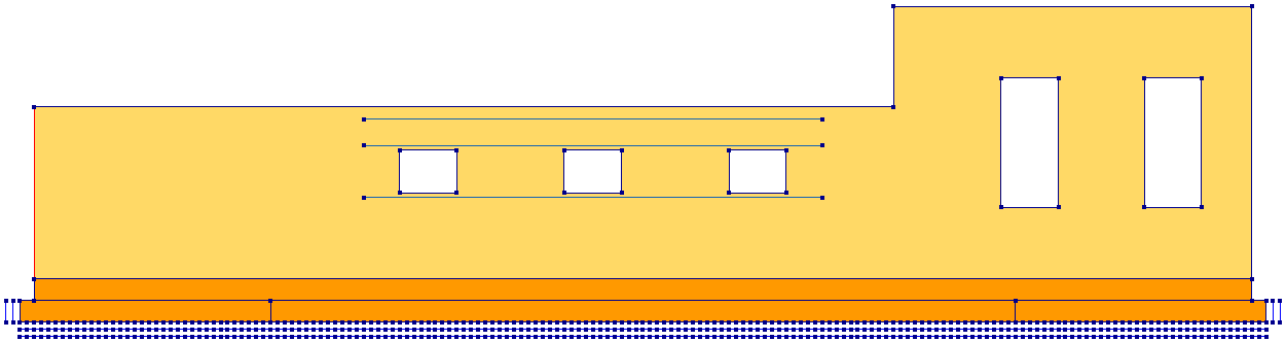

Figure 1.3 numerical model of the farmhouse façade considered (with bed joint reinforced repointing)

1.4 Report outline

This report is divided into six separate chapters. Chapter 1 provides the background problem, gaps, research questions and used research methodology. Chapter 2 shows the results of the performed literature study, where various aspects related to numerical modelling of masonry structures under seismic loading are discussed. Chapter 3 outlines the numerical modelling approach of both the experimentally tested masonry walls, as well as the masonry façade considered. Chapter 4 concerns the validation of the numerical modelling approach used for the masonry facade, by comparing the numerically and experimentally obtained results of the masonry walls. Chapter 5 provides the numerical results obtained for the masonry façade, where comparisons between the different models will be made. Chapter 6 will present the final conclusions and recommendations that follow from the work done in this report.

2 Literature study

A preliminary literature review is presented in this chapter. Failure mechanisms of URM structures are investigated more in-depth. Bed joint reinforced repointing is discussed as well as the different aspect important in numerical modelling of the façade. Finally, seismic analysis methods will be investigated.

2.1 Damage of unreinforced masonry structures

Several mechanisms can be identified that can cause damage to unreinforced masonry structures. In this section the two most relevant for this research are discussed. These are damage due to settlement and seismic loading.

2.1.1 Subsidence-induced damage of unreinforced masonry structures

The damage that is encountered due to settlement of masonry structures is in most cases just in terms of small cracks. Depending on the location of the maximum settlement displacement with respect to the building, small cracks will start to occur either in the lower or upper parts of the masonry structure. This damage is usually not a direct threat to the structural safety of the building, but it can be a starting point for further damaging of the masonry structure (Giardina, 2013). Ground settlement can be seen in Figure 2.1, together with the hogging and sagging parts of the building.

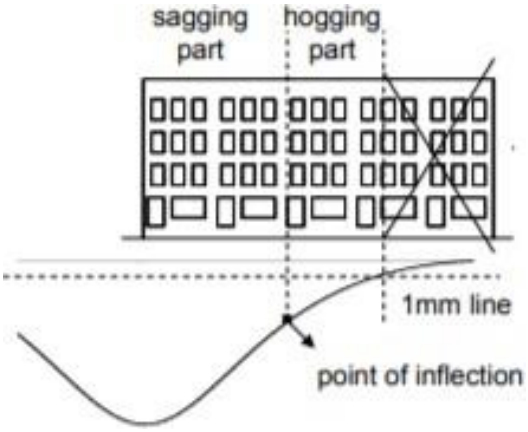

Figure 2.1 sagging and hogging of a building subjected to ground settlement (Giardina, 2013)

2.1.2 Seismic-induced damage of unreinforced masonry structures

URM walls have different failure modes. These failure mechanisms can occur in-plane, but also out-of-plane. Therefore, it is important to consider the failure mechanisms of URM walls in both directions. Interaction between the in-plane and out-of-plane failure mechanisms is possible (Bruneau, 1994).

There are four main in-plane failure mechanisms that can be distinguished in laterally loaded URM walls (El Gawady et al., 2006). These are: shear failure, sliding failure, rocking failure and toe crushing. These in-plane failure mechanisms are visualized in Figure 2.2.

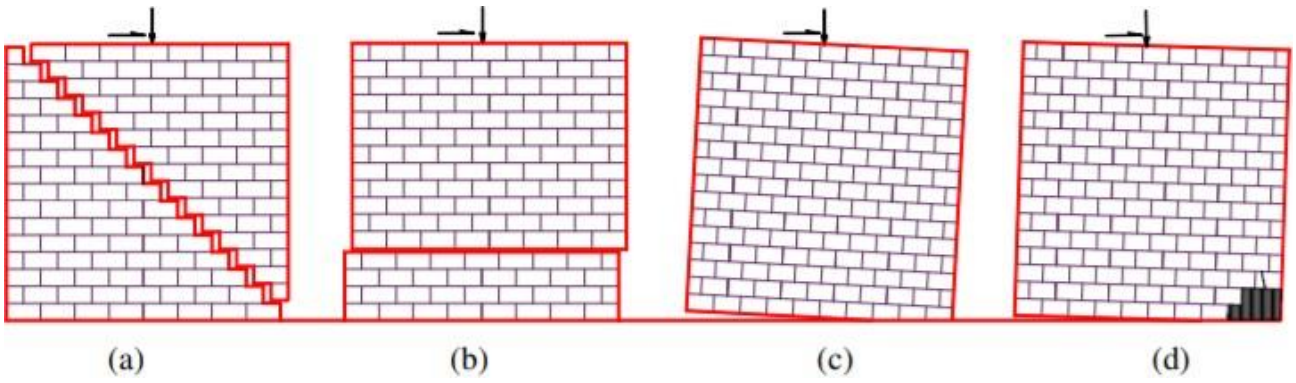

Figure 2.2 in-plane failure mechanisms of URM walls (a) shear failure; (b), sliding failure; (c) rocking failure and (d) toe crushing (El Gawady et al., 2006

Out-of-plane failure mechanism also occur in URM walls. This is due to the bidirectional nature of the earthquake (Bruneau, 1994). But more importantly because of the fact that the investigated facade is not geometrically symmetric in longitudinal and lateral direction, especially due to the application of bed joint reinforced repointing. There are eight main out-of-plane failure mechanisms that can be distinguished (D'Ayala, Esperanza, 2003) as shown in Figure 2.3.

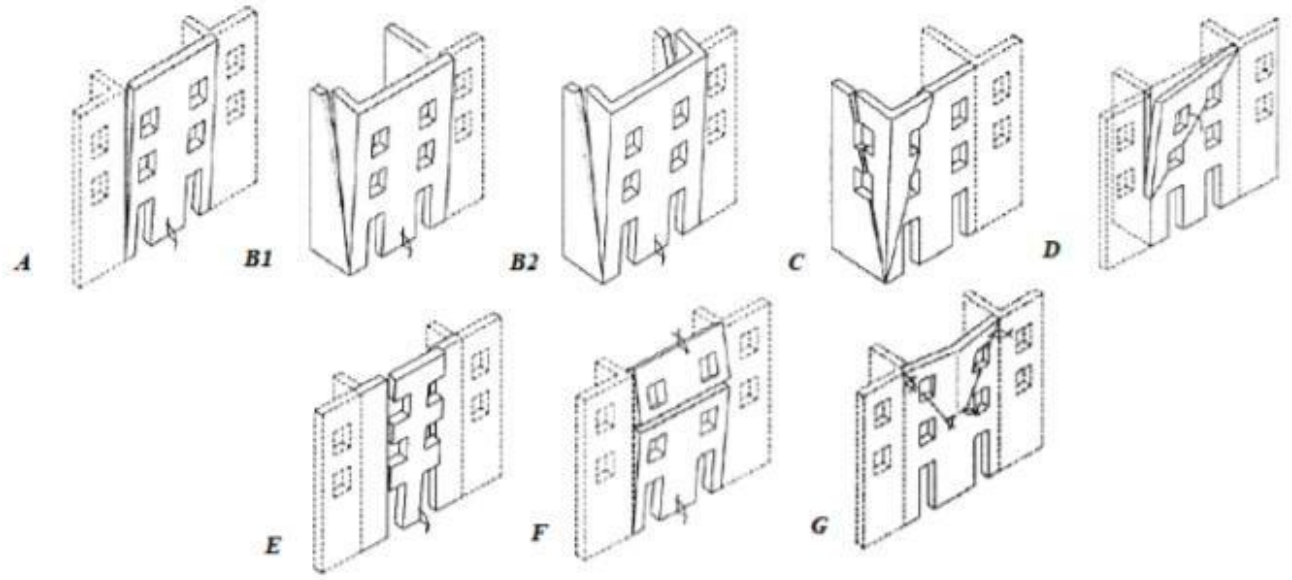

Figure 2.3 out-of-plane failure mechanisms of URM walls (Bui, Limam, 2012)

Not all failure mechanisms shown in Figure 2.3 can be integrated in the numerical model, since the façade is modelled in the 2D-plane. This means that failure mechanism B1, B2, C and G will not be accounted for in this research project.

2.2 Bed joint reinforced repointing

Bed joint reinforced repointing is a strengthening technique commonly applied to URM structures, that suffer subsidence-induced damage, to increase its performance in both ULS and SLS. In the Netherlands it is often used for URM walls that are damaged by ground settlement. Over the last few years research has been set up to see whether its application is effective against human induced earthquakes (Groningen).

The strengthening method includes cutting slots in the masonry's bed joints. Then installing steel reinforcement bars in the cut slot and using repair mortar to fix the bar. The mortar joint is repointed using the original mortar during construction. An extensive list of steps is given below (Licciardello, Esposito, 2019):

The advantage of this strengthening measure is that it increases the capacity of the masonry structure in both ULS and SLS. Since there are a lot of historical buildings in the Groningen area, this strengthening technique, in this case, is more focused towards increasing the SLS performance. Another reason for applying this technique here is the fact that it doesn't alter the aesthetics of the (historical) building after application. The different steps involved in bed joint reinforced repointing are shown in Figure 2.4 and they are:

- Cut a slot with a depth of 40 mm in the 100 mm mortar bed joint, figure 2.4(a);
- Remove the remaining mortar pieces and clean the slot with a vacuum cleaner, figure 2.4(b);
- Wet with clean water the mortar joint before the installation of the spiral ties, figure 2.4(c);
- Mix the repair mortar, HeliBond (figure 2.4(d)), and inject it in the slot using a gun, figure 2.4(e);
- Insert the spiral bar in the repair mortar, figure 2.4(f);
- Inject a second layer of repair mortar in the slot ensuring a complete coverage, figure 2.4(g);
- Repoint the mortar joint by applying the mortar used during the construction of the specimen, figure 2.4(h).

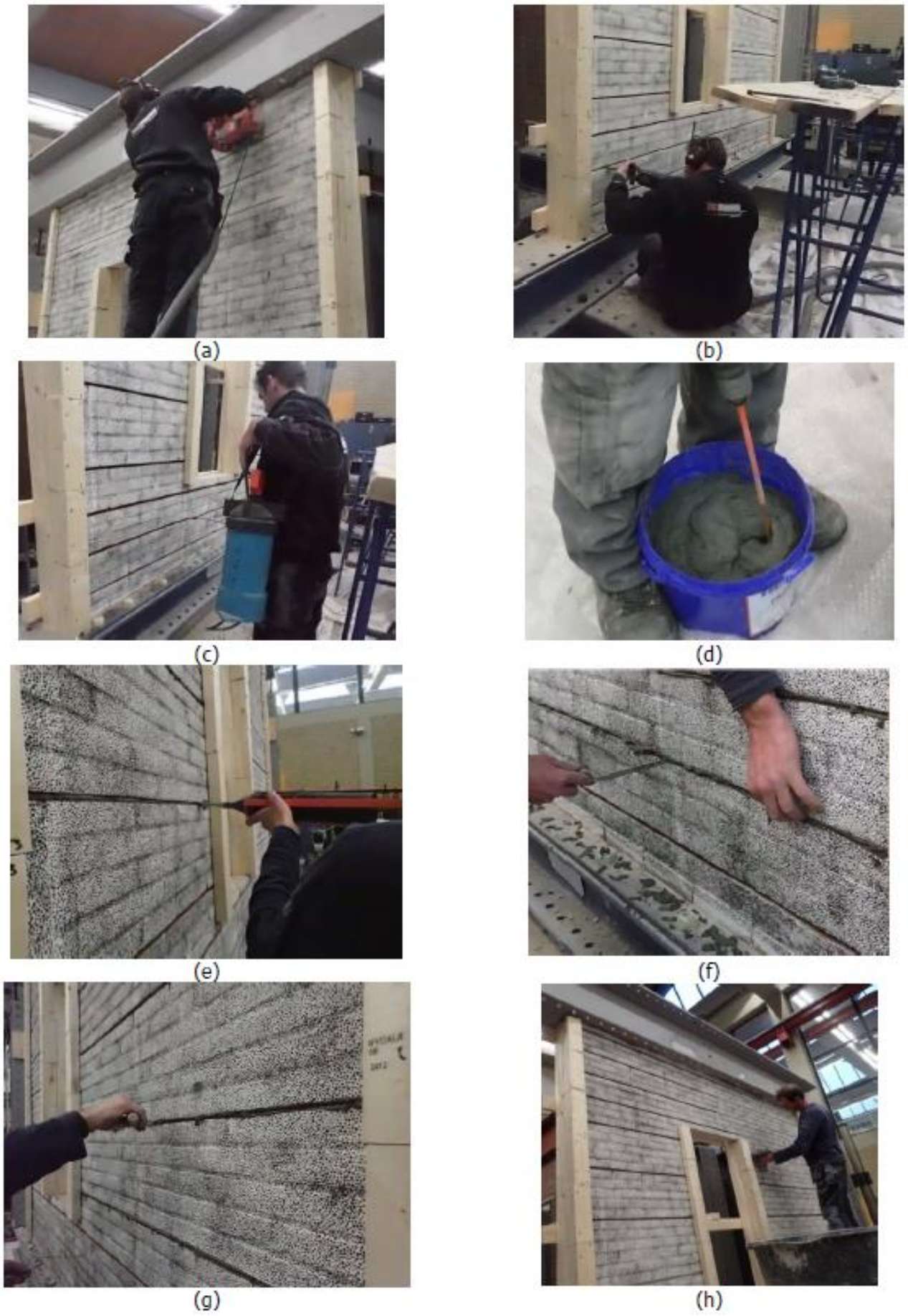

Figure 2.4 installation procedure of the bed joint reinforcement in a URM wall (Licciardello, Esposito, 2019)

2.3 Numerical modelling of masonry structures

Different options are available for numerically modelling the masonry, reinforcing steel and soil-structure interaction. An overview of these options are given in the following sections.

2.3.1 Numerical modelling of the masonry

There are three different ways of modelling masonry elements (Lourenco, 1996). Namely detailed micro-modelling, simplified micro-modelling and macro modelling, as shown in Figure 2.5. The method of modelling the masonry should be chosen in accordance with the specific objectives of the research as well as the required computational time. An optimum between accuracy and efficiency has to be found.

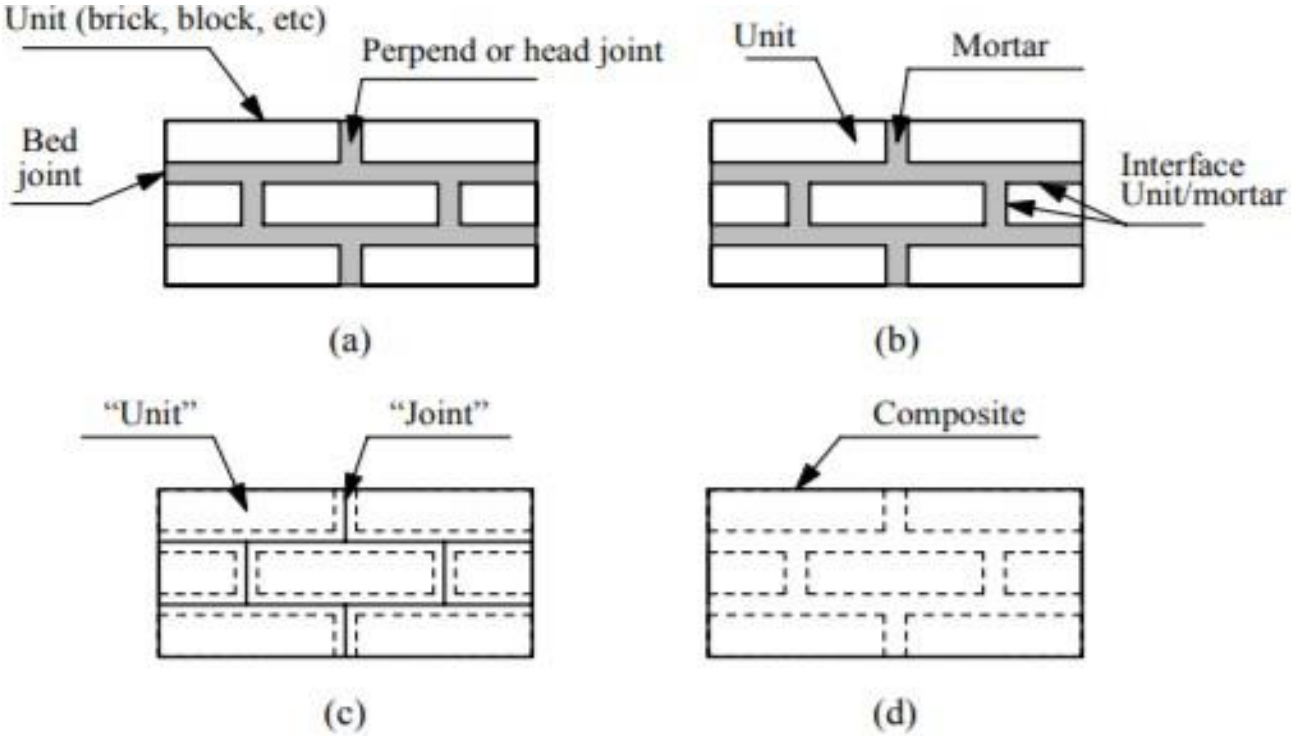

Figure 2.5 modelling strategies for masonry structures (a) physical model of the masonry sample; (b) detailed micro- modelling; (c) simplified micro-modelling and (d) macro-modelling (Lourenco, 1996)

The three different ways of modelling masonry structures are:

- Detailed micro-modelling considers three different aspects of masonry, namely the unit (also called brick), mortar and the interface between these two. The interaction between brick, mortar and interface can be investigated in depth using this modelling strategy.
- Simplified micro-modelling assumes the interface between the mortar and brick and the mortar itself are lumped together to form a line joint. Consequently, the bricks are enlarged to ensure geometrical compatibility of the model. This model is less representative of the physical reality since the Poisson's effect of the mortar is not included.
- Macro-modelling of the masonry is done by lumping the unit, mortar and interface in one homogenous anisotropic continuum. The masonry is modelled as a composite material. Using this modelling method, not all failure modes are taken into account and is therefore more practice oriented (larger structures).

In numerical modelling of masonry, a distinction between two major approaches can be made: the discrete cracking model and the smeared cracking model. Which is more beneficial is dependent on the specific objectives and characteristics of the research project.

The use of interface elements implies that the first two modelling methods, mentioned above, are examples of a discrete cracking approach. The discrete cracking model introduces discontinuities is the displacement field based on the principles of fracture mechanics (Jendele et al., 1996).

Possible crack locations must be predefined by the user using interface elements. If stresses in the crack exceed a predefined value, a crack appears. Numerical modelling of masonry in this manner is labour intensive since every possible crack location has to be manually defined by the user. Using this model one runs the risk that not all possible crack locations are correctly identified beforehand and that, after running the numerical analysis, cracking will propagate in a different manner compared to reality. This will make the results of the finite element analysis less trustworthy. However, this method is very intuitive and easy to conceptualize as the cracks appear how we observe them in reality. Interpretation is thus more straightforward. This approach can give very accurate results, given that all possible crack locations are identified, and implemented, correctly.

The macro-modelling approach is a smeared cracking model. The smeared cracking model smears, as the name suggests, the crack over the area of a mesh generated continuum element regardless of the orientation. Often this area corresponds to the area of one integration point (Jendele et al., 1996). Due to the fact that this approach is less labour intensive and more suitable for analysing larger structures, it is applied more often in practice. This approach can still deliver accurate results and usually reduces the computation requirements significantly. The interpretation of the results, however, is often a bit more tricky and less intuitive due to the fact that the way cracks are modelled in this approach is not how we observe it in reality.

In recent years, more modelling strategies for masonry structures have been developed (D'Altri et al., 2019). These can be divided into four main categories: block-based models, continuum homogenous models, geometry-based models and macroelement models. Each of these modelling approaches has its own advantages and disadvantages.

The discrete cracking model can be identified as a block-based model, while the smeared cracking model is shared under continuum homogenous models. In the geometry-based models the structure is represented as a rigid body, where the geometry of the structure basically represents the only major model input. These models are mainly focused on limit state solutions. In macroelement models two main components of a masonry structure are modelled: the piers and spandrels. These need to be defined beforehand. Macroelement models are mainly used in finding the seismic response of the masonry structures with multiple stories. Due to the limitations of the last two mentioned modelling approaches it is preferred to use either a block-based model or continuum homogenous model.

Engineering masonry model (EMM)

The EEM was developed in 2016 by DIANA FEA in collaboration with Prof. J.G. Rots from Delft University of Technology. It is a smeared failure model that was developed for cyclic loading of masonry structures since the total strain crack model (TSCM) is unable to correctly capture the energy absorption during cyclic loading. This is because the TSCM is based on secant unloading and loading. The EEM, however, can describe the masonry's behaviour more accurately, since it is based on a strong stress decay using the original linear stiffness. Additionally, a shear failure mechanism based on the Coulomb friction failure criterion is included. This means that tension, compression and, more importantly, shear failure is taken into account.

The EMM considers the anisotropy of the masonry by using different stiffness' in the direction of the bed- and head joints with a Poisson's ratio equal to zero, resulting in an orthotropic material. The model can be applied using plane stress elements or curved shell elements. (DIANA 10.4 user's manual, 2020). However, in the past convergence issues have been encountered using the EMM (Mahmoudimotlagh, 2020).

The following failure mechanisms are considered by adopting this model:

- Tensile cracking of the bed joint
- Compressive crushing in the direction normal to the bed joint
- Tensile cracking of the head joint
- Compressive crushing in the direction normal to the head joint
- Cracking in the direction normal to diagonal stair step cracks
- Frictional shear sliding
- Out-of-plane shear failure

There are four predefined cracks in the element's plane. One in the direction of the bed joint, one in the direction of the head joint and two in a diagonal direction defined by a user defined angle that is based on the geometry of the brick-laying. This is shown in Figure 2.6.

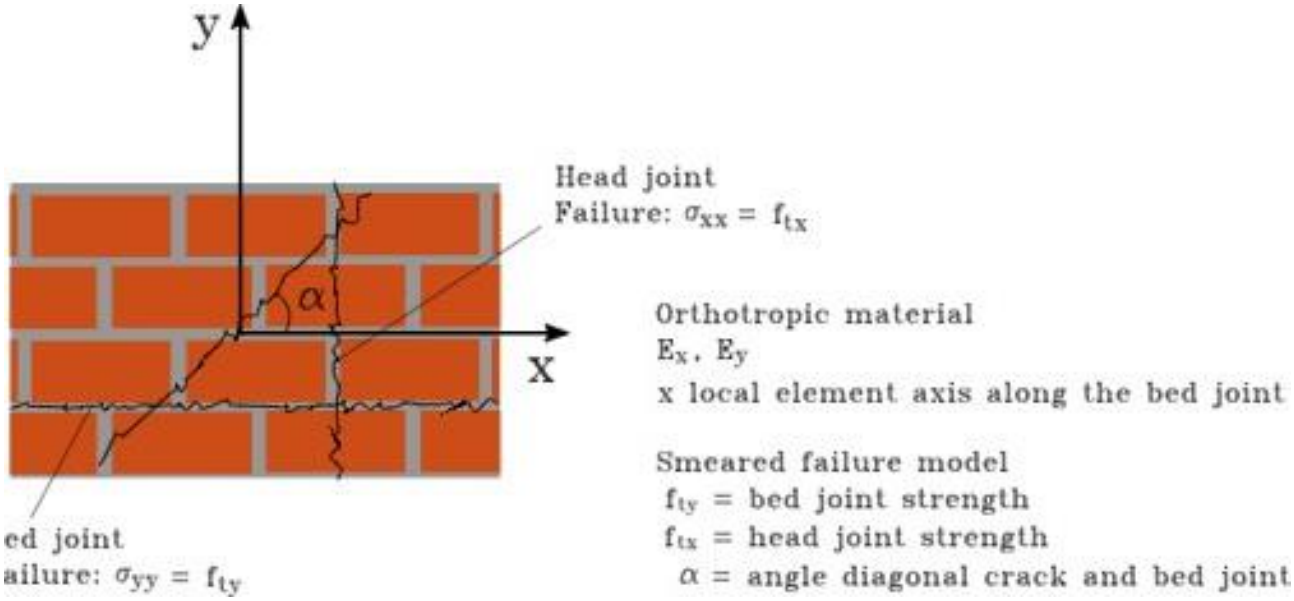

Figure 2.6 characteristics of the EMM (DIANA 10.4 user's manual, 2020)

As mentioned before, the model takes tension (cracking), compression (crushing) and shearing into account. Pre-defined stress-strain models for these failure types are already implemented in the EMM. These are shown in Figure 2.7.

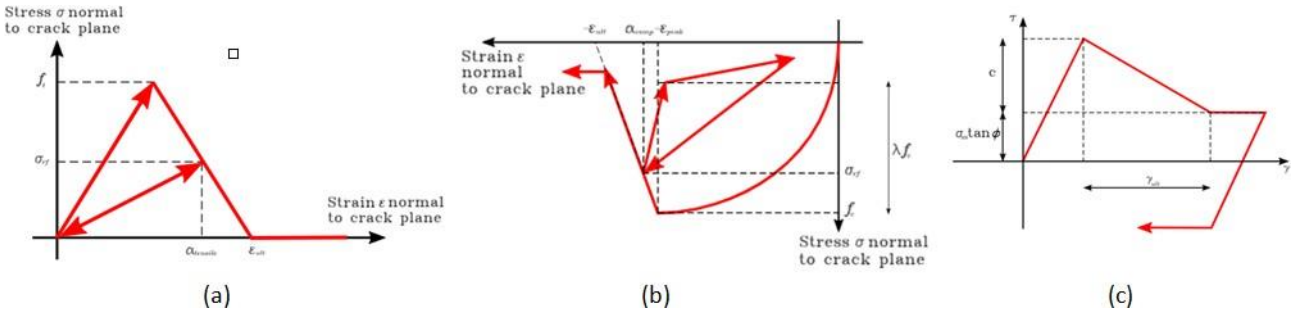

Figure 2.7 stress-strain model for (a) cracking; (b) crushing and (c) shearing (DIANA 10.4 user's manual, 2020)

For cracking the tensile stress-strain curve is defined by the Young's Modulus (E), tensile strength (f_t) and crack energy (G_{ft}) in the bed- and head joint direction, and the band width (h). The softening curve is linear and secant loading and unloading is assumed. See Figure 2.7(a).

For crushing the compressive stress strain curve is defined by the Young's Modulus (E), compressive strength (f_c) and crack energy (G_{ft}), the band width (h) and a factor n defined as:

$$n = \frac{E\varepsilon_{peak}}{f_c} \tag{2.1}$$

This curve is parabolic and there is *no* secant loading and unloading in this case. See Figure 2.7(b).

For shearing the stress-strain curve is defined by the cohesion (c), friction angle (ϕ) and the band width (h). Optionally, a shear energy (G_{fs}) can be specified. If this is the case the cohesion will decrease linearly with the cumulative frictional shear strain γ_{cum} until its value has diminished to zero at a shear strain of $\gamma = \gamma_{ult}$. If the shear energy is not defined the cohesion will be used for all shear strains γ. See Figure 2.7(c).

2.3.2 Numerical modelling of steel reinforcement

Two different methods of numerical modelling of the steel can be considered, namely embedded reinforcements and bond-slip reinforcements.

- When using embedded reinforcements, the reinforcement is fixed inside the continuum elements. This also means that the displacement field of the reinforcement and continuum element is the same. The displacement field of the reinforcement is dictated by that of the so-called mother elements. Including non-linearity and bon-slip behaviour of the reinforcement is not possible. There is a perfect bond between the reinforcement and continuum elements and no bond-slip is allowed to occur.
- When using bond-slip reinforcement the reinforcement is not fixed inside the continuum elements. The displacement field of the reinforcement and continuum elements is not necessarily the same. Including non-linearity of the reinforcement and bond-slip behaviour is possible. There is not a perfect bond between the reinforcement and continuum elements and bond-slip is allowed to occur.

The non-linearity and bond-slip behaviour of the reinforcement must be specified by the user. The non-linearity of the reinforcement is usually provided by the manufacturer and the bond-slip behaviour should be determined based on experimental data. Examples of these relations are shown in Figure 2.8(a) and Figure 2.8(b) respectively.

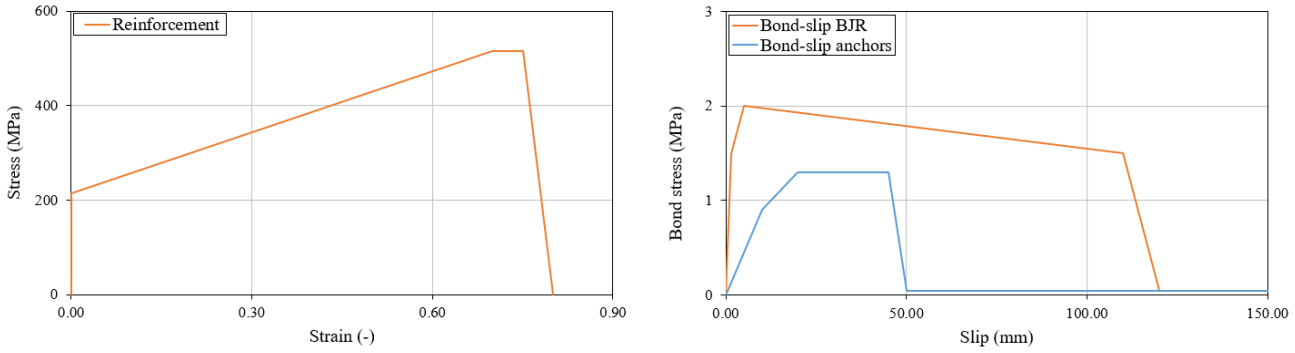

(a) (b)

Figure 2.8 relations of the reinforcement for (a) the non-linearity and (b) the bond-slip behaviour

2.3.3 Numerical modelling of soil-structure interaction

Soil-structure interaction (SSI) can be modelled using springs and dashpots at the soil-structure interface (NEHRP Consultants Joint Venture, 2012). Interaction of the foundation and soil is done by adding a series of distributed vertical and horizontal springs and dashpots at the soil-structure interface. This is shown in Figure 2.9. It should be noted that in the case of a static seismic analysis the need for dashpots disappears and using only distributed springs is sufficient. Strengthening of the foundation is done through restoring the façade to its initial position and/or through an increase in the foundation stiffness.

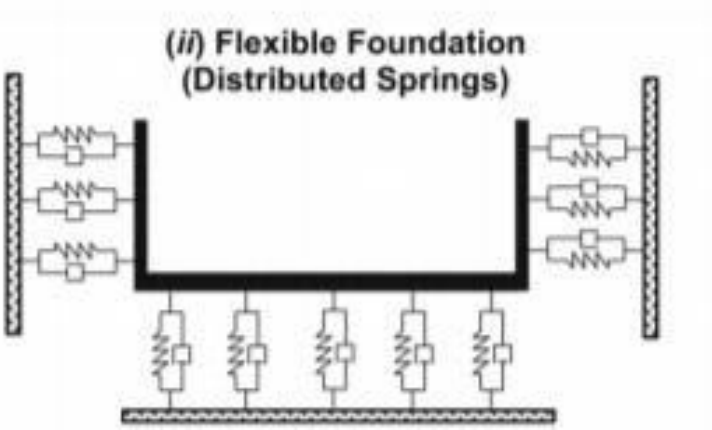

Figure 2.9 modelling soil-structure interaction using distributed springs (NEHRP Consultants Joint Venture, 2012)

2.4 Seismic analysis methods

Human induced earthquakes have been an increasing problem in the Groningen region. Different seismic analysis methods are available for different applications. In this chapter we will only look at the nonlinear analysis methods, as it is expected that cracking and yielding of the material will occur, meaning that a linear procedure is not sufficient.

2.4.1 Eigenvalue analysis

The first step in performing a seismic analysis is the eigenvalue analysis. This is done by obtaining the eigenfrequency and its corresponding modal shapes, which can serve as an input for further seismic investigation. The eigenvalues and modal shapes are dependent on the layout of the structure investigated (DIANA 10.4 user's manual). Since ground settlement is included in the scope of this research, it is harder to determine the modal shapes, as the structure will be deformed prior to the nonlinear finite element analysis.

2.4.2 Pushover Analysis

Pushover analyses are usually useful for assessing the seismic vulnerability of masonry structures. Lateral forces are distributed, in different manners over the height of the structure. Examples are a uniform load distribution over the height, or a parabolic distribution over the height, which can then be lumped into nodal forces over the height of the structure (see Figure 2.10). A pushover analysis is a static, nonlinear seismic analysis method. There are two main types of pushover analysis that are interesting in the context of this research project. These are the modal pushover analysis and the cyclic pushover analysis:

- In the modal pushover analysis an equivalent lateral force distribution, that is approximately equivalent to the first modal shape, is introduced (DIANA 10.4 user's manual). The load is incrementally increased in steps. In this way the structure can be loaded up to failure and a base shear-displacement curve can be constructed, giving information about the seismic capacity of the structure (Najam, 2017).

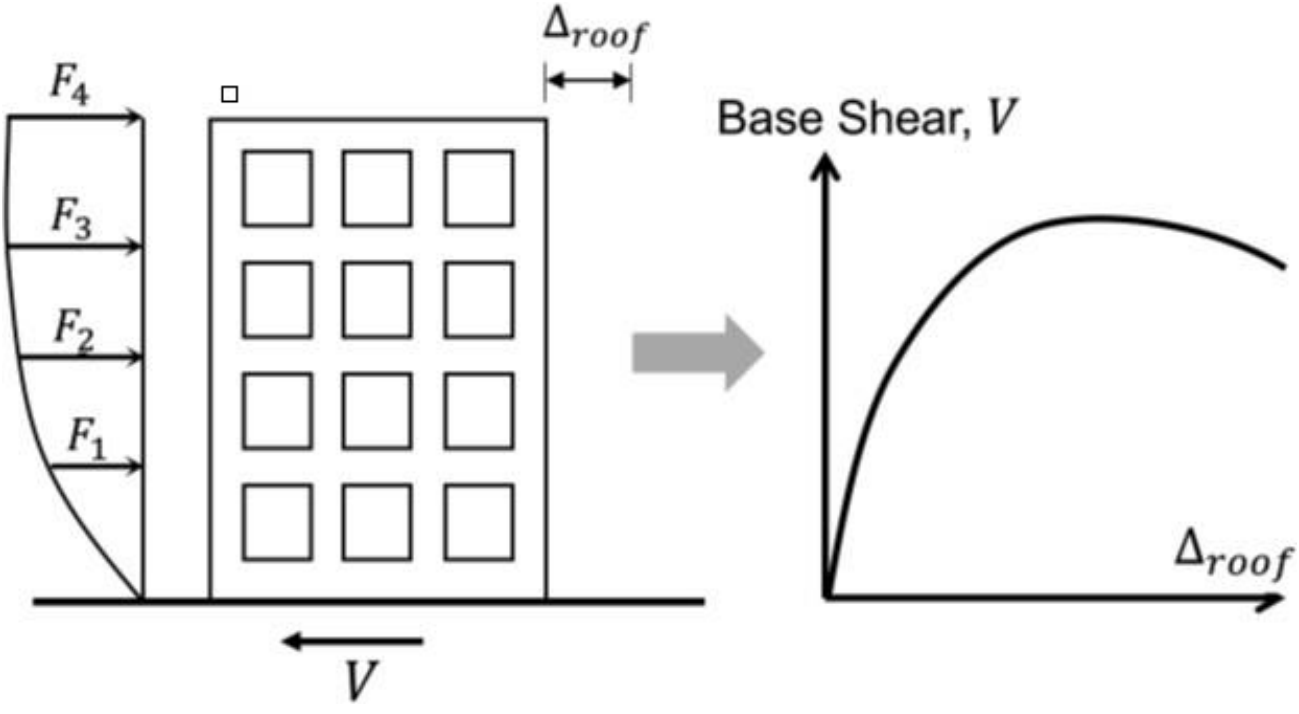

Figure 2.10 modal pushover analysis (Najam, 2017)

- The cyclic pushover analysis is an extension of the conventional pushover analysis. In this analysis the load direction keeps changing in a series of equal but opposite pushover analyses. In every new load step, the stiffness obtained from the previous cycle is used. This causes the cracks to open and close resulting in hysteresis loops in the force-displacement diagram; characteristic of quasi-brittle materials such as masonry. This is shown in Figure 2.11. The green area corresponds to the dissipated energy in a loading cycle.

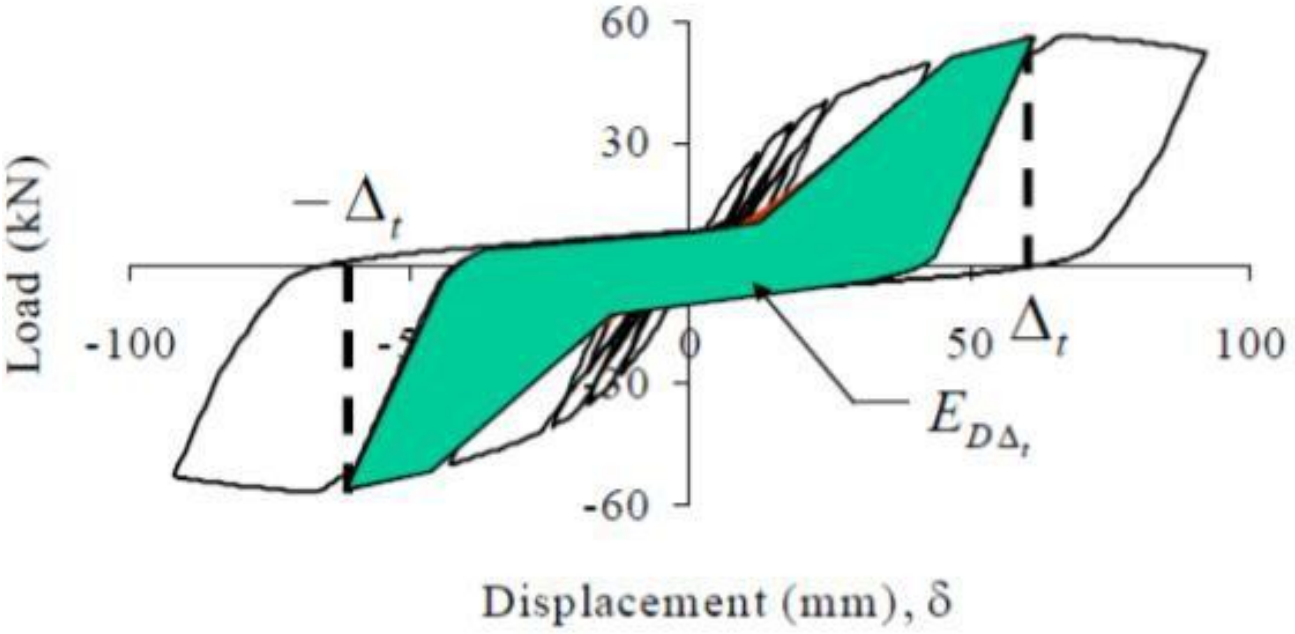

Figure 2.11 cyclic pushover analysis (University of Buffalo, 2009)

2.4.3 Nonlinear time history analysis

In the nonlinear time history analysis, the seismic action is a function of the acceleration (or displacement) and time. This means that the complete structural response in time can be found. The time histories have three different components. Two in the horizontal direction (in- and out of plane) and one in the vertical direction. Using this approach all modes are studied at once, compared to the pushover analysis, which considers only one mode at a time. A nonlinear time history analysis is a dynamic, nonlinear seismic analysis method.

2.4.4 Incremental dynamic analysis

Incremental dynamic analysis uses (like nonlinear time history analyses) recorded ground motions as input for the seismic analysis. A structure is subjected to this ground motion and its structural response is calculated. However, in this type of analysis the ground motion is amplified by certain factors until the structures collapses in ULS. This type of analysis is realistic as it is how the structure would be excited in-field. An incremental dynamic analysis is a dynamic, nonlinear seismic analysis method.

2.5 Conclusions

An unstrengthened (URM) nonlinear finite element model, alongside models including bed-joint reinforced repointing and partially reinforced masonry, were developed. Both ground settlement and seismic loading have been included in these models, to accurately model the in-field conditions of the masonry façade. After validation of the most appropriate modelling approach for simulating progressive damage in masonry, numerical modelling of the masonry façade will be done. It is expected that both bed joint reinforced repointing and foundation strengthening has a positive effect on the structural performance in both in SLS (serviceability limit state) and ULS (ultimate limit state).

In this research an orthotropic smeared cracking model (a macro-modelling strategy of the masonry) named the engineering masonry model (EMM) has been adopted, since mainly the global behaviour of the façade is of interest. Manually introducing interface elements throughout the facade will be too labour intensive, due to the size of the considered façade. Furthermore, this approach would result in a very high computational

requirement, given that every brick is to be modelled individually. Especially when considering the number of steps required to perform the full seismic analysis.

Other smeared cracking models, like the total strain cracking model (TSCM) often underestimate the energy absorption under cyclic loading in the masonry. The engineering masonry model improves on this. It is therefore usually recommended in cyclic loading conditions, such as seismic loading.

To correctly model the situation as it would be in-field, a nonlinear time history analysis was adopted using ground motions (as a base excitation), recorded in the Groningen region. This type of seismic analysis generally provides the most accurate solution in seismic analyses. The downside of this method is that it can be complex to perform and has a high computational requirement, compared to a more simplistic pushover analysis, for example. The reason it was decided against performing an incremental dynamic analysis is simple: this research focuses on both SLS and ULS related issues, which excludes the incremental dynamic analysis as a viable method to research both areas.

3 Numerical Modelling Approach

3.1 Introduction

This section outlines the approach that is followed in numerical modelling of masonry walls, as well as the masonry farmhouse façade. The former is used in validation of modelling assumptions made for the façade, by comparison of the developed nonlinear finite element models with experimental results. This is done in chapter 4. This chapter (chapter 3) describes the most appropriate (followed) numerical modelling approach for simulating progressive damage in masonry retrofitted with bed joint reinforced repointing in more detail. Different aspect of the numerical models will be discussed, including the geometry and finite element model, boundary and loading conditions, constitutive models and analysis procedure.

3.2 Finite element model of masonry walls

Validation of the modelling assumptions made for the façade was done through numerical modelling of an unstrengthened and strengthened wall retrofitted with bed joint reinforcement, which were numerically modelled previously (Drougkas et al., 2020; Mahmoudimotlagh, 2020). The numerical models are based on an experimental campaign done previously at TU Delft (Licciardello, Esposito, 2019). The walls considered, and their characteristics, as tested during the experimental campaign, are presented before the numerical modelling approach is elaborated further.

3.2.1 Experimental campaign

The setup used for testing the masonry walls, named TUD-COMP 41 and TUD-COMP 45 is shown in Figure 3.1(Korswagen et al., 2019). The dimensions of the wall are 3070 × 2690 × 100mm^3 (length × height × thickness). The window opening has dimensions 780 × 1510mm^2 (length × height). The concrete lintel above the window opening has dimensions 980 × 50 × 100mm^3 (length × height × thickness). On top of the wall a steel beam (HEB600) was placed, through which a horizontal monotonic prescribed deformation was applied. A constant overburden stress of 0.12N/mm^2 was present. This includes the weight of the steel beam and some additional dead weight. The bottom of the wall was connected to a steel beam (HEB300) which did not allow for any translation or rotation. The steel frame was set in a cantilever configuration, allowing free rotation of the wall at the top side (Drougkas et al., 2020). Prior to testing pre-damage has been manually introduced at certain points in order to simulate settlement damage of the wall, see Figure 3.1(b).

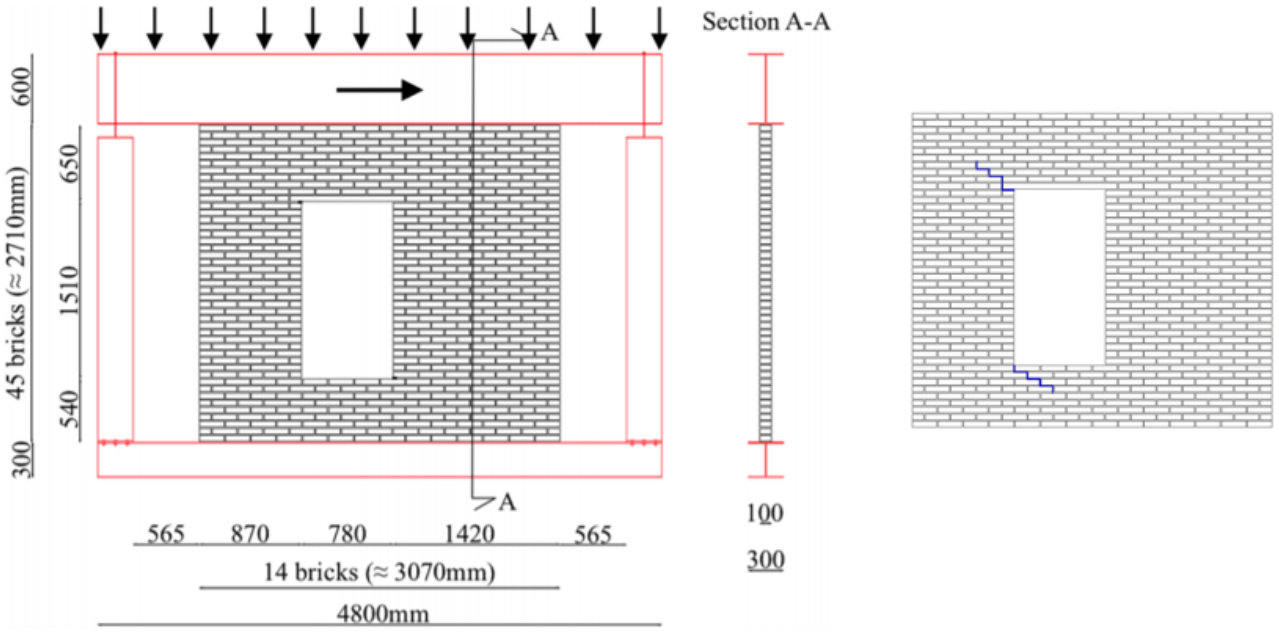

(a) (b)

Figure 3.1(a) test setup of the walls (Korswagen et al., 2019) and (b) initial pre-damage (Licciardello, Esposito, 2019)

Both TUD-COMP 41 and TUD-COMP 45 were tested up to light damage (phase 1 and 2) in multiple cycles, each consisting of 30 runs. After this the wall named TUD-COMP 45 was strengthened using bed joint reinforced repointing and was tested under phase 1 and 2 again, after which both walls were tested up to near collapse (phase 3) in multiple cycles, each consisting of varying amounts of runs. The loading schemes of phases 1, 2 and 3 are shown in Figure 3.2.

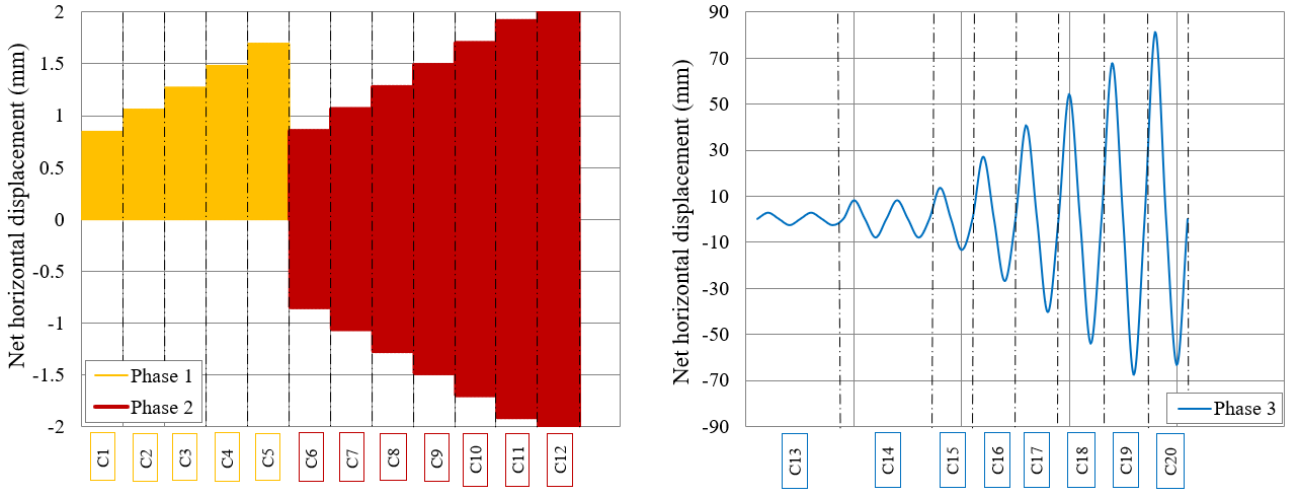

(a) (b)

Figure 3.2 loading scheme for (a) phase 1 and 2 and (b) phase 3

Different aspect of the numerical model will now be discussed, including the geometry and finite element model, boundary and loading conditions, constitutive models and analysis procedure.

3.2.2 Geometry and finite element model

The dimensions of the wall are based on the ones elaborated in section 3.2.1. For the masonry wall and concrete lintel, 8-noded quadrilateral plane stress elements (CQ16M) are considered with a high, 3 × 3 Gauss, integration scheme. The top steel beam is modelled using 3-noded class-III beam elements (CL9BE) with a regular, 2-point Gauss, integration scheme. Considering that the load is applied at the centre of the HEB600 steel beam, the beam elements are placed 300mm above the top of the wall and connected to the plane stress elements via a 3-noded structural interface (CL12I) with a high, 5-point Newton Cotes, integration scheme. An element size of 50mm was selected. The discretization method for the reinforcement is *element-by-element*. In Table 3.1 the finite element types and their properties are given. Figure 3.3(a) shows the finite element model with reinforcements and in Figure 3.3(b) the meshed numerical model.

Structural component	FE type	DOFs	Interpolation scheme	Integration scheme	Shape dimension	Topological dimension	Element count
Masonry wall/ concrete	CQ16M	u_x u_y	Quadratic	3 × 3 Gauss	2D	2D	2816
Steel beam	CL9BE	u_x u_y ϕ_z	Quadratic	2-point Gauss	2D	1D	61
Wall-beam interface	CL12I	u_x u_y	Quadratic	5-point Newton-Cotes	2D	2D	61

Table 3.1 finite element types and their characteristics

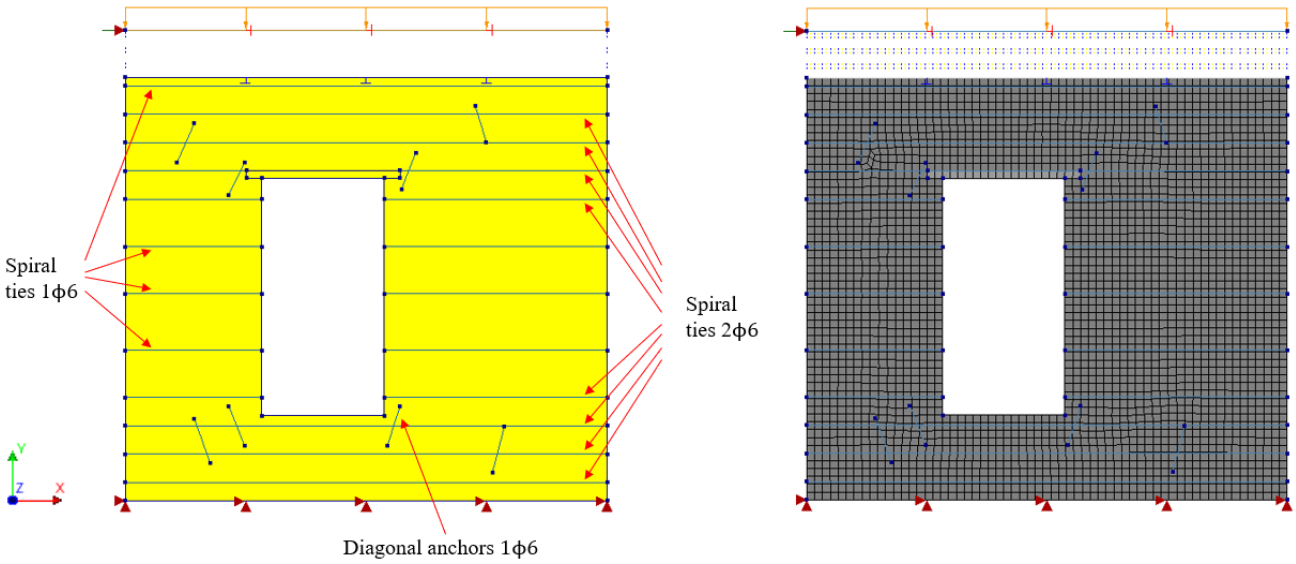

(a) (b)

Figure 3.3 the (a) geometry of the finite element model and (b) meshed geometry of the wall

3.2.3 Boundary and loading conditions

At the bottom side of the wall translation in both the horizontal and vertical direction is restraint. This means the wall, at this location, cannot translate in these directions, as well as rotate in-plane. This ensures that the wanted cantilever configuration is achieved. A support at the top left side of the steel beam is implemented to allow for a horizontal monotonic deformation to be prescribed at this location.

There are different types of loads introduced in the model to best simulate reality. First of all, there is the self-weight of the masonry wall and concrete lintel. This is automatically calculated by the software when entering the mass density of both the masonry and concrete.

Self-weight of the steel beam atop of the wall is present. The mass density of the steel beam is entered as 0, since the self-weight of the steel beam, along with some other dead loads, is already included in the overburden pressure (σ_y) of 0.12N/mm^2. This means that the line load used is:

$$q_y = \sigma_y \cdot t_{wall} = -12 \text{ N/mm} \quad (1)$$

Since there is a peak in the capacity curves it was decided to apply a prescribed deformation at the top of the steel beam in order to correctly capture the post-peak behaviour. It is important to note that while in the experiments a cyclic load was applied, in this study monotonic loading conditions are considered; separate monotonic analyses are performed in the negative and positive loading direction. The magnitude of the prescribed deformation is set in increments of 0.04mm up to -40mm and +44mm for the negative and positive loading direction respectively for the unstrengthened masonry wall. For the strengthened wall this was up to -67.2mm and +81.2mm.

3.2.4 Constitutive models

For different parts of the model, different constitutive models have been considered. These are the masonry, the concrete lintel and beam, the beam-wall interface and the reinforcement. In this section these are elaborated in more detail.

Masonry

The masonry was modelled using the engineering masonry model (EMM). After preliminary analyses it was decided that the head-joint failure type ‘tensile strength defined by head-joint friction’ is in best agreement with the experimental results. The material properties used in the numerical simulations are based on tests done during an earlier experimental campaign (Licciardello, Esposito, 2019) focused on material characterisation.

The specimens constructed in July 2018 are taken as reference for the input of the EMM parameters in study of the walls, because these were constructed in the same period as the tested walls. If no data is available for certain properties during this construction period, the experimental data obtained from the specimens constructed in October 2016 is used (in practice this means only the elasticity parameters). The walls were tested in 2019.

In accordance with Eurocode 6 (NEN-EN 1996, 2005) the shear modulus is taken as:

$$G_{xy} = 0.4E_y \tag{3.1}$$

The bed- and head-joint tensile strength and tensile fracture energy are calculated as follows:

$$f_t = f_{tx} = f_{ty} = \frac{2}{3} f_w \tag{3.2}$$

$$G_{ft} = 0.025(2f_t)^{0.7} \tag{3.3}$$

Where f_w is defined as the masonry flexural bond strength with the moment vector parallel to the bed joints and in the plane of the wall.

The friction angle is calculated from the coefficient of friction as follows:

$$\phi = tan^{-1}(\mu) \tag{3.4}$$

The angle between stepped diagonal crack and bed joint (α) is based on the brick dimensions, which are 210 × 50 × 100mm^3 (length × height × thickness).

The factor to strain at compressive strength, as well as the unloading factor, are based on the masonry type. In an experimental campaign carried out at TU Delft previously, solid clay bricks were used, which have a factor to strain at compressive strength of n = 1.6. The unloading factor is not applicable in this scenario, since only monotonic pushover analyses have been done and no cyclic loading is included in numerical analysis of the walls.

The fracture energy in shear is not based on this experimental campaign, because it was never recorded. Instead, it has been taken from an earlier experimental campaign carried out at TU Delft (Jafari, Esposito, 2017)

Table 3.2 shows an overview of the EMM parameters in numerical analysis of the walls, as well as the farmhouse façade. The table includes the experimentally determined material properties, as well as the values given by different authors. The last column includes the author's own choices.

			Material properties of the walls					Material properties of the façade
Property	**Symbol**	**Unit**	**From experiments**		**Used in numerical modelling of the walls**			
Elasticity parameters			October 2016	July 2018	Mahmoudimotlagh	Drougkas	Frankenmolen	
Elastic modulus of masonry parallel to bed joints	E_x	MPa	3207	-	3207	2497	3207	1450
Elastic modulus of masonry perpendicular to bed joints	E_y	MPa	4590	3190	4590	3571	4590	2000
Shear modulus of masonry	G_{xy}	MPa	-	-	1627	1500	1836	900
Masonry density	ρ	kg/m^3	1708	1628	1708	1624	1628	1600
Cracking parameters								
Masonry flexural strength	f_x	MPa	0.16	-	-	-	-	-
Flexural bond strength (MPa)	f_w	MPa	0.15	0.08	-	-	-	-
Bed joint tensile strength	f_{ty}	MPa	-	-	0.107	0.08	0.053	0.05
Minimum head-joint tensile strength	f_{tx}	MPa	-	-	0.107	0.08	0.053	0.15
Fracture energy in tension	G_{ft}	N/mm	-	-	0.0085	0.0069	0.0052	0.0025
Residual tensile strength	$f_{t,res}$	MPa	-	-	-	-	-	-
Angle between stepped diagonal crack and bed joint	α	rad	-	-	0.5	0.5	0.5	0.5
Crushing parameters								
Compressive strength	f_c	MPa	14.02	12.93	12.93	11.35	12.93	4.0
Fracture energy in compression	G_{fc}	N/mm	28.52	28.63	28.63	35.59	28.63	10.0
Factor to strain at compressive strength	n	-	-	-	4	3	1.6	1.6
Unloading factor	u	-	-	-	0.25	1	-	0.85
Shear failure parameters								
Coefficient of friction	μ	-	0.69	0.82	-	-	-	-
Friction angle	ϕ	rad	-	-	0.6868	0.6868	0.6868	0.50
Cohesion	c	MPa	0.20	0.13	0.13	0.13	0.13	0.075
Fracture energy in shear	G_{fs}	N/mm	-	-	0.15	0.3	0.15	0.025

Table 3.2 EMM material properties for the masonry of the walls by different authors, and the farmhouse façade

Concrete lintel and steel beam

Since the concrete is stronger and stiffer than the masonry, cracking of the concrete lintel is not expected. Consequently, a linear isotropic constitutive model is adopted for the concrete. The same holds for the steel beam; it is modelled with a linear isotropic constitutive model. The material properties of the concrete lintel and steel beam are given in Table 3.3.

Element	Young's Modulus (N/mm^2)	Poisson's ratio (-)	Mass density (kg/m^3)
Concrete lintel	20000	0.2	2400
Steel beam	210000	0.3	0

Table 3.3 material properties of the concrete lintel and steel beam

Wall-beam interface

Since the HEB600 beam is glued on top of the masonry wall, it is assumed there is no slip between the steel beam and masonry wall. To ensure this a linear elastic interface is applied at the wall-beam interface. A dummy stiffness is introduced that is not too high, which could lead to problems in the analysis of the wall. The dummy stiffness' are calculated as:

$$k_n = \frac{1000 \cdot E_s}{l_{mesh}} = 4.2 \cdot 10^6 \text{ N/mm}^3 \tag{3.5}$$

$$k_t = \frac{1000 \cdot G_s}{l_{mesh}} = 1.6 \cdot 10^6 \text{ N/mm}^3 \tag{3.6}$$

Where the shear modulus of steel is taken as 80GPa. The term l_{mesh} is the element size used, equal to 50mm.

Steel reinforcement

Two types of steel reinforcement can be distinguished, namely the bed joint reinforcement (BJR) and diagonal anchors. All the bars have a diameter of 6mm. For the location of the reinforcements see Figure 3.3(a). Both have the same stress-strain diagram given in Figure 3.4(a). The yield stress of the steel reinforcement is 215MPa, while the maximum stress is 515MPa. The bond-slip relation is different for the bed joint reinforcement and diagonal anchors. These can be found in Figure 3.4(b).

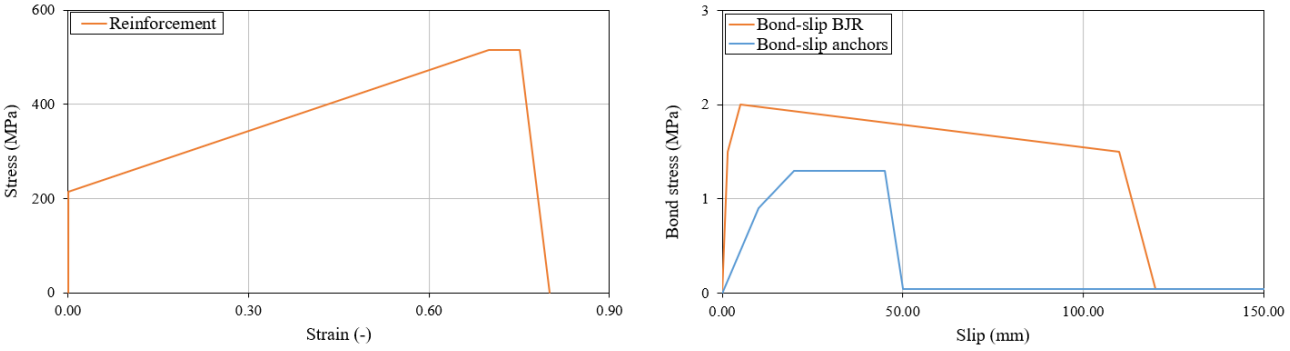

(a) (b)

Figure 3.4 the(a) stress-strain diagram of reinforcing steel and (b) bond-slip relation BJR and diagonal anchors

3.2.5 Analysis procedure

The analysis procedure of the unstrengthened wall was carried out with the secant method using the Broyden-Fletcher-Goldfarb-Shanno (BFGS) method based on the previous iteration. Due to convergence issues the strengthened case was carried out using the Regular Newton-Raphson method based on tangential stiffness. A line search was implemented to reduce the amount of non-convergence. For both analyses a reference case was adopted. In this reference case a load step size of 0.04mm was used. The use of arc-length control has been excluded. A displacement *or* force convergence norm of 0.005 was implemented. Both geometrical and material nonlinearity have been considered. The parallel direct sparse method is used for solving the system of equations, with a tolerance of 10^{-6} with a maximum of 250 iterations. Four variations cases were carried out to find the analysis setting giving optimal results in terms of initial stiffness, peak load, crack pattern and crack widths. These are presented and discussed in section 4.2.1.

3.3 Finite element model of masonry façade

Basic numerical models of the farmhouse façade have been developed previously at TU Delft. This model was used as a starting point and built upon and extended further. The numerical modelling approach, and corresponding assumptions, are outlined in more detail in this section. As stated before, these modelling assumptions were verified by numerical models, based on an experimental campaign done at TU Delft (Licciardello, Esposito, 2019), in chapter 4. It was decided that in numerical modelling of the farmhouse façade the EMM would be adopted.

The masonry façade is comprised of two parts: the left side of the façade, which is part of the shed, and the right side of the façade, which is part of the house. The dimensions are $12.0 \times 2.4 \times 0.21m^3$ (length × height × thickness) and $5.0 \times 3.8 \times 0.21m^3$ respectively. Thus, the total length of the façade is 17.0m. Three small window openings, with dimensions $0.8 \times 0.6m^2$ (length × height) are located around the middle of the façade. Two larger window openings, with dimensions $0.8 \times 1.8m^2$ are located on the right side of the façade. This part of the façade is shown in yellow in Figure 3.5.

The foundation of the façade has a total height of 0.6m. This is split up into two parts: an upper part, of 0.3m, with the same thickness as the wall above, and a lower part, also of 0.3m, with a thickness of 0.61m. Furthermore, the lower part of the foundation extends by 0.2m on either side of the façade, giving it a total length of 17.4m. This is shown in orange in Figure 3.5. For clarity's sake the external loads, boundary conditions and interface connections have been omitted in this figure. In the rest of this section, the numerical modelling approach is elaborated further.

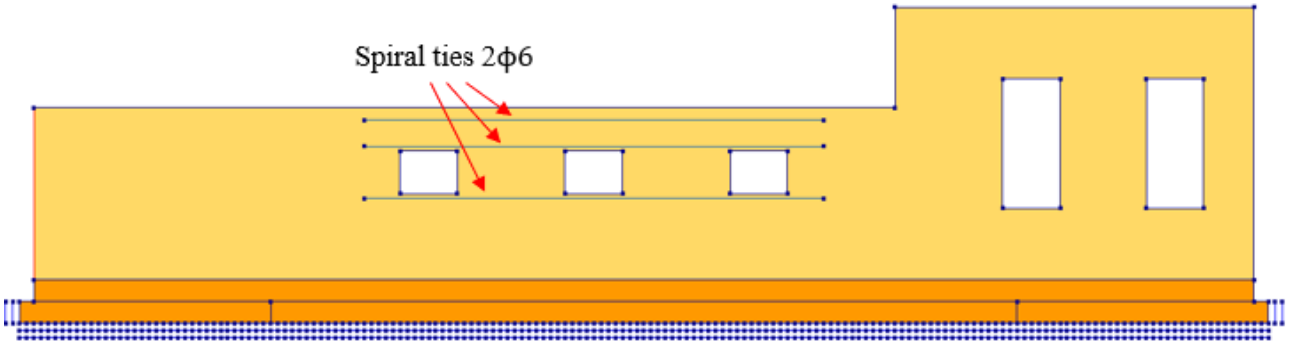

(a)

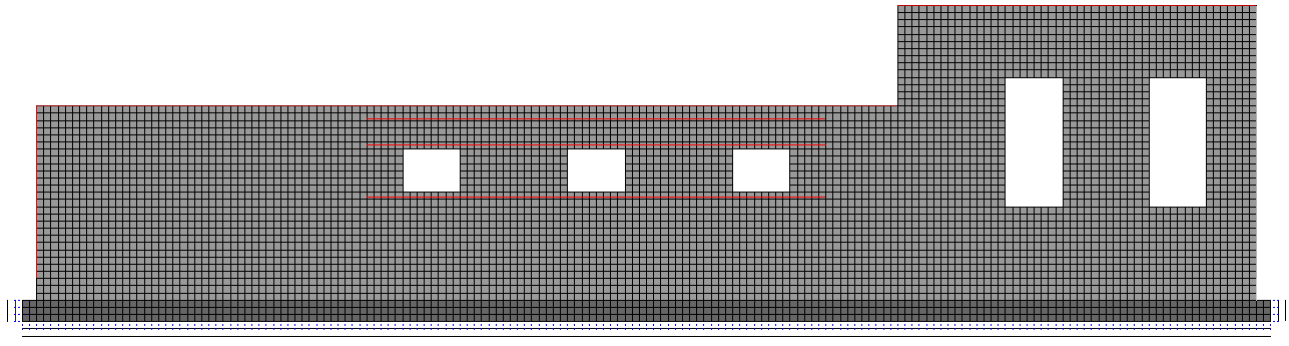

(b)

Figure 3.5 the (a) geometry of the finite element model and (b) meshed geometry of the façade

3.3.1 Geometry and finite element model

A short description of the geometry and finite element model of the façade is presented in this section. Table 3.4 shows an overview of the finite element types and their properties. For clarity, these are broken down into several aspects below, namely: the masonry façade and foundation, lateral constraints and dummy elements, soil-structure interface and mass elements. The finite element types and integration schemes are based on the ones used in analysis of the masonry walls. An element size of 100mm was selected. The discretization method for the reinforcement is *element-by-element*. Figure 3.5(a) shows the finite element model with reinforcements and in Figure 3.5(b) the meshed numerical model is shown.

Structural component	FE type	DOFs	Interpolation scheme	Integration scheme	Shape dimension	Topological dimension	Element count
Masonry façade/ foundation	CQ16M	u_x u_y	Quadratic	3 × 3 Gauss	2D	2D	5380
Lateral constraints /dummy elements	CL9BE	u_x u_y ϕ_z	Quadratic	2-point Gauss	2D	1D	428
Soil-structure interface	CL12I	u_x u_y	Quadratic	5-point Newton-Cotes	2D	2D	360
Mass elements	CL6TM	u_x u_y	Quadratic	3-points Gauss	2D	1D	232

Table 3.4 finite element types and their characteristics

Masonry façade and foundation

The dimensions of the masonry façade and foundation are based on the ones elaborated in section 3.3. For these parts of the facade 8-noded quadrilateral plane stress elements (CQ16M) are considered, with a high, 3 × 3 Gauss, integration scheme.

Lateral constraints and dummy elements

Two lateral constraints were placed at either side of the façade, to account for the effects (constraints) of the out-of-plane vertical walls. These linear elastic beam elements have a fictitious cross-section of $0.21 \times 0.21 m^2$, the thickness of the wall. Furthermore, massless dummy elements were applied below and to the side of the foundation, at an arbitrary location, for implementation of the soil-structure interface. Modelling of these elements was done using 3-noded class-III beam elements (CL9BE) with a regular, 2-point Gauss, integration scheme

Soil-structure interface

To reduce the computational effort required, it was decided to not model the soil itself, but instead model its effects trough soil-structure interaction. This was done in the form of a series of vertically and horizontally distributed springs and dashpots, which were connected to two sets of dummy elements for both the springs and dashpots, and the foundation of the façade. For the soil-structure interaction 3-noded structural interface elements (CL12I) are considered, with a high, 5-point Newton-Cotes, integration scheme.

Mass elements

To account for inertia effects of the structure under earthquake loading, distributed mass elements are used at the free-standing edges of the façade (yellow part in Figure 3.5). For the mass elements 3-noded line elements (CL6TM) are considered, with a high, 3-point Gauss, integration scheme. In Table 3.4 all these finite element type and their properties are given.

3.3.2 Boundary and loading conditions

In the numerical model of the farmhouse façade, horizontal and vertical restraints are applied over the length of both sets of dummy elements, which are in turn connected to the foundation through interface elements. This ensures that the soil-structure behaviour is correctly observed when seismic loading is applied at the dummy elements.

There are three distinct loading phases during analysis, namely: gravity loading, settlement loading and seismic loading. These loading phases are in a sequential order and will be discussed in more detail below. For the analysis procedure of each loading phase, please refer to section 3.3.4.

Gravity load

During this phase the self-weight of the various parts of the façade are used to calculate the gravity load. Furthermore, a vertical overburden load (σ_y), due to timber floors and a timber roof, is present at the top of both the left and right side of the façade. The pressures are 3kPa and 20kPa respectively. This means that the line loads, used for the left and right side respectively, are:

$$q_{y,l} = \sigma_{y,l} \cdot t_{wall} = -0.62 \text{ N/mm} \tag{3.7}$$

$$q_{y,r} = \sigma_{y,r} \cdot t_{wall} = -4.48 \text{ N/mm} \tag{3.8}$$

Settlement load

A settlement load was introduced to simulate pre-existing masonry damage. This was implemented by applying a settlement, with a certain shape and amplitude, along the foundation of the façade (with length 17.4m). The settlement shape considered is depicted in Figure 3.6. The maximum amplitude of the settlement was set to -4.90mm.

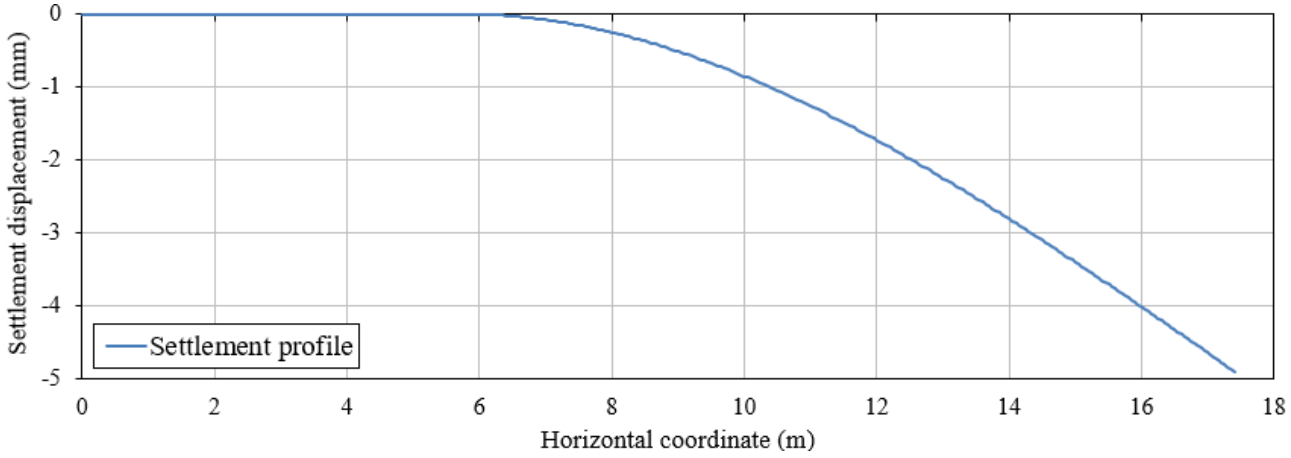

Figure 3.6 settlement profile along the foundation

Seismic load

The seismic load that is used as ground motion is the Zeerijp earthquake in 2018. Previous research (Korswagen et al., 2019) considered two different seismic stations, one located *near* the epicentre, and one located *far* from the epicentre. Furthermore, two different soil types: soil A (a good soil) and soil B (a bad soil) were considered. The soil properties were extracted from existing soil profiles, taken from the Groningen region. This research has shown that for the farmhouse façade considered in this research, the combination of soil A and the far earthquake is critical. This is the basis for the research done in this thesis.

The acceleration time-history of the far earthquake has been recorded by a seismic station. Since residual base drift of the façade was observed during earlier research, using acceleration time-histories, it was decided to instead use the displacement time-history. Double integration was performed on the provided data to obtain the displacement time-history.

To reduce the computational effort required, it was decided to cut-off part of the signal at the beginning and end. The part of the signal with displacements smaller than 1/20th of the peak amplitude was removed; this value was chosen to ensure the main status of the structure would not change due to the resulting cut-off. Ultimately, a PGV of 64mm/s was determined critical and still likely to occur in this area of the Groningen region. This corresponds to a maximum amplitude of the horizontal displacement of 4.46mm. The results, for the horizontal and vertical displacement time-histories, can be found in Figure 3.7 and 3.8 respectively. The seismic load was then applied to the dummy elements used for connecting the distributed springs.

Time shift and spatial amplification/reduction are considered to more realistically model the structural behaviour of the façade. This is especially crucial considering we are dealing with a long façade. Time shift accounts for the fact that it takes time for seismic waves to travel along the foundation, while spatial amplification/reduction accounts for the increase or decrease of energy of the seismic wave while it propagates through the soil. The values used are taken at foundation level, based on a soil model previously developed (Korswagen et al., 2019). The results, for both the horizontal and vertical direction, can be found in Figure 3.9 and 3.10. It is important to note that these values are discretized, since a step-size of 1ms was selected in the analysis procedure (see section 3.3.4).

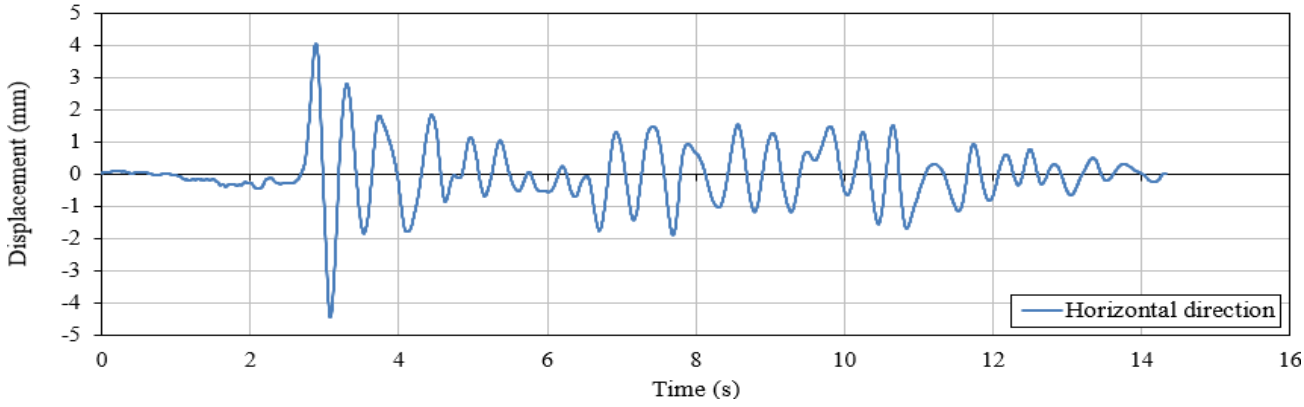

Figure 3.7 Normalised displacement time-history of the seismic record in horizontal direction

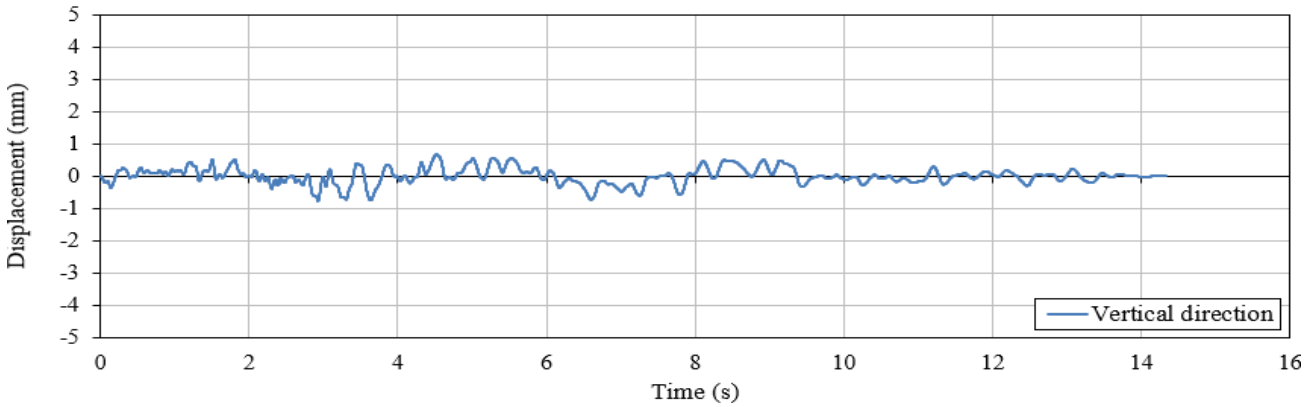

Figure 3.8 Normalised displacement time-history of the seismic record in vertical direction

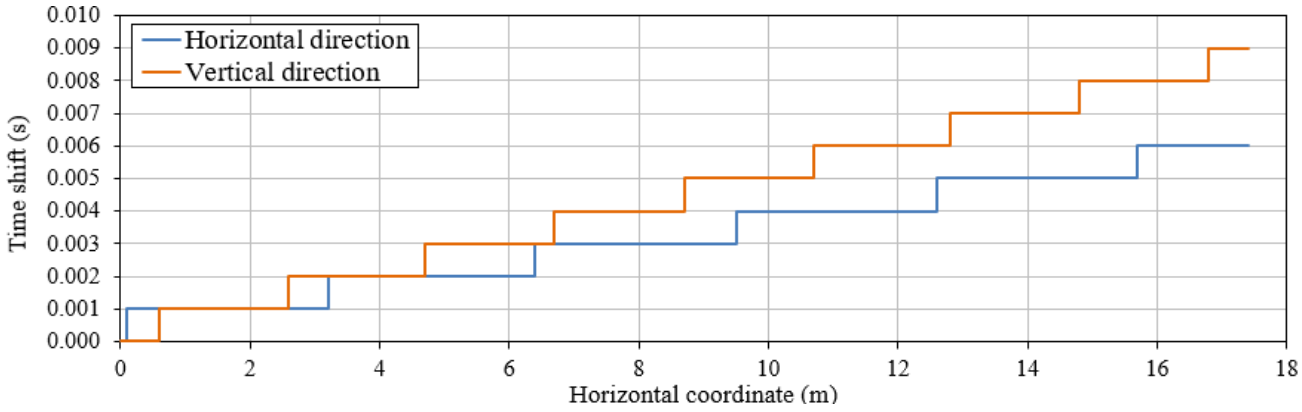

Figure 3.9 Time shift of displacements in horizontal and vertical direction along the foundation

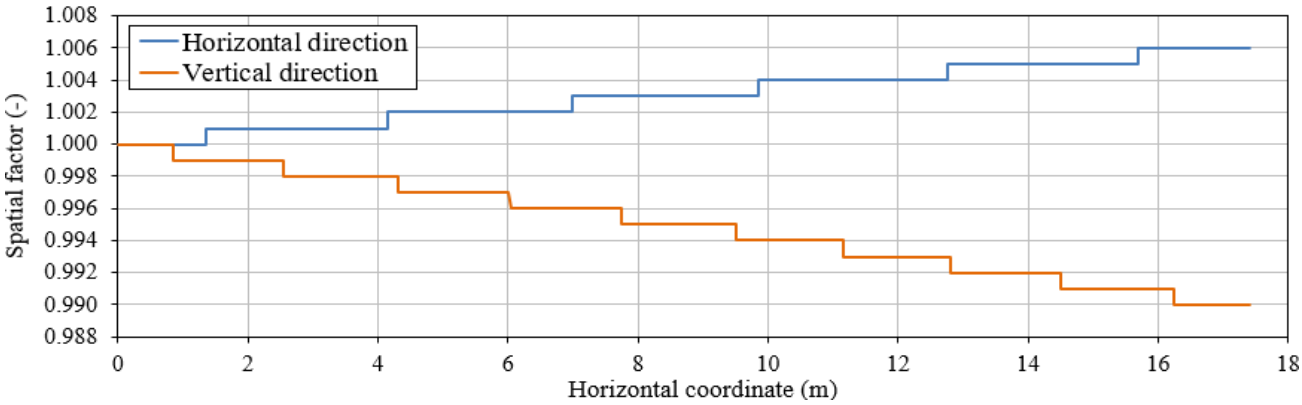

Figure 3.10 Spatial amplification/reduction of displacements in horizontal and vertical direction along the foundation

3.3.3 Constitutive models

Rayleigh damping has been included in the numerical models and is defined as follows:

$$\boldsymbol{C} = a\boldsymbol{M} + b\boldsymbol{K} \tag{3.9}$$

Where the damping matrix, **C**, is a product of the mass and stiffness matrices, **M** and **K** respectively. A 2% damping base on the first two modes is used. The damping coefficients, a and b, are found through eigenvalue analysis of the façade. These are:

$a = 1.9297$ /s
$b = 1.8401 \cdot 10^{-4}$ s

For different parts of the model, different constitutive models have been considered. These are the masonry and foundation, the lateral constraints and dummy element, the soil-structure interface, the mass elements and the steel reinforcement. In this section these are elaborated in more detail.

Masonry

The masonry façade was modelled using the EMM. A summary of the material properties of the masonry, used in analysis of the farmhouse façade, can be found in Table 3.2, given previously. Verification of this smeared failure model is shown in chapter 4. The material properties of the masonry are different for the façade, compared to the walls. Here, the material properties are taken from a previous investigation (Korswagen et al., 2019) of the façade, which were based on the masonry conditions in-field. The masonry and foundation were assigned the same material properties. Now, the unloading factor is of importance in analysis due to the presence pf seismic (cyclic) loading. It was found to be 0.85, meaning unloading occurs closely to the linear elastic branch (Jafari, 2021).

Lateral constraints and dummy elements

The two lateral constraints, used to account for the effects (constraints) of the out-of-plane vertical walls, are modelled using a linear isotropic constitutive model. These two linear elastic beam elements have the same elastic modulus perpendicular to the bed joints (E_y) as the in-plane walls.

The dummy elements, used in the implementation of the soil-structure interface, have also been modelled using a linear isotropic constitutive model. The material properties of the lateral constraints and dummy elements are given in Table 3.5.

Element	Young's Modulus (N/mm^2)	Poisson's ratio (-)	Mass density (kg/m^3)
Lateral constraints	2000	0.16	0
Dummy elements	9999	0.09	0

Table 3.5 material properties of the lateral constraints and dummy elements

Soil-structure interface

Soil-structure interaction has been accounted for through a series of vertically and horizontally distributed springs and dashpots. Two sets of dummy elements were placed around the perimeter of the foundation of the façade: one for the springs and one for the dashpots. The interfaces were configured in the following way:

1. The springs were implemented using a non-linear interface with certain stiffness moduli and a Coulomb friction law. A cohesion of 0.1N/mm^2 and a friction/dilatancy angle of 0.61 rad was used. No tensile strength is assigned as to prevent the façade being pulled down during application of the settlement load.
2. The dashpots were implemented using a linear interface with *zero* stiffness and certain damping coefficients.

The stiffness moduli of the springs and damping coefficients of the dashpots are calculated according to the Gazetas approach outlined in the NEHRP Consultants Joint Venture report (2012). Here, a distinction is made between three different parts, with different interface properties, of the soil-structure interaction: the two vertical sides, two stiffer horizontal lateral sides and a less stiff horizontal middle part. The interface properties are given in Table 3.6. Note that, as said, even though the stiffness properties and damping coefficients are shown here in one table, they are applied separately in the numerical models.

Spring location	Normal Stiffness (N/mm^3)	Shear stiffness (N/mm^3)	Normal damping coefficient (Ns/mm^3)	Shear damping coefficient (Ns/mm^3)
Vertical sides	$2.3397 \cdot 10^{-1}$	0	$5.0707 \cdot 10^{-3}$	0
Lateral sides	$1.4199 \cdot 10^{-1}$	$2.9186 \cdot 10^{-2}$	$4.6753 \cdot 10^{-4}$	$6.3253 \cdot 10^{-4}$
Middle	$3.7212 \cdot 10^{-2}$	$2.9186 \cdot 10^{-2}$	$6.6419 \cdot 10^{-4}$	$6.3253 \cdot 10^{-4}$

Table 3.6 Stiffness moduli and damping coefficients of the interface elements

Mass elements

The mass elements, used to account for the inertia effects of the structure under earthquake loading, are placed at the free-standing edges of the façade. Stiffness of these elements is not specified, since these boundary elements only affect the inertia mass. The same weight distribution has been applied in both normal and tangential direction. The material properties of the mass elements are given in Table 3.7.

Boundary	Total mass (tons)	Distributed mass (T/m)
Top left	3.8	0.32
Top right	2.3	0.46
Left lateral	2.4	0.98
Right lateral	4.9	1.30

Table 3.7 material properties of the mass elements

Steel reinforcement

The steel reinforcement used in analysis of the façade is identical to the one used for the walls. Therefore the reader is referred back to Figure 3.4, where the material properties of the steel reinforcement are shown. Please note that no diagonal anchors are applied in analysis of the façade.

3.3.4 Analysis procedure

Three different loading phases are used in analysis of the façade. Namely, a gravity & overburden (gravity first and overburden second), settlement, and seismic loading phase. Each phase was carried out with the secant method using the Broyden-Fletcher-Goldfarb-Shanno (BFGS) method based on the previous iteration. A line search was implemented to reduce the amount of non-convergence. The use of arc-length control has been excluded. Both geometrical and material nonlinearity were considered, as well as transient effects. The parallel direct sparse method is used for solving the system of equations, with a tolerance of 10^{-6}. A maximum of 500 iterations was used in the seismic loading phase for all models except the ones with an amplified seismic load. In these models a maximum of 100 iterations as used, due to various considerations. For a more in-depth reasoning behind this, the reader is referred to appendix A. Different load steps and convergence norms were adopted for each loading phase. A summary can be found in Table 3.8.

Initially, the force & energy norms from the settlement loading phase were also used in the seismic loading phase. However, it turned out that this model was numerically less stable than the one where force & displacement norms were used, even though the results are almost identical. For the settlement loading phase it was decided to continue using the force & energy norms, since the crack patterns obtained were neater.

Loading phase	Load step size	Iterative method	Convergence norms	Tolerances
Gravity & overburden	2 x [0.1(10)]	Secant BFGS	Force	$1 \cdot 10^{-3}$
			Displacement	$1 \cdot 10^{-3}$
			Energy	$1 \cdot 10^{-3}$
Settlement	$\frac{1}{98}$ (98)	Secant BFGS	Force	$1 \cdot 10^{-2}$
			Energy	$1 \cdot 10^{-4}$
Seismic	0.001s (= 1ms)	Secant BFGS	Force	$1 \cdot 10^{-3}$
			Displacement	$1 \cdot 10^{-3}$

Table 3.8 overview of the analysis procedure of the façade

4 Model Validation

This chapter describes the validation of the most appropriate modelling approach for simulating progressive damage in masonry retrofitted with bed joint reinforced repointing. Investigations, with respect to the head-joint failure type of the engineering masonry model, various analysis procedure settings, iterative method and interpolation scheme, were carried out. Furthermore, a sensitivity analysis of the material properties was performed. These optimal analysis settings, found in numerical modelling of the masonry walls, were then used in numerical analysis of the masonry farmhouse (chapter 5). Validation of the optimal modelling approach was done by comparison of the numerical and experimental results of both the unstrengthened and strengthened masonry walls for various parameters, such as the initial stiffness, peak load, crack pattern and crack widths.

4.1 Numerical results

In this section the numerical and experimental results will be shown and compared for both the unstrengthened and strengthened masonry wall. The numerical modelling approach, found in section 3.2, and analysis method described in section 4.2.5 were used in numerical analysis of the walls. To compare the evolution of the crack patterns in the walls, a scaled principal strain was introduced, showing the uncracked, partially cracked and fully cracked areas in the wall. These correspond to dark blue, light blue and green respectively in the contour plots for the scaled principal strains. The corresponding cracking and ultimate strain are defined as:

$$\varepsilon_{cr} = \frac{f_t}{E_x} = 1.7 \cdot 10^{-5} \tag{4.1}$$

$$\varepsilon_{ult} = \frac{2G_{ft}}{hf_t} = 0.0039 \tag{4.2}$$

Where h is the crack bandwidth of the element, defined for higher order two-dimensional elements as (DIANA 10.4 user's manual, 2020)

$$h = \sqrt{A} = l_{mesh} = 50\ mm \tag{4.3}$$

Different options for the head-joint failure type were considered. It was decided to adopt the 'tensile strength head-joint defined by friction' failure type, since these gave the most appropriate result for all cases, mainly in terms of crack patterns. When using the head-joint failure type 'diagonal stair-case cracks' non-convergence was obtained and, in some cases, even divergence, early in the analysis.

4.1.1 Unstrengthened masonry wall

Figure 4.1 shows the capacity curves of the experiment and reference case for the unstrengthened masonry wall. Convergence was found in every load step; the displacement norm is the one that usually converges over the force norm. More information regarding the convergence can be found in section 4.2.3.

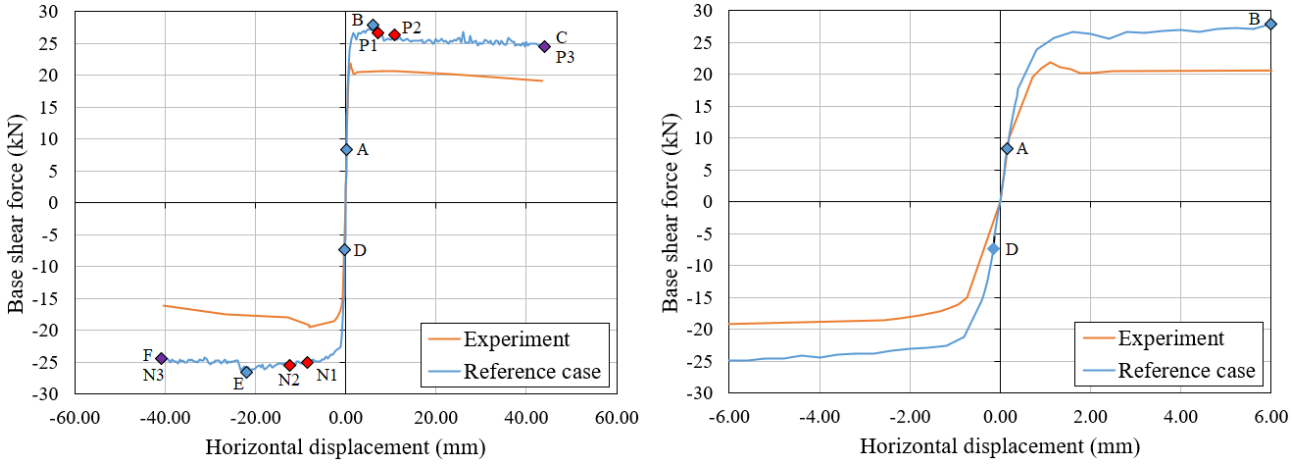

(a) (b)

Figure 4.1 capacity curves of the experiment and reference case for (a) -60mm to 60mm and (b) -6mm to 6mm

Points of interested are marked (A-F) in Figure 4.1. These points are determined as follows:

- Point A: crack initiation in the positive (+) direction.
- Point B: peak load in the positive (+) direction
- Point C: cut-off of the analysis in the positive (+) direction
- Point D: crack initiation in the negative (-) direction.
- Point E: peak load in the negative (-) direction
- Point F: cut-off of the analysis in the negative (-) direction

A summary of the points of interest for the unstrengthened wall is presented in Table 4.1. These values make it possible to make certain conclusions about the initial stiffness and peak load of the numerical models compared to the experimental results. In the experiment, loading was stopped at the points C and F, but complete failure of the wall was never reached. In the numerical model the same thing can be seen; there is no failure of the wall at these points. Since data from the experiment is only available up to these two points it was decided to stop the analyses here. In Figure 4.2 the crack patterns at a displacement of ±100.0mm are shown when the analyses are allowed to continue. More extended cracked areas are identified in both loading directions for a displacement of ±100.0mm.

Point	Description	EMM Force (kN)	EMM displacement (mm)	Experimental force (kN)	Experimental displacement (mm)
A	Crack initiation (+)	8.4	0.16	10.0	0.20
B	Peak load (+)	28.0	6.00	21.8	1.12
C	Cut-off for analysis (+)	24.6	44.00	19.1	43.63
D	Crack initiation (-)	-7.3	-0.16	-15.1	-0.73
E	Peak load (-)	-26.6	-22.00	-19.4	-7.97
F	Cut-off for analysis (-)	-24.5	-40.80	-16.1	-40.30

Table 4.1 points of interest and their corresponding displacements and forces

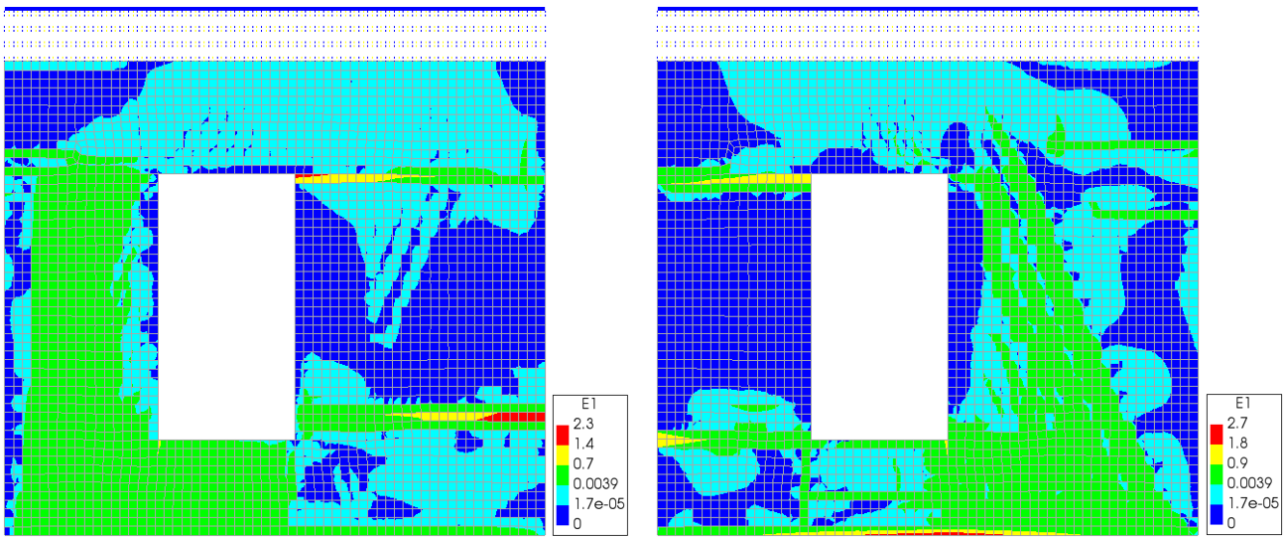

(a) displacement = -100.0mm (b) displacement = +100.0mm

Figure 4.2 crack patterns of the numerical model at ±100.0mm

Figure 4.3 to 4.10 compare experimental (Licciardello, Esposito, 2019) and numerical crack patterns. The numerical results are shown in terms of principal strain (E1); the contour scale has been selected such that the dark blue color ($E1 < 1.7 \cdot 10^{-5}$) represents uncracked areas and the light blue color ($1.7 \cdot 10^{-5} < E1 < 0.0039$) represents partially opened cracks; other colors represent fully opened cracks (green, yellow and red). A different maximum principal strain was achieved in negative and positive loading direction. Therefore, the scales differ in Figure 4.3 and 4.9. These figures correspond to the points P1 to P3 for the positive loading direction and N1 to N3 for the negative loading direction, as shown in Figure 4.1.

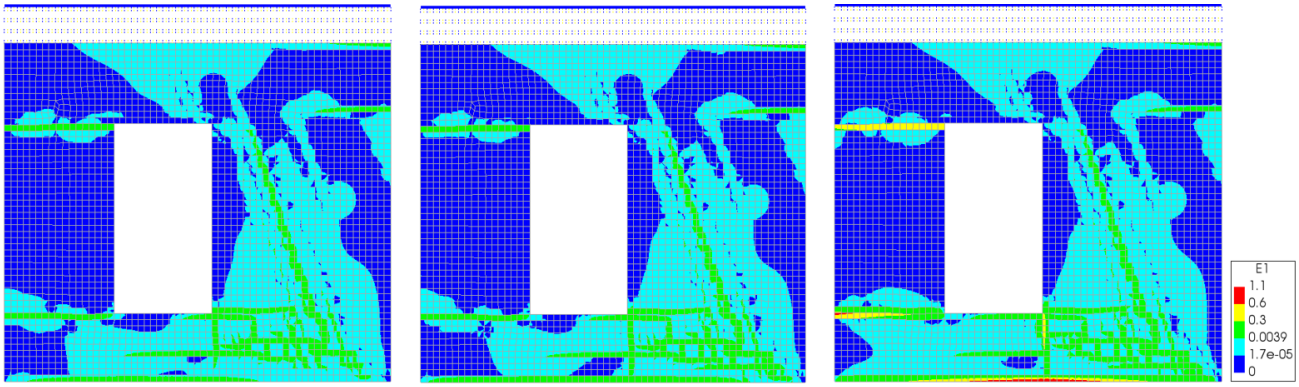

(a) displacement = +7.89mm (b) displacement = +11.11mm (c) displacement = +43.63mm

Figure 4.3 crack patterns of the numerical model at points P1 to P3 during positive loading

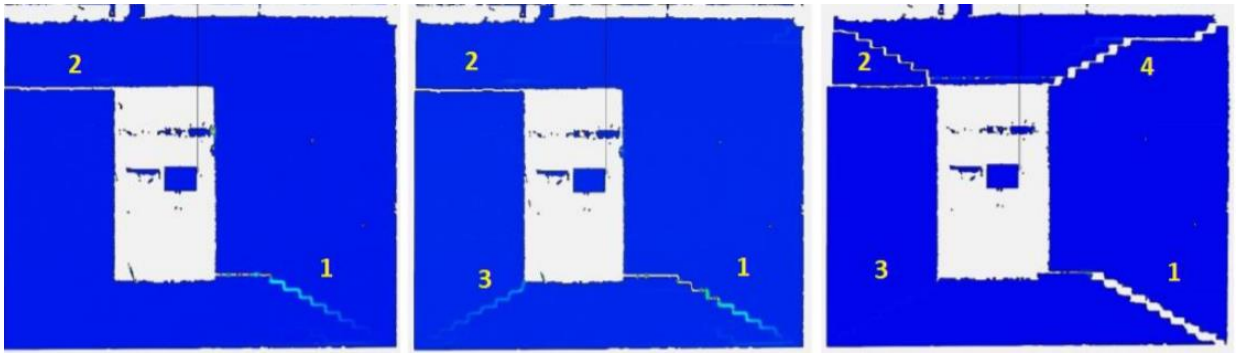

(a) displacement = +7.89mm (b) displacement = +11.11mm (c) displacement = +43.63mm

Figure 4.4 crack patterns of the experiment at various point during positive loading (Licciardello, Esposito, 2019)

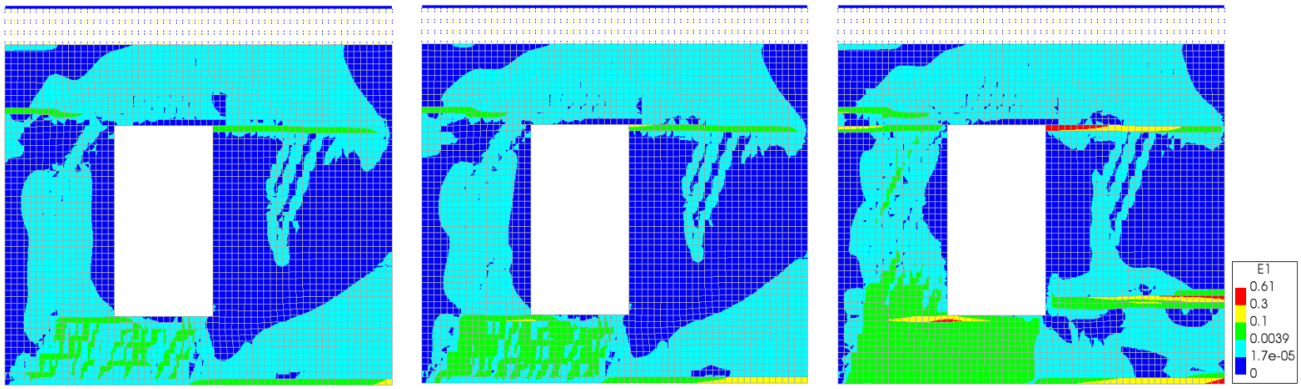

(a) displacement = -7.97mm (b) displacement = -12.82mm (c) displacement = -40.22mm

Figure 4.5 crack patterns of the numerical model at points N1 to N3 during negative loading

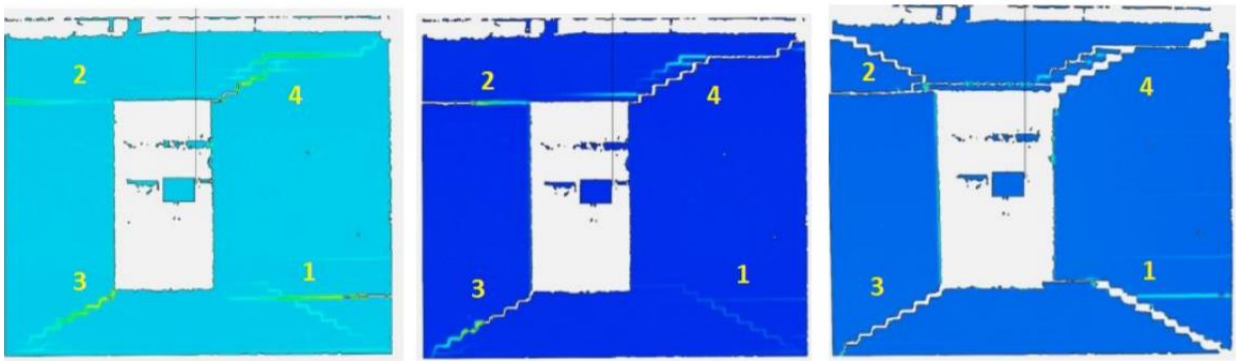

(a) displacement = -7.97mm (b) displacement = -12.82mm (c) displacement = -40.22mm

Figure 4.6 crack patterns of the experiment at various point during negative loading (Licciardello, Esposito, 2019)

Toe crushing is not observed at any point during the analysis in the negative loading direction. However, in the positive loading direction toe crushing is observed already at a displacement of +15.20mm. In Figure 4.7 the moment toe crushing is observed is shown. Here the principal stress, S2, is larger than the compressive strength of the masonry (f_c = 12.92MPa).

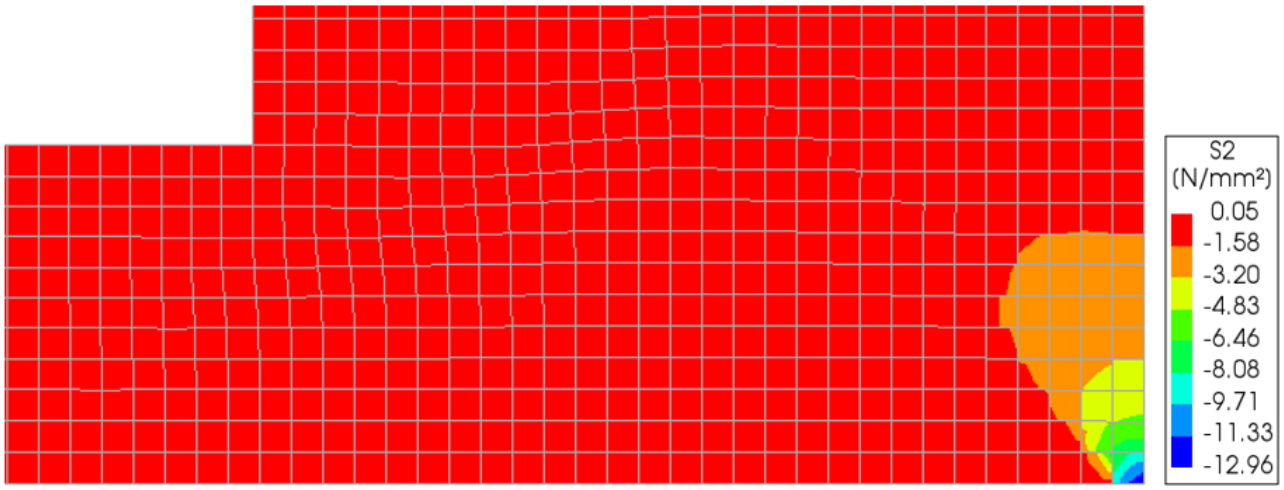

Figure 4.7 toe crushing in the positive loading direction at a displacement = +15.20mm

The unscaled principal strains at the end of analysis in the negative and positive loading direction direction are shown in Figure 4.8 together with the deformed shape.In the negative loading direction the maximum principal strain is 0.61 while in the positive loading direction this is 1.1. In the negative loading direction rocking of the right pier was identified, as well as the left pier, but of smaller magnitude. Rocking at the bottom of the wall is also seen. In the positive loading direction rocking of the left pier and bottom of the wall was found.

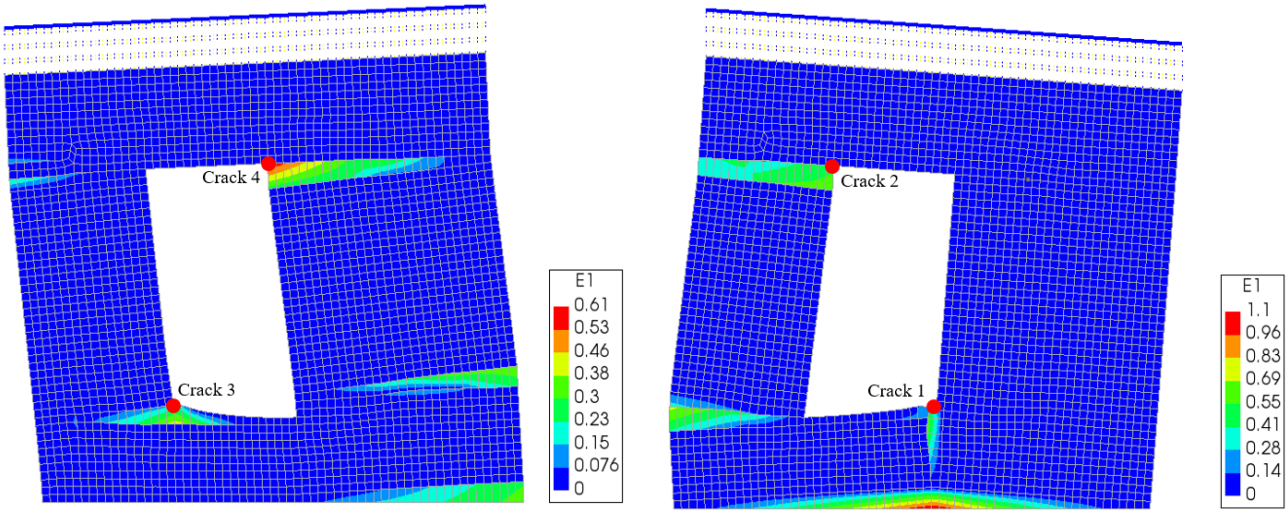

(a) displacement = -40.22mm (b) displacement = +43.63mm

Figure 4.8 deformed shape (scale factor 0.07) at the end of analysis in (a) negative direction and (b) positive direction

The maximum crack widths recorded during the experiment, at the end of phase 2 (displacement of ±2.00mm), for the locations 1 to 4 are shown in Table 4.2. The maximum crack widths found in the numerical model at this point are also noted and the locations where they occur are shown by a red dot in figure 4.12. It should be noted that the values of the crack widths at the integration points are taken. A significant difference between numerical and experimental results is observed. Generally, the numerical results overestimate the maximum crack widths, except for location 2. Crack widths of phase 3 of the experiment were not recorded.

	Maximum crack width (mm)			
Case	**Location 1**	**Location 2**	**Location 3**	**Location 4**
Experiment	0.44	2.13	0.55	0.52
Reference case	1.44	1.37	0.85	1.02

Table 4.2 maximum crack widths; experiment vs. the reference case for different locations

As shown in Figure 4.1, the initial stiffness in the numerical model (the reference case) under positive loading is in good accordance with the results from the experiment. The error (overestimation) of the initial stiffness is +5.3%. Under negative loading the numerical model overestimates the initial stiffness by +54.7%; however, it should be considered that experimentally the wall was already damaged when loaded in the negative direction due to the first cyclic loading phase in the positive loading direction only. Meaningful conclusions about the initial stiffness under negative loading can therefore not be made.

The numerical model overestimates the peak load under positive loading by +28.4%; for loading in the negative direction the overestimation is +37.1%. Overestimation of the peak loads is due to the fact that the masonry wall was loaded in a cyclic manner during the experiment, as opposed to two separate monotonic analyses in the positive and negative loading direction during numerical modelling. Cracking due to the cyclic nature of the experimental loading is therefore not accounted in the numerical models. Additionally, some damage was already present prior to testing, after which the wall was loaded up to light damage in two phases, before loading up to near collapse in the third phase. Cracking was thus already present before loading up to near failure. This explains the difference in peak loads between the numerical and experimental results.

The crack patterns found in the numerical simulations (Figure 4.3 and 4.5) are not in complete agreement with the experimental results (Figure 4.4 and 4.6). The horizontal and diagonal cracks at location 1 are simulated in a correct manner, although a more extended cracked area is identified in the numerical model, as opposed to more localised cracking in the experiment. The same is observed for the crack at location 3. The horizontal crack at location 2 is observed in both the numerical and experimental results, but the diagonal cracks at location 2 and 4 are not correctly simulated in the numerical model. The diagonal crack at location 2 is captured incorrectly due to the presence of pre-damage at this location prior to testing. In Figure 3.1(b) at location 2, a diagonal crack has already been manually introduced in order to simulate settlement damage. This in turn influences the crack pattern found after loading up to light damage in phase 1 and 2, prior to loading up to near collapse, in phase 3. Additionally, the nature of the EMM is of key here. Application of this smeared failure model is mainly beneficial during cyclic loading of masonry. A monotonic loading protocol is applied in the numerical modelling of the wall, as opposed to a cyclic loading protocol in the experiments. This ensures opening and closing of the cracks to be absent. Therefore, horizontal cracks are likelier to form, as opposed to the diagonal cracks found in the experiment. It is assumed that the bed- and head joints have the same tensile strength. In reality it could be that the head joints are weaker than the bed joints. This could explain the large diagonal shear crack in the right pier when loading in the positive direction. Furthermore, cracking of the bottom of the wall is found in the numerical models in both the positive and negative loading direction, while it is absent in the experiment. However, other experimental research done on these walls (Korswagen et al., 2019) has shown that cracking at the bottom of the wall is very much possible. Furthermore, toe crushing is observed in the numerical models already at a relatively small displacement of +15.20mm, while in the experiments it was not recorded at all.

The maximum crack width at location 2 is -35.7% smaller in the numerical model compared to the experiment. This is because at this location pre-damage is present prior to testing. This allows the crack to propagate faster during the experiments, resulting in a larger crack width. Because of this the crack width growth at location 2 is dominant over that of location 1, while during the numerical analysis it is the other way around. This results in a maximum crack width at location 1 that is +227.3% larger for the numerical model. The cracks widths found in the numerical model at locations 3 and 4 are +54.5% and +96.2% larger respectively, compared to the experiment. Due to the overestimation of the stiffness in negative loading direction, compared to the experiment, crack initiation starts at lower displacements. This results in higher crack widths at the same level of displacement (±2.00mm). The convergence results are discussed in the section 4.2.3.

4.1.2 Strengthened masonry wall

When applying the secant method on the strengthened wall divergence occurs very early on in the analysis; at a horizontal top displacement of 0.44mm. The resulting displacement are shown in Figure 4.9. The displacements in one of the diagonal anchors are of extremely high magnitude. Different types of solvers (BGFS, Broyden and Crisfield), load steps, use of arc-length control, convergence norms and line searches were implemented to solve this issue, but to no avail. Instead, the Regular Newton-Raphson method has been implemented in the numerical model of the strengthened wall.

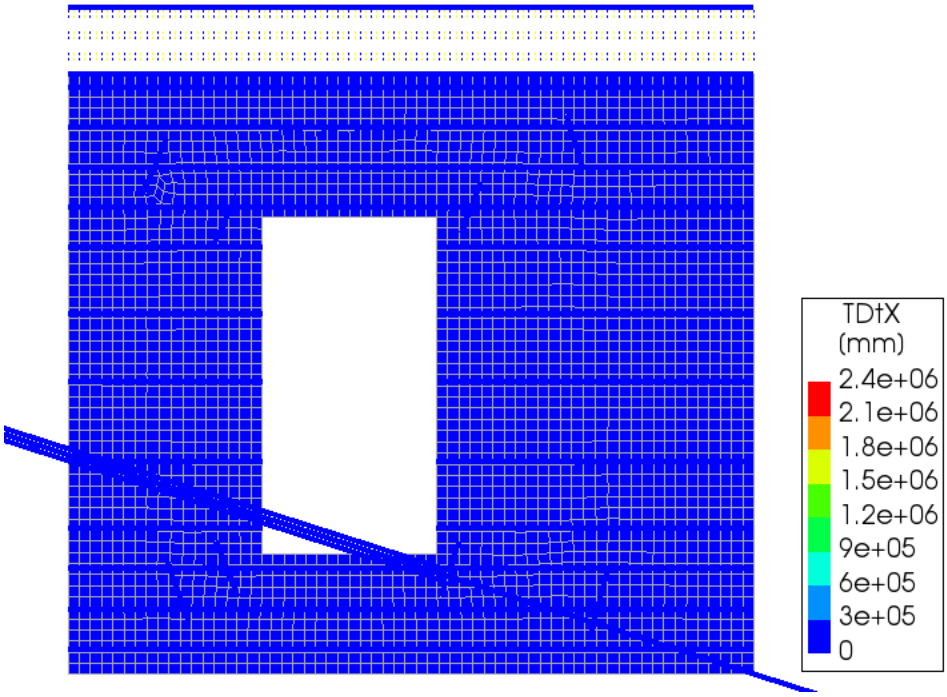

Figure 4.9 displacements of the strengthened wall at divergence (secant method)

Figure 4.10 shows the capacity curve of the experiment and reference case for the strengthened masonry wall. A summary of the points of interest (A-F) is presented in Table 4.3. In the experiment, loading was stopped at the points C and F, but complete failure of the wall was never reached. Convergence was not found in every load step; non-convergence was found in 16 and 99 load steps for the negative and positive loading direction respectively. The displacement norm is the one that usually converges over the force norm. An overview of the convergence history is shown in figure 4.15. Non-convergence was found when the maximum number of 250 iterations is reached.

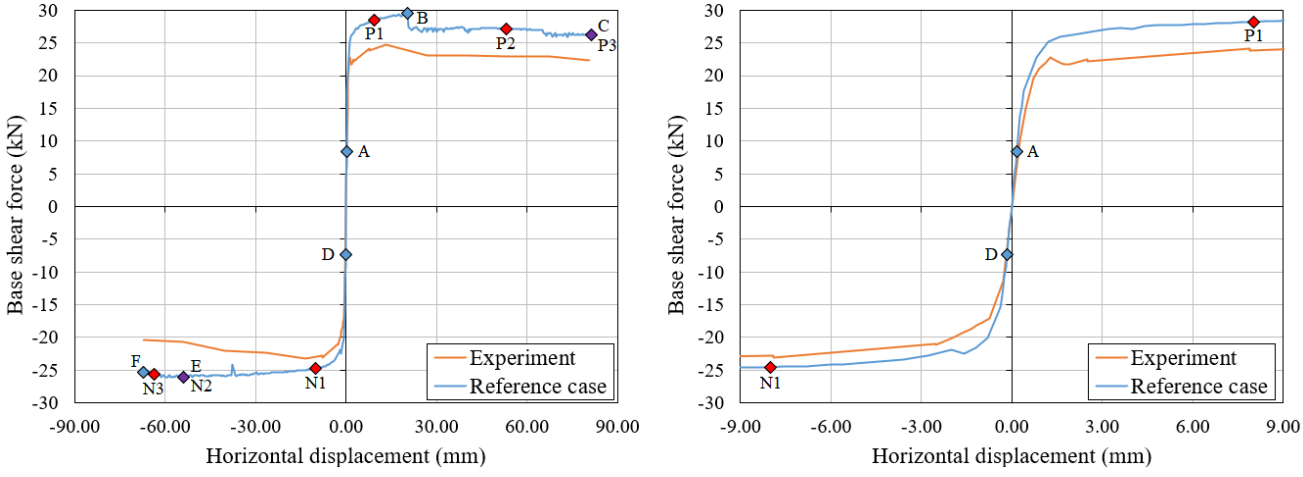

Figure 4.10 capacity curves of the experiment and reference case for (a) -90mm to 90mm and (b) -9mm to 9mm

Point	Description	EMM Force (kN)	EMM Displacement (mm)	Experimental Force (kN)	Experimental Displacement (mm)
A	Crack initiation (+)	8.4	0.16	10	0.25
B	Peak load (+)	29.5	20.40	24.8	13.28
C	Cut-off for analysis (+)	26.3	81.20	22.3	80.77
D	Crack initiation (-)	-7.3	-0.16	-11.4	-0.29
E	Peak load (-)	-26.1	-54.00	-23.2	-13.29
F	Cut-off for analysis (-)	-25.3	-67.20	-20.4	-67.28

Table 4.3 points of interest and their corresponding displacements and forces

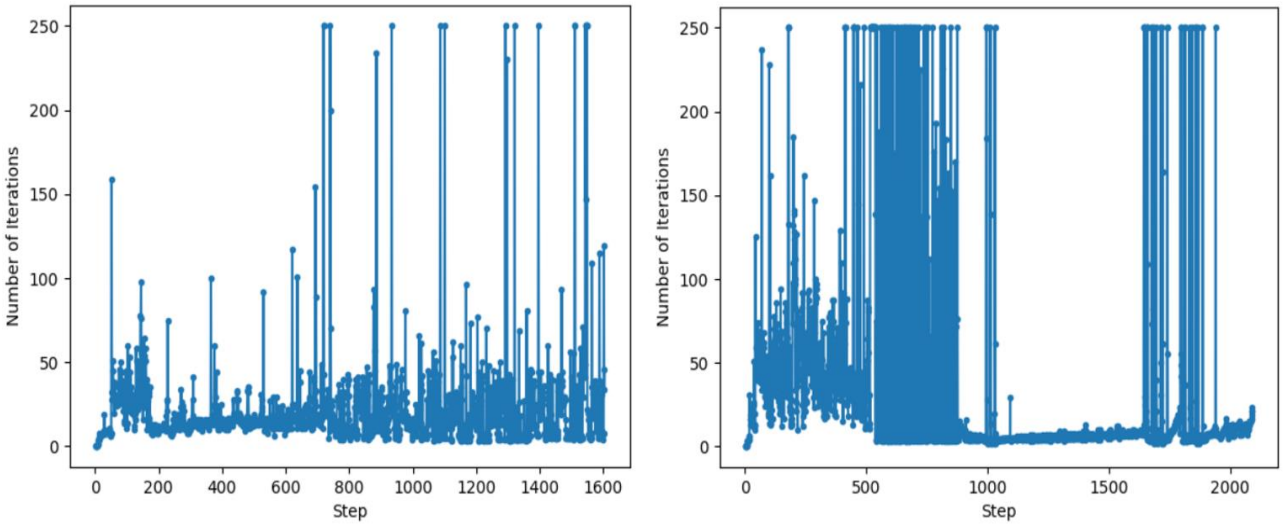

(a) (b)

Figure 4.11 iteration history of the reference case under (a) negative loading and (b) positive loading

Figure 4.12 to 4.19 compare experimental (Licciardello, Esposito, 2019) and numerical crack patterns. The numerical results are shown in terms of principal strain (E1); the contour scale has been selected such that the dark blue color ($E1 < 1.7 \cdot 10^{-5}$) represents uncracked areas and the light blue color ($1.7 \cdot 10^{-5} < E1 < 0.0039$) represents partially opened cracks; other colors represent fully opened cracks (green, yellow and red). A different maximum principal strain was achieved in negative and positive loading direction. Therefore, the scales differ in Figure 4.12 and 4.18. These figures correspond to the points P1 to P3 for the positive loading direction and N1 to N3 for the negative loading direction, as shown in Figure 4.10.

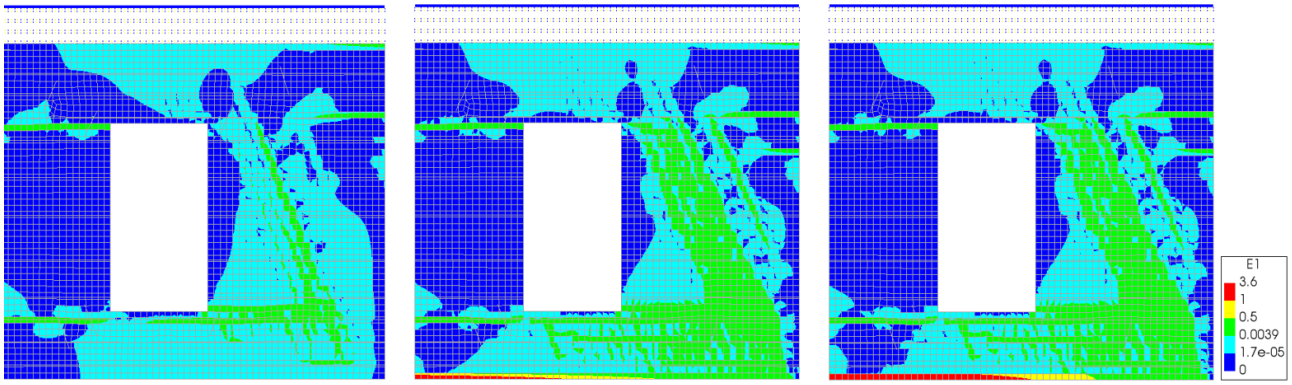

(a) displacement = +7.89mm (b) displacement = +53.77mm (c) displacement = +80.96mm

Figure 4.12 crack patterns of the numerical model at points P1 to P3 during positive loading

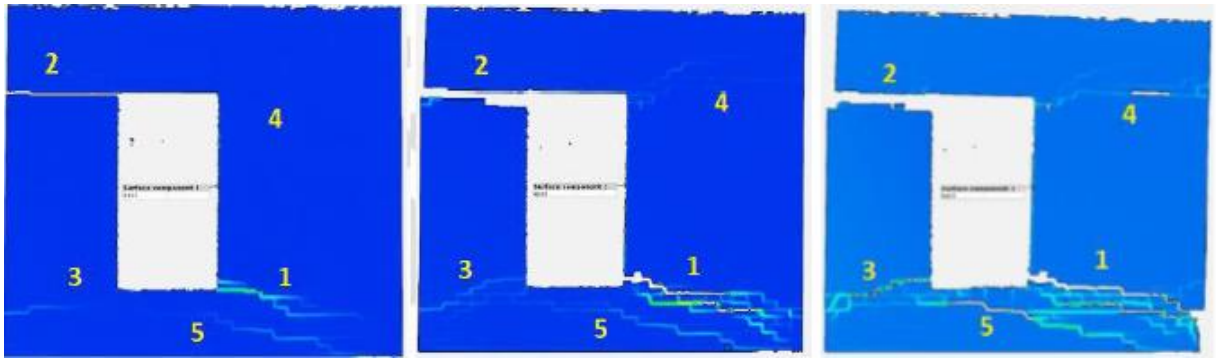

(a) displacement = +7.89mm (b) displacement = +53.77mm (c) displacement = +80.96mm

Figure 4.13 crack patterns of the experiment at various point during positive loading (Licciardello, Esposito, 2019)

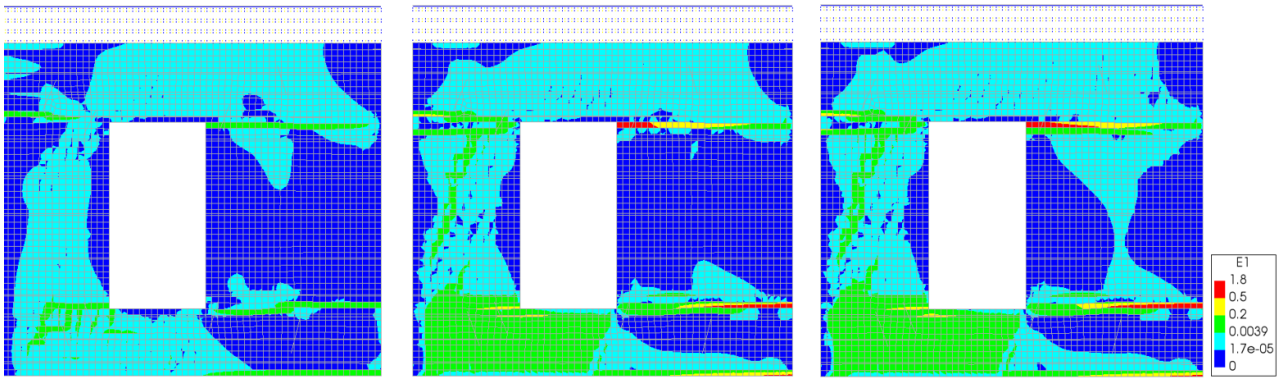

(a) displacement = -7.90mm (b) displacement = -53.80mm (c) displacement = -63.31mm

Figure 4.14 crack patterns of the numerical model at points N1 to N3 during negative loading

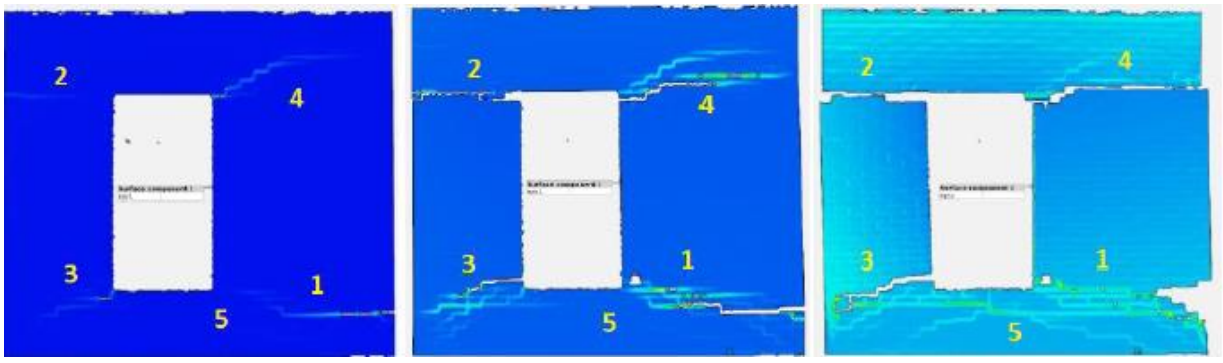

(a) displacement = -7.90mm (b) displacement = -53.80mm (c) displacement = -63.31mm

Figure 4.15 crack patterns of the experiment at various point during negative loading (Licciardello, Esposito, 2019)

Toe crushing is not observed at any point during the analysis in the negative loading direction. However, in the positive loading direction toe crushing is observed at a displacement of +26.40mm. In Figure 4.16 the moment toe crushing is observed is shown. Here the principal stress S2 is larger than the compressive strength of the masonry (f_c = 12.92MPa).

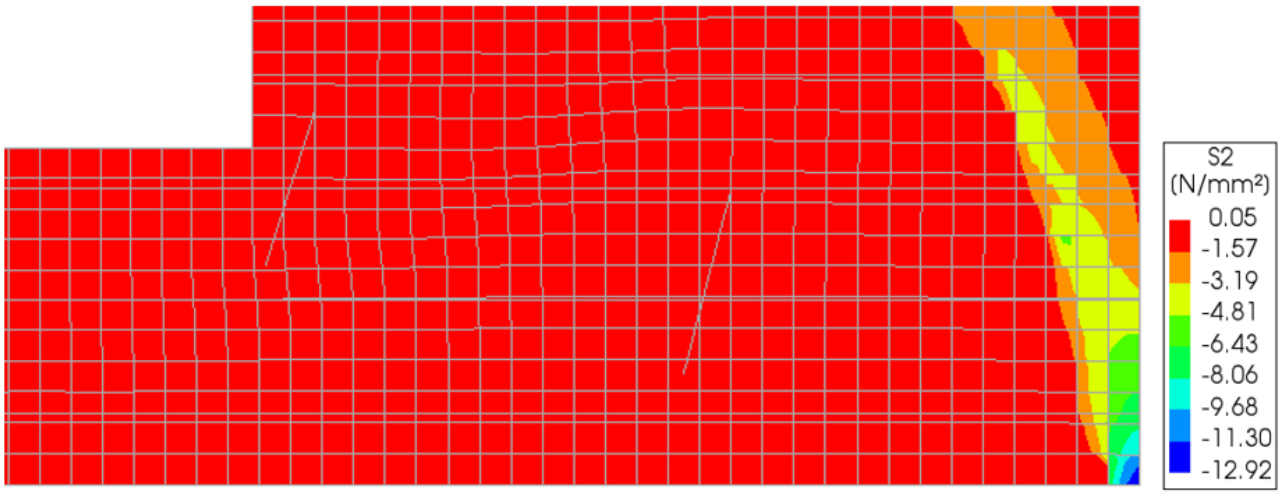

Figure 4.16 toe crushing in the positive loading direction at a displacement = +26.40mm

The unscaled principal strains at the end of analysis in the negative and positive loading direction direction are shown in Figure 4.17 together with the deformed shape. In the negative loading direction the maximum principal strain is 1.8 while in the positive loading direction this is 3.6. In the negative loading direction rocking of the right pier can be identified. Slight rocking of the bottom of the wall is also seen. In the positive loading direction rocking of the bottom of the wall was found.

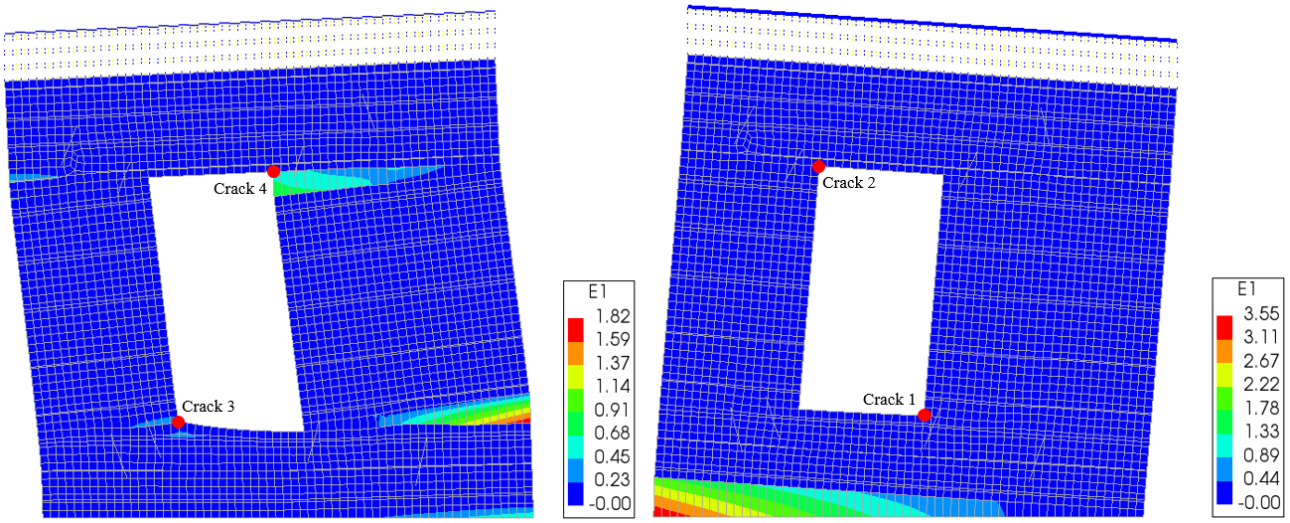

(a) displacement = -63.31mm (b) displacement = +80.96mm

Figure 4.17 deformed shape (scale factor 0.07) at the end of analysis in (a) negative direction and (b) positive direction

The Von Mises stresses over the length of the reinforcement bars, at the cut-off of the analysis, is shown in Figure 4.18. Nowhere in the reinforcement yielding of the steel (f_y = 215MPa) occurs. The results of the Von Mises stresses are in agreement with the crack patterns found; the stresses are developed in the regions where extensive cracking is encountered. For both the negative and positive loading directions mainly the bed joint reinforcement is activated and not the diagonals.

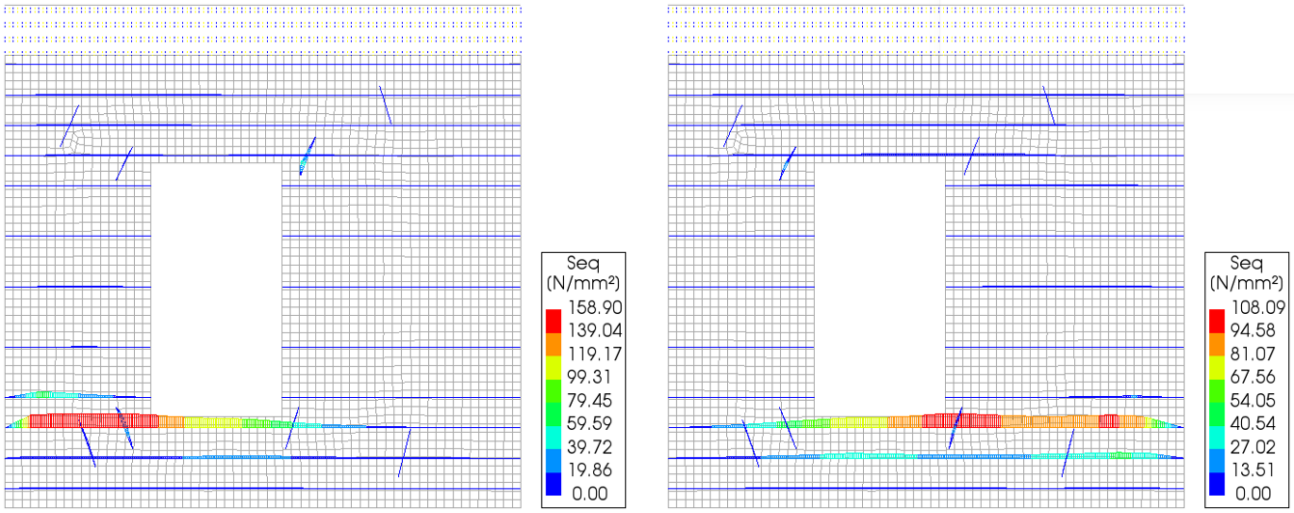

(a) displacement = -60.31mm (b) displacement = -80.96mm

Figure 4.18 Von Mises stress in the reinforcement in (a) negative direction and (b) positive direction

The relative shear displacements (slip) in the local x-direction of the reinforcement are shown in Figure 4.19. The bed joint reinforcement undergoes barely any slip, while the diagonal anchors are subjected to greater amounts of slip, especially in the negative loading direction. The maximum slip is found in the negative direction, at the diagonal next to the top right corner of the window. The slip of the diagonal at his location is 20.74mm. This means that it is in the horizontal plateau of the bond-slip curve. For all the other reinforcement it is still in the upward branch of the bond-slip curve.

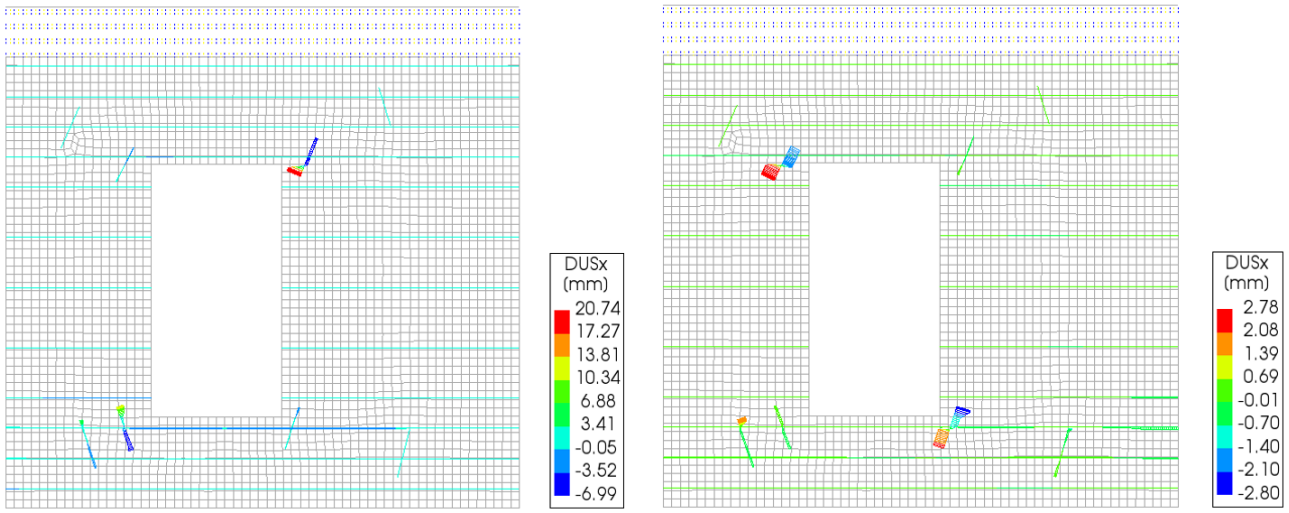

(a) displacement = -60.31mm (b) displacement = +80.96mm

Figure 4.19 amount of slip in the reinforcement in (a) negative direction and (b) positive direction

The maximum crack widths recorded during the experiment, at the end of phase 2 (displacement of ±2.00mm), for the locations 1 to 4 are shown in Table 4.4. The crack width for location 5 was not recorded during the experiment. The maximum crack widths found in the numerical model at these points are also noted and the locations where they occur is shown by red dots in Figure 4.17. It should be noted that the values of the crack widths at the integration points are taken. A significant difference between numerical and experimental results is observed. The numerical results overestimate the maximum crack widths. Crack widths of phase 3 of the experiment were not recorded.

	Maximum crack width (mm)			
Case	**Location 1**	**Location 2**	**Location 3**	**Location 4**
Experiment	0.51	1.06	0.44	0.40
Reference case	1.82	1.82	0.68	1.16

Table 4.4 maximum crack widths at end of phase 2; experiment vs. the reference case for different locations

From Table 4.3 it becomes clear that the error in the initial stiffness of the numerical model (the reference case) under positive loading is +31.3%. This is because in the experiments a lower initial stiffness was found for the strengthened wall compared to the unstrengthened wall. Under negative loading the numerical model overestimates the initial stiffness by +16.1%; however, it should be considered that, experimentally, the wall was already damaged when loaded in the negative direction due to the first cyclic loading phase in the positive loading direction only. Meaningful conclusions about the initial stiffness under negative loading can therefore not be made.

The numerical model overestimates the peak load under positive loading by +19.0%. For loading in the negative direction the overestimation is +12.5%. There is good agreement between the numerical and experimental results. However, overestimation of the peak loads is partly due to the reasons mentioned in section 4.1.1 (on the unstrengthened wall). Furthermore, the non-convergence of the analyses of the strengthened wall are a contributing factor. Application of the reinforcement does not have a significant influence on the peak load reached, but mainly on the ductility of the wall.

The crack patterns found in the numerical simulation are in quite good agreement with the experimental results. The cracked areas at the bottom (location 1, 3 and 5) are simulated in an adequate manner over the course of the analysis, although the crack at location 5 isn't observed until later in the numerical model. Toe crushing is identified in the numerical results at the locations 1 and 5, which is confirmed by the experimental results. The horizontal cracks found at locations 1 and 3 in the experiment, in the negative and positive loading direction respectively, are correctly captured by the numerical model. The crack at location 2 is correctly captured now, because the diagonal crack that appeared at this location in the unstrengthened wall is now restricted due to the diagonal anchors. The crack at location 4 however is simulated is a less appropriate manner, just like in the unstrengthened wall. More of a diagonal crack should form here to correctly capture the cracking behaviour. It is assumed that the bed- and head joints have the same tensile strength. In reality it could be that the head joints are weaker than the bed joints. This could explain the large diagonal shear crack in the right pier. Furthermore, cracking of the bottom of the wall is found in the numerical models in both the positive and negative loading direction, while it is absent in the experiment. However, other experimental research done on these walls (Korswagen et al., 2019) has shown that cracking at the bottom of the wall is very much possible.

The crack widths at all the locations are overestimated by quite a lot, between +70.0% and 256.9%. Due to the overestimation of the initial stiffness in both loading directions, compared to the experiments, crack initiation starts at lower displacements. This results in higher crack widths at the same level of displacement (±2.00mm).

4.2 Sensitivity analysis

Sensitivity analyses were carried out on the unstrengthened wall in order to investigate the influence of various analysis procedure parameters, material properties, iterative method and interpolation scheme on the behaviour of the numerical analysis. It was found that results were most accurate in terms of initial stiffness, peak load, crack patterns and crack width when quadrilateral elements were used in combination with the secant method.

4.2.1 Analysis procedure investigation

Four variations with respect to the load step size, use of arc-length control and convergence norms have been performed for the unstrengthened masonry wall to find the optimal analysis procedure settings in terms of initial stiffness, peak load, crack pattern and crack widths. The goal was to investigate the effect of different analysis options when using the secant method. It was found that the previously discussed reference case gave the most appropriate results. The configuration of this case is used in the analysis of the unstrengthened and strengthened masonry wall. The different cases investigated are summarized in Table 4.5.

Case	Load step size (mm)	Arc-length control	Convergence norms
Reference case	-0.04(1000) and +0.04(1100)	No	Displacement: 0.005 or Force: 0.005
Load step size case	-0.2(201) and +0.2(220)	No	Displacement: 0.005 or Force: 0.005
Arc-length control case	-0.04(1005) and +0.04(1100)	Yes	Displacement: 0.005 or Force: 0.005
Convergence norms case	-0.04(1005) and +0.04(1100)	No	Displacement: 0.01 or Force: 0.01

Table 4.5 variations of the reference case

In Figure 4.20 and 4.21 the capacity curves are shown for the experiment, reference case and variation cases. It should be noted that while loading in the positive direction, using arc-length control, the finite element solver initially found the right equilibrium path, but suddenly switched to the equilibrium path for negative loading. This is the reason there are two black lines (arc-length control case) in the negative loading direction. The points of interest (A-F) are not marked for a clearer overview, but the values can be found in Table 4.6. Convergence was found in every load step. The displacement norm was usually the one that converged.

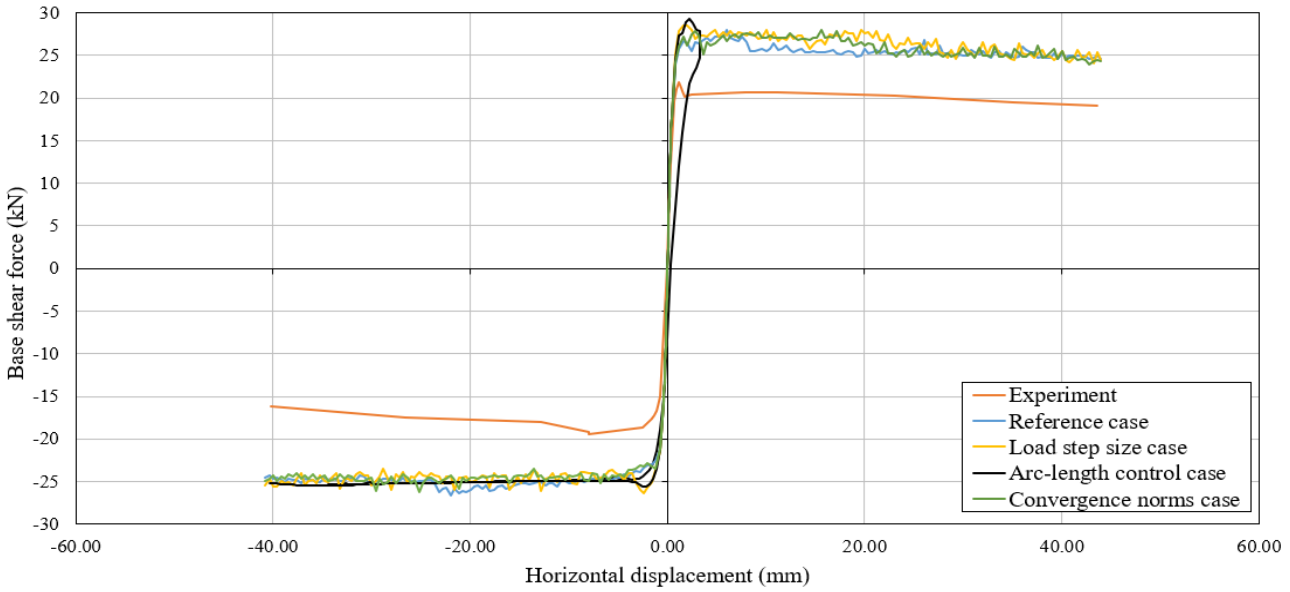

Figure 4.20 capacity curves of the experiment and all cases for -60mm to 60mm

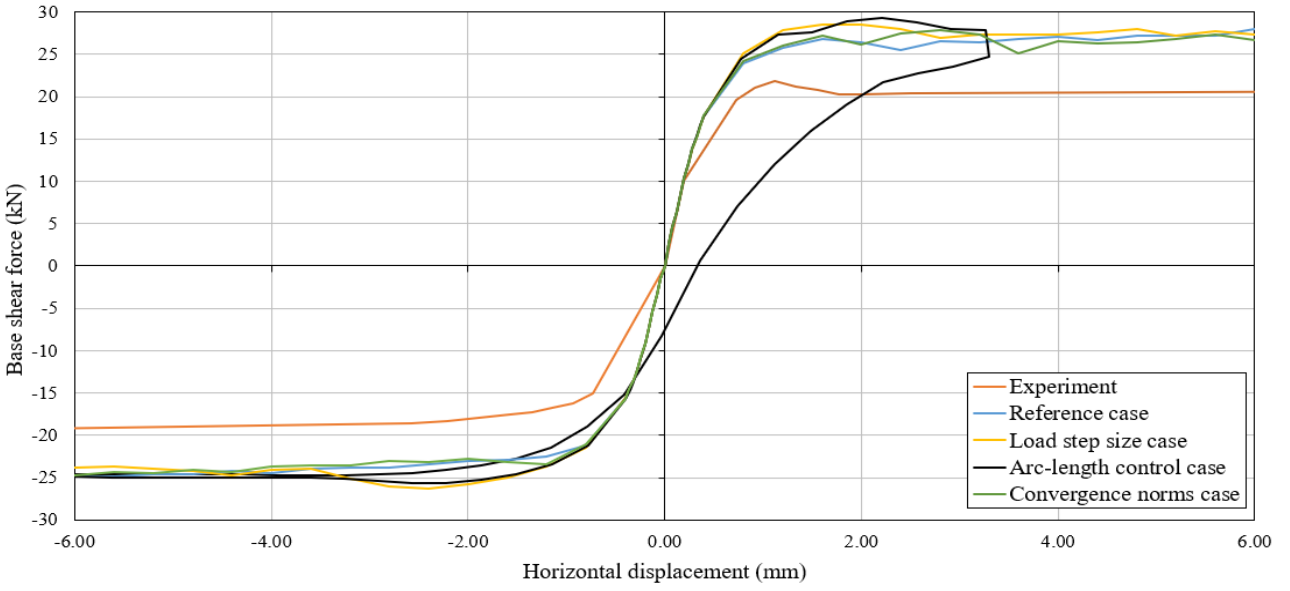

Figure 4.21 capacity curves of the experiment and all cases for -6mm to 6mm

Point	Physical quantity	Experiment	Reference case	Load step size case	Arc-length control case	Convergence norms case
A	Displacement (mm)	0.20	0.16	0.16	0.16	0.16
	Force (kN)	10.0	8.4	8.4	8.4	8.4
B	Displacement (mm)	1.12	6.00	1.60	2.21	15.60
	Force (kN)	21.8	28.0	28.6	29.4	28.0
C	Displacement (mm)	43.63	44.00	44.00	-34.04	44.00
	Force (kN)	19.1	24.6	24.5	-25.3	24.3
D	Displacement (mm)	-0.73	-0.16	-0.16	-0.16	-0.16
	Force (kN)	-15.1	-7.3	-7.3	-7.3	-7.3
E	Displacement (mm)	-7.97	-22.00	-2.4	-2.57	-25.20
	Force (kN)	-19.4	-26.6	-26.3	-25.6	-26.3
F	Displacement (mm)	-40.30	-40.80	-40.80	-40.32	-40.80
	Force (kN)	-16.1	-24.5	-25.5	-25.2	-24.9

Table 4.6 Points of interest and their corresponding displacements and forces

As seen in Table 4.6, Figure 4.20 and 4.21, the different cases all have the same initial stiffness under both positive and negative loading. The peak loads between the cases barely differ with a maximum variation of +5.0% under positive loading and +3.7% under negative loading for the reference case vs. the arc-length control case. Furthermore, the capacity curves for all the cases are quite similar except for the arc-length control case under positive loading, because the incorrect equilibrium path is followed here.

Figure 4.22 to 4.25 compare the crack patterns of the four cases. Two displacement levels have been identified in both the negative and positive loading direction that clearly show the difference in crack patterns. The results are compared for relatively small displacements, since for larger displacements more extended crack patterns are found that are more homogenous. This is appropriate: the displacements, as a base excitation, in the analysis of the farmhouse façade are small.

For the negative direction loading direction the chosen displacement levels are -4.80mm and -2.00mm. For the positive loading direction, they are +2.00mm and +6.80mm. The figure of a displacement of +6.80mm is missing for the arc-length control case, because the equilibrium path for negative loading was followed. The numerical results are shown in terms of principal strain (E1); the contour scale has been selected such that the dark blue color ($E1 < 1.7 \cdot 10^{-5}$) represents uncracked areas and the light blue color ($1.7 \cdot 10^{-5} < E1 < 0.0039$) represents partially opened cracks. It was decided, for clear illustration purposes, to only adopt one color for fully opened cracks, namely red.

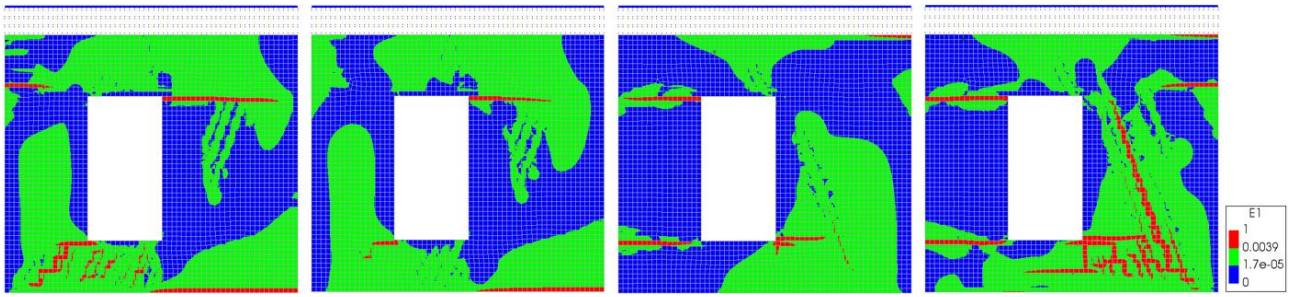

(a) displacement =-4.80mm (b) displacement =-2.00mm (c) displacement =-+2.00mm (d) displacement =+6.80mm

Figure 4.22 crack patterns at various points for the reference case

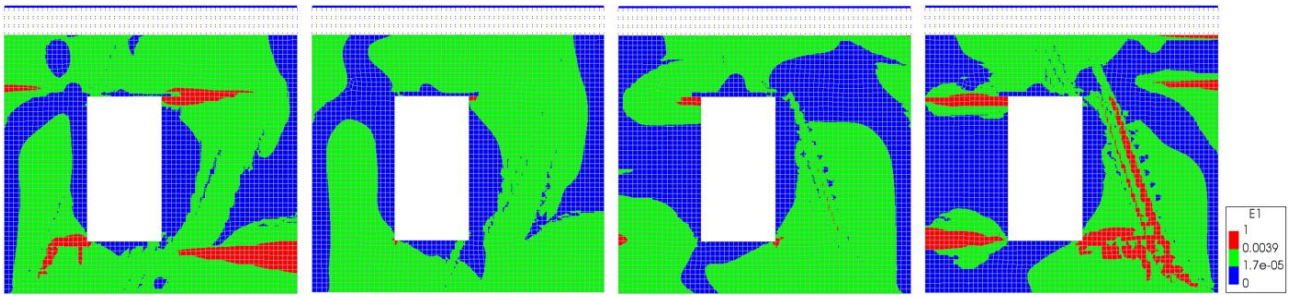

(a) displacement =-4.80mm (b) displacement =-2.00mm (c) displacement =-+2.00mm (d) displacement =+6.80mm

Figure 4.23 crack patterns at various points for the load-step size case

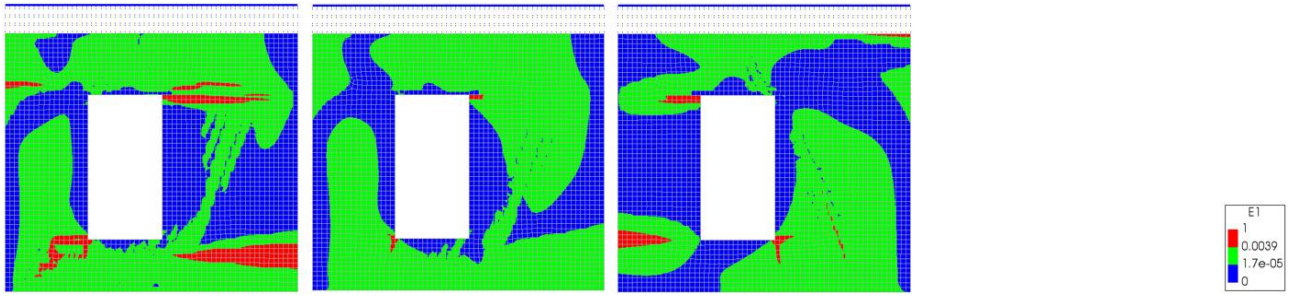

(a) displacement =-4.80mm (b) displacement =-2.00mm (c) displacement =-+2.00mm

Figure 4.24 crack patterns at various points for the arc-length control case

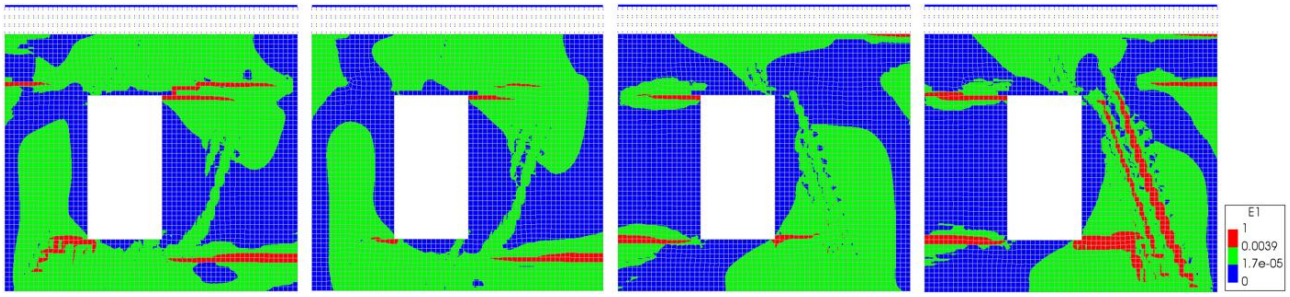

(a) displacement =-4.80mm (b) displacement =-2.00mm (c) displacement =-+2.00mm (d) displacement =+6.80mm

Figure 4.25 crack patterns at various points for the convergence norms case

Compared to the reference case the other cases all show a more extended cracked area. At a displacement of -4.80mm the crack at the bottom left corner of the window is therefore simulated in a less appropriate way for the variation cases due to extended cracking of the masonry. The variation cases simulate the horizontal crack at the right side of the wall better compared to the reference case. However, other experimental research done on these walls (Korswagen et al., 2019) has shown that cracking at the bottom of the wall, instead of the right side, is very much possible. At a displacement of -2.00mm it found that for the load step size and arc-length control cases barely any cracking is observed at all, which is not in agreement with the experiments.

The same is true for a displacement of +2.00mm. At a displacement of +6.80mm the crack at the bottom right corner of the window is incorrectly simulated for the variation cases. Once again, a more extended cracked area, instead of localised diagonal cracking, is observed. For the convergence norms case a mainly horizontal and vertical crack even forms at this location. In terms of maximum crack widths there are no great differences between the reference case and variation cases.

Optimal results, in terms of cracks patterns were found for the reference case. Therefore, it was decided to continue working with the reference case as a framework for the rest of the numerical models.

4.2.2 Material properties

The behaviour of the wall is predominantly determined by tensile failure. Therefore, it was decided that investigation of the sensitivity of the numerical model with respect to the elastic properties, tensile bed- and head joint strength and tensile fracture energy was of most interest. To investigate this the three material properties were decreased and increased by 50% with respect to the original material properties given in Table 3.2. A summary of the material properties used in the sensitivity analysis is given in Table 4.7.

Symbol	Unit	Original	50% decrease	50% increase
E_x	MPa	3207	1603.5	4810.5
E_y	MPa	4590	2295	6885
G_{xy}	MPa	1836	918	2754
f_t	MPa	0.053	0.027	0.08
G_{ft}	N/mm	0.0052	0.0026	0.0078

Table 4.7 Overview of material properties used in the sensitivity analysis

In order to compare the crack patterns and crack widths, it was decided to compare these at the end of analysis for both the positive and negative loading direction, meaning at +43.63mm and -40.22mm respectively. It should be noted that by changing these material properties the cracking and ultimate strain are changed. In the figures related to crack patterns the uncracked, partially cracked and fully cracked are still dark blue, light blue and green, yellow or red, respectively. The numerical model with the reduced load step size (0.2mm instead of 0.04mm) was adopted to reduce the computational effort required. The red dot in the figures of the crack patterns show the location where the maximum crack width is found.

Elastic properties

The sensitivity analysis carried out for the elastic properties was done by decreasing and increasing the parameters E_x, E_y, and G_{xy} by 50%, all at the same time, in order to investigate the orthotropic behaviour of the masonry more in-depth. The tensile strength and fracture energy remain the same. The capacity curves of the experiment and sensitivity of the elastic properties are shown in Figure 4.26. An overview of the sensitivity analysis of the elastic properties is given in Table 4.8.

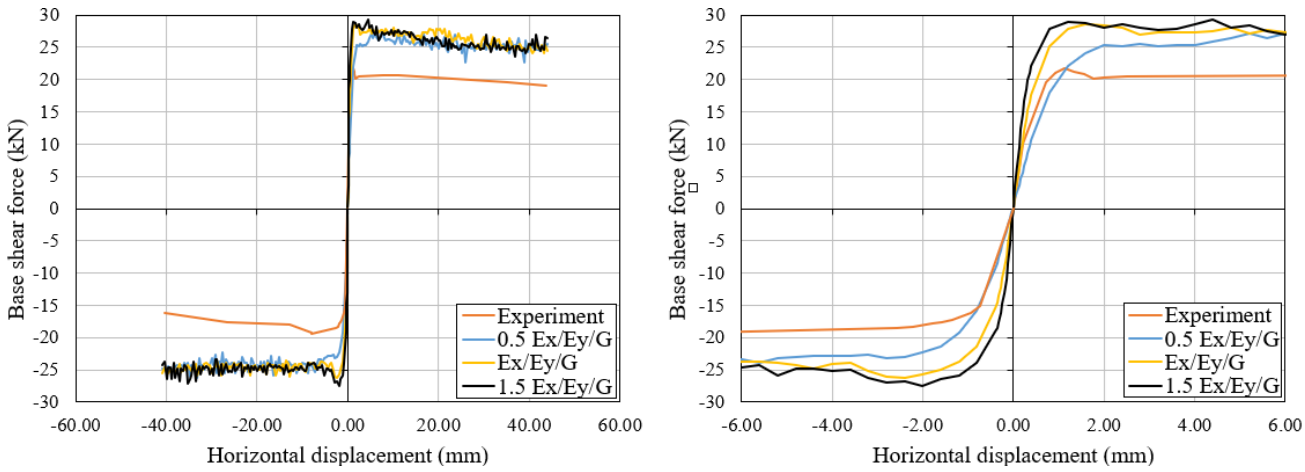

Figure 4.26 capacity curves of the experiment and sensitivity of the elastic properties for (a) -60mm to 60mm and (b) -6mm to 6mm

	Stiffness in (+) direction	Stiffness in (-) direction	Peak load in (+) direction	Peak load in (-) direction	Crack width in (+) direction	Crack width in (-) direction
Unit	kN/mm	kN/mm	kN	kN	mm	mm
Original	52.7	45.5	28.6	-26.3	32	21
50% decrease	27.4	23.2	27.5	-26.3	41	28
50% increase	79.9	70.0	29.3	-27.5	22	19

Table 4.8 Overview of the sensitivity analysis of the elastic properties

Decreasing the elastic properties by 50% results in a decrease of the initial stiffness of -49% and -48% for the negative and positive loading direction respectively. On the other hand; increasing the elastic properties by 50% results in an increase of the initial stiffness of +53% and +51% for the negative and positive loading directions respectively. This is logical because the stiffness properties are directly related to the initial stiffness. Thus, it can be concluded that the initial stiffness is sensitive to changes in the elastic properties.

Decreasing the elastic properties by 50% results in a decrease of the peak load of up to -4%. On the other hand; increasing the elastic properties by 50% results in an increase of the peak load of up to +5%. Thus, it can be concluded that the peak load is insensitive to changes in the elastic properties.

Decreasing the elastic properties by 50% results in an increase of the crack width of around +30%. On the other hand; increasing the elastic properties by 50% results in a decrease of the crack width of around -10% to -30%. Thus, it can be concluded that the crack width is sensitive to changes in the elastic properties.

In Figure 4.27 and 4.28 the crack patterns are shown for the negative and positive loading direction. From the figures it is obvious that decreasing or increasing the elastic properties by 50% has little effect on the evolution of the crack pattern. When increasing the elastic properties, a slightly larger cracked area is found. This is logical since the cracking strain is lower when the elastic properties are increased. It was found that increasing the elastic properties reduces the magnitude of the diagonal shear crack found in the right pier.

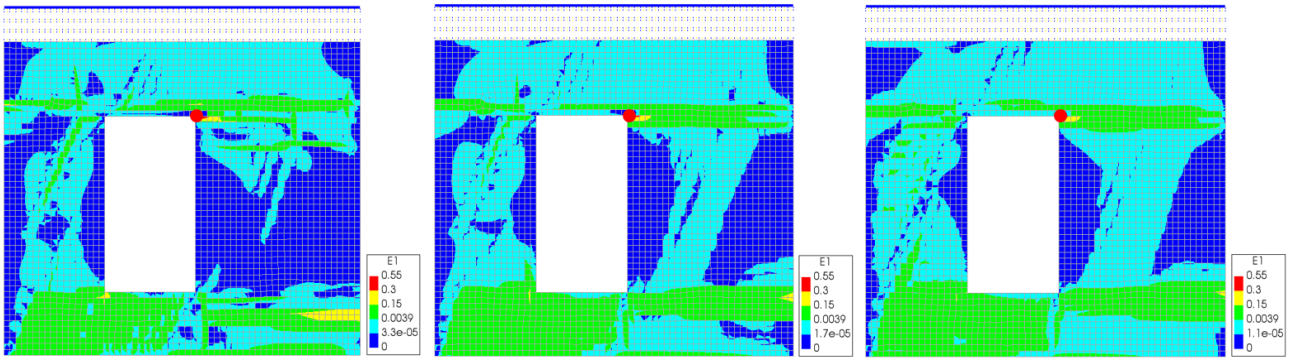

(a) 50% decreased $E_x/E_y/G_{xy}$ (b) $E_x/E_y/G_{xy}$ (c) 50% increased $E_x/E_y/G_{xy}$

Figure 4.27 crack patterns during negative loading for elastic properties when (a) 50% decreased (b) base values and (c) 50% increased

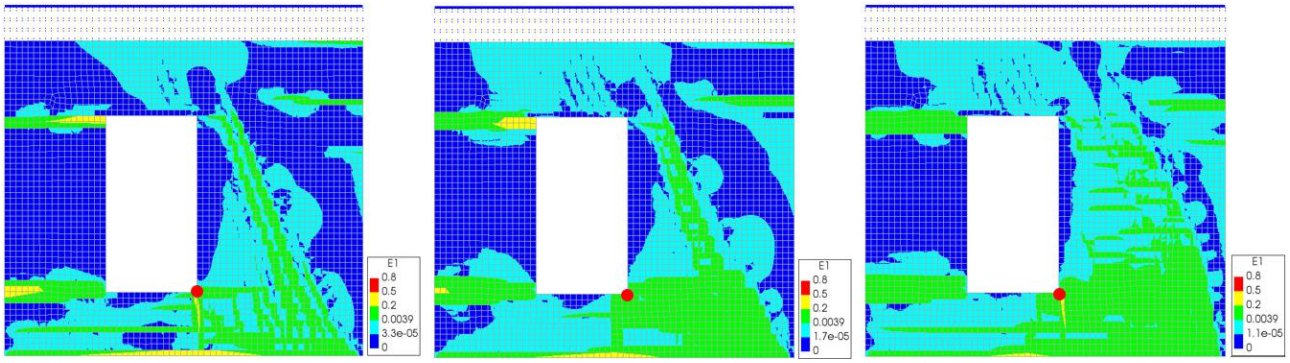

(a) 50% decreased $E_x/E_y/G_{xy}$ (b) $E_x/E_y/G_{xy}$ (c) 50% increased $E_x/E_y/G_{xy}$

Figure 4.28 crack patterns during positive loading for elastic properties when (a) 50% decreased (b) base values and (c) 50% increased

Tensile bed- and head joint strength

The sensitivity analysis carried out for the tensile bed- and head joint strength was done by decreasing and increasing the parameters f_{tx} and f_{ty} by 50%, at the same time, because it is assumed that f_t=f_{tx}=f_{ty}. The tensile fracture energy (as well as the elastic properties) remains the same, even though in reality they are related. The capacity curves of the experiment and sensitivity of the tensile strength are shown in Figure 4.29. An overview of the sensitivity analysis of the tensile strength is given in Table 4.9. The initial stiffness is excluded from this table because it is independent from the tensile strength.

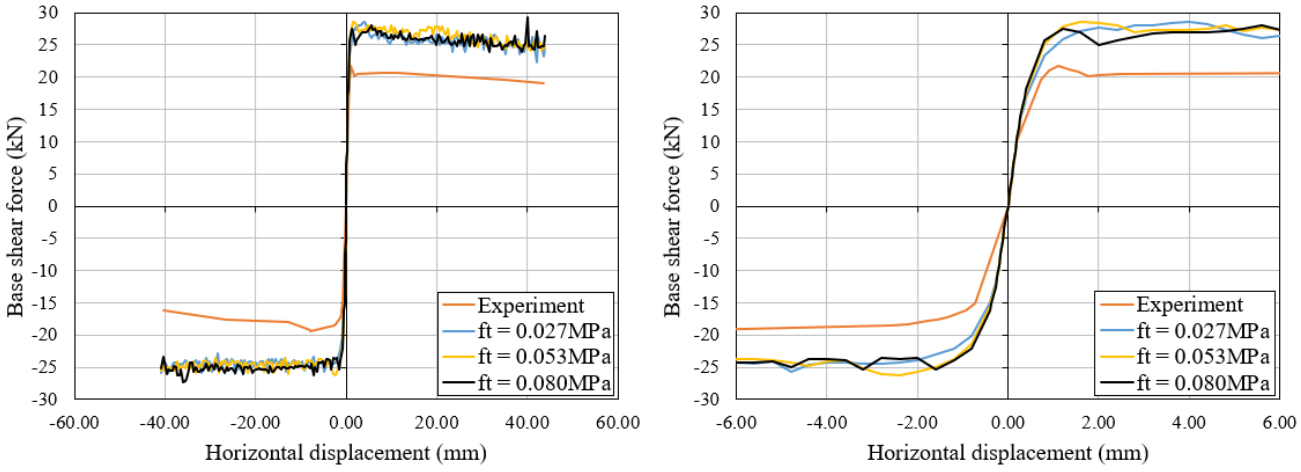

Figure 4.29 capacity curves of the experiment and sensitivity of the tensile strength for (a) -60mm to 60mm and (b) -6mm to 6mm

	Peak load in (+) direction	Peak load in (-) direction	Crack width in (+) direction	Crack width in (-) direction
Unit	kN	kN	mm	mm
Original	28.6	-26.3	32	21
50% decrease	28.6	-26.1	45	20
50% increase	29.3	-27.1	22	20

Table 4.9 Overview of the sensitivity analysis of the tensile strength

Decreasing the tensile strength by 50% results in a decrease of the peak load of up to -1%. On the other hand; increasing the tensile strength by 50% results in an increase of the peak load of up to +3%. Thus, it can be concluded that the peak load is insensitive to changes in the tensile strength.

Decreasing the tensile strength by 50% results in a decrease of -5% and increase of +41% of the crack width for the negative and positive loading direction respectively. On the other hand; increasing the tensile strength by 50% results in a decrease of the crack width of -5% and -31% for the negative and positive loading directions respectively. It appears that decreasing or increasing the tensile strength has little to no effect on the crack width in the negative loading direction, while it has a great influence on the crack width in the positive loading direction. Therefore it can still be concluded that the crack width is sensitive to changes in the tensile strength.

In Figure 4.30 and 4.31 the crack patterns are shown for the negative and positive loading direction respectively. From Figure 4.30 it is obvious that decreasing the tensile strength by 50% increases the cracked area while the crack widths remain more or less the same. On the other hand, when the tensile strength is increased by 50% the cracked area is reduced while the crack widths remain more or less the same. This can be explained by the fact that when loading in the negative direction, and decreasing the tensile strength by 50%, the governing failure mechanism is tension opening instead of shearing, resulting in crack widths that barely differ in this case. When loading in the positive direction (Figure 4.31) the governing failure mechanism is tension opening for both decreasing and increasing the tensile strength by 50%. This results in larger crack widths when decreasing the tensile strength.

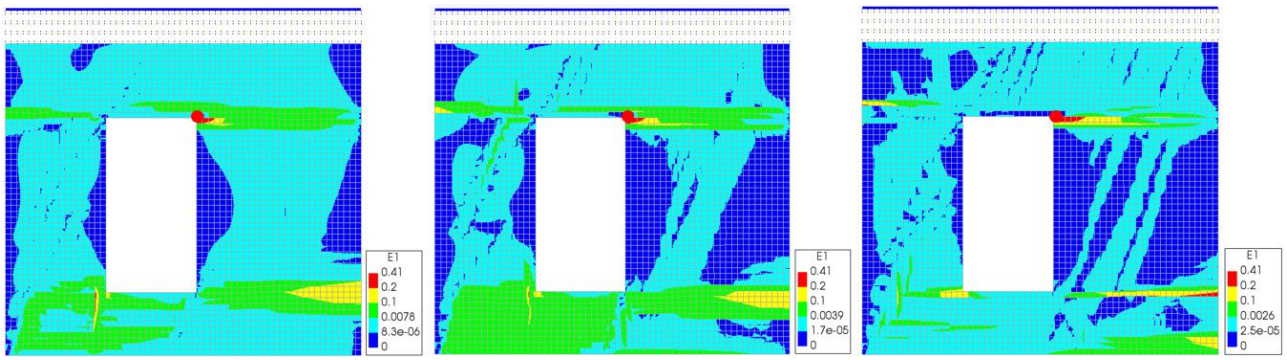

(a) f_t = 0.027MPa (b) f_t = 0.053MPa (c) f_t = 0.080MPa

Figure 4.30 crack patterns during negative loading for tensile strength when (a) 50% decreased (b) base values and (c) 50% increased

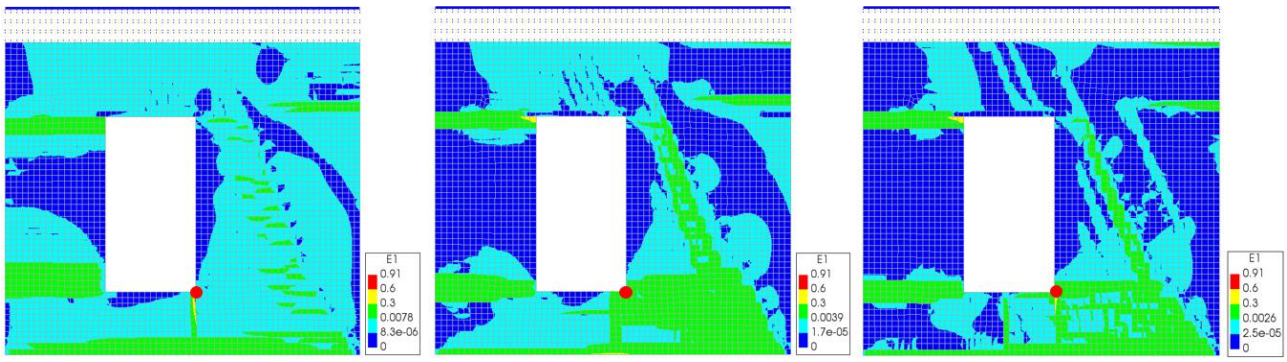

(a) f_t = 0.027MPa (b) f_t = 0.053MPa (c) f_t = 0.080MPa

Figure 4.31 crack patterns during positive loading for tensile strength when (a) 50% decreased (b) base values and (c) 50% increased

Tensile fracture energy

The sensitivity analysis carried out for the tensile fracture energy was done by decreasing and increasing the parameters G_{ft} by 50%. The elastic properties and fracture energy remain the same. The capacity curves of the experiment and sensitivity of the tensile strength are shown in Figure 4.32. An overview of the sensitivity analysis of the tensile fracture energy is given in Table 4.10. The initial stiffness is excluded from this table because it is independent from the tensile strength.

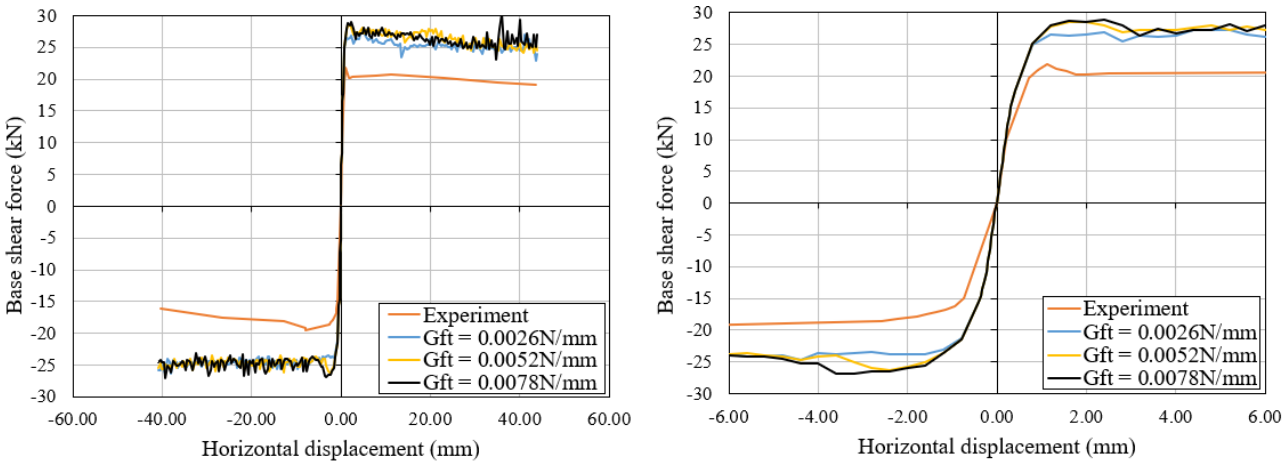

(a) (b)

Figure 4.32 capacity curves of the experiment and sensitivity of the tensile fracture energy for (a) -60mm to 60mm and (b) -6mm to 6mm

	Peak load in (+) direction	Peak load in (-) direction	Crack width in (+) direction	Crack width in (-) direction
Unit	kN	kN	mm	mm
Original	28.6	-26.3	32	21
50% decrease	27.3	-26.4	41	20
50% increase	30.3	-27.1	28	23

Table 4.10 Overview of the sensitivity analysis of the tensile fracture energy

Decreasing the tensile fracture energy by 50% results in a decrease of up to -5% of the peak load. On the other hand; increasing the tensile fracture energy by 50% results in an increase of the peak load of up to +6%. Thus, it can be concluded that the peak load is insensitive to changes in the tensile fracture energy.

Decreasing the tensile fracture energy by 50% results in a decrease of -4.8% and increase of +28.1% of the crack width for the negative and positive loading direction respectively. On the other hand, increasing the tensile fracture energy by 50% results in an increase of +9.5% and decrease of -12.5% of the crack width for the negative and positive loading directions respectively. Therefore, it can still be concluded that the crack width is sensitive to changes in the tensile fracture energy.

In Figure 4.33 and 4.34 the crack patterns are shown for the negative and positive loading direction respectively. In Figure 4.33 it is obvious that decreasing or increasing the tensile fracture energy by 50% has little effect on the evolution of the crack pattern. For the positive loading direction (Figure 4.34) it is found that decreasing the tensile fracture energy by 50% increases the cracked area. As for the tensile strength, when loading in the negative direction decreasing the tensile strength by 50% makes the governing failure mechanism tension opening instead of shearing, resulting in crack widths that barely differ in this case. When loading in the positive direction the governing failure mechanism is tension opening for both decreasing and increasing the tensile strength by 50%. This results in larger crack widths when decreasing the tensile strength.

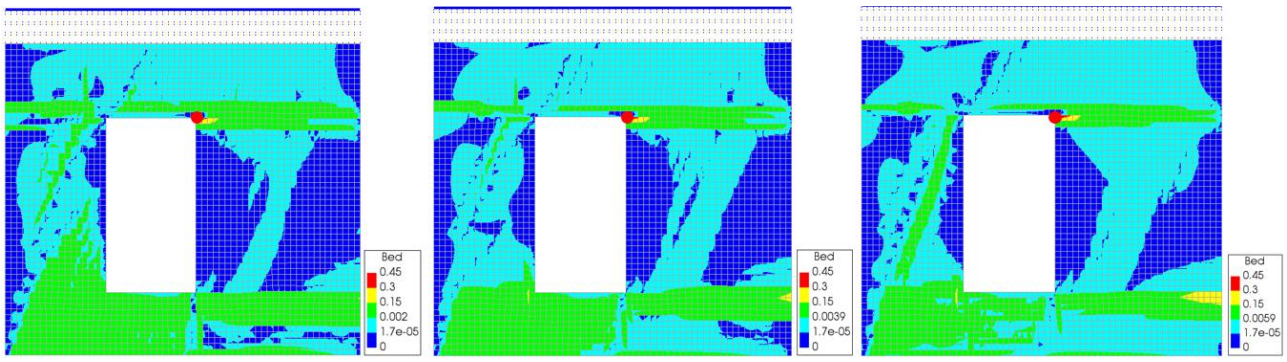

(a) G_{ft} = 0.0026N/mm (b) G_{ft} = 0.0052N/mm (c) G_{ft} = 0.0078N/mm

Figure 4.33 crack patterns during negative loading for tensile fracture energy when (a) 50% decreased (b) base values and (c) 50% increased

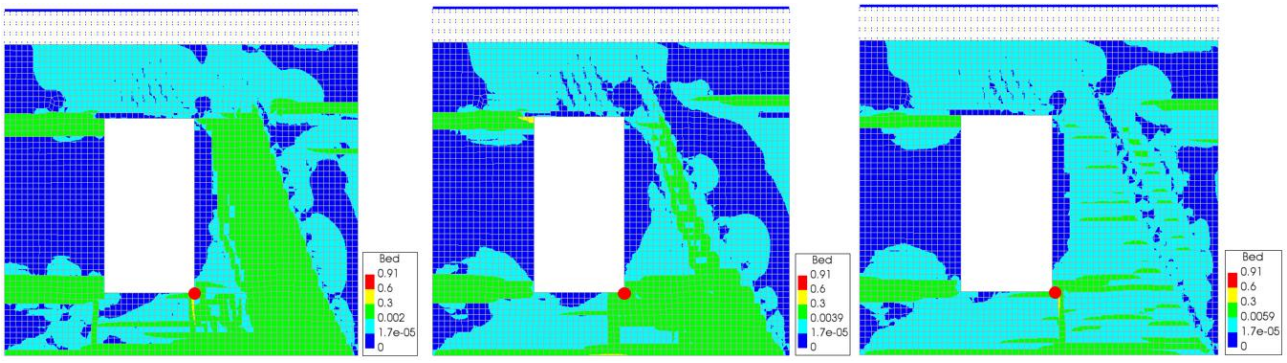

(a) G_{ft} = 0.0026N/mm (b) G_{ft} = 0.0052N/mm (c) G_{ft} = 0.0078N/mm

Figure 4.34 crack patterns during negative loading for tensile fracture energy when (a) 50% decreased (b) base values and (c) 50% increased

4.2.3 Iterative method

Two different iterative methods have been considered to investigate the influence of the iterative method on the behaviour of the wall. These are the secant method with BGFS, based on the previous iteration, and regular Newton-Raphson method, based on tangential stiffness. A line search, with the default settings, has been applied for the regular Newton-Raphson method (RNR) to reduce the amount of non-converged steps. The analysis procedure is carried out as shown in Table 4.5 (reference case). The capacity curves of the experiment, secant method and RNR method are shown in Figure 4.35. An overview of the analysis results is shown in Table 4.11. The initial stiffness is excluded from this table because it is independent from the iterative method used.

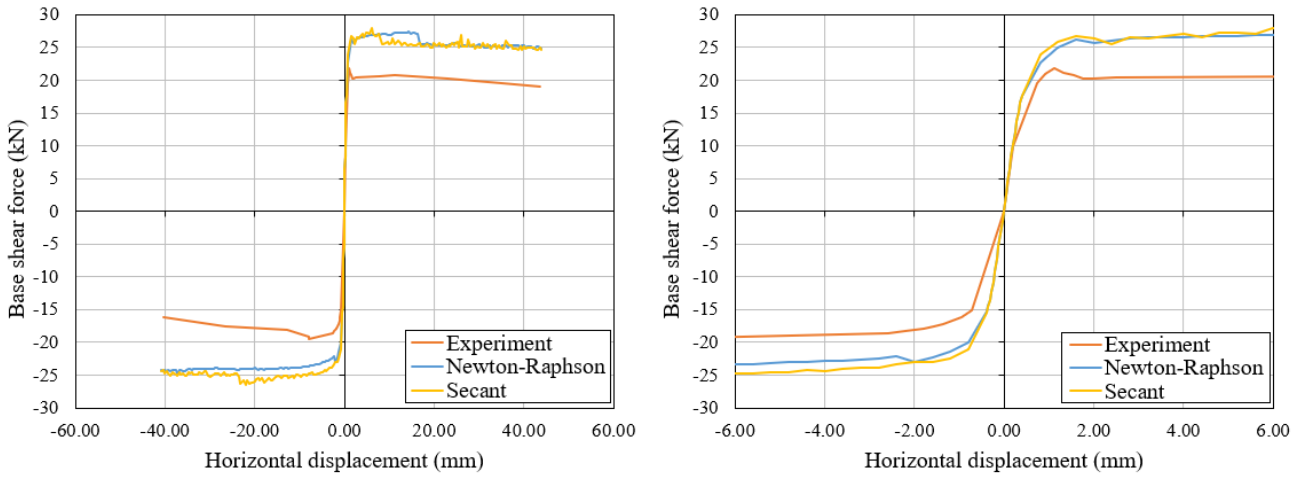

Figure 4.35 capacity curves of the experiment, secant method and Regular Newton-Raphson method for (a) -60mm to 60mm and (b) -6mm to 6mm

	Peak load in (+) direction	Peak load in (-) direction	Maximum principal strain (+) direction	Maximum principal strain (-) direction
Unit	kN	kN	-	-
Experiment	21.8	-19.4	n.a.	n.a.
Secant method	28.0	-26.6	1.1	0.61
RNR method	27.4	-24.2	1.1	1.2

Table 4.11 peak loads and maximum principal strains for the experiment, secant method and Regular Newton-Raphson method in positive and negative loading direction

The secant method overestimates, compared to the experiment, the peak load under positive loading by +28%; for loading in the negative direction the overestimation is +37%. The RNR method overestimates, compared to the experiment the peak load under positive loading by +26%; for loading in the negative direction the overestimation is +25%.

Figure 4.36 to 4.37 show the crack patterns at various points during the analysis. These correspond to the points where the crack patterns are shown of the experiment of the unstrengthened wall, in section 4.1.1. The results in terms of crack patterns are very similar for both iterative methods. The biggest difference is seen in the maximum principal strain. For the positive loading direction these are the same, namely 1.1, but for the negative loading direction these are 0.61 and 1.2 for the secant method and RNR method respectively.

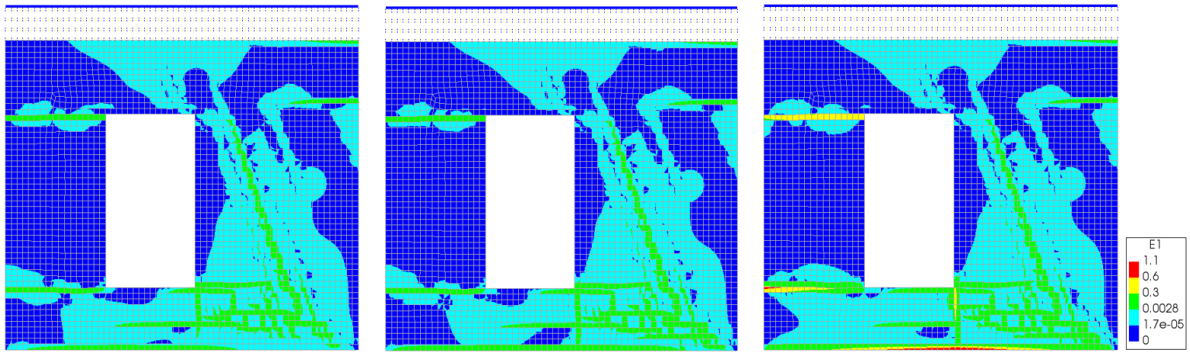

(a) displacement = +7.89mm (b) displacement = +11.11mm (c) displacement = +43.63mm

Figure 4.36 crack patterns at various points under positive loading using the secant method

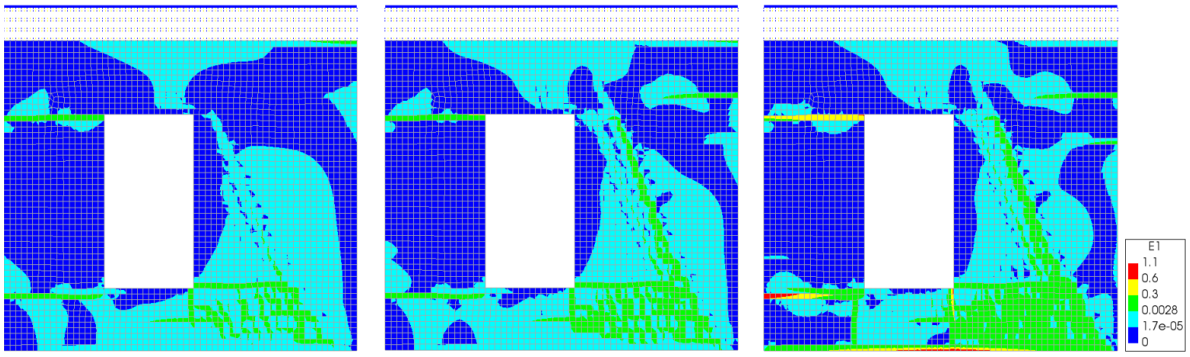

(a) displacement = +7.89mm (b) displacement = +11.11mm (c) displacement = +43.63mm

Figure 4.37 crack patterns at various points under positive loading using the RNR method

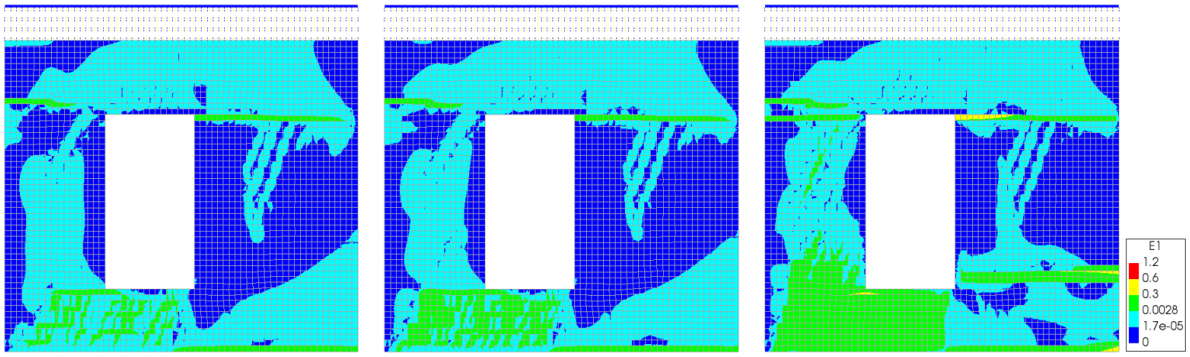

(a) displacement = -7.97mm (b) displacement = -12.82mm (c) displacement = -40.22mm

Figure 4.38 crack patterns at various points under negative loading using the secant method

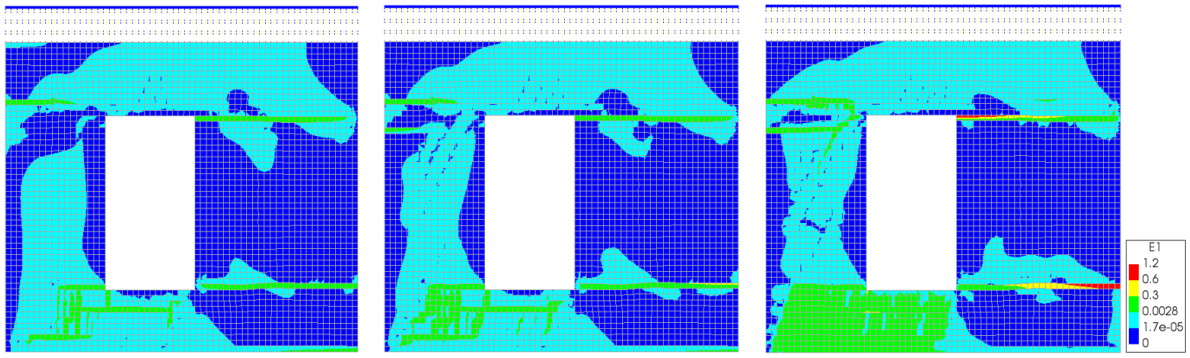

(a) displacement = -7.97mm (b) displacement = -12.82mm (c) displacement = -40.22mm

Figure 4.39 crack patterns at various points under negative loading using the RNR method

In terms of initial stiffness, peak load and crack pattern there is not much of a difference between the secant method and RNR method. A large difference in the maximum principal strain is encountered between the two iterative methods under loading in the negative direction. The large maximum principal strain, when applying the RNR method, in negative loading direction are unrealistic based on a previous numerical investigation of the wall (Mahmoudimothlagh, 2020). In this research very accurate results were obtained using the TSCM instead of the EMM, which is more suitable for monotonic loading. Furthermore, there is always convergence when using the secant method (see Figure 4.40). When using the RNR method there are some non-converged steps over the course of the analysis (see Figure 4.41). There are 14 and 17 non-converged steps for the positive and negative loading direction respectively. When convergence is reached, which is most often the displacement norm, the error in the converged norm is of greater magnitude when using the RNR method compared to the secant method. This is why the maximum principal strain is much larger with the RNR method compared to the secant method in negative loading direction.

Based on these shortcomings of the RNR method compared to the secant method it was decided to continue the rest of the analyses using the secant method. However, the results of the RNR are still acceptable. Therefore, the RNR method was used in the analysis of the strengthened wall, since divergence occurred early in the analysis using the secant method. For analysis of the farmhouse façade both iterative methods can be considered based on the optimal results obtained there.

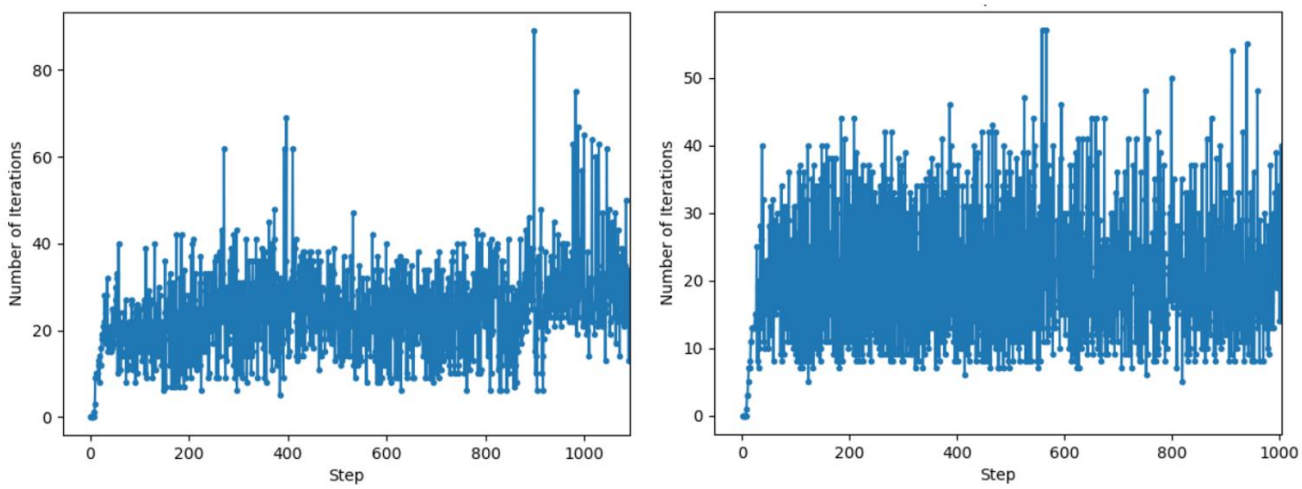

(a) (b)

Figure 4.40 convergence history using the secant method under (a) positive loading and (b) negative loading

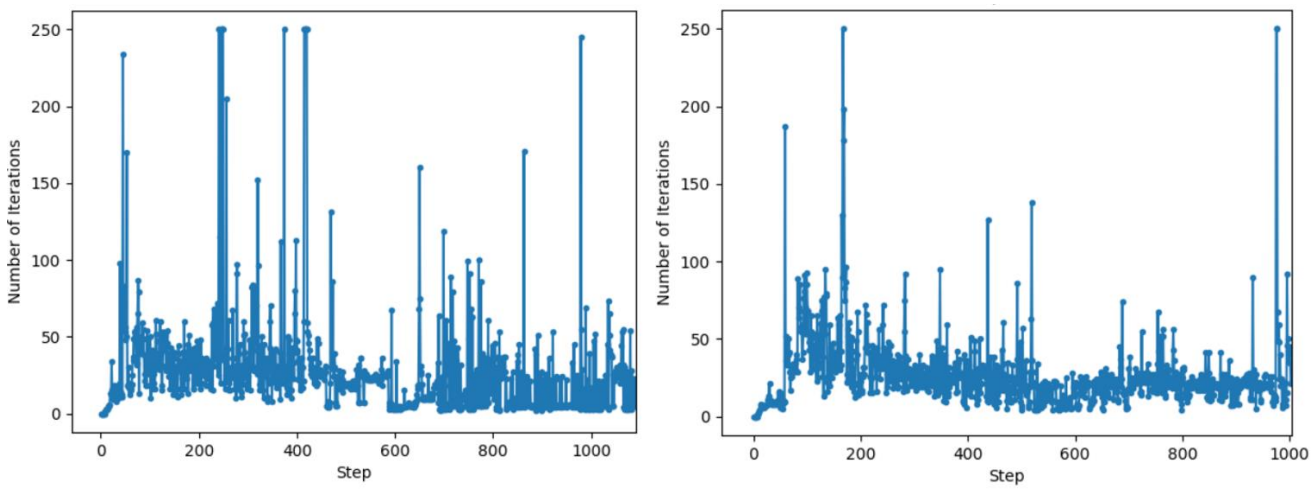

(a) (b)

Figure 4.41 convergence history using the RNR method under (a) positive loading and (b) negative loading

4.2.4 Interpolation scheme

Linear and quadratic elements have been considered in order to investigate the influence of the interpolation scheme on the behaviour of the wall. The capacity curves of the experiment, linear elements and quadratic elements are shown in Figure 4.42. An overview of the analysis results is shown in Table 4.12. The initial stiffness is excluded from this table because it is independent from the element type used in this specific case.

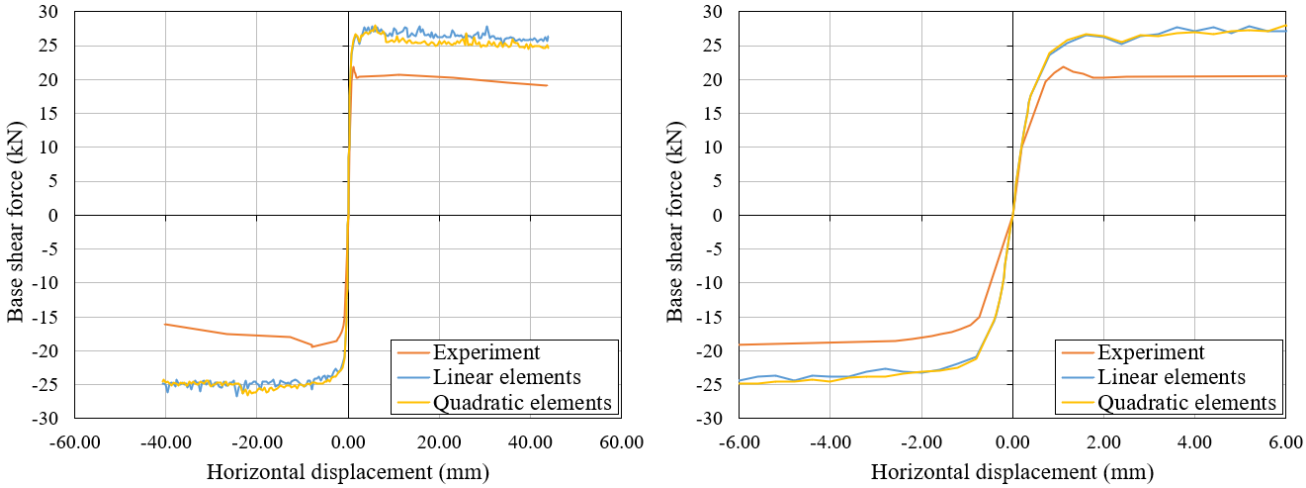

Figure 4.42 capacity curves of the experiment, linear elements and quadratic elements for (a) -60mm to 60mm and (b) -6mm to 6mm

	Peak load in (+) direction	Peak load in (-) direction	Maximum principal strain (+) direction	Maximum principal strain (-) direction
Unit	kN	kN	-	-
Experiment	21.8	-19.4	n.a.	n.a.
Linear elements	27.9	-26.1	0.53	0.55
Quadratic elements	28.0	-26.6	1.1	0.61

Table 4.12 peak loads and maximum principal strains for the experiment, linear elements and quadratic elements

The numerical model with linear elements overestimates, compared to the experiment, the peak load under positive loading by +28%; for loading in the negative direction the overestimation is +35%. The model with quadratic elements overestimates, compared to the experiment, the peak load under positive loading by +28%; for loading in the negative direction the overestimation is +37%.

Figure 4.43 to 4.46 show the crack patterns at various points during the analysis. These correspond to the points where the crack patterns are shown of the experiment of the unstrengthened wall, in section 4.4.1. The results in terms of crack patterns are very similar for both element types. The maximum principal strain in the positive loading direction these are quite different, namely 0.53 and 1.1 for the linear and quadratic elements respectively. This is 0.55 and 0.61 for the negative loading direction.

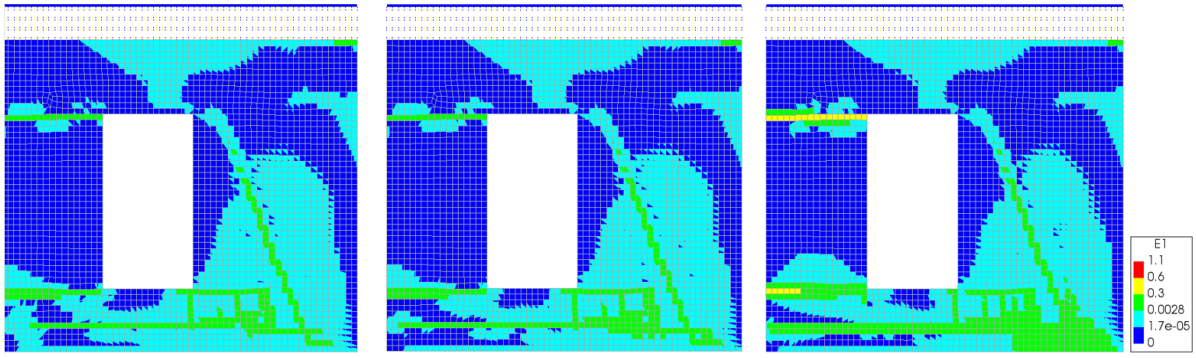

(a) displacement = +7.89mm (b) displacement = +11.11mm (c) displacement = +43.63mm

Figure 4.43 crack patterns at various points under positive loading using linear elements

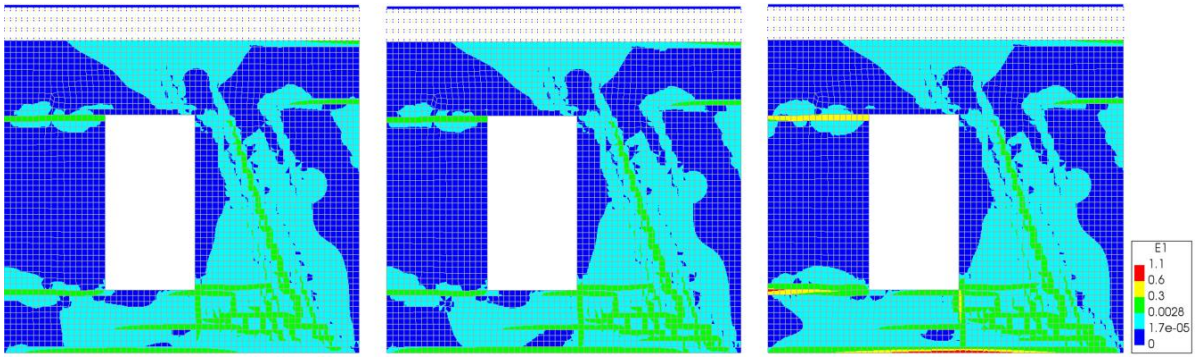

(a) displacement = +7.89mm (b) displacement = +11.11mm (c) displacement = +43.63mm

Figure 4.44 crack patterns at various points under positive loading using quadratic elements

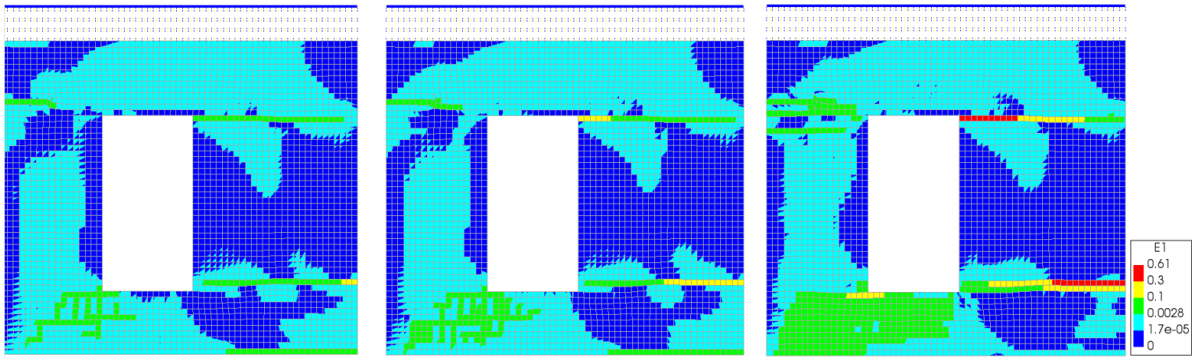

(a) displacement = -7.97mm (b) displacement = -12.82mm (c) displacement = -40.22mm

Figure 4.45 crack patterns at various points under negative loading using linear elements

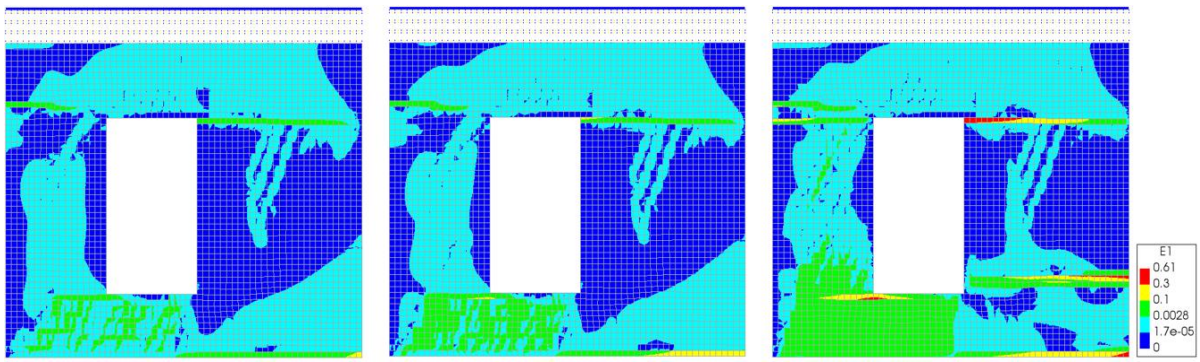

(a) displacement = -7.97mm (b) displacement = -12.82mm (c) displacement = -40.22mm

Figure 4.46 crack patterns at various points under negative loading using quadratic elements

In terms of initial stiffness, peak load and crack pattern there is not much difference. A large difference in the maximum principal strain is encountered between the two element types under loading in the positive direction. The maximum principal strain of 0.53 when using linear elements are unrealistic based on previous research done (Mahmoudimotlagh, 2020). In this research very accurate results were obtained using the TSCM instead of the EMM, which is more suitable for monotonic loading. This is also true when considering the crack widths for both element types. For linear two-dimensional elements the crack bandwidth is defined as $h = \sqrt{2A}$, compared to $h = \sqrt{A}$ for higher order two-dimensional elements. When using linear elements, this results in a maximum crack width of 37.5mm, while for the numerical model using quadratic elements it is 57.6mm. In the previously mentioned research, a maximum crack width of 48.8mm was found, meaning quadratic elements more closely simulate the crack widths found in this report.

Based on this it was decided to continue the rest of the analyses using quadratic elements. It is also preferred to use quadratic elements for practical reasons, since preliminary numerical analyses of the farmhouse façade have already been carried out using quadratic elements (Korswagen et al., 2017).

4.3 Conclusions

To accurately model the behaviour of the masonry walls, the engineering masonry model (EMM) was adopted. Here the head-joint failure type that gave most appropriate results was ‘tensile strength head-joint defined by friction’. The numerical models of the unstrengthened and strengthened walls are in relatively good agreement with the experimental results. Comparison between the results was done in terms of initial stiffness, peak load, crack patterns and crack widths. Since the experimentally tested masonry walls were subjected to three distinctly different loading phases, as opposed to monotonic loading in the numerical models, slight differences can be observed between the numerical and experimental results.

The effects of bed joint reinforced repointing on the performance of the masonry walls is clear. Although it does not have a great impact in terms of initial stiffness and peak load, a clear increase in displacement capacity (ductility) of the structure is observed. Furthermore, a significant reduction in the cracked area, as well as the recorded crack widths, was observed at similar levels of displacement of the top of the wall. This is where the added benefit of bed joint reinforced repointing, in terms of the performance of the structure, becomes evident.

A sensitivity analysis was carried out to investigate the influence of various model parameters on the obtained numerical results. The sensitivity analysis revealed that optimal results, in terms the earlier mentioned quantities, are obtained when using the secant method with BFGS and quadratic elements. These 8-noded quadratic elements provided more accurate numerical results, in terms of maximum principal strains, compared to linear finite elements. The regular Newton-Raphson method also provides acceptable results, but use of the secant method with BFGS is preferred, based on convergence considerations. The outcomes of the sensitivity analysis will be the starting point in numerical analysis of the masonry farmhouse.

Variation of the material parameters (elastic properties, tensile bed- and head joint strength and tensile fracture energy) has shown that most of the investigated results are insensitive to change of these properties. The exception here is the crack width. It has become clear that changes in certain material properties can significantly affect the crack widths found during analysis.

From this it is concluded that the engineering masonry model is a robust smeared failure model that quite accurately predicts the results of the experiments. Furthermore, it is known that the EMM performs specifically well under cyclic loading conditions, like seismic loading, meaning it should perform especially well in seismic analysis of the masonry farmhouse.

5 Numerical Results of Masonry Façade

5.1 Introduction

This chapter will present the results of various numerical investigations done on the masonry façade. The following sections will show the results of each model, and its governing mechanisms, in-depth. First, the numerical results of the unstrengthened, unreinforced masonry (URM), façade, as in-field, will be presented. Then, the façade strengthened with bed joint reinforced (BJR) repointing is covered, where various PGVs are considered, after which the results of a numerical model with partially reinforced masonry are shown. For all of these, the analysis procedure described in section 3.3.4 has been used. After this, in section 5.5, a comparison, and summary, of the obtained results will be given. Finally, conclusions will be drawn, at the end of this chapter.

A scaled principal strain, as used in analysis of the masonry walls, was omitted since, unlike with the masonry wall, the bed- and head joints are characterized by differing tensile strengths. Instead, the crack patterns were analysed, using the principal crack widths. A damage value ψ_D is introduced to evaluate the evolution of damage in the façade. This damage parameter is defined as follows (Korswagen et al., 2019):

$$\psi_D = 2{n_c}^{0.15} \cdot {c_w}^{0.3} \tag{5.1}$$

Where n_c is the number of cracks in the structure and c_w is the width-weighted and length-averaged crack width of the structure. This parameter c_w is defined as follows:

$$c_w = \frac{\sum_{i=1}^{n_c} c_{w,i}^2 \cdot c_{L,i}}{\sum_{i=1}^{n_c} c_{w,i} \cdot c_{L,i}} \tag{5.2}$$

Where $c_{w,i}$ and $c_{L,i}$ are the maximum crack width and length of each individual crack in the structure.

5.2 Unstrengthened masonry façade

As seen in the description of the analysis procedure, in section 3.3.4, three distinct loading phases can be identified in numerical analysis of the unstrengthened masonry façade. Namely, a gravity & overburden loading phase, a settlement loading phase and a seismic loading phase. In this section the results of these three loading phases will be shown and discussed.

5.2.1 Gravity & overburden loading

To correctly simulate the in-field structural condition of the façade the gravity & overburden loads are introduced first. The vertical displacements at the end of the gravity & overburden loading phase are shown in Figure 5.1. Sagging of the middle part of the façade is observed, with a maximum vertical displacement of -0.61mm. The normal stiffness of the interface elements in this middle part are substantially lower than at the lateral ends of the structure, resulting in larger displacements in the centre, compared to the edges.

Cracking of the masonry is not observed at the end of the loading phase. The highest value of maximum principal strain (Figure 5.2) is observed around the window corners, however they do not reach the cracking strain.

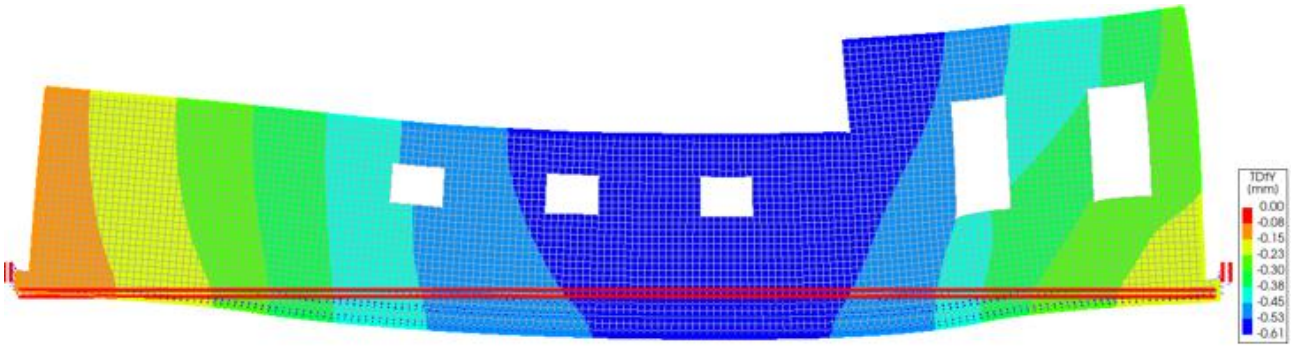

Figure 5.1 vertical displacements at the end of the gravity & overburden loading phase (scale factor 0.05)

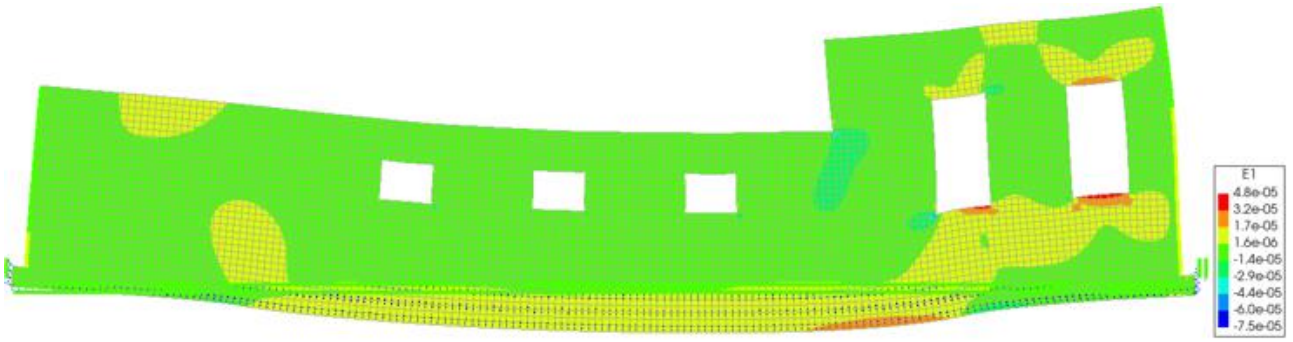

Figure 5.2 Maximum principal strains at the end of the gravity & overburden loading phase (scale factor 0.05)

5.2.2 Settlement loading

A settlement profile in accordance with the one shown in Figure 3.6 is applied to the base of the façade. The maximum amplitude of the prescribed deformation was -4.90mm. The vertical displacements at the end of the settlement phase are shown in Figure 5.3. As can be seen, these displacements follow the settlement profile nicely. The maximum vertical displacement is -4.97mm, slightly higher than the maximum amplitude of the settlement load, due to residual displacements from the previous loading phase.

Substantial cracking is observed at the end of the settlement phase. Three main cracks can be identified, denoted as location 1, 2 and 3. The locations where the maximum crack widths are recorded are shown in Figure 5.4. The location where these cracks appear is logical; they all form around the window corners, in the area where the curvature of the settlement profile is the greatest. Additionally, minor cracks are starting to propagate at different locations around the façade, mainly around corners.

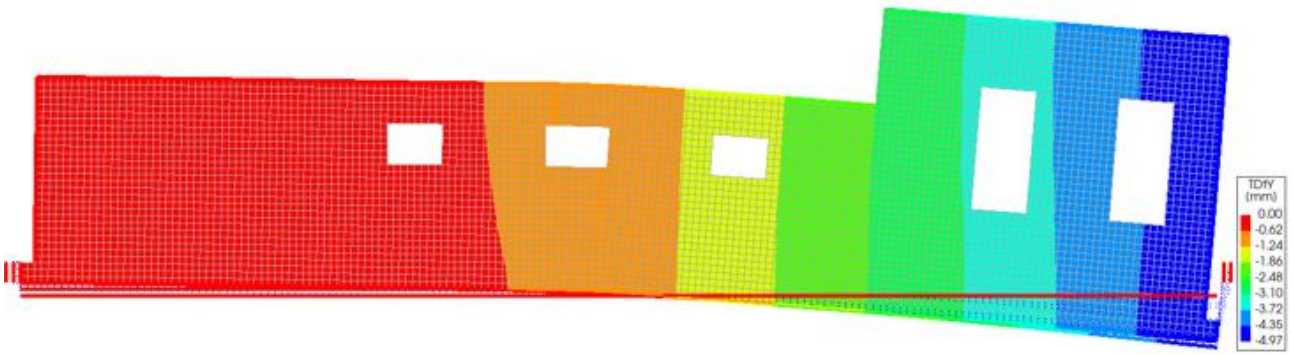

Figure 5.3 vertical displacements at the end of the settlement loading phase (scale factor 0.05)

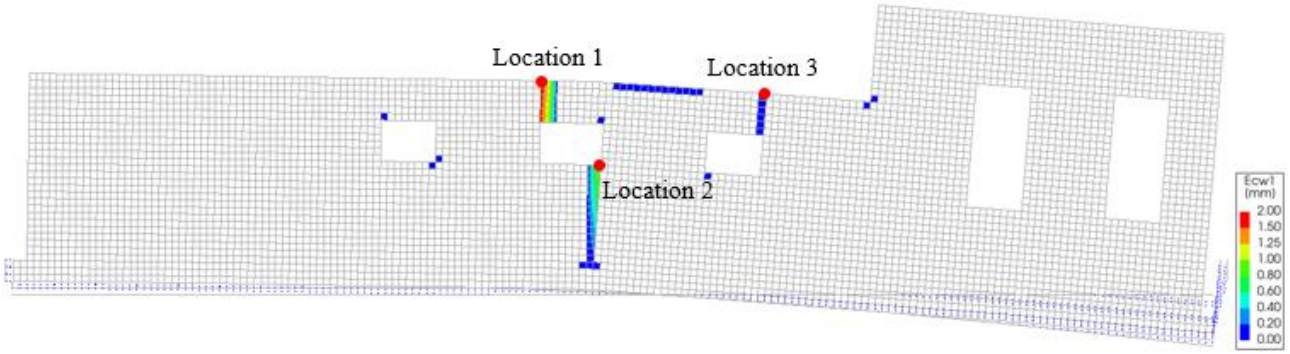

Figure 5.4 crack widths at the end of the settlement loading phase (scale factor 0.05)

The recorded maximum crack widths of these three main cracks, formed during the settlement loading phase, and their lengths, can be found in Table 5.1. These are used to compute the damage value $\psi_{D,main}$ at the end of the settlement phase. A second damage value $\psi_{D,total}$ is introduced, accounting for all the cracks formed during the analysis, even those with a relatively small crack width. This way, the major and minor cracks can be analysed separately. After the settlement loading phase, this results in damage value of:

$\psi_{D,main} = 2.55$
$\psi_{D,total} = 2.83$

	Location 1	**Location 2**	**Location 3**
Crack width (mm)	1.77	1.09	0.22
Crack length (mm)	600	1500	600

Table 5.1 maximum crack widths and lengths of major cracks at the end of the settlement loading phase

5.2.3 Seismic loading phase

Normally, in construction of the capacity curves, the horizontal top node displacements are considered, relative to a fixed base. Since a nonlinear time history analysis is carried out time (inertial) effects must be considered. Since in this case the seismic loads are applied at the dummy elements below the bottom nodes of the foundation, a relative horizontal displacement, Δu, is introduced that is defined as follows:

$$\Delta u = u_{P,top} - u_{P,bottom} \tag{5.3}$$

Where $u_{P,top}$ and $u_{P,bottom}$ are the *phased* horizontal displacements of the top and bottom node respectively. Use of phased horizontal displacements ensure that only horizontal displacements found during seismic loading are considered. This effectively means that residual horizontal displacements due to the previous two loading phases are excluded. Thus, these phased displacements start at zero at the start of the seismic loading phase, when the base shear force is also still zero. In equation (5.3) the bottom node is the one that is directly below the top node of any given location, but at foundation level.

Using the expected seismic load (PGV of 64mm/s) as input, multiple capacity curves were constructed and analysed. Figure 5.5 shows an overview of the researched nodes, used in the capacity curves, where the top nodes are denoted in red and the corresponding bottom nodes below, in blue. Eventually, it was decided to further investigate the capacity curve found on the far most right side of the façade, shown with a black arrow in the figure, since at this location the largest relative displacements were found. The resulting capacity curve can be found in Figure 5.6.

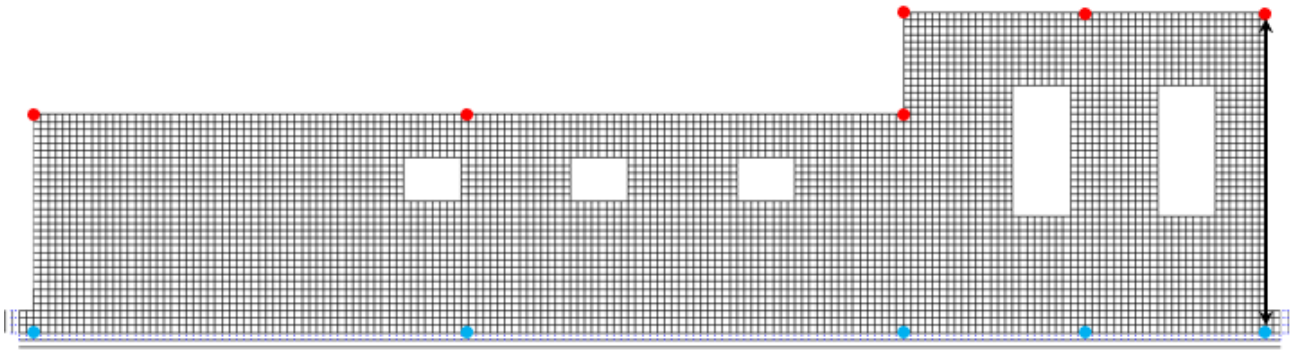

Figure 5.5 nodes used in construction of the capacity curves

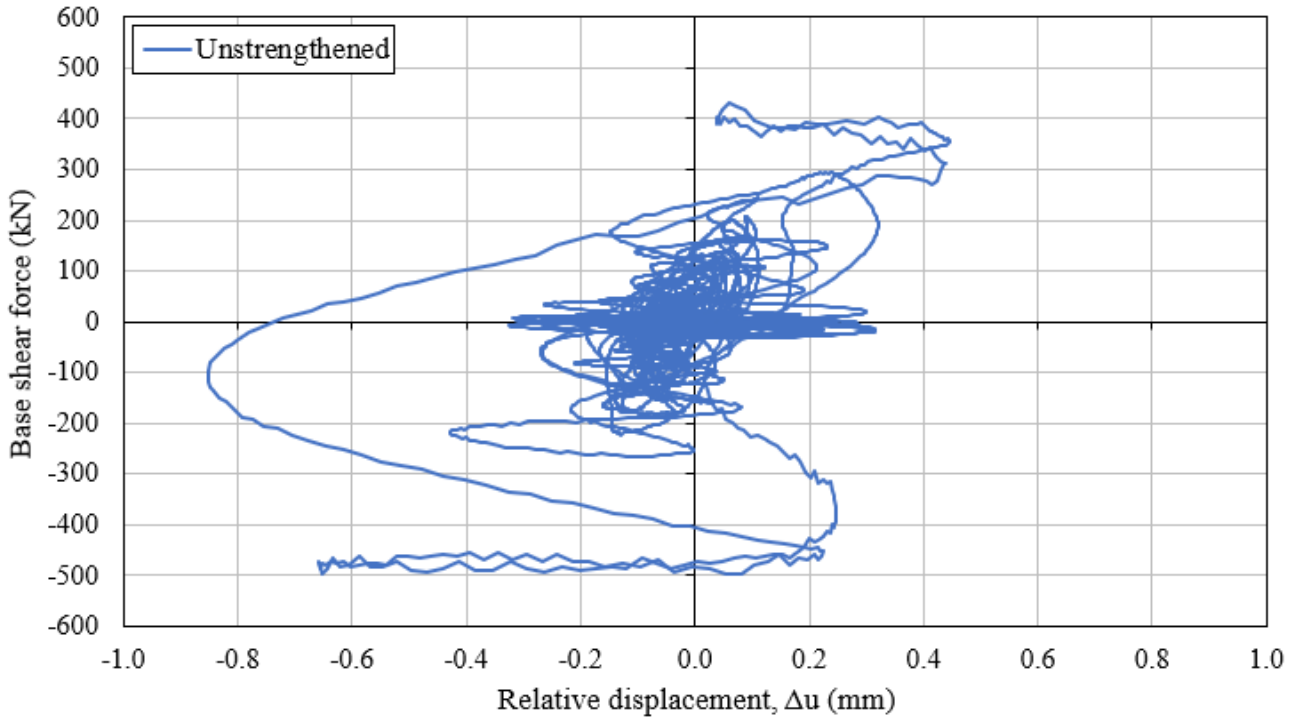

Figure 5.6 capacity curve of the unstrengthened façade (far most right side)

The first thing that is immediately evident from the capacity curve, is that there are a lot of horizontal loops; a large relative displacement is registered, while the base shear force stays more or less the same. Unlike what one might expect, this horizontal looping behaviour is not observed near peaks in the horizontal displacement of the bottom nodes, but rather at the local maxima/minima of the base shear force. In its simplest form, the equations of motion, for multiple degrees of freedom, can be written as follows:

$$\boldsymbol{M\ddot{u} + C\dot{u} + Ku = F_{ext}} \tag{5.4}$$

Due to the nature of the seismic load, a low frequency motion, it turns out that the magnitude of the base shear force is mainly governed by the forces generated due to viscous damping (velocity), and barely by the springs (displacement) and mass of the structure (acceleration). In Figure 5.7 the normalised horizontal velocity of the bottom node and corresponding base shear force is shown. For clarity, the colours of these graphs are black and red. It is clear here that the velocity and base shear force have the same shape and only minor differences between the two can be observed. At the peaks of the base shear force, and the horizontal velocity, the latter quickly reduces in magnitude. Due to inertia effects this results in a drift of the top node compared to the bottom node, meaning a large relative displacement is recorded, while the base shear force remains more constant.

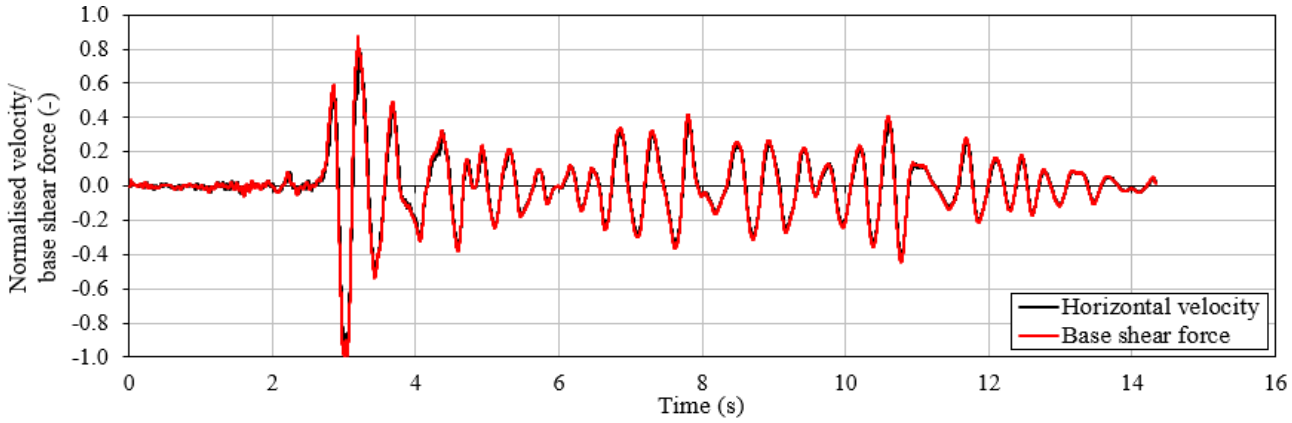

Figure 5.7 Normalised horizontal velocity of the bottom node and base shear force

This means that peaks in the displacement graph occur closely to where the base shear, and horizontal velocity, is zero, which is what would be expected. Furthermore, this behaviour is the cause for the clutter seen around the centre of the capacity curve. At the start of the motion, low amplitude, high frequency seismic waves predominantly occur, causing many, small, horizontal loops near the centre of this curve.

After analysis of the numerical model, several points of interest are identified around the (absolute) maximum displacement and base shear force. Points of interest are marked (A-E) in Figure 5.8, where the load path (running from A to E) is highlighted in orange. These points are determined as follows:

- Point A: maximum crack width recorded at location 1 & 2
- Point B: intermediate point (maximum crack width at location 3 after unloading of location 1 & 2)
- Point C: peak base shear force in the negative (-) direction
- Point D: maximum crack width recorded at location 3
- Point E: peak base shear force in the positive (+) direction

For clarity, these points of interest are also shown in Figure 5.9. Here, a section of the base shear force over time graph, running from 2.9s to 3.2s, is shown. The complete graph, over the course of seismic loading, can be found in the top-left corner.

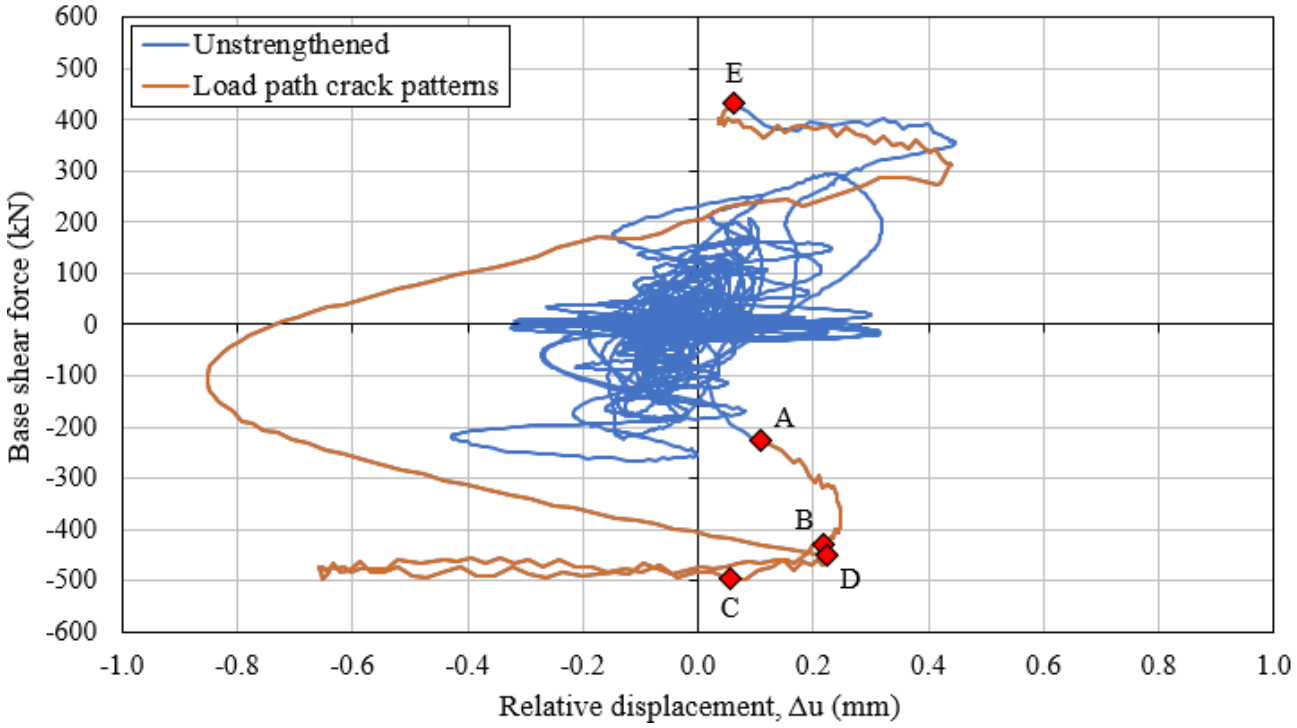

Figure 5.8 capacity curve of the unstrengthened façade with points of interest (orange line and A-E markers)

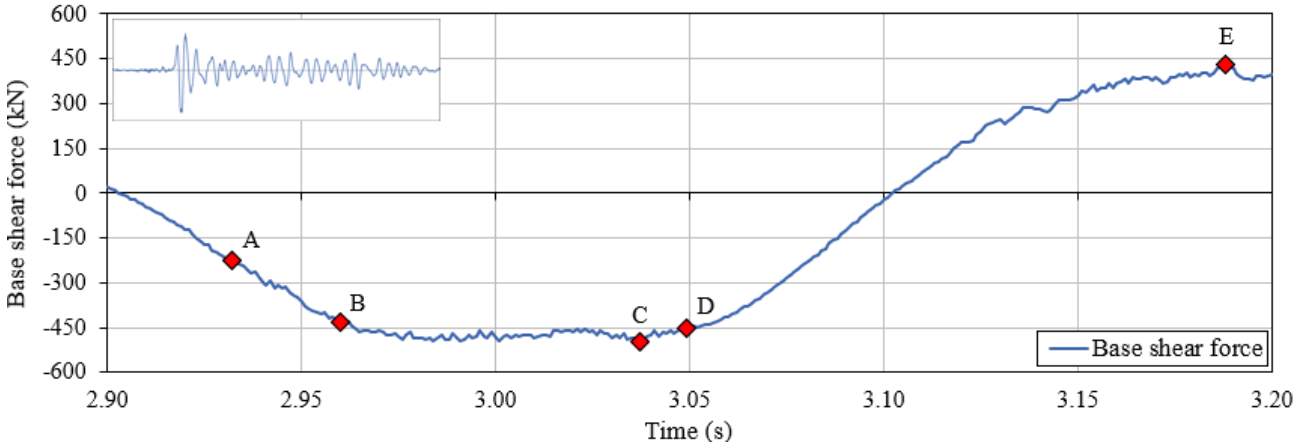

Figure 5.9 section of the base shear over time of the unstrengthened façade, with the points of interest (A-E)

In Figure 5.10(a) to 5.10(e) the crack patterns at the points of interest (A-E) are shown, as well as the crack pattern at the end of analysis, see Figure 5.10(f). The corresponding crack widths can be found in Table 5.2 (maxima are in bold). The only crack that increases in crack length is the one at location 2, to a length of 1600mm, as the cracks at location 1 and 3 are fully formed and could no longer increase in length. Examination of the crack patterns show that there is no formation of any new major cracks during seismic loading. Previous research (Korswagen et al., 2019) has shown that this is often the case for façades that have a small height to length ratio (H/L). These structures are less prone to damage due to seismic loading, compared to structures which have a large H/L ratio. These structures are, generally, more susceptible to settlement damage.

	Crack width (mm)			$\psi_{D,main}$ (-)	$\psi_{D,total}$ (-)
Point	**Location 1**	**Location 2**	**Location 3**		
After settlement	1.77	1.09	0.22	2.55	2.83
A	**1.91**	**1.23**	0.25	**2.62**	**3.09**
B	1.42	0.98	0.42	2.40	2.88
C	1.09	0.65	0.49	2.18	2.57
D	1.01	0.63	**0.56**	2.15	2.53
E	1.09	0.51	0.00	2.05	2.61
End of analysis	1.59	0.98	0.21	2.47	2.95

Table 5.2 recorded crack widths and damage values at various points of for the unstrengthened facade

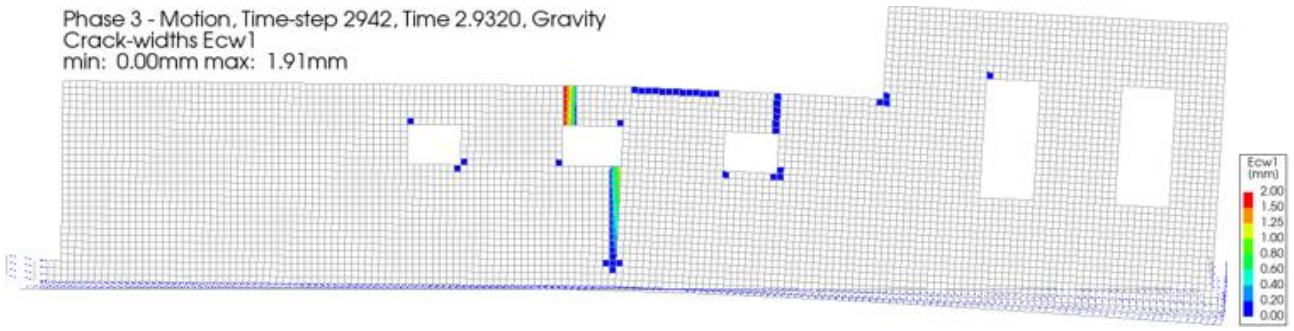

(a) point A (scale factor 0.05)

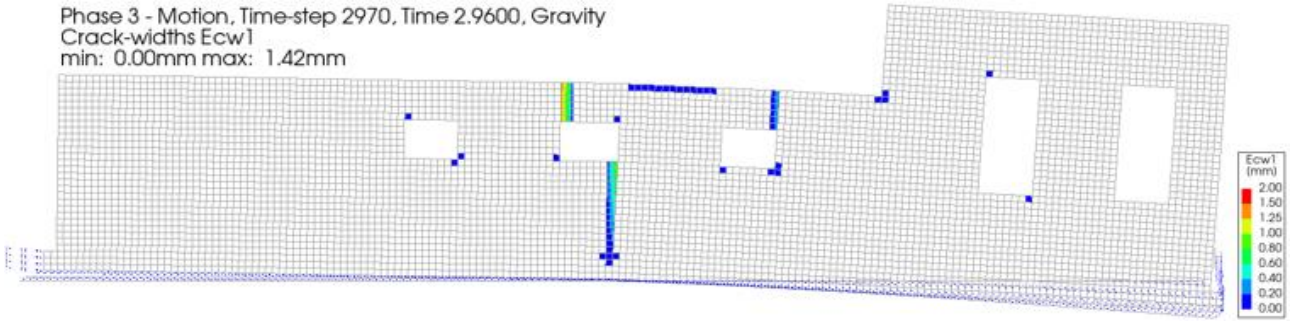

(b) point B (scale factor 0.05)

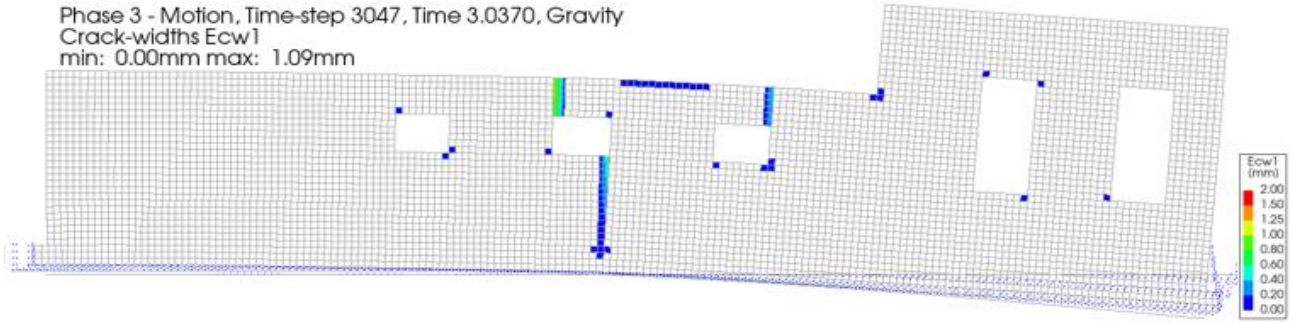

(c) point C (scale factor 0.05)

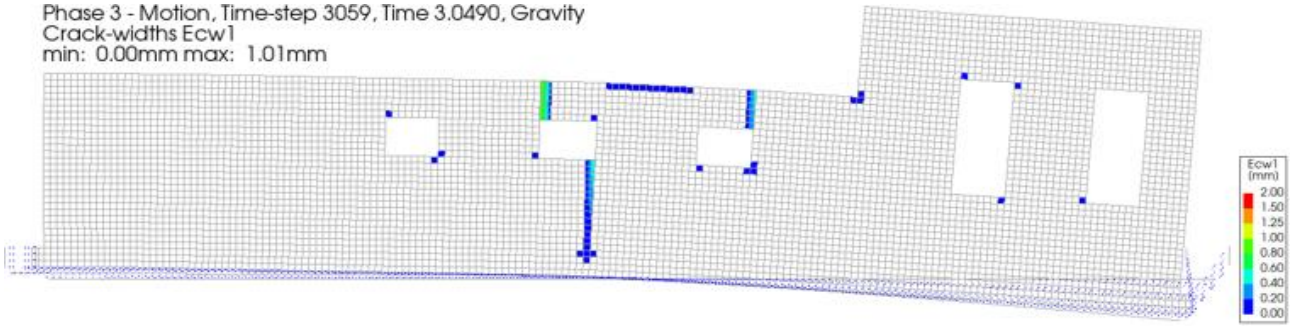

(d) point D (scale factor 0.05)

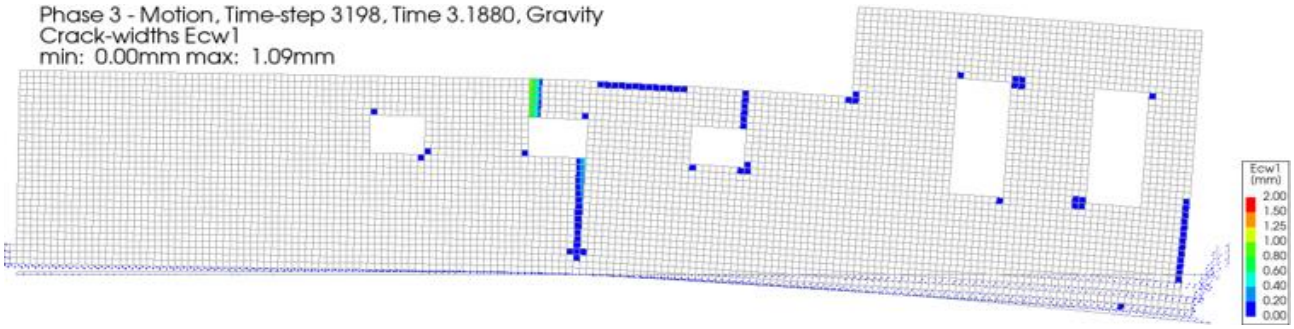

(e) point E (scale factor 0.05)

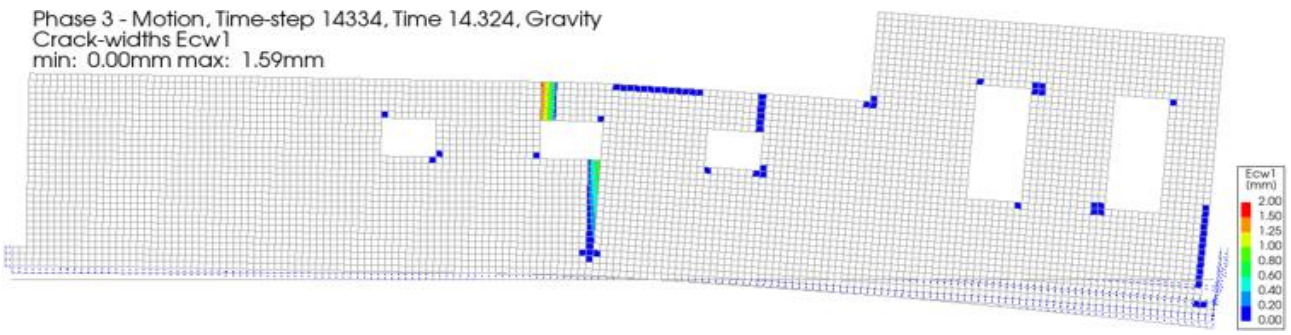

(f) end of analysis (scale factor 0.05)

Figure 5.10 crack patterns at the points of interest (A-E) and at end of analysis for the unstrengthened façade

In a relatively short period (±250ms), around the peaks in base shear force, substantial changes are found in the status of the structure. Here, the maximum crack widths are found, as well as the peaks in the base shear force. Due to the cyclic nature of the seismic load, and its corresponding inertia effects, opening and closing of cracks is observed.

In Figure 5.10(a) the crack pattern at point A is shown. Here, the maximum crack width at location 1 & 2 are recorded. Furthermore, an increase in the crack length at location 2 is found, increasing its total length to 1600mm. When seismic loading continues something interesting happens. Unloading of the cracks at location 1 & 2 is observed, while an increase in crack width at location 3 is recorded. This continues until the *local* maximum crack width at location 3 is reached, which is denoted as point B (intermediate point) and is shown in Figure 5.10(b).

Shortly after, a plateau in the base shear force is reached, initially closing all cracks simultaneously. This behaviour is caused by a combination of the previously mentioned effect, where large relative displacements are found at the peaks of the base shear force, and the time shift. The time shift causes parts of the structure to move at different rates. It turns out that near peaks in the shear force, closing of cracks is amplified because of this phenomenon. This behaviour is reinforced by the fact that there is a positive vertical motion at this point, increasing the rate at which cracks close. This is also the reason opening of some cracks and closing of others at the same time is observed, as in Figure 5.10(a) to 5.10(b). The time shift causes a redistribution of loads towards the crack at location 3. Sometime after reaching this plateau relaxation of the façade is observed, and subsequently cracks start to open again and the peak base shear force in negative direction is found. The crack pattern at this point, C, is shown in Figure 5.10(c). This opening of cracks continues and the *global* maximum crack width at location 3 is found. The crack pattern at this point, D, is shown in Figure 5.10(d).

Then, a large change in direction of the motion causes a peak in the relative displacement of -0.85mm and closing of cracks is once again observed, until the peak load in positive direction is reached. The crack pattern of this point, E, is shown in Figure 5.10(e). As can be seen in Table 5.2, the crack at location 3 is even completely closed at this point. Furthermore, there are quite a few minor cracks that have formed during this stage of the motion. The crack pattern at the end of analysis is shown in Figure 5.10(f). When comparing Figure 5.10(e) with 5.10(f), it is obvious that there is barely any evolution of damage, since the peak of the motion has already been reached.

Traditionally, one would expect to see cracks opening when the base shear is at its peak. That is not always true in this case. This is because the base shear forces are mainly governed by viscous damping, causing these forces to be closely correlated to the velocity of the structure, and subsequently the resulting relative displacements. This, in combination with the fact that the load is applied where the boundaries are located and the fact inertia effects are present, ensure that there is sometimes closing of cracks at these moments. The maximum crack widths therefore do not necessarily appear when the base shear force is not at a peak.

From Table 5.2 it becomes evident that during seismic loading no major increase in crack widths are found for the locations 1 & 2, while for location 3 it is quite substantial. The maximum total damage value ($\psi_{D,total,max}$) found during seismic analysis, is found at point A. The total damage value is the damage value that quantifies the damage in the façade due to *all* the cracks found at any given point. Here, an increase in crack width of +7.9%, +12.8% and +13.6% for location 1, 2 and 3 respectively is found, compared to after settlement loading.

A damage value of the main cracks of $\psi_{D,main} = 2.63$ is calculated, a mere +2.7% increase compared to the $\psi_{D,main}$ found after settlement. However, when minor cracks are included in the calculation a damage value of $\psi_{D,total} = 3.09$ is found, an increase of +9.2% compared to the damage value after settlement. Clearly, as the analysis proceeds, mainly the minor cracks drive up the final damage values. This effect is also seen at the other points of interest (B to E) considered. The maximum increase in crack width at location 3, at point D, is +154.5%. Toe crushing is not observed. A discussion of the force capacity (base shear force) and relative displacement will be done in section 5.5, when comparing the unstrengthened and strengthened façade.

At the end of analysis, a reduction of the crack widths is found, compared to after settlement loading. A reduction in crack width of -10.2%, -10.1% and -4.5% for location 1, 2 and 3 respectively is found. Here, the damage value of the main cracks is $\psi_D = 2.47$, a reduction of -3.1%. This reduction in crack widths is due to the inertia effects that are encountered during seismic loading. The constant loading and unloading of the façade leave it in a state where, at the end of analysis, the cracks are narrower than after settlement. Furthermore, extensive cracking of certain areas is observed at the end of analysis. And, as stated earlier: as the analysis proceeds, mainly the minor cracks drive up the final damage values. At the end of analysis, the total damage value is $\psi_{D,total} = 2.95$, an increase of +4.2% compared to the damage value after settlement. Now, it has become clear that the increase in damage due to seismic loading is small, compared to the damage due to settlement loading. It can therefore be concluded that this type of façade is more sensitive to damage due to settlement loading, compared to seismic loading. Table 5.3 shows the percentage changes in cracks widths at the locations 1, 2 and 3, as well as the damage values, compared after settlement loading, when the $\psi_{D,total}$ is maximum (in this case point A) and at the end of analysis.

Compared to after settlement	Δw_1	Δw_2	Δw_3	$\Delta \psi_{D,main}$	$\Delta \psi_{D,total}$
At $\psi_{D,total,max}$	+7.9%	+12.8%	+13.6%	+2.7%	+9.2%
At end of analysis	-10.2%	-10.1%	-4.5%	-3.1%	+4.2%

Table 5.3 percentage changes in crack widths and damage values during seismic loading, compared to after settlement loading, for the unstrengthened facade

Convergence was found in every load step of the gravity & overburden and settlement loading phases. In the start steps (these are the first 10 steps of the analysis) of the seismic loading phase, very large displacement variations and out of balance forces were found. This can be seen in Figure 5.11, which shows the convergence results during the seismic loading phase. This is because during these start steps DIANA encountered issues equilibrating internal and external forces, since no external load was applied here yet. However, it was determined this is not an issue, since there was no change in the status of the structure (in terms of displacements and crack widths) during or after the start steps. During the seismic load phase itself, non-convergence was found in 3 time-steps. This comes down to a non-convergence rate of 0.02%, defined as percentage of time steps that did not convergence (in this case 3 out of 14324). It was always the displacement norm that encountered non-convergence, when the maximum number of 500 iterations was reached.

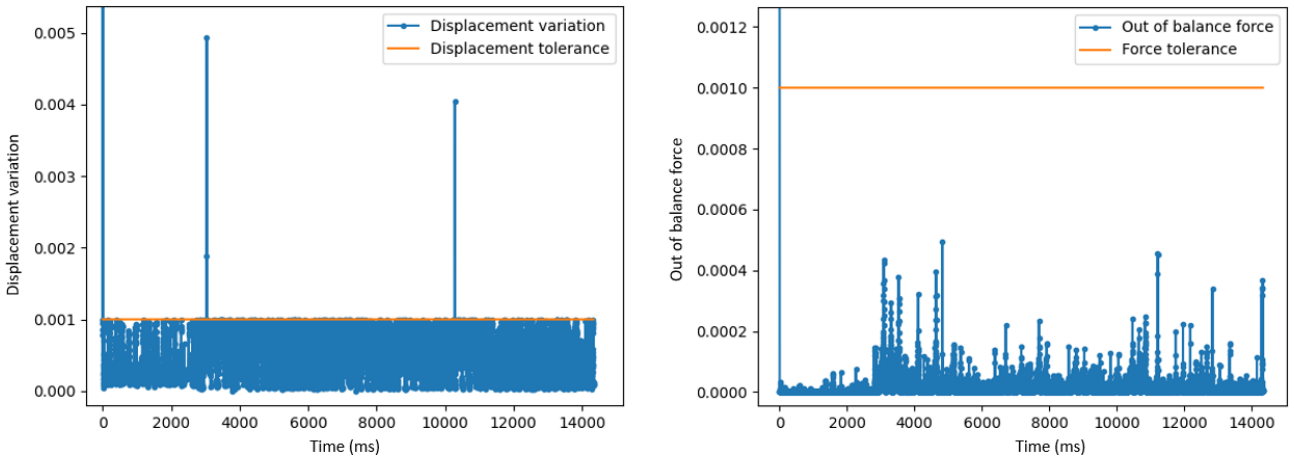

(a) (b)

Figure 5.11 convergence history during seismic loading of the unstrengthened façade for (a) the displacement norm and (b) the force norm

5.3 Strengthened masonry façade

Various investigations with respect to the effects of bed joint reinforced repointing, under combined settlement and seismic loading, on the structural response of the façade, have been carried out. This section outlines the results of two types of seismic load. First the results of a numerical analysis using the previously determined expected seismic load (PGV of 64mm/s) are provided (as used in analysis of the unstrengthened façade). After this the results for two amplified seismic motions are shown. In this case an amplification of the motion by a factor 1.5 and 2, corresponding to a PGV of 96mm/s and 128mm/s respectively.

5.3.1 Expected seismic load

Again, three distinct loading phases can be identified in numerical analysis of the façade strengthened with bed joint reinforced repointing. However, in this section only the results of the seismic loading phase are presented, since the gravity & overburden and settlement loading phases are identical to the one for the unstrengthened façade. The steel reinforcement is applied *after* the settlement loading phase. This means that prior to seismic loading there are no stresses and strains in the steel reinforcement ($\varepsilon = 0$). The PGV is now 64mm/s. The abbreviation used in the discussion for this façade is 'strengthened BJR (1x EQ)'.

Also, for the strengthened façade multiple capacity curves were constructed and analysed. The same combination of nodes as previously, was deemed critical, and work was continued with this curve. The capacity curve and the points of interest are marked (A-D) in Figure 5.12 where the load path (running from A to D) is highlighted in orange. Please note that the meaning of the points has changed; the maximum crack width at location 3 now occurs *before* the peak base shear force in negative direction is reached. Furthermore, the intermediate point has been removed. Thus, these points are now determined as follows:

- Point A: maximum crack width recorded at location 1 & 2
- Point B: maximum crack width recorded at location 3
- Point C: peak base shear force in the negative (-) direction
- Point D: peak base shear force in the positive (+) direction

These points of interest are also shown in Figure 5.13. Here, a section of the base shear force over time graph, running from 2.9s to 3.2s, is shown. The complete graph, over the course of seismic loading, can be found in the top-left corner.

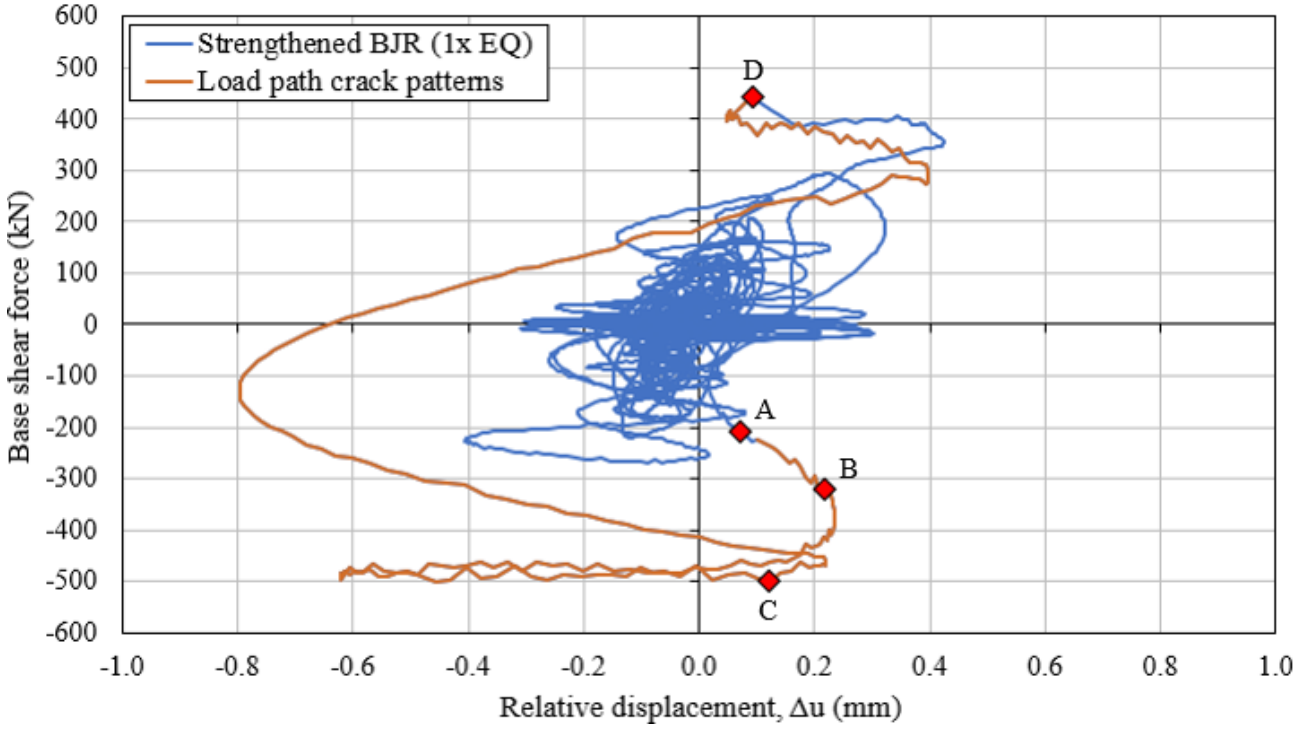

Figure 5.12 capacity curve of the strengthened BJR (1x EQ) façade with the points of interest (orange line and A-D markers)

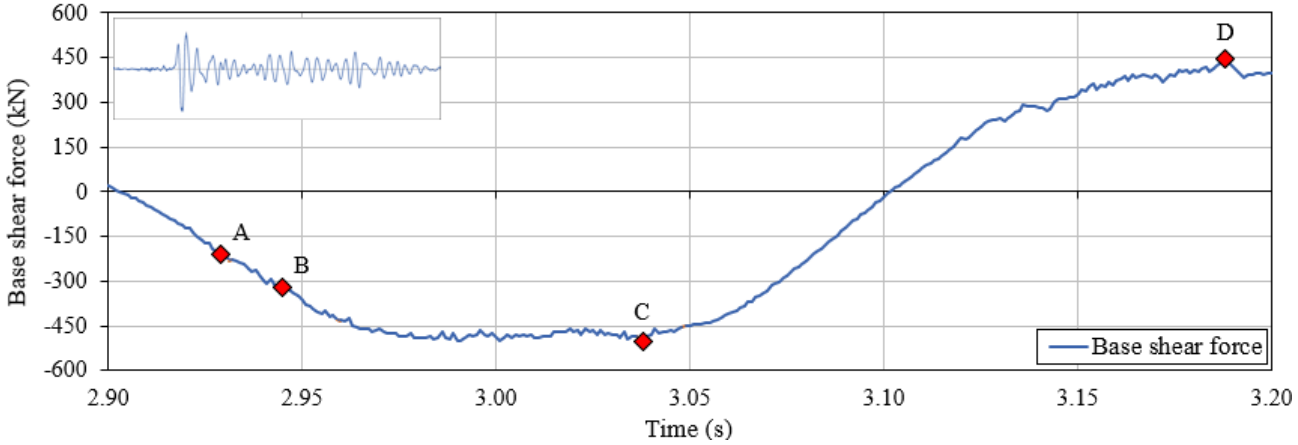

Figure 5.13 section of the base shear over time of the strengthened BJR (1x EQ) façade, with the points of interest (A-D)

One of the key differences, compared to the unstrengthened façade, is that the maximum crack width for location 3 now occurs *before* the peak base shear force in negative direction is reached. This is because the crack at location 3 is closer to one of the edges of the reinforcement, compared to location 1 and 2, causing it to open earlier.

In Figure 5.14(a) to 5.14(d) the crack patterns at the points of interest (A-D) are shown, as well as the crack pattern at the end of analysis, see Figure 5.14(e). The corresponding crack widths can be found in Table 5.4 (maxima are in bold). Once again, the only main crack that increases in length is the one at location 2, to a length of 1600mm.

	Crack width (mm)			$\psi_{D,main}$(-)	$\psi_{D,total}$ (-)
Point	**Location 1**	**Location 2**	**Location 3**		
After settlement	1.77	1.09	0.22	2.55	2.83
A	**1.82**	**1.15**	0.27	**2.57**	**2.92**
B	1.73	1.14	**0.32**	2.54	2.89
C	1.59	0.98	0.28	2.46	2.78
D	1.46	0.76	0.00	2.25	2.72
End of analysis	1.71	1.05	0.19	2.52	2.89

Table 5.4 recorded crack widths and damage values at various points of interest during seismic loading

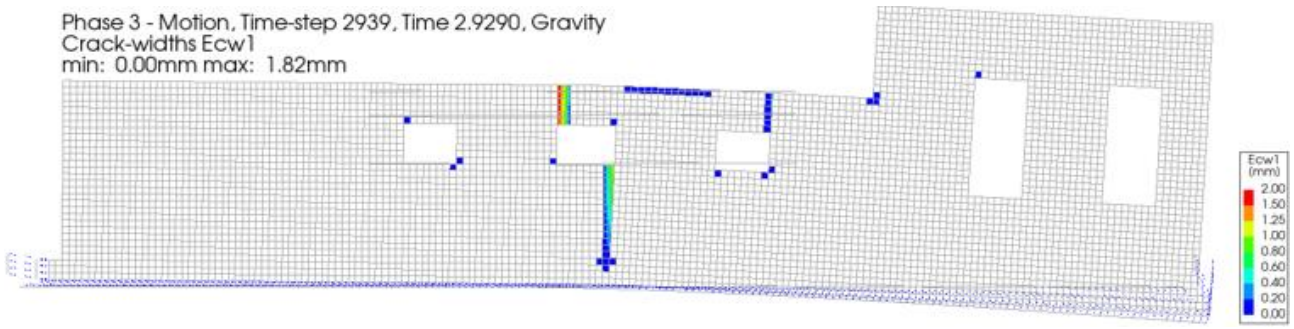

(a) point A (scale factor 0.05)

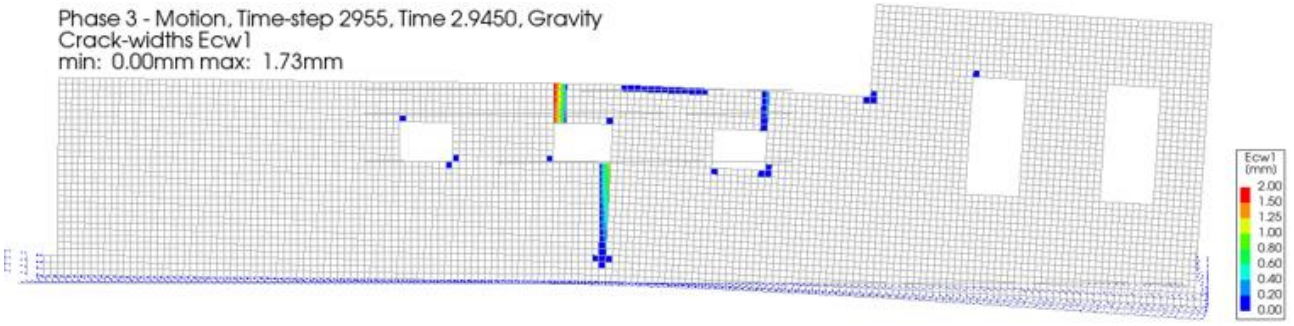

(b) point B (scale factor 0.05)

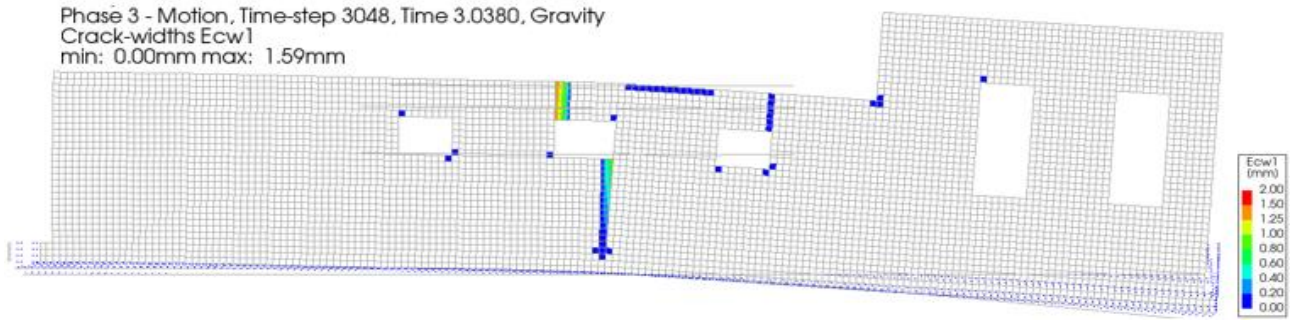

(c) point C (scale factor 0.05)

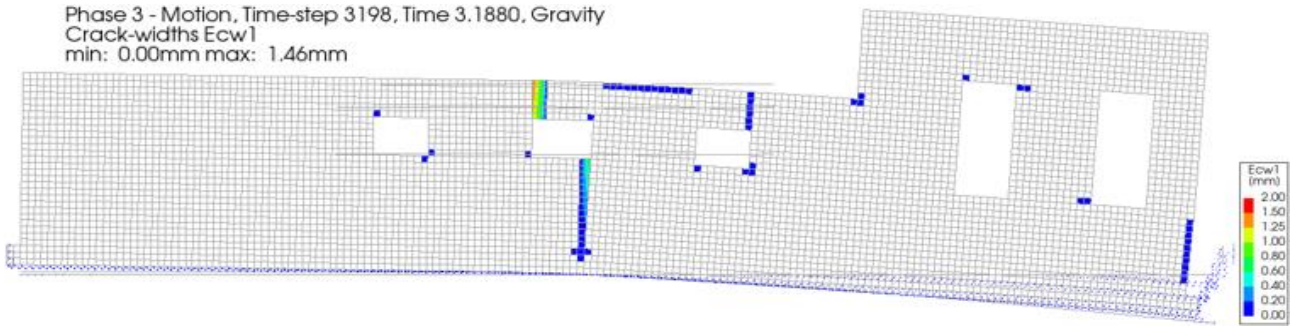

(d) point D (scale factor 0.05)

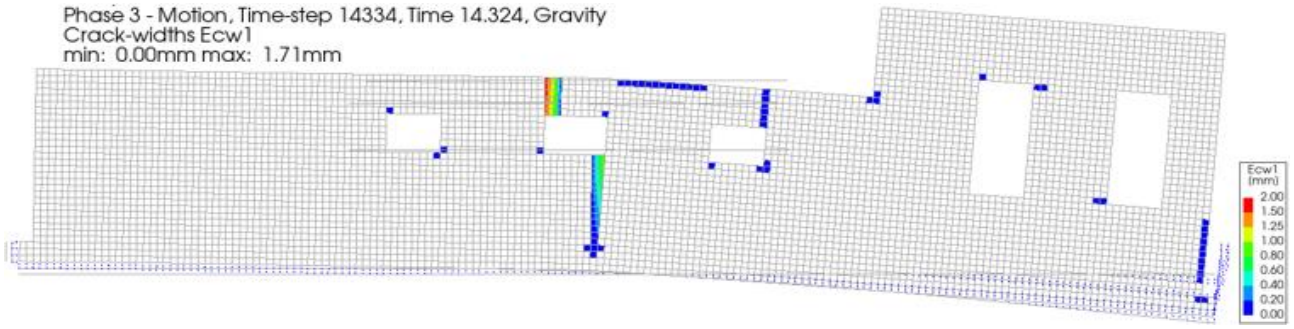

(e) end of analysis (scale factor 0.05)

Figure 5.14 crack patterns at the point of interest (A-D) and at end of analysis for the strengthened BJR (1x EQ) façade

Since the shape of the capacity curve of the strengthened façade is nearly identical to the capacity curve of the unstrengthened façade, the behaviour and observations made in section 5.2.3 remain valid. This in turn causes the crack patterns in Figure 5.14(a) to 5.14(e) to be very similar to the ones of the unstrengthened wall, see Figure 5.10. However, due to addition of reinforcement, a reduction in crack formation and propagation is observed during seismic loading and at the end of analysis, compared to the unstrengthened façade.

The maximum Von Mises stresses found during analysis is 58.8N/mm^2 and is shown in Figure 5.15. The results are shown over the length of the reinforcement bars. The Von Mises stresses agree with the crack patterns found; the stresses are developed in the regions where cracking is encountered. The Von Mises stresses are lower than the yielding limit ($f_y = 215$MPa), see Figure 3.4. The corresponding (maximum) relative shear displacements (slip), between the masonry and steel reinforcement, in the local x-direction of the reinforcement is shown in Figure 5.16. The bed joint reinforcement undergoes barely any slip. The absolute maximum slip was found to be 0.10mm, meaning it is still in the initial linear branch of the bond-slip curve, see Figure 3.4.

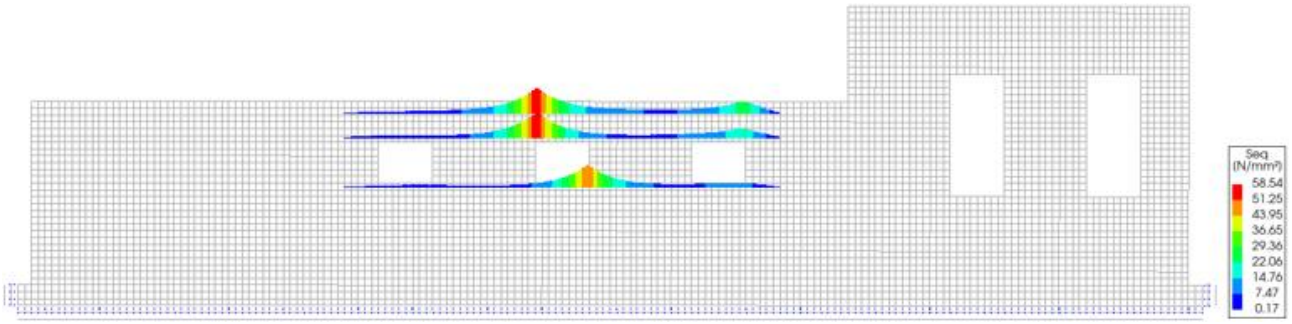

Figure 5.15 Von Mises stresses in the reinforcement (undeformed)

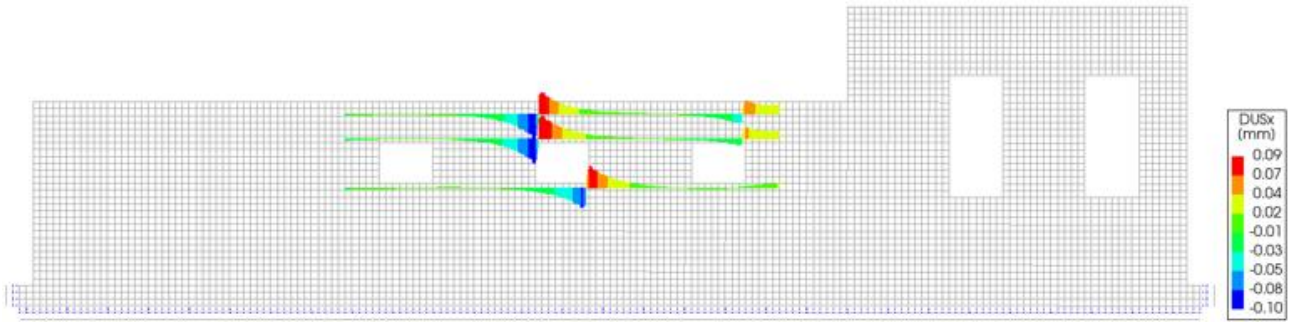

Figure 5.16 amount of slip in the reinforcement (undeformed)

Figure 5.17 shows the convergence history for the strengthened BJR (1xEQ) façade. In each time step, both convergence criteria had to be met to obtain convergence. Again, non-convergence was observed in the start steps. During the rest of the analysis, non-convergence was found in only 2 time-steps: a non-convergence rate of 0.01%. It was always the displacement norm that encountered non-convergence, when the maximum number of 500 iterations was reached.

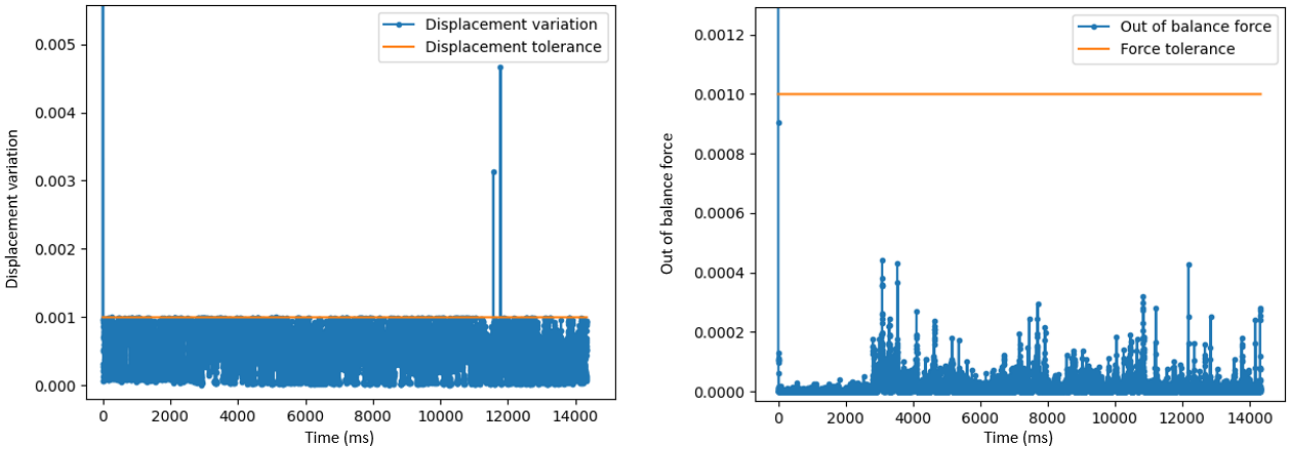

(a) (b)

Figure 5.17 convergence history during seismic loading of the strengthened BJR (1x EQ) façade for (a) the displacement norm and (b) the force norm

5.3.2 Amplified seismic load

This section shows the numerical results of the strengthened façade, but now using various amplified seismic loads. First, the results of an amplification of the expected seismic load by a factor 1.5 (corresponding to a PGV of 96mm/s) will be shown, after which the numerical results of amplification of the signal by a factor 2 (PGV of 128mm/s) are presented. Please note that these analyses a maximum of 100 iterations per time step was used, instead of 500 iterations. This was done to reduce the computational effort required. The reader is referred to appendix A for validation that this reduction is warranted.

Amplified seismic load: factor 1.5

Once again, only the results of the seismic loading phase are presented, since the results of the gravity & overburden and settlement loading phases are identical to the ones provided in section 5.2. Prior to seismic loading there are no stresses and strains in the steel reinforcement ($\varepsilon = 0$). The PGV is now 96mm/s. The abbreviation used in the discussion for this façade is 'strengthened BJR (1.5x EQ)'.

Also, for this numerical model multiple capacity curves were constructed and analysed. The same combination of nodes as previously, was deemed critical, and work was continued with this curve. The capacity curve and the points of interest are marked (A-E) in Figure 5.18, where the load path (running from A to E) is highlighted in orange. For this analysis the maximum crack width at locations 1 & 2 does not occur simultaneously. In this case the maximum crack width at location 2 is found first and then the maximum crack width at location 3 is found. After this the peaks in base shear force are found, and finally, the maximum crack width at location 1 is observed. Thus, these points are now determined as follows:

- Point A: maximum crack width recorded at location 2
- Point B: maximum crack width recorded at location 3
- Point C: peak base shear force in the negative (-) direction
- Point D: peak base shear force in the positive (+) direction
- Point E: maximum crack width recorded at location 1

These points of interest are also shown in Figure 5.19. Here, a section of the base shear force over time graph, running from 2.9s to 3.25s, is shown. The complete graph, over the course of seismic loading, can be found in the top-left corner.

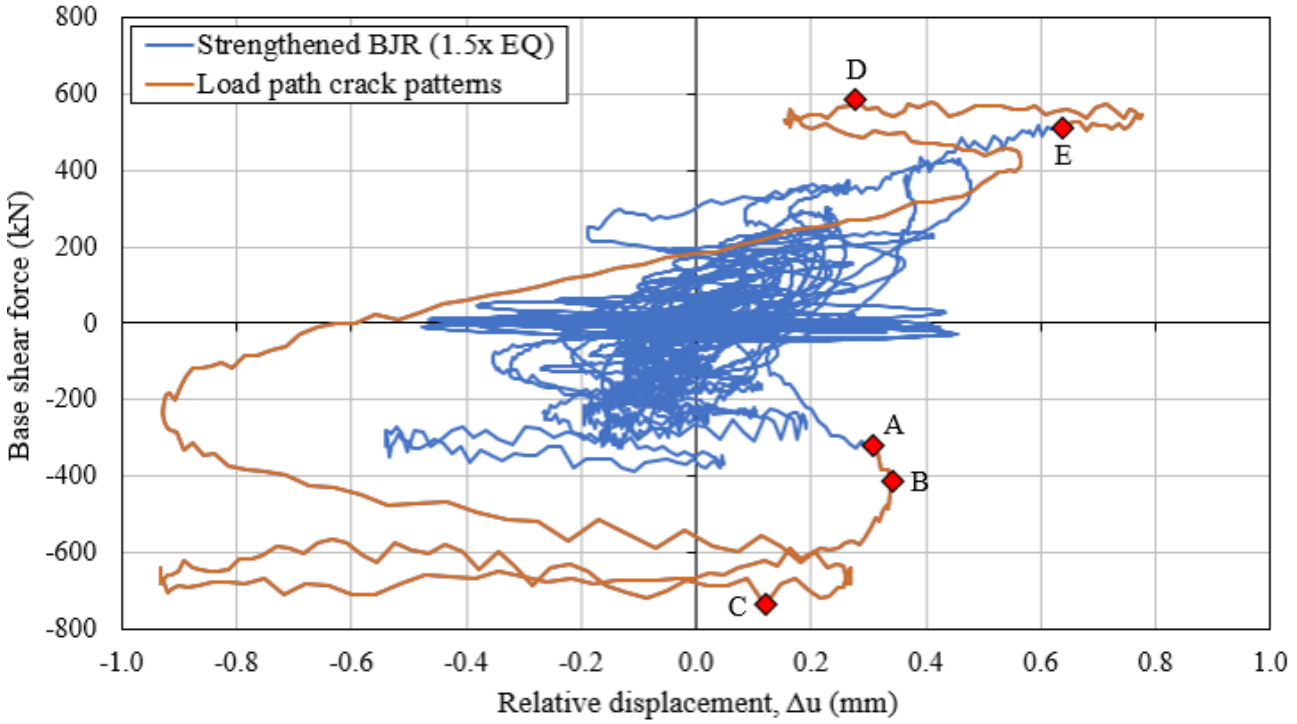

Figure 5.18 capacity curve of the strengthened BJR (1.5x EQ) façade with various points of interest (orange line and A-E markers)

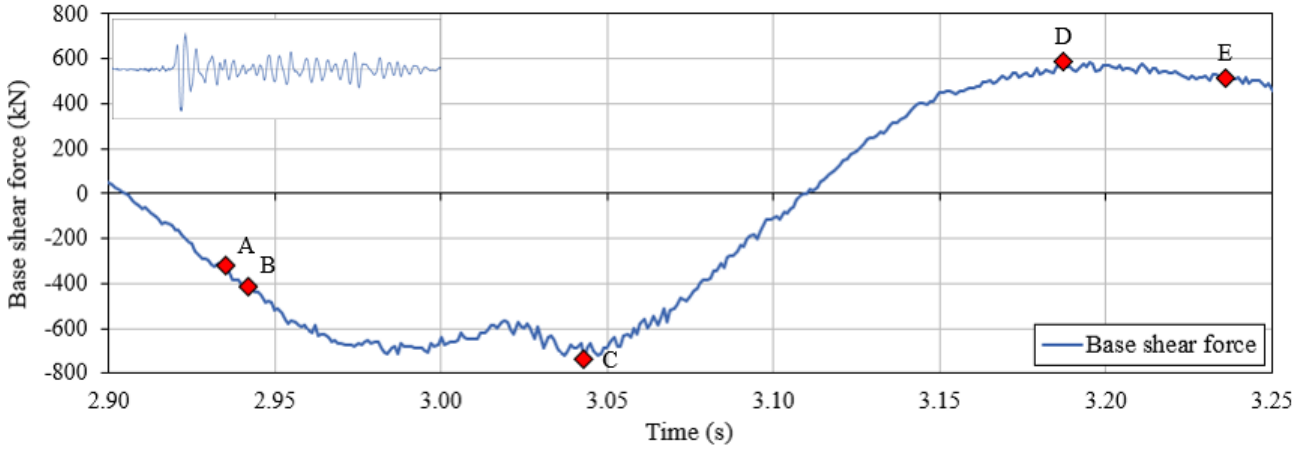

Figure 5.19 section of the base shear over time of the strengthened BJR (1.5x EQ) façade, with the points of interest (A-E)

Figure 5.20(a) to 5.20(e) shows the crack patterns at the points of interest (A-E) are shown, as well as the crack pattern at the end of analysis, see Figure 5.20(f). The corresponding crack widths can be found in Table 5.5 (maxima are in bold). Once again, the only main crack that increases in length is the one at location 2, to a length of 1600mm.

	Crack width (mm)			$\psi_{D,main}$(-)	$\psi_{D,total}$ (-)
Point	**Location 1**	**Location 2**	**Location 3**		
After settlement	1.77	1.09	0.22	2.55	2.83
A	1.79	**1.19**	0.36	2.57	3.03
B	1.71	1.16	**0.38**	2.54	3.00
C	0.50	0.10	0.02	1.73	2.07
D	1.63	0.77	0	2.31	2.99
E	**1.95**	1.14	0.16	**2.62**	**3.37**
End of analysis	1.72	0.95	0.10	2.51	3.05

Table 5.5 recorded crack widths and damage values at various points of interest during seismic loading

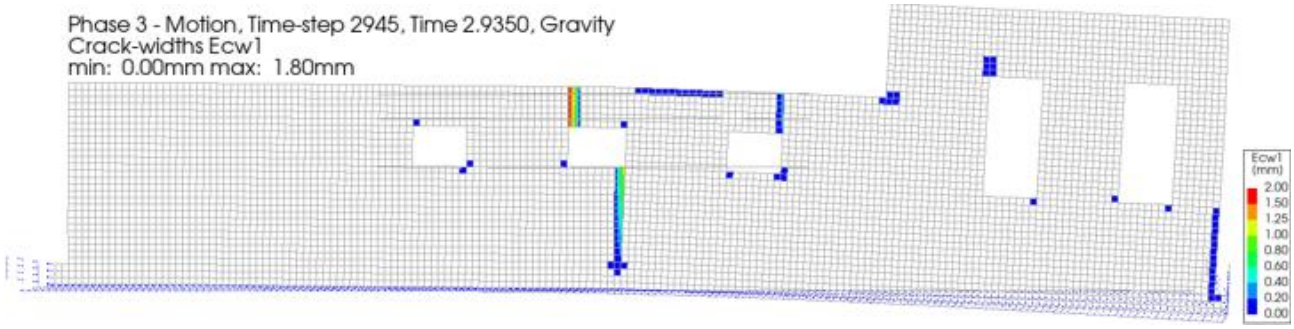

(a) point A (scale factor 0.05)

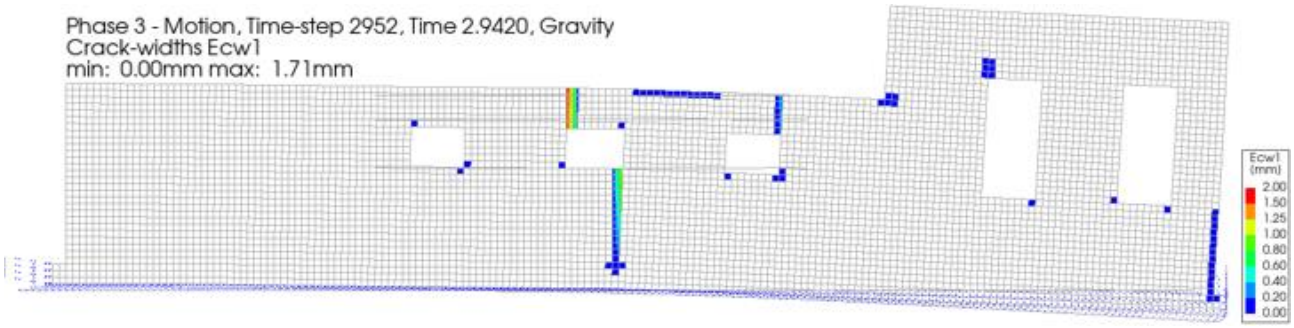

(b) point B (scale factor 0.05)

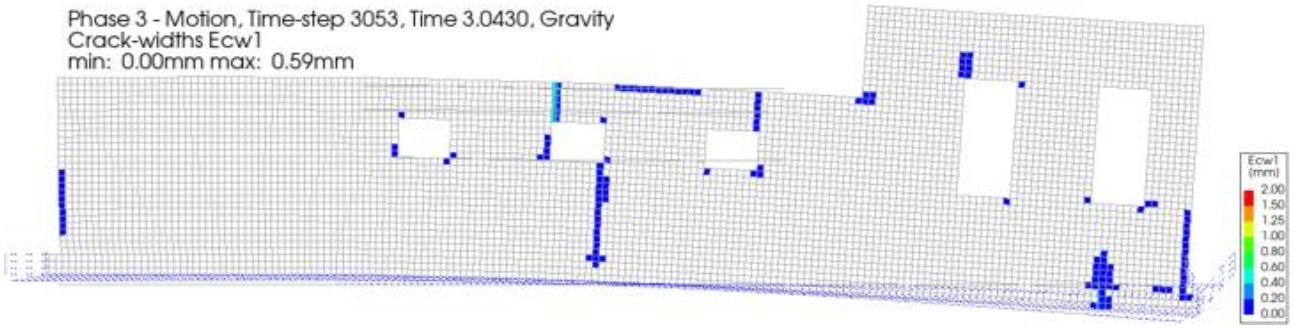

(c) point C (scale factor 0.05)

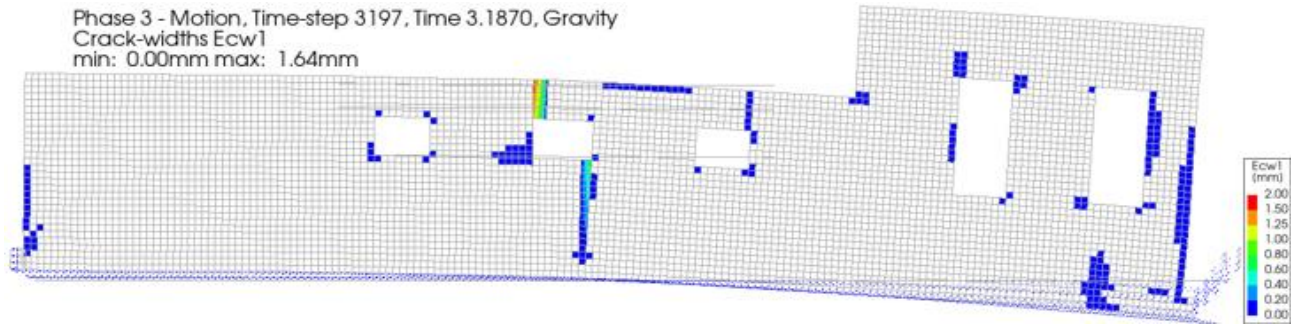

(d) point D (scale factor 0.05)

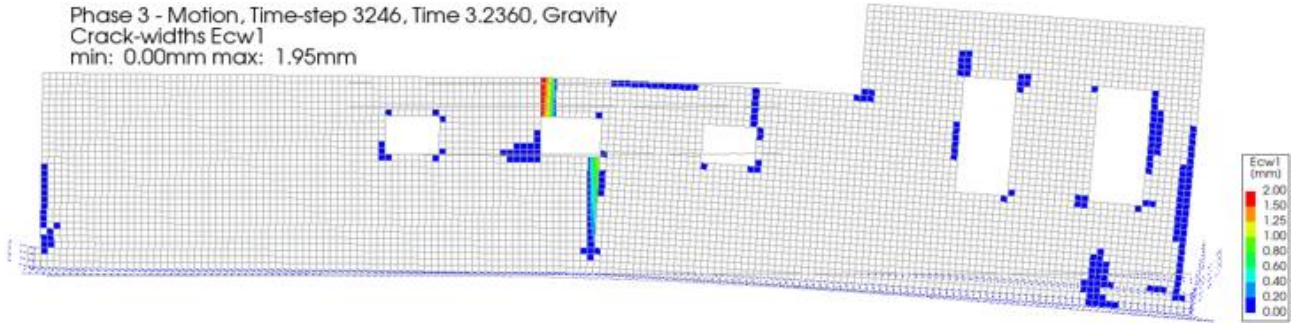

(e) point E (scale factor 0.05)

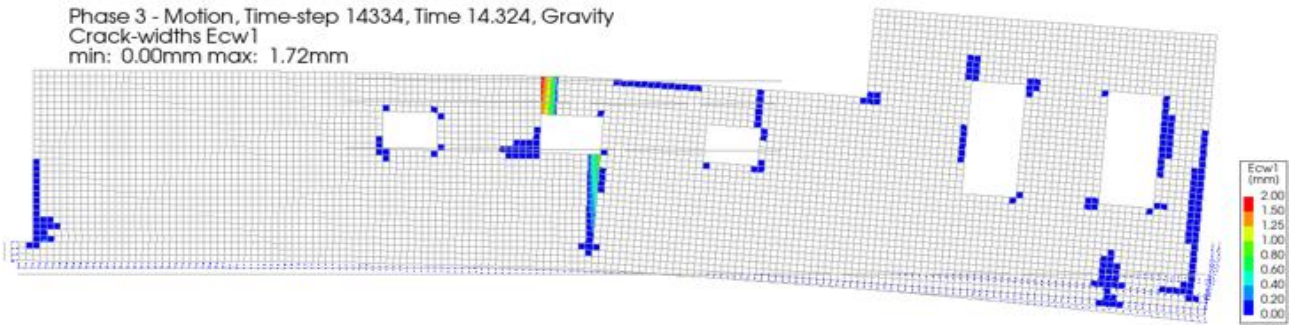

(f) end of analysis (scale factor 0.05)

Figure 5.20 crack patterns at the point of interest (A-E) and at end of analysis for the strengthened BJR (1.5x EQ) façade

The maximum Von Mises stresses found during analysis is 126.7N/mm^2 and is shown in Figure 5.21. The results are shown over the length of the reinforcement bars. The Von Mises stresses agree with the crack patterns found; the stresses are developed in the regions where cracking is encountered. The Von Mises stresses are lower than the yielding limit ($f_y = 215$MPa), see Figure 3.4. The corresponding (maximum) relative shear displacements (slip), between the masonry and steel reinforcement, in the local x-direction of the reinforcement is shown in Figure 5.22. The bed joint reinforcement undergoes barely any slip. The absolute maximum slip was found to be 0.32mm, meaning it is still in the initial linear branch of the bond-slip curve, see Figure 3.4.

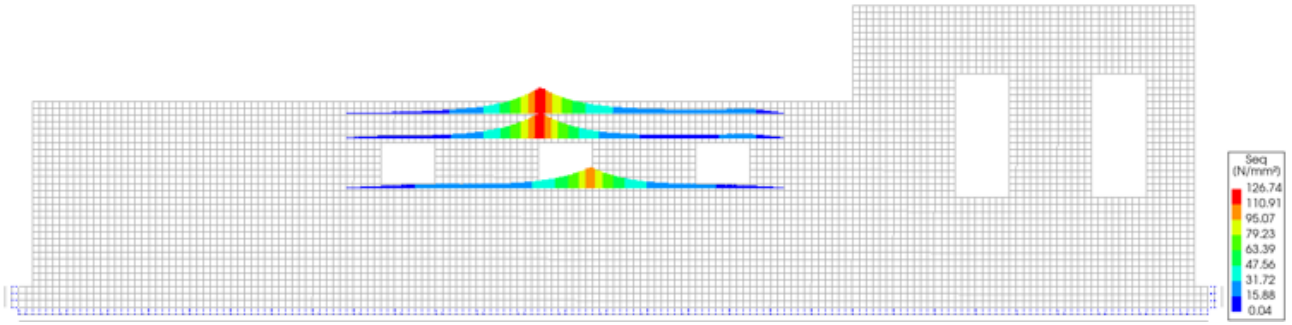

Figure 5.21 Von Mises stresses in the reinforcement (undeformed)

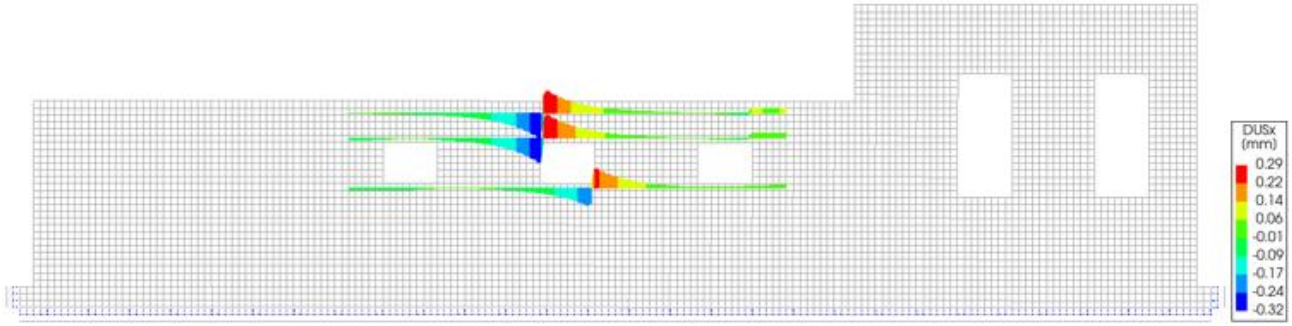

Figure 5.22 amount of slip in the reinforcement (undeformed)

Figure 5.23 shows the convergence history for the strengthened BJR (1.5x EQ) façade. In each time step, both convergence criteria had to be met to obtain convergence. Again, non-convergence was observed in the start steps. Near the peak of the motion, extended cracking of certain areas of the façade was observed. This cracking resulted from this point on in heavy non-convergence at times. Please note that, as stated earlier, a maximum of 100 iterations per time step was used, instead of 500 previously, to reduce the computational effort required (see appendix A for validation of this decision). In total 2152 time-steps encountered non-convergence: a non-convergence rate of 15.0%, which is quite large. Most of the time, it was the displacement norm that encountered non-convergence, when the maximum number of 100 iterations was reached. An exceedance of the displacement tolerance of up to 35 times was found. However, for the force norm this was not the case. Here, non-convergence of the force tolerance was found very sparsely and in case of non-convergence the exceedance of the tolerance was minimal (much lower than one magnitude of 10). Therefore it was concluded that although non-convergence was found in many steps, the results of the analysis were decently trustworthy.

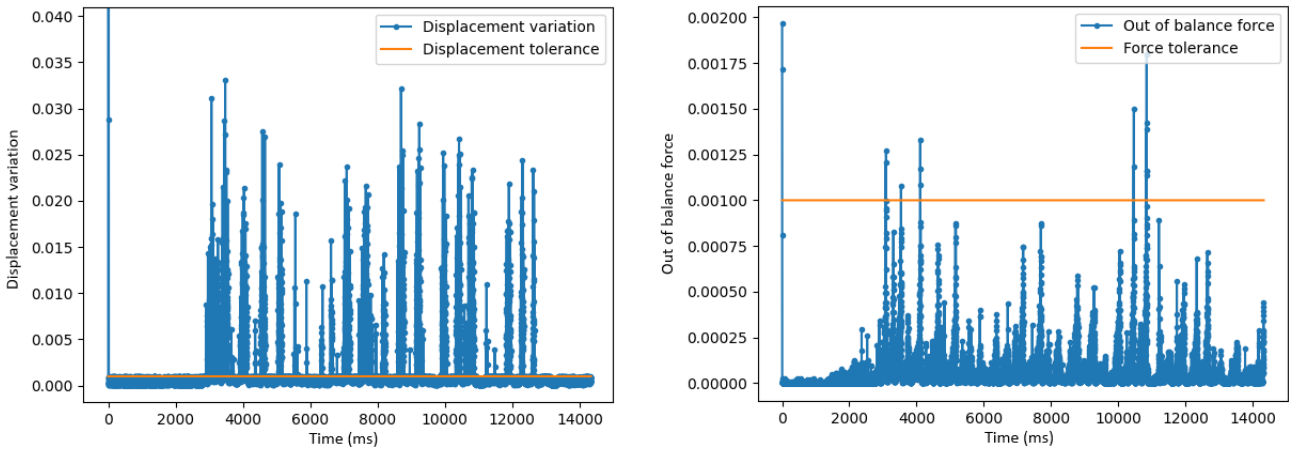

(a) (b)

Figure 5.23 convergence history during seismic loading of the strengthened BJR (1.5x EQ) façade for (a) the displacement norm and (b) the force norm

Amplified seismic load: factor 2

Once again, only the results of the seismic loading phase are presented, since the results of the gravity & overburden and settlement loading phases are identical to the ones provided in section 5.2. Prior to seismic loading there are no stresses and strains in the steel reinforcement ($\varepsilon = 0$). The PGV is now 128mm/s. The abbreviation used in the discussion for this façade is 'strengthened BJR (2x EQ)'.

Also, for this numerical model multiple capacity curves were constructed and analysed. The same combination of nodes as previously, was deemed critical, and work was continued with this curve. The capacity curve and the points of interest are marked (A-C) in Figure 5.24. where the load path (running from A to D) is highlighted in orange. For this analysis the maximum crack widths at locations 1 & 3 occurs simultaneously. Thus, these points are now determined as follows:

- Point A: maximum crack width at location 2
- Point B: peak base shear force in the negative (-) direction
- Point C: peak base shear force in the positive (+) direction
- Point D: maximum crack width at location 1 & 3

These points of interest are also shown in Figure 5.25. Here, a section of the base shear force over time graph, running from 2.85s to 3.25s, is shown. The complete graph, over the course of seismic loading, can be found in the top-left corner, where the failure of the façade, at 4.5s, is marked with a red marker.

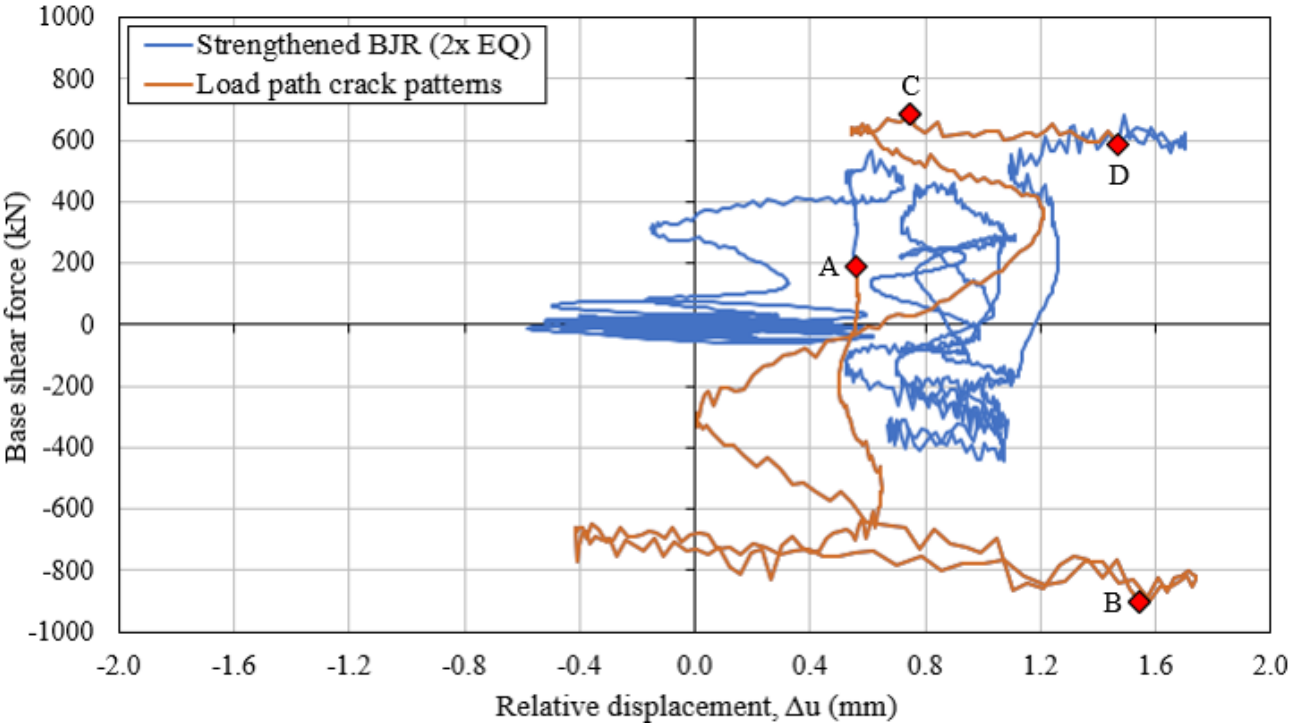

Figure 5.24 capacity curve of the strengthened BJR (2x EQ) façade with various points of interest (orange line and A-D markers)

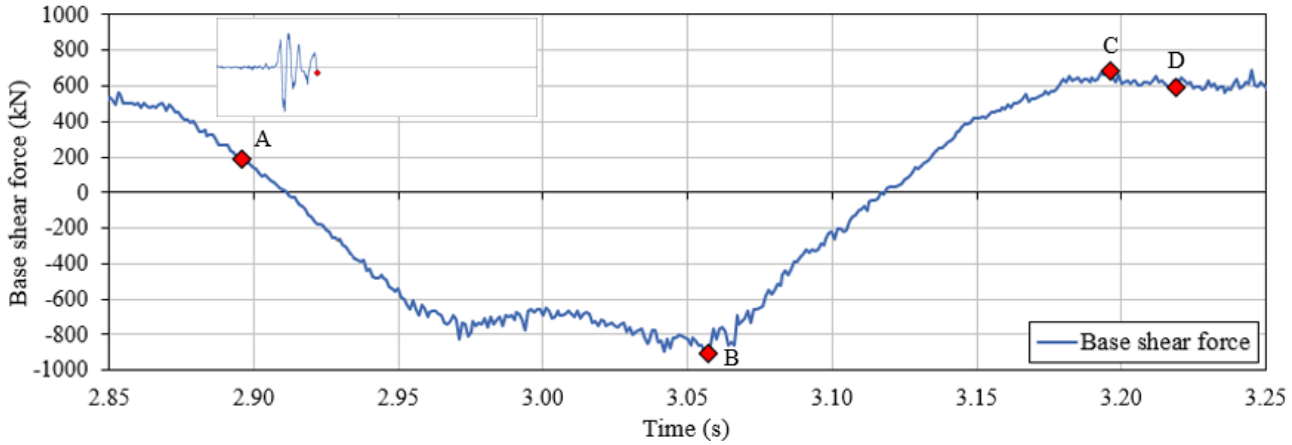

Figure 5.25 section of the base shear over time of the strengthened BJR (2x EQ) façade, with the points of interest (A-D)

In Figure 5.26(a) to 5.26(d) the crack patterns at the points of interest (A-D) are shown, as well as the crack pattern at the end of analysis, see Figure 5.26(e). The corresponding crack widths can be found in Table 5.6 (maxima are in bold). Now, of the main cracks, the one at location 2 completely cracks until it has reached the bottom of the foundation.

	Crack width (mm)			$\psi_{D,main}$(-)	$\psi_{D,total}$ (-)
Point	**Location 1**	**Location 2**	**Location 3**		
After settlement	1.77	1.09	0.22	2.55	2.83
A	2.69	**1.80**	0.14	**2.93**	3.73
B	0.48	0.47	0.48	1.89	2.53
C	2.51	1.38	0.13	2.80	3.93
D	**2.89**	1.66	**0.55**	2.92	**4.02**
End of analysis	1.77	0.91	0.36	2.48	3.88

Table 5.6 recorded crack widths and damage values at various points of interest during seismic loading

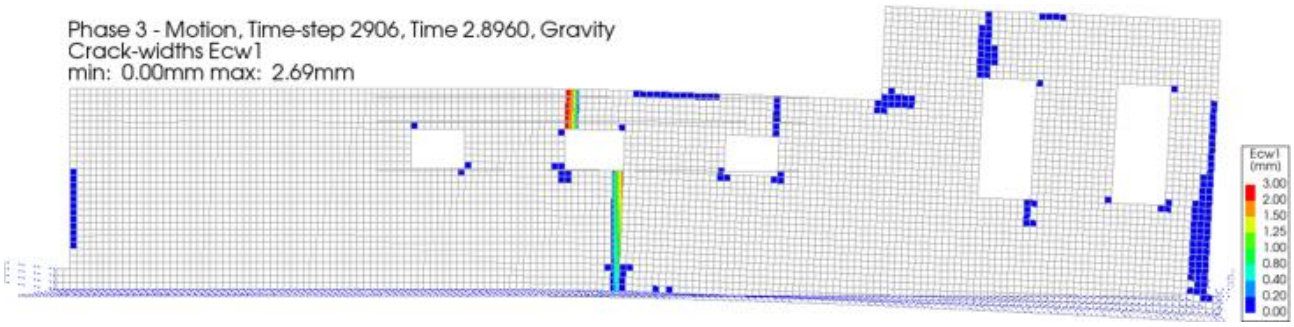

(a) point A (scale factor 0.05)

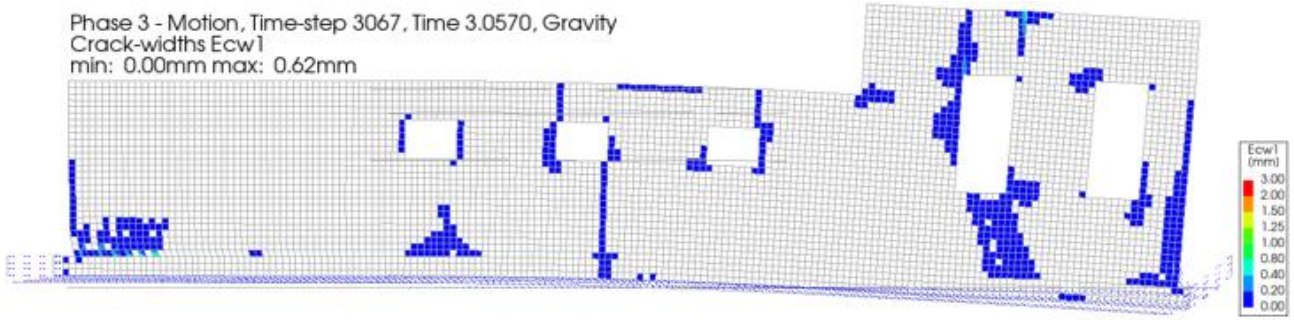

(b) point B (scale factor 0.05)

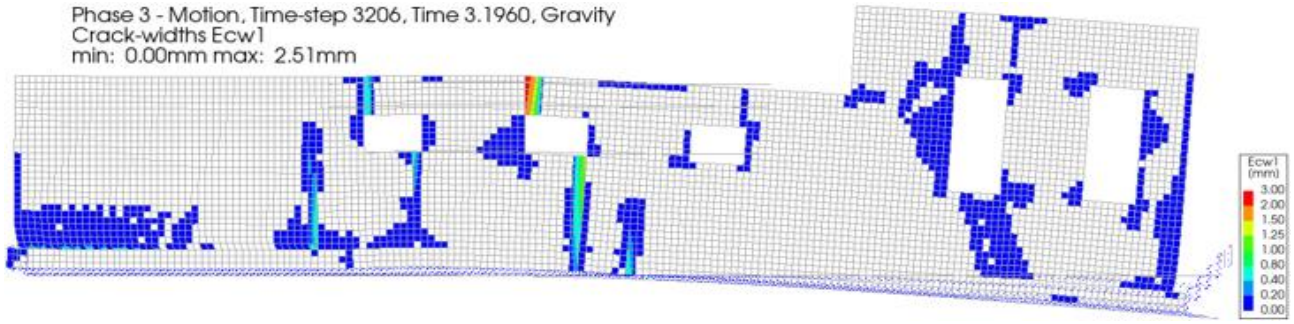

(c) point C (scale factor 0.05)

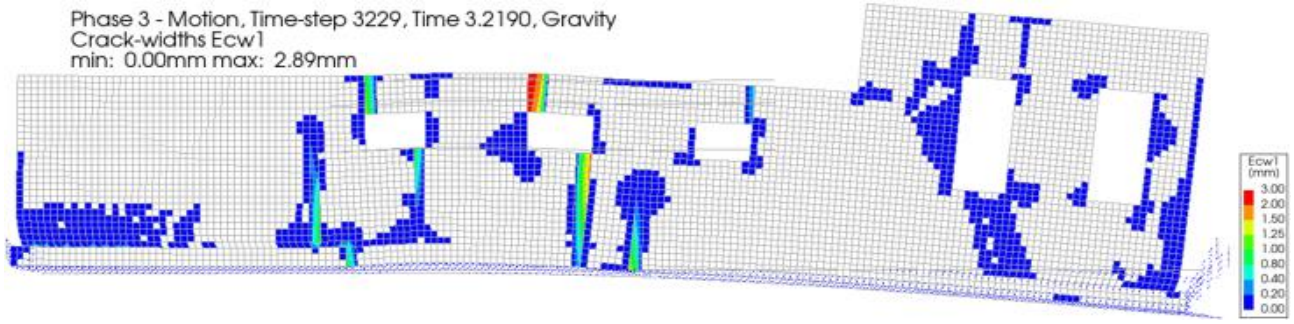

(d) point D (scale factor 0.05)

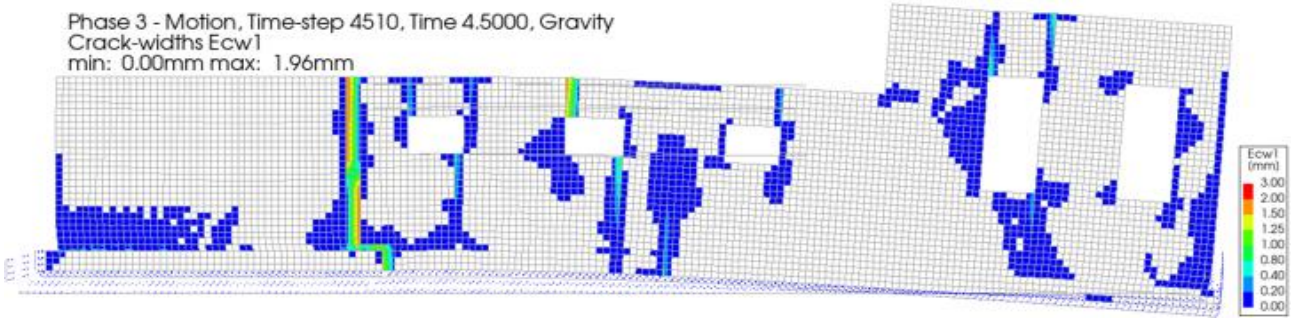

(e) failure, end of analysis (scale factor 0.05)

Figure 5.26 crack patterns at the point of interest (A-D) and at end of analysis for the strengthened BJR (2x EQ) façade

When amplifying the seismic load by a factor 2, extensive cracking of the façade is many regions is observed. Many new major cracks form over the course of the analysis. This results in a major crack forming over the full height of the façade at the left side of the façade. Major non-convergence was observed from going forward. Therefore it was concluded that at this point failure of the façade had occurred.

The maximum Von Mises stresses found during analysis is 142.0N/mm^2 and is shown in Figure 5.27. The results are shown over the length of the reinforcement bars. The Von Mises stresses agree with the crack patterns found; the stresses are developed in the regions where cracking is encountered. The Von Mises stresses are lower than the yielding limit ($f_y = 215$MPa), see Figure 3.4. The corresponding (maximum) relative shear displacements (slip), between the masonry and steel reinforcement, in the local x-direction of the reinforcement is shown in Figure 5.28. The bed joint reinforcement undergoes barely any slip. The absolute maximum slip was found to be 0.36mm, meaning it is still in the initial linear branch of the bond-slip curve, see Figure 3.4.

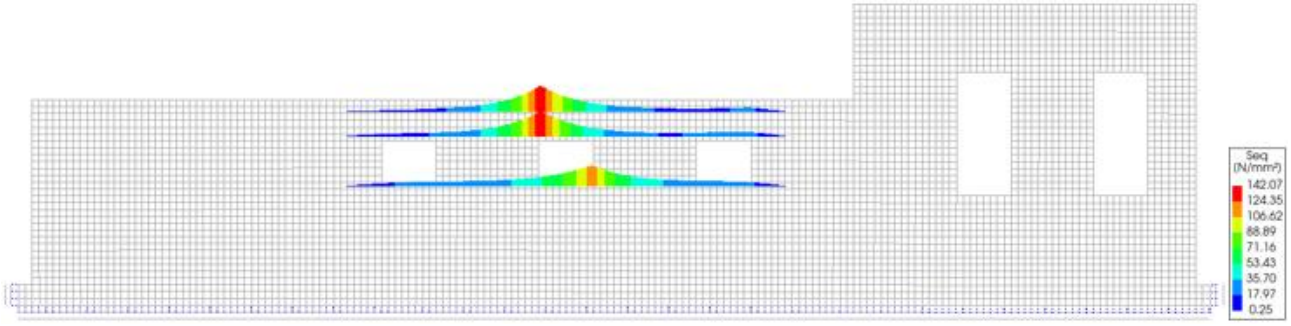

Figure 5.27 Von Mises stresses in the reinforcement (undeformed)

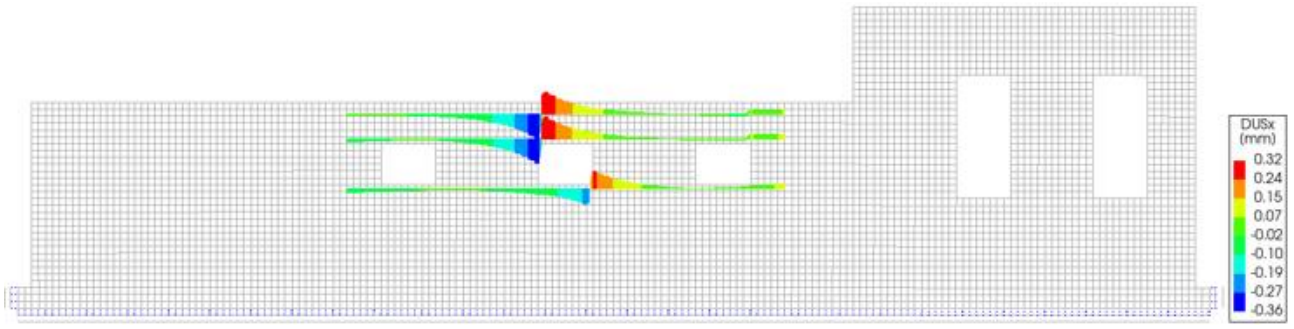

Figure 5.28 amount of slip in the reinforcement (undeformed)

Figure 5.29 shows the convergence history for the strengthened BJR (2x EQ) façade. In each time step, both convergence criteria had to be met to obtain convergence. Again, non-convergence is observed in the start steps. Near the peak of the motion, extended cracking of certain areas of the façade was observed. This cracking resulted, as for the previous model, but more severely, in heavy non-convergence at times. Please note that, as stated earlier, a maximum of 100 iterations per time step was used, instead of 500 previously, to reduce the computational effort required (see appendix A for validation of this decision). In total 1022 time-steps encountered non-convergence. A non-convergence rate of 22.7%, which is very large. Therefore, the results of this analysis are to be taken with a grain of salt. Most of the time, it was the displacement norm that encountered non-convergence, when the maximum number of 100 iterations was reached. An exceedance of the displacement tolerance of up to 60 times was found. However, for the force norm this was not the case. Here, non-convergence of the force tolerance was found very sparsely and in case of non-convergence the exceedance of the tolerance was minimal (much lower than one magnitude of 10). Therefore it was concluded that although non-convergence was found in many steps, the results of the analysis were decently trustworthy.

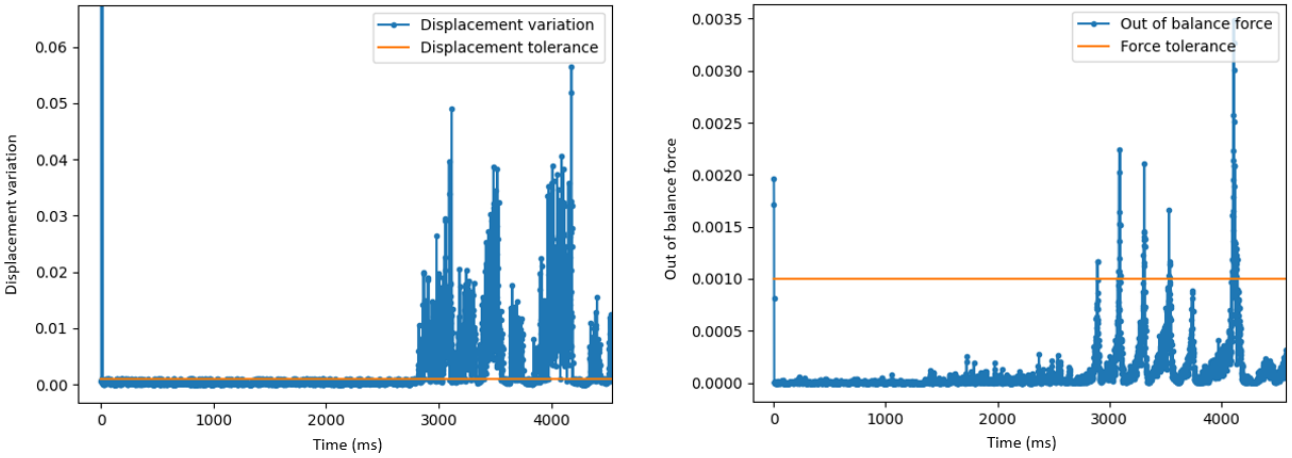

(a) (b)

Figure 5.29 convergence history during seismic loading of the strengthened BJR (2x EQ) façade for (a) the displacement norm and (b) the force norm

5.4 Partially reinforced masonry façade

In this section a partially reinforced masonry façade is studied, simulating the case in which the bed joint reinforcement is applied during the construction phase. It is important to note that the developed numerical model is a theoretical case, rather than a practical one, where reinforcement may be applied in more bed joints rather than only at the selected locations. The bed joint reinforcement is applied after the gravity & overburden phase, prior to the start of the settlement loading phase. Since the bed joint reinforcement is applied prior to settlement loading, there are no stresses and strains in the steel reinforcement (ε=0). The abbreviation used in the discussion for this façade is 'partially reinforced masonry'.

After application of the settlement load it was found that there are very low levels of cracking in the façade, since now the bed joint reinforcement also provides resistance against settlement loading, instead of just seismic loading. Since the façade is very sensitive to settlement damage it logically follows that the crack widths would be substantially lower after settlement, compared to the previously presented models. The cracks, shown in Figure 5.30, that do appear are, once again, mainly concentrated around window corners, with a maximum crack width of only 0.03mm. These cracks appearing near the window corners stop propagating once they reach the location of the steel reinforcement bars. At the end of the settlement loading phase, the Von Mises stresses are now rather constant over the length of the reinforcement bars, due to the nature of the applied load. A maximum value of 23.0N/mm^2 was found, as seen in Figure 5.31, which is lower than the yielding limit ($f_y = 215$MPa), see Figure 3.4. The relative shear displacements in the local x-direction of the reinforcement are negligible and are therefore not shown here.

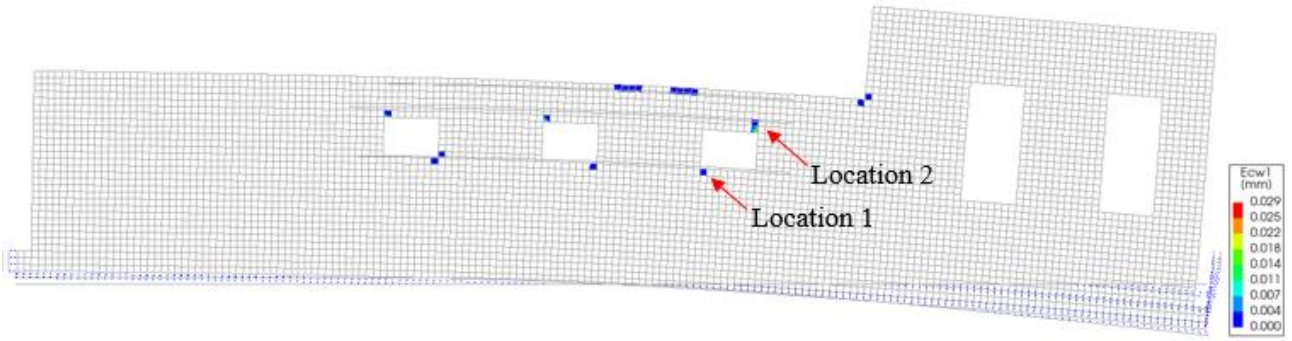

Figure 5.30 crack widths at the end of the settlement loading phase (scale factor 0.05)

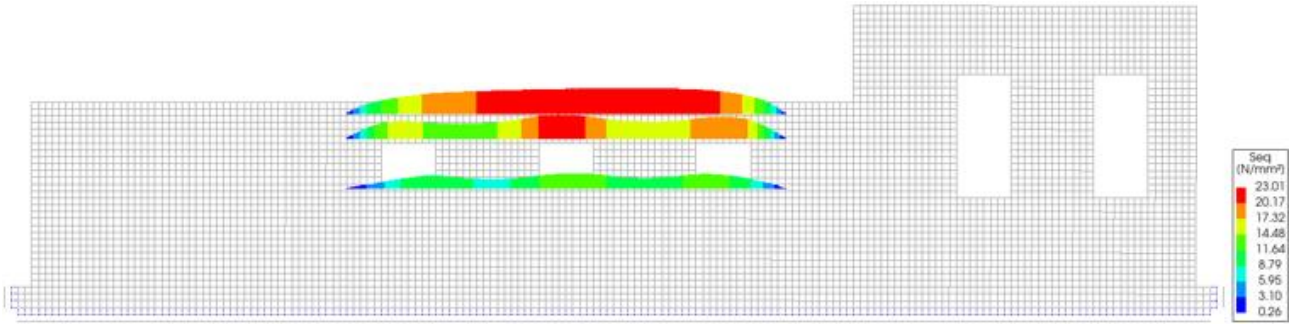

Figure 5.31 Von Mises stresses in the reinforcement at the end of the settlement loading phase (undeformed)

For the capacity curves, the same combination of nodes was deemed critical. Major cracks at two different locations were identified over the course of the analysis, as seen in Figure 5.30. The capacity curve and the points of interest are marked (A-D) in Figure 5.32, where the load path (running from A to D) is highlighted in orange. These points are determined as follows:

- Point A: maximum crack width recorded at location 1
- Point B: maximum crack width recorded at location 2
- Point C: peak base shear force in the negative (-) direction
- Point D: peak base shear force in the positive (+) direction

These points of interest are also shown in Figure 5.33. Here, a section of the base shear force over time graph, running from 2.9s to 3.2s, is shown. The complete graph, over the course of seismic loading, can be found in the top-left corner.

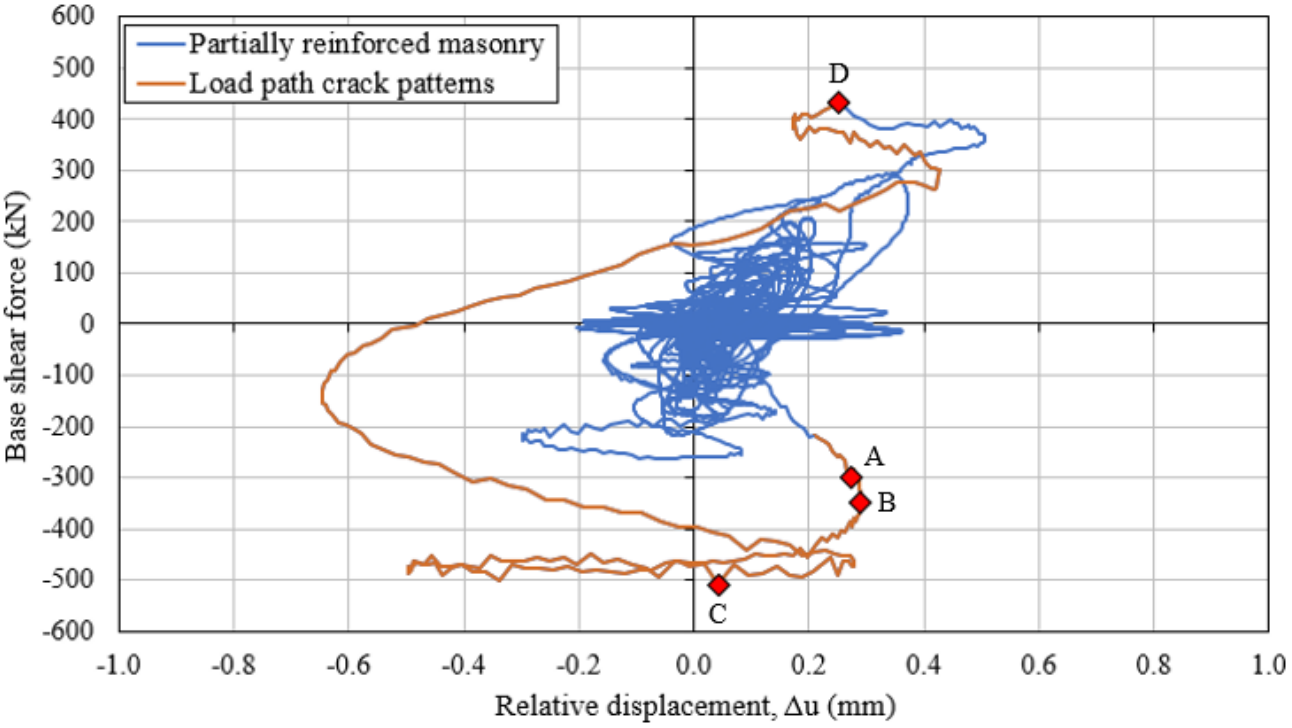

Figure 5.32 capacity curve of the (before settlement) strengthened façade with various points of interest (orange line and A-D markers)

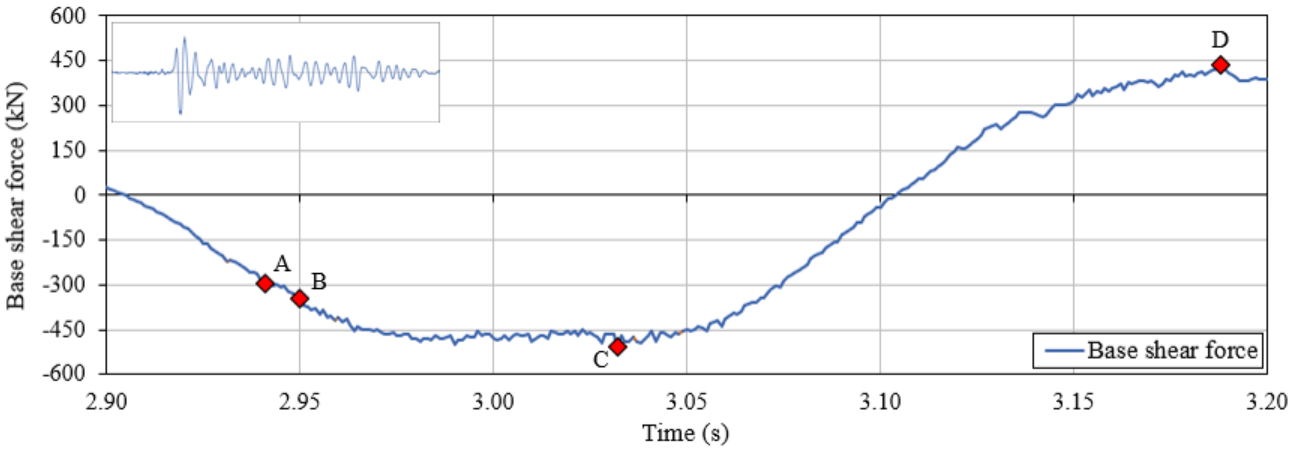

Figure 5.33 enlargement of the base shear over time of the (before settlement) strengthened wall, with the points of interest (A-D)

In Figure 5.34(a) to 5.34(d) the crack patterns at the points of interest (A-D are shown, as well as the crack pattern at the end of analysis see Figure 5.34(e). The corresponding crack widths, for the locations 1 and 2, can be found in Table 5.7 (maxima are in bold). The damage values for the settlement phase are not included, since they are so minor: this would give a skewed image of the evolution of damage, during analysis. Now, the damage value $\psi_{D,main}$ concerns the cracks formed at locations 1 and 2. The crack lengths are omitted in the table, but obviously considered for the calculation of the damage values.

	Crack width (mm)		$\psi_{D,main}$(-)	$\psi_{D,total}$ (-)
Point	**Location 1**	**Location 2**		
After settlement	0.01	0.03	n.a.	n.a.
A	**0.46**	0.79	1.92	2.35
B	0.45	**0.80**	**1.92**	**2.36**
C	0.23	0.46	1.61	1.99
D	0.24	0.43	1.59	2.03
End of analysis	0.39	0.63	1.76	2.25

Table 5.7 recorded crack widths and damage values at various points of interest during seismic loading

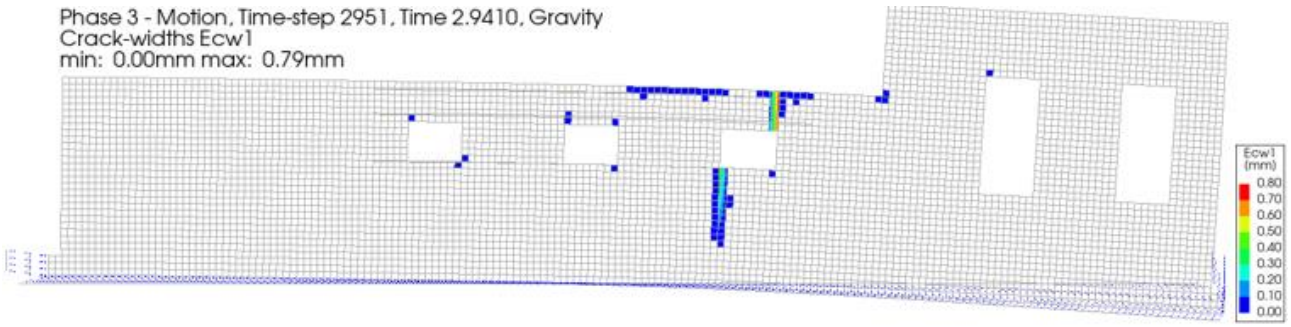

(a) point A (scale factor 0.05)

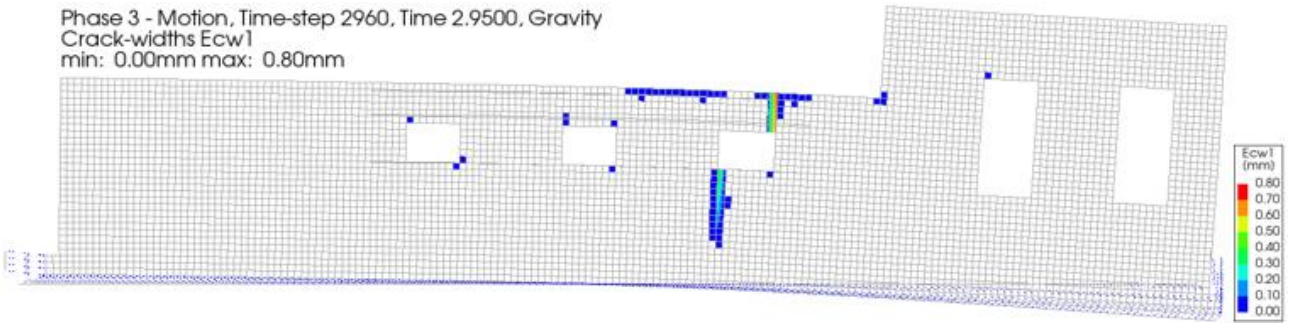

(b) point B (scale factor 0.05)

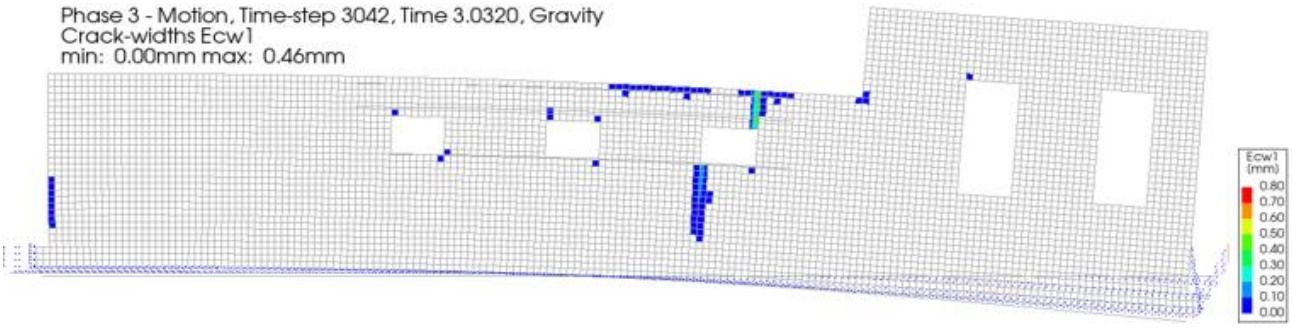

(c) point C (scale factor 0.05)

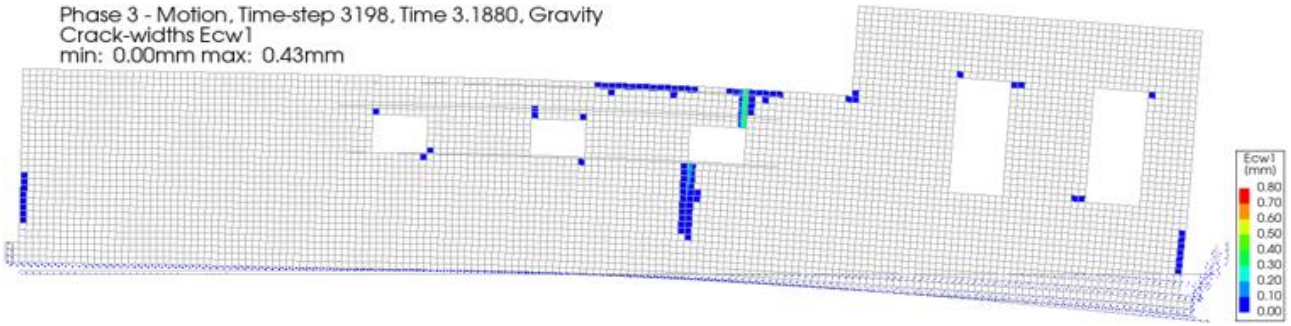

(d) point D (scale factor 0.05)

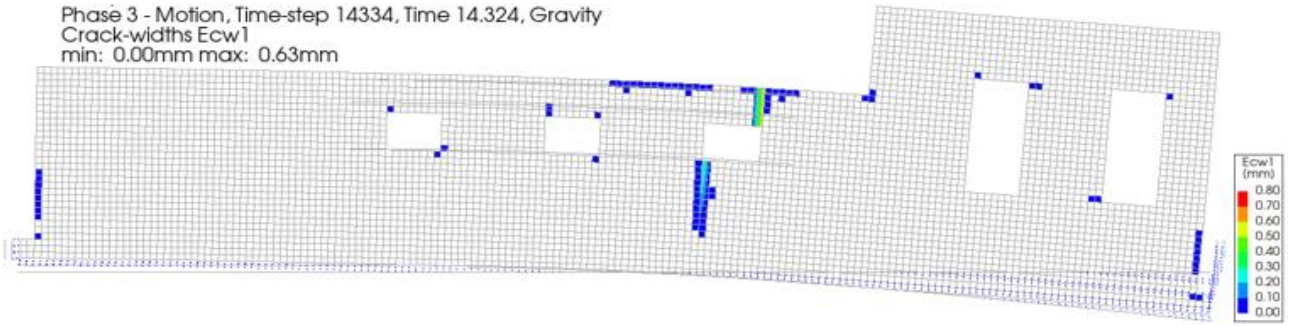

(e) end of analysis (scale factor 0.05)

Figure 5.34 crack patterns at various point of interest (A-D) and at the end of analysis

The maximum Von Mises stresses found during analysis is 98.2N/mm^2 and is shown in Figure 5.35. The results of the Von Mises stresses agree with the crack patterns found; the stresses are developed in the regions where cracking is encountered. Nowhere in the reinforcement yielding of the steel ($f_y = 215$MPa) occurs, see Figure 3.4. The corresponding (maximum) relative shear displacements (slip), between the masonry and steel reinforcement, in the local x-direction of the reinforcement is shown in Figure 5.36. The bed joint reinforcement still undergoes barely any slip. The absolute maximum slip was found to be 0.20mm. This amount of slip means that it is still in the initial linear branch of the bond-slip curve, see Figure 3.4.

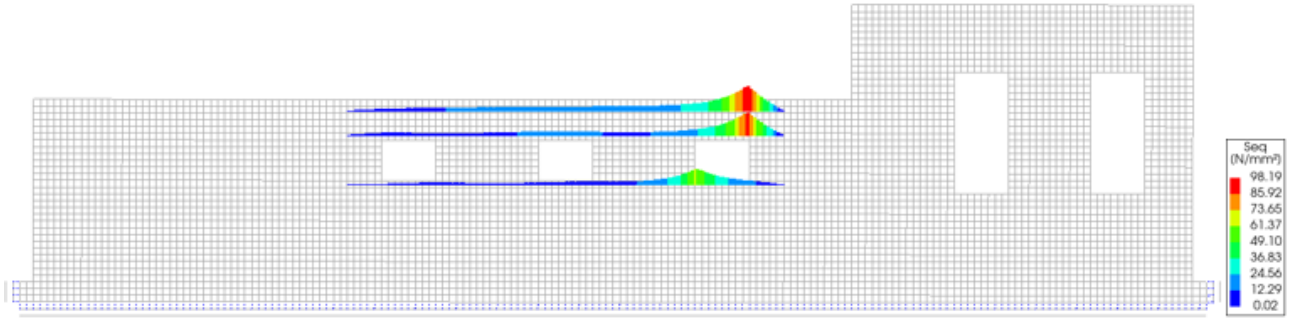

Figure 5.35 Von Mises stresses in the reinforcement (undeformed)

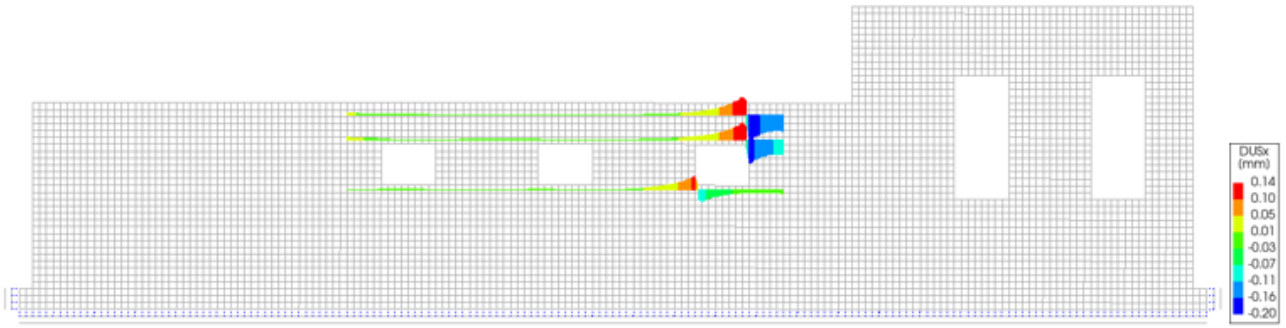

Figure 5.36 amount of slip in the reinforcement (undeformed)

Figure 5.37 shows the convergence history for the partially reinforced masonry façade. In each load or time step, all the convergence criteria had to be met to obtain convergence. Convergence was found in every load step of the gravity & overburden and settlement loading phases. In the seismic load phase, non-convergence was, once again, observed in the start steps. During the rest of the analysis, non-convergence was found in 100 time steps: a non-convergence rate of 0.7%. Around the peak load quite severe non-convergence was found, while later in the analysis minor non-convergence rates were observed. It was mainly the displacement norm that encountered non-convergence when the maximum number of 500 iterations was reached.

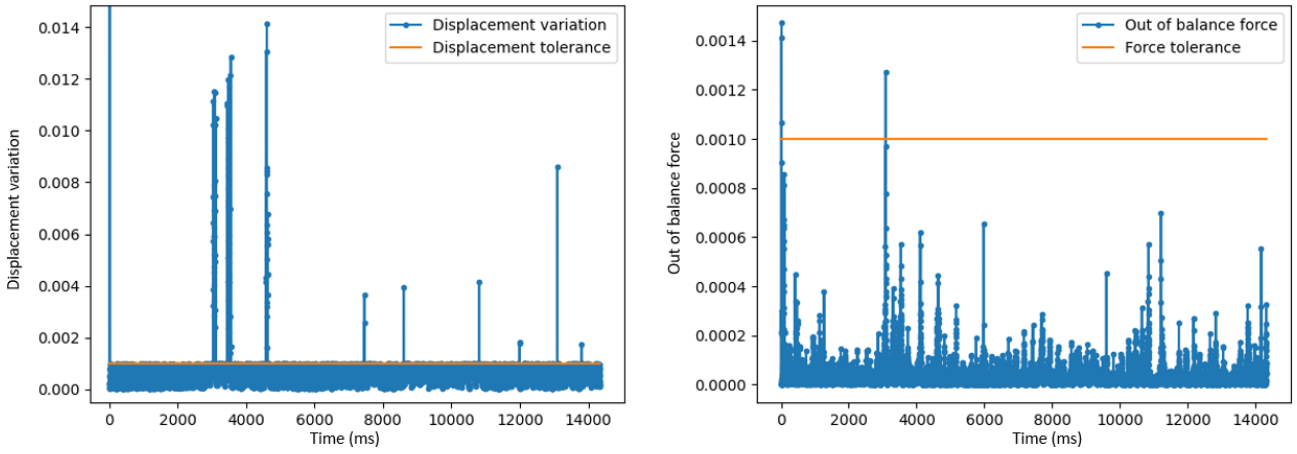

(a) (b)

Figure 5.37 convergence history during seismic loading of the bed joint reinforced and partially reinforced masonry façade for (a) the displacement norm and (b) the force norm

5.5 Comparison of numerical results

Various comparisons between the analysed numerical models are shown in this section. Each section provides a discussion as well. At the end an overview of the obtained results will be given, for clarity.

5.5.1 Comparison of strengthened and unstrengthened façade

In this section, comparison of the numerical results of the strengthened façades, including the ones with an amplified seismic load, and the unstrengthened façade will be made. For the models with an amplified seismic load, a comparison to the strengthened façade with the expected load is done.

Strengthened BJR (1x EQ)

When comparing the capacity curves of the unstrengthened and strengthened BJR (1x EQ) façades, it immediately becomes evident that the shapes are very similar. Both capacity curves are shown in Figure 5.38. From this, two things can be observed for the strengthened BJR (1x EQ), compared to the unstrengthened one. First, although there is an increase in force capacity (base shear force), compared to the unstrengthened façade, it is very minor. This has been observed previously in analysis of the masonry walls, where it was found that use of bed joint reinforced repointing did not result in a significant increase of the force capacity. Secondly, a reduction in the maximum relative displacement was found, which indicates, as with the masonry walls, that there is an increase in displacement capacity. This is logical, since addition of steel reinforcement increases the in-plane stiffness of the façade. This results in smaller relative displacements between the top and bottom node. This effect is most apparent near the steel reinforcement, but also extends to the rest of the wall. The force capacity in positive and negative direction varies by +2.7% and +0.7% respectively. The maximum relative displacement in positive and negative direction varies by -4.4% and -5.9% respectively. A summary of the values found for both the unstrengthened and strengthened BJR (1x EQ) façades can be found in Table 5.8.

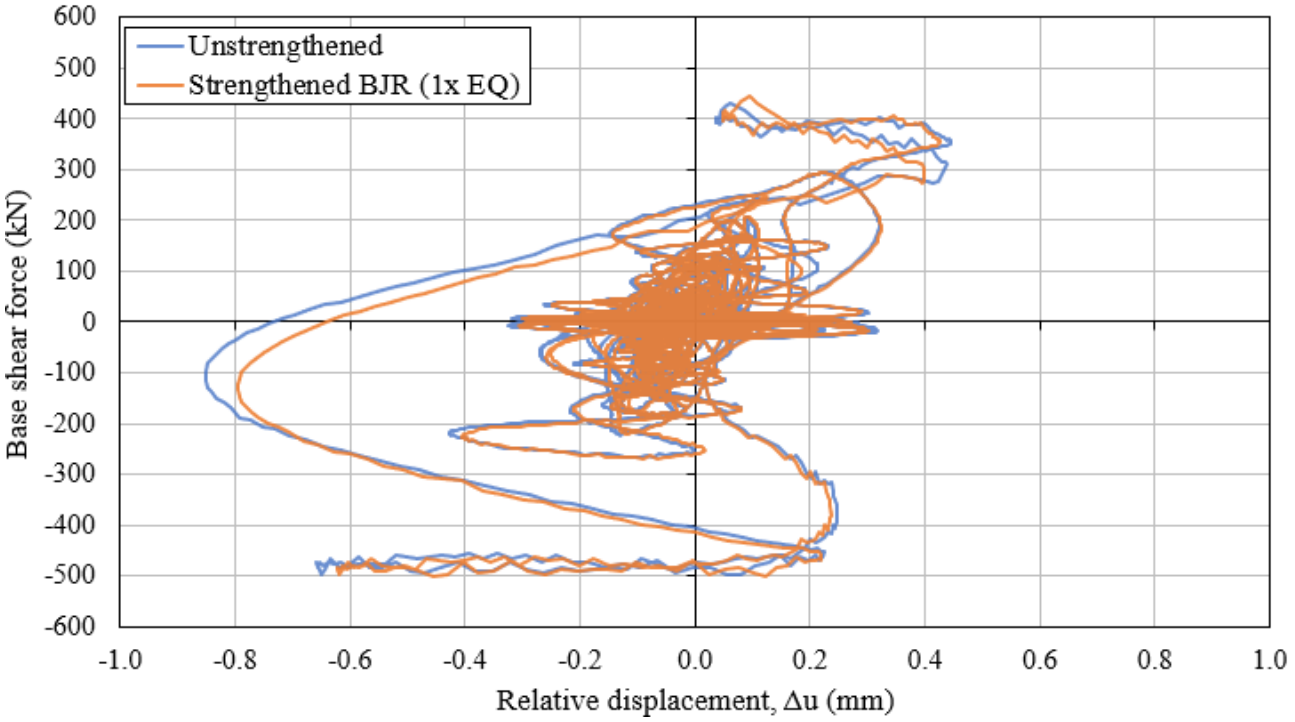

Figure 5.38 capacity curves of the unstrengthened and strengthened BJR (1x EQ) façades

Façade	Capacity in positive (+) direction (kN)	Capacity in negative (-) direction (kN)	Peak Δu in positive (+) direction (mm)	Peak Δu in negative (-) direction (mm)
Unstrengthened	432.0	-497.6	0.45	-0.85
Strengthened BJR (1x EQ)	443.5	-501.2	0.43	-0.80

Table 5.8 overview of the force capacity and peak relative displacements of the unstrengthened and strengthened BJR (1x EQ) façade

The biggest differences between the two façades can be found in the evolution of the crack pattern (and crack widths) over the course of the analysis. When comparing the crack patterns found in Figure 5.10 and Figure 5.14 less cracked areas are observed for the strengthened façade BJR (1x EQ), compared to the unstrengthened façade. This was also observed for the masonry walls, where the strengthened masonry wall showed significant less cracking at any level of displacement, compared to the unstrengthened one.

Although the effect is less clear for the masonry façades, this effect is still visible, mainly in the most-right part of the façade, where no steel reinforcement is applied. The reason it is less visible for the masonry façades, compared to the masonry walls, is because, as stated earlier, the increase in damage due to seismic loading is small. Again, after the peak of the motion, there is barely any evolution of damage.

Like for the unstrengthened façade, the maximum damage values are found at point A. Table 5.8 shows the percentages differences of the crack widths and damage values of the strengthened BJR (1x EQ) façade, compared to the unstrengthened façade, when the damage values are maximum, and at the end of analysis. From the table it becomes evident, logically, that due to application of reinforcement, a reduction in crack widths (except for location 3) and damage values is found when $\psi_{D,total,max}$ is reached. However, when looking at the evolution of crack widths during analysis, it was noted that the extra stiffness due to application of reinforcement works both ways. Just like there is a reduction in the increase of the crack widths, there is a reduction in the decrease of the observed crack widths during periods of crack closing. The reinforcement prevents closing of the cracks. This means that the reinforcement basically works as a buffer, where the peaks in the maximum and minimum crack widths are reduced. This is also the reason larger crack widths are recorded at the end of analysis of the strengthened BJR (1x EQ) façade, for locations 1 & 2, compared to the unstrengthened façade. This in turn results in a larger value of $\Delta\psi_{D,main}$, compared to the unstrengthened façade. However, when taking the minor cracks into account the total damage value of the strengthened BJR (1x EQ) façade is lower than that of the unstrengthened one, meaning less minor cracking has occurred in this analysis.

Compared to unstrengthened facade	Δw_1	Δw_2	Δw_3	$\Delta\psi_{D,main}$	$\Delta\psi_{D,total}$
At $\psi_{D,total,max}$	-4.7%	-8.0%	+8.0%	-1.9%	-5.5%
At end of analysis	+7.5%	+7.1%	-9.5%	+2.0%	-2.0%

Table 5.8 percentage changes in crack widths and damage values of the strengthened BJR (1x EQ) façade, compared to the unstrengthened façade

Strengthened BJR (1.5x EQ)

The capacity curves of the unstrengthened and strengthened BJR (1x EQ) façades, as well as the strengthened BJR (1.5x EQ), are shown in Figure 5.39. The general shape of the capacity curve of the latter is similar to the capacity curves of the unstrengthened and strengthened (1x EQ) façades. The biggest difference can be found in terms of force capacity and the maximum relative displacements. Because the seismic signal is now amplified by a factor 1.5, logically, the resulting base shear force and relative displacements are larger, in both positive and negative direction.

When comparing to the unstrengthened façade, it is found that amplification of the seismic load by a factor 1.5 results in an increase in force capacity in positive and negative direction varies by +35.4% and +47.9% respectively. The maximum relative displacement in positive and negative direction varies by +73.3% and +9.4% respectively.

When comparing to the strengthened BJR (1x EQ) façade, an increase in force capacity in positive and negative direction varies by +31.8% and +46.8% respectively. The maximum relative displacement in positive and negative direction now varies by +81.4% and +16.3% respectively. A summary of the values found for the unstrengthened, strengthened BJR (1x EQ) and the strengthened BJR (1.5x EQ) façades can be found in Table 5.9.

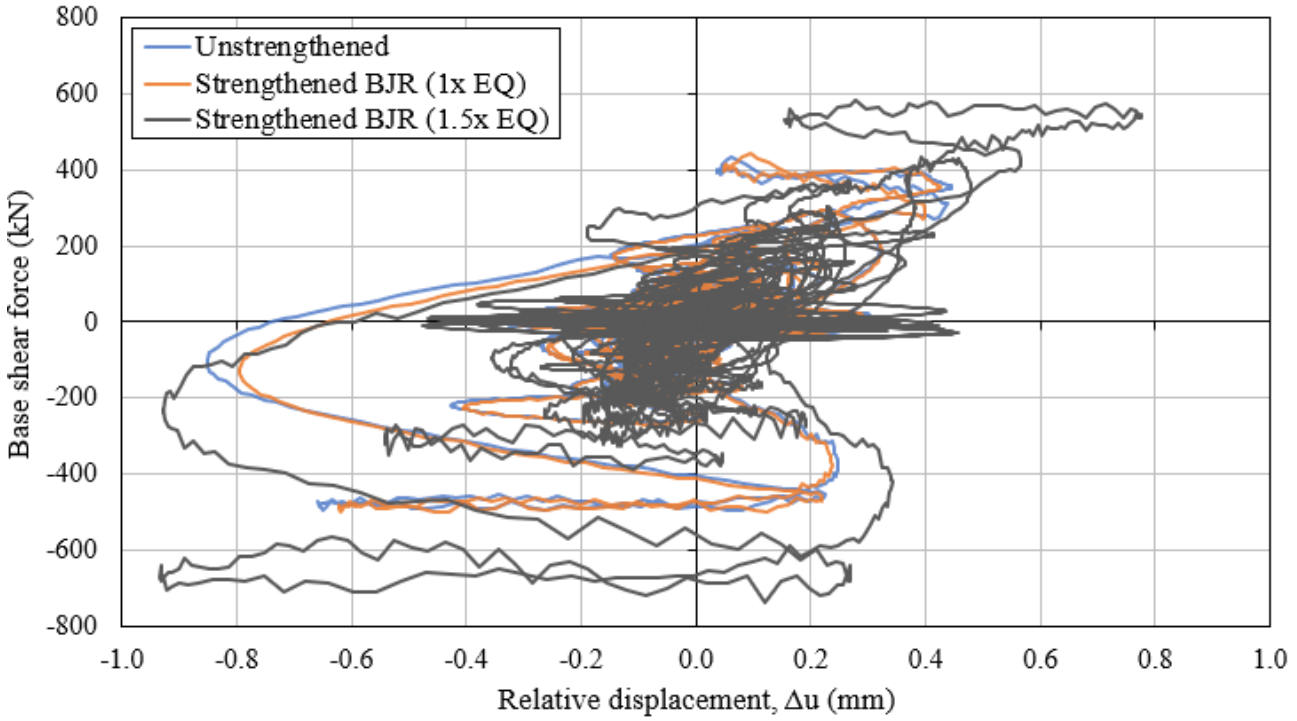

Figure 5.39 capacity curves of the unstrengthened, strengthened BJR (1x EQ) and strengthened BJR (1.5x EQ) façades

Façade	Capacity in positive (+) direction (kN)	Capacity in negative (-) direction (kN)	Peak Δu in positive (+) direction (mm)	Peak Δu in negative (-) direction (mm)
Unstrengthened	432.0	-497.6	0.45	-0.85
Strengthened BJR (1x EQ)	443.5	-501.2	0.43	-0.80
Strengthened BJR (1.5x EQ)	584.9	-736.1	0.78	-0.93

Table 5.9 overview of the force capacity and peak relative displacements of the unstrengthened, strengthened BJR (1x EQ) and strengthened BJR (1.5x EQ) façades

Big differences in the evolution of the crack pattern (and crack widths) between the strengthened BJR (1.5x EQ) (Figure 5.20), unstrengthened (Figure 5.10) and strengthened (Figure 5.14) façades were observed. Logically, the amplified seismic load resulted in much more extended cracking, especially in the most-right side of the façade, where no steel reinforcement is present. Two of these cracks are worth mentioning. First, the crack on the most-left side of the façade. Here, a horizontal crack appears to form where the foundation meets the rest of the façade. This indicates that at this location initiation of shear failure is observed, as shown in Figure 2.2(b), due to the magnitude of the seismic load and its resulting inertia effects. The maximum crack width here, at the end of analysis, is substantial, namely 0.40mm. Furthermore, at the bottom-right side of the façade a vertical crack, starting at the bottom of the foundation, is found. This can be attributed to the implemented time shift. Larger magnitude seismic loads result in a larger difference of displacement between two adjacent sections, where the time shift is applied, leading to vertical cracks that initiate at the foundation level. The maximum crack width here, at the end of analysis, is substantial, namely 0.19mm. Once again, after the peak of the motion, there is barely any evolution of damage.

Now, the maximum damage values are found at point E, instead of A (as is the case for the unstrengthened and strengthened BJR (1x EQ) façades). Table 5.10 shows the percentages differences of the crack widths and damage values of the strengthened BJR (1.5x EQ) façade, compared to the unstrengthened and strengthened BJR (1.5x EQ) façades, when the damage values are maximum, and at the end of analysis. Since the $\psi_{D,total,max}$ is now found at a different moment in the analysis, compared to the unstrengthened and strengthened BJR (1x EQ) façades, a direct comparison of the crack widths is impossible, due to opening and closing of cracks.

Therefore, instead of looking at the difference in crack widths at specific locations, as done previously, a new parameter Δw_{max} is introduced. This parameter is defined as the percentage change of the maximum crack width encountered, at $\psi_{D,total,max}$ or at the end of analysis, compared to either the unstrengthened or strengthened BJR (1x EQ) façade.

From Table 5.10 below, it becomes evident that amplification of the seismic signal by a factor 1.5 results in an increase in maximum crack width, as well as the recorded damage values, which is obviously what would be expected. For the crack widths at the end of analysis, when comparing to the strengthened BJR (1x EQ) façade, only a minor increase is found. This is because more extensive cracking areas are formed now, during seismic loading. The cracking of these areas results in unloading of the main cracks, where steel reinforcement is applied. This mechanism is obvious when looking at the parameter $\Delta\psi_{D,main}$, where not much a change of the value of this parameter is seen between the strengthened BJR (1.5x EQ) façade and the unstrengthened/strengthened BJR (1x EQ) façades.

Compared to unstrengthened façade	Δw_{max}	$\Delta\psi_{D,main}$	$\Delta\psi_{D,total}$
At $\psi_{D,total,max}$	+2.1%	0%	+9,1%
At end of analysis	+8.2%	+1.6%	+3.4%
Compared to strengthened BJR (1x EQ) façade			
At $\psi_{D,total,max}$	+7.1%	+1.9%	+15.4%
At end of analysis	+0.6%	-0.4%	+5.5%

Table 5.10 percentage changes in crack widths and damage values of the strengthened BJR (1.5x EQ) façade, compared to the unstrengthened and strengthened BJR (1x EQ) façades

When comparing the strengthened BJR (1.5x EQ) façade with the strengthened BJR (1x EQ) façade, a large increase in the maximum Von Mises stress, and corresponding slip, between the masonry and steel reinforcement, is found. For the maximum Von Mises stress and increase of +115.5% is found, while for the relative shear displacement an increase of +220.0% is seen.

Strengthened BJR (2x EQ)

The capacity curves of the unstrengthened and strengthened BJR (1x EQ) façades, as well as the strengthened BJR (2x EQ), are shown in Figure 5.40. The shape of the capacity curve of the latter is now quite different from the other two. After the initial low amplitude phase of the seismic signal, where low base shear forces are observed, it appears that the capacity curve of the strengthened BJR (2x EQ) façade has undergone a shift to the right, relative to the capacity curves of the other façades. The explanation is straightforward: after the initial low amplitude phase of the signal, extended cracking of the masonry is observed, mainly at the top most-right side of the façade. This cracking causes the top node to shift to the right side (positive side), relative to the bottom node. Since phased displacements are considered in the calculation of the relative displacement, a clear shift of the capacity curve (from the origin of the F-Δu graph) to the right side is observed. This results in a higher maximum relative displacement in the positive direction, compared to the unstrengthened and strengthened façades, while for the negative direction it is lower.

When comparing the strengthened BJR (2x EQ) façade with the unstrengthened façade, it is found that there is a variation in force capacity in positive and negative direction of +58.4% and +81.7% respectively. The maximum relative displacement in positive and negative loading direction varies by +286.7% and -31.8% respectively.

When comparing the strengthened BJR (2x EQ) façade with the strengthened BJR (1x EQ) façade, the force capacity in positive and negative direction increases by +54.3% and +80.3% respectively. The maximum relative displacement in positive and negative loading direction increases by +304.7% and decreases by -27.5% respectively. A summary of the values found for all three façades can be found in Table 5.11.

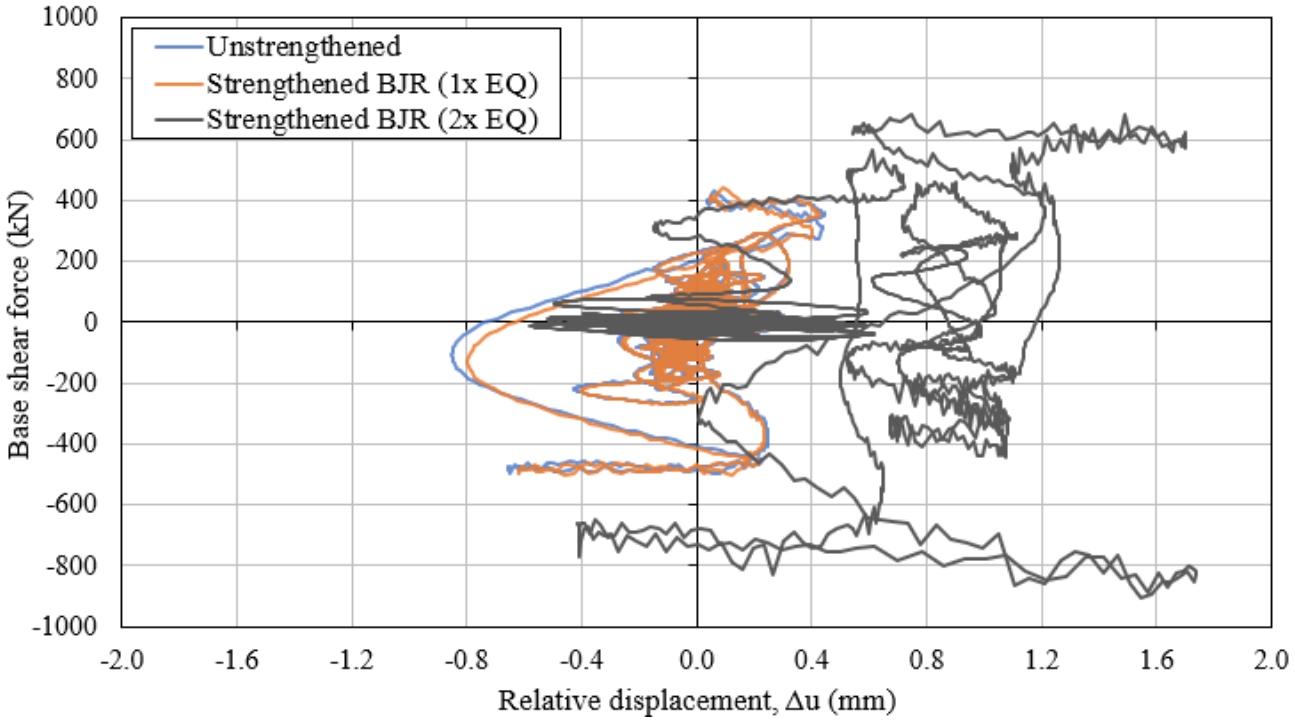

Figure 5.40 capacity curves of the unstrengthened, strengthened BJR (1x EQ) and strengthened BJR (2x EQ) façades

Façade	Capacity in positive (+) direction (kN)	Capacity in negative (-) direction (kN)	Peak Δu in positive (+) direction (mm)	Peak Δu in negative (-) direction (mm)
Unstrengthened	432.0	-497.6	0.45	-0.85
Strengthened BJR (1x EQ)	443.5	-501.2	0.43	-0.80
Strengthened BJR (2x EQ)	684.4	-904.0	1.74	-0.58

Table 5.11 overview of the force capacity and peak relative displacements of the unstrengthened, strengthened BJR (1x EQ) and strengthened BJR (2x EQ) façades

As for the comparison with the strengthened BJR (1.5x EQ) façade, big differences in the evolution of the crack pattern (and crack widths) between the strengthened BJR (2x EQ) (Figure 5.26) and unstrengthened (Figure 5.10) and strengthened BJR (x1 EQ) (Figure 5.14) façades were observed. Again, the amplified seismic load resulted in much more extended cracking all throughout the façade, especially there where no steel reinforcement is present. However, due to the extensive damage formed during the peak of the signal, further cracking of the façade is also observed after this peak. This results in a large crack, located at the left side of the façade, over the complete height, as seen in Figure 5.26(e). After investigation it was decided that it could be concluded that failure has now occurred.

Now, the maximum damage values are found at point D, instead of A (as is the case for the unstrengthened and strengthened BJR (1x EQ) façades). Table 5.12 shows the percentages differences of the crack widths and damage values of the strengthened BJR (1.5x EQ) façade, compared to the unstrengthened and strengthened BJR (1.5x EQ) façades, when the damage values are maximum, and at the end of analysis.

From this table, it becomes evident that amplification of the seismic signal by a factor 2 results in an increase in maximum crack width, as well as the recorded damage values, which is obviously what would be expected. The mechanism explained previously, in the section of the strengthened BJR (1.5x EQ), are also valid here and are therefore not repeated.

Compared to unstrengthened façade	Δw_{max}	$\Delta \psi_{D,main}$	$\Delta \psi_{D,total}$
At $\psi_{D,total,max}$	+51.3%	11.4%	+30.1%
At end of analysis	+11.3%	+0.1%	+31.5%
Compared to strengthened BJR (1x EQ) façade			
At $\psi_{D,total,max}$	+58.8%	+13.6%	+37.7%
At end of analysis	+3.5%	-1.6%	+34.3%

Table 5.12 percentage changes in crack widths and damage values of the strengthened BJR (1.5x EQ) façade, compared to the unstrengthened and strengthened BJR (1x EQ) façades

When comparing the strengthened BJR (2x EQ) façade with the strengthened BJR (1x EQ) façade, a large increase in the maximum Von Mises stress, and corresponding slip, between the masonry and steel reinforcement, is found. For the maximum Von Mises stress and increase of +141.5% is found, while for the relative shear displacement an increase of +260.0% is seen.

5.5.2 Comparison of partially reinforced and (un)strengthened façade

The capacity curves of the unstrengthened and strengthened façades, as well as the façade retrofitted with bed joint reinforced repointing and partially reinforced masonry, are shown in Figure 5.41. An interesting difference in force capacity for the positive and negative direction is found, compared to the strengthened façade. For the negative direction it is slightly higher, as expected, while for the positive direction is lower. This is not what would be expected, and the difference is attributed to (minor) numerical instability of the model. Not long after the peak base shear force in negative direction, a lot of non-converged time steps are encountered, causing an underestimation of the capacity in this direction. The convergence results are shown at the end of this section.

Furthermore, the same behaviour as seen for the strengthened BJR (2x EQ) façade is found: a shift of the capacity curve to the right side, relative to the capacity curves of the other façades. The explanation is similar: substantial cracking at the locations 1 and 2 is observed quite early in the seismic loading phase. This cracking causes the top node to shift to the right side (positive side), relative to the bottom node. This results, once again, in a higher maximum relative displacement in the positive direction, compared to the unstrengthened and strengthened BJR (1x EQ) façades, while for the negative direction it is lower. The range of the relative displacement is defined as:

$$\Delta u_{range} = \Delta u_{max} - \Delta u_{min} \tag{5.5}$$

From this is becomes evident that, although there is a shift to the right of the capacity curve, the range of the relative displacement is smaller for the façade retrofitted with bed joint reinforced repointing and partially reinforced masonry, compared to the unstrengthened and strengthened façades. This means the displacement capacity has increased, relative to the other researched façades.

When comparing the façade retrofitted with bed joint reinforced repointing and partially reinforced masonry with the unstrengthened façade, it is found that there is a variation in force capacity in positive and negative direction of +0.3% and +2.5% respectively. The maximum relative displacement in positive and negative loading direction varies by +13.3% and -23.5% respectively.

When comparing the façade retrofitted with bed joint reinforced repointing and partially reinforced masonry with the strengthened façade, the force capacity in positive and negative direction varies by -2.3% and +1.7% respectively. The maximum relative displacement in positive and negative loading direction varies by +18.6% and -18.8% respectively. A summary of the values found for all three façades can be found in Table 5.13.

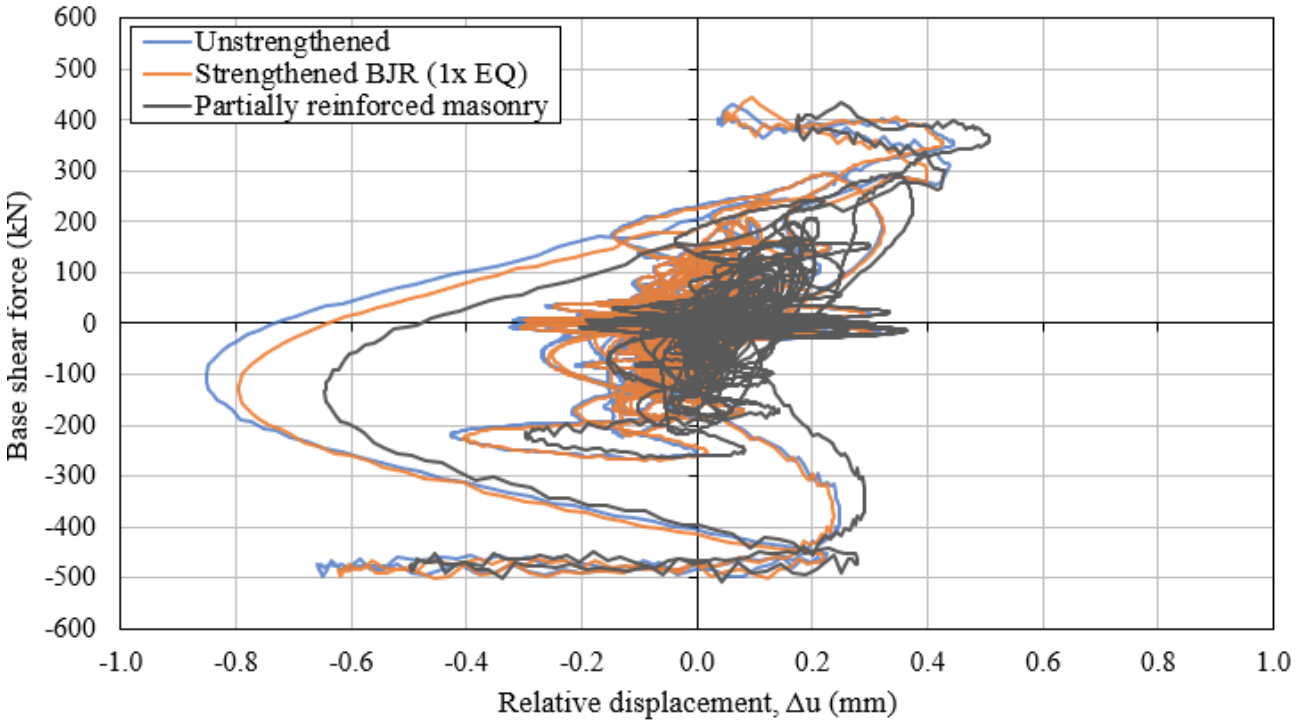

Figure 5.41 capacity curves of the unstrengthened, strengthened BJR (1x EQ) and strengthened BJR + partially reinforced masonry façades

Façade	Capacity in positive (+) direction (kN)	Capacity in negative (-) direction (kN)	Peak Δu in positive (+) direction (mm)	Peak Δu in negative (-) direction (mm)
Unstrengthened	432.0	-497.6	0.45	-0.85
Strengthened BJR (1x EQ)	443.5	-501.2	0.43	-0.80
Strengthened BJR + partially reinforced masonry	433.2	-509.9	0.51	-0.65

Table 5.13 overview of the force capacity and peak relative displacements of the unstrengthened, strengthened BJR (1x EQ) and strengthened BJR + partially reinforced masonry façades

Big differences in the evolution of the crack pattern (and crack widths) between the façade retrofitted with bed joint reinforced repointing and partially reinforced masonry (Figure 5.34) and unstrengthened (Figure 5.10) and strengthened (Figure 5.14) façades were observed. In the numerical model of the façade retrofitted with bed joint reinforced repointing and partially reinforced masonry, the steel reinforcement is now applied *before* the settlement loading phase. This results in a severe reduction in cracks widths at the end of this loading phase (Figure 5.30), compared to the unstrengthened and strengthened façade (Figure 5.4). There is practically no significant cracking observed. Then, quite early in the seismic loading phase, cracking at the locations 1 and 2 is found. The locations where cracking occurs differ from the previously discussed models. These cracks now appear more to the sides of the reinforcement bars. The reinforcement bar layout was based on the crack pattern found after application of the settlement load, and even though the bars extend the advised 500mm to the side of the crack at location 1 and 2, cracking is observed here. A slight increase in minor cracking is observed, compared to the strengthened façade. Once again, after the peak of the motion, there is barely any evolution of damage.

Now, the maximum damage values are found at point B, instead of A (as is the case for the unstrengthened and strengthened façades). Table 5.14 shows the percentages differences of the maximum crack widths, and the damage values, of the façade retrofitted with bed joint reinforced repointing and partially reinforced masonry, compared to the unstrengthened and strengthened façade, when the damage values are maximum, and at the end of analysis.

From this table, it becomes evident that when using a combination of partially reinforced masonry and bed joint reinforced repointing, a sharp reduction in the maximum crack widths is found, as well as the recorded damage values, when comparing to the unstrengthened and strengthened façades. This makes sense since, as stated previously, long façades are more susceptible to settlement damage, compared to seismic loading. By applying both techniques simultaneously, the damage caused by settlement is dramatically reduced, which in turn significantly reduces both the maximum crack widths and damage values, during and at the end of the seismic loading phase.

Compared to unstrengthened façade	Δw_{max}	$\Delta \psi_{D,main}$	$\Delta \psi_{D,total}$
At $\psi_{D,total,max}$	-58.1%	-26.7%	-23.6%
At end of analysis	-60.3%	-28.7%	-23.7%
Compared to strengthened BJR (1x EQ) façade			
At $\psi_{D,total,max}$	-56.0%	-25.6%	-19.2%
At end of analysis	-63.2%	-30.2%	-22.1%

Table 5.14 percentage changes in crack widths and damage values of the strengthened BJR + partially reinforced masonry façade, compared to the unstrengthened and strengthened BJR (1x EQ) façades

When comparing the façade retrofitted with bed joint reinforced repointing and partially reinforced masonry with the strengthened façade, a large increase in the maximum Von Mises stress, and corresponding slip, between the masonry and steel reinforcement ,is found. For the maximum Von Mises stress and increase of +67.0% is found, while for the relative shear displacement an increase of +100.0% is seen.

5.5.3 Summary

A short overview of the, most important, obtained results will be given below. This is done in terms of the total damage values and maximum crack widths at the end of analysis (Figure 5.42 and Figure 5.43), as well as the maximum observed total damage values and corresponding maximum crack widths over the course of the seismic loading phase (Figure 5.44 and Figure 5.45).

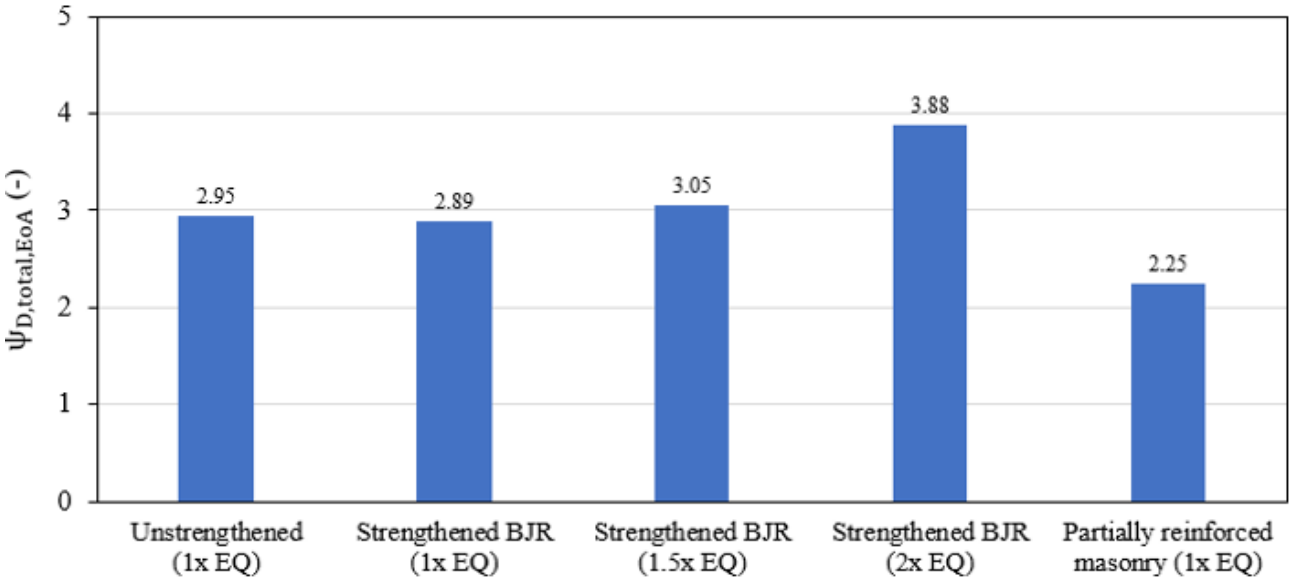

Figure 5.42 total damage values of the different numerical models at the end of analysis.

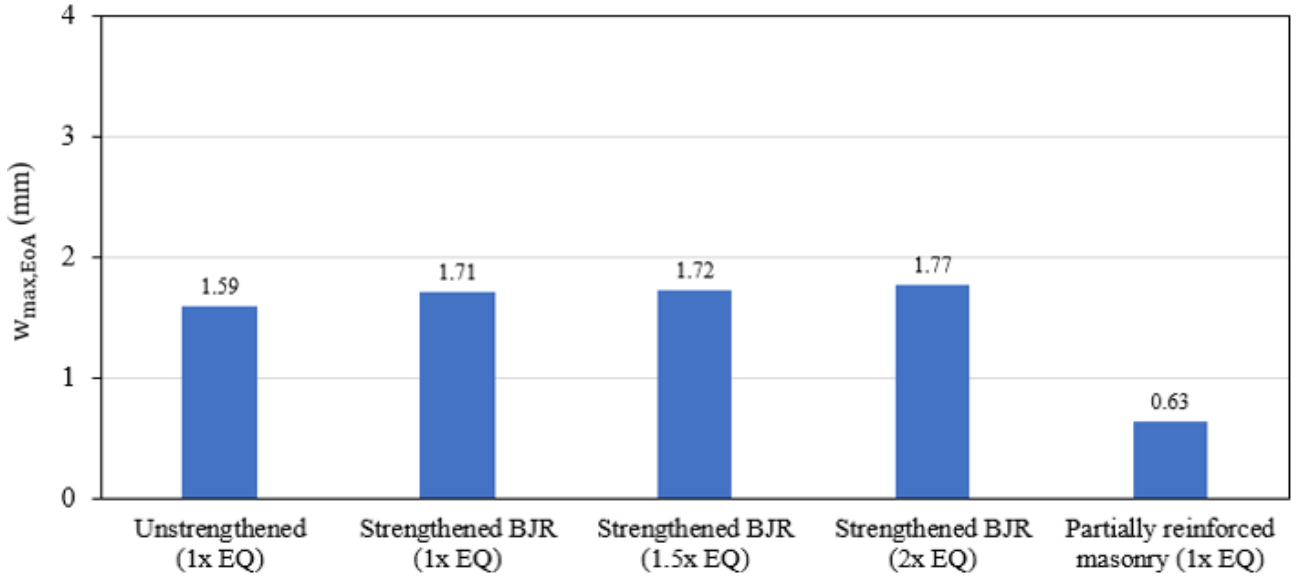

Figure 5.43 maximum crack widths of the different numerical models at the end of analysis.

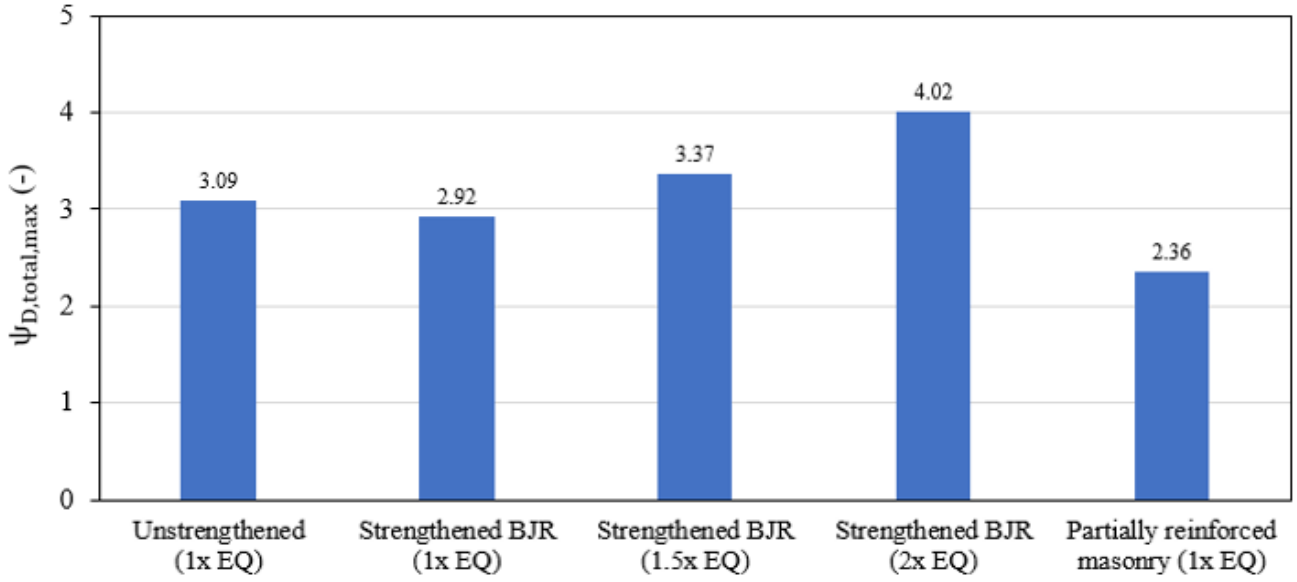

Figure 5.44 maximum total damage values of the different numerical models found during seismic loading

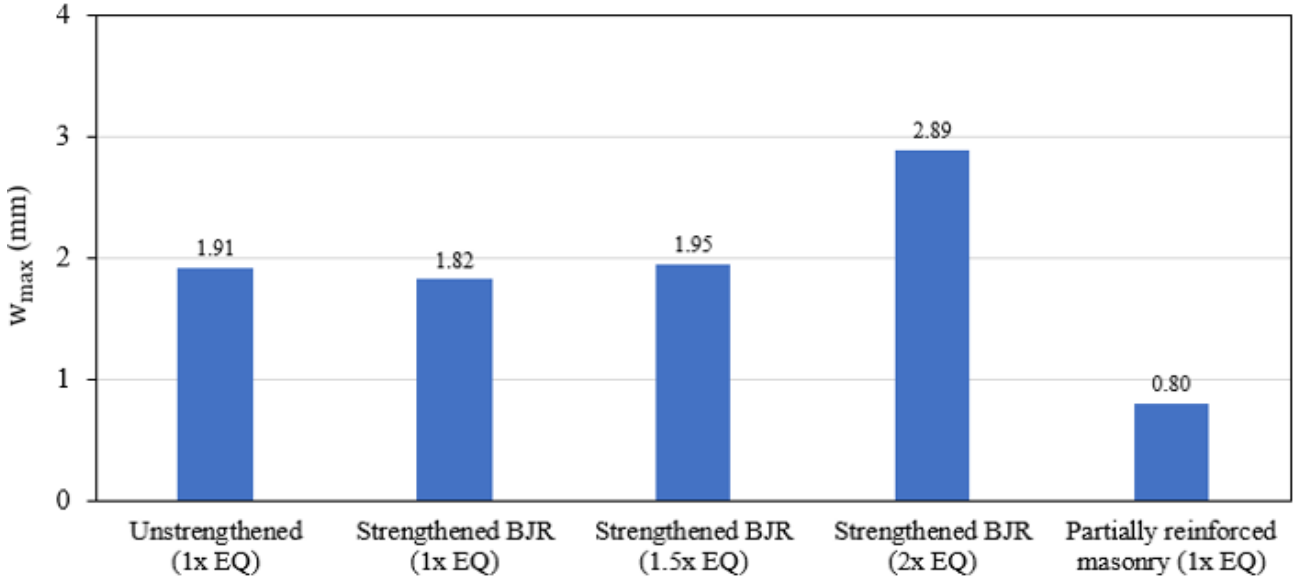

Figure 5.45 maximum crack widths of the different numerical models found during seismic loading

5.6 Conclusions

Several numerical models have been developed to investigate the added benefit of bed joint reinforced repointing, during seismic loading, on the performance of the structure. Namely, the unstrengthened façade, a façade strengthened with only bed joint reinforced repointing, where various PGVs are considered, and a numerical model with partially reinforced masonry where bed joint reinforcement was applied during the construction phase of the façade.

From the numerical analyses of the masonry façade, it immediately becomes evident that the additional damage due to seismic loading is small, compared to the damage already present, caused by ground settlement. Thus, damage in the facade is mainly governed by ground settlement, and less so by seismic loading. This structural behaviour is often observed for structures with a small height to length (H/L) ratio (Korswagen et al., 2019). Furthermore, it is seen that during seismic loading, the base shear force, due to soil-structure interaction, is mainly governed by viscous damping (velocity), and not so much by the mass (acceleration) and distributed springs (displacement) of the structure. When the seismic loading of the façade is initiated, a few additional observations are made:

1. Horizontal loops appear in the capacity curves (base shear force versus relative displacement), there where local peaks in the base shear force are observed
2. Opening and closing of cracks is observed.
3. No significant increase in the crack length of major cracks is found, because two out of three are already fully formed during settlement. Instead, minor crack formation is observed. Damage due to minor cracking becomes dominant in the total damage values.
4. After the peak in the base shear force, no significant change in terms of crack patterns is observed (not true for the numerical model using amplification of the seismic load by a factor 2).

When strengthening the façade with bed joint reinforced repointing, the steel reinforcement is applied after the settlement loading phase has been concluded. By comparing the strengthened façade with the unstrengthened one, no significant increase in force capacity is found, while there is a reduction in the maximum relative displacement. These observations are consistent with the ones obtained experimentally and numerically for the in-plane loaded masonry walls. Furthermore, a reduction in crack formation and propagation is observed, resulting in lower crack widths and damage values during peaks of seismic loading, compared to the unstrengthened façade. However, the steel reinforcement does not only restrict the opening of cracks, but also the closing of cracks. This results in larger crack widths at certain locations at the end of analysis, compared to the unstrengthened façade. Amplification of the seismic load results in an increase in force capacity, as well as an increase in the observed relative displacements. When the input signal is amplified by a factor 1.5, more extensive cracking is observed in the façade, compared to the numerical models where the expected load has been prescribed, causing an increase in crack widths and damage values at every point during seismic loading, as well as at the end of analysis. When the input signal is amplified by a factor 2, damage very quickly ramps up and large cracked areas are found throughout the façade. This in turn causes a very sharp rise in crack widths and damage values, compared to the unstrengthened and strengthened BJR (1x EQ) façades. Although quite some time steps are non-converged, for the numerical models using an amplified load, the results can still be considered decently trustworthy, since the number and magnitude of exceedance of the force norm is minimal.

Application of partial reinforcement of the masonry, with bed joint reinforced repointing, results in a numerical model equivalent to the situation where the steel reinforcement is applied before initiation of the settlement loading phase. After the initial settlement loading phase, no significant cracking is observed, since the bed joint reinforcement now also provides resistance against settlement loading, instead of just seismic loading. Then, when seismic loading is initiated, cracking occurs early in the analysis, giving rise to a slight shift of the capacity curve in the positive direction. No significant increase in force capacity is found, while a further reduction in relative displacements is observed, compared to the unstrengthened façade, as well as the façade strengthened only with bed joint reinforced repointing. The crack widths and damage values, during seismic analysis, are significantly lower, compared to the previously mentioned façades.

All the performed numerical analyses showed very low levels of relative shear displacements (slip) between the masonry and steel reinforcement. The maximum absolute slip found over all the numerical analyses was 0.36mm (for the numerical model with an amplified seismic load by a factor 2), which is still very early in the initial linear branch of the bond-slip curve. Non-linear behaviour of the bond-slip curve starts only at a slip of 1.50mm. This means that, looking back, the reinforcement could have safely been modelled as embedded bars in the finite element models, instead of using a non-linear bond-slip relationship. This is similar to what was found for the masonry walls, where, although high levels of slip were recorded in the diagonal anchors, relatively low levels of slip were found in the bed joint reinforcement.

Furthermore, yielding of the reinforcement is not observed anywhere. These results indicate that the steel reinforcement is overdesigned. A less conservative design approach regarding the steel reinforcement would be warranted in this case, meaning fewer bars could have been used than is now the case. However, if it is decided to use the steel reinforcement layout and amount used in this research, the reinforcement could also have been safely modelled with a linear elastic material model. Both these conclusions should be considered, if applicable, in future research, to reduce the computational effort required.

6 Conclusions and recommendations

In the 1960s a large natural gas field was discovered in the Dutch province of Groningen, in the northern part of the Netherlands. Due to gas extraction, localised earthquakes started occurring in the 1990s. In this part of the country large numbers of buildings are constructed using unreinforced masonry (URM). Damage due to seismic activity in the region poses a threat to the structural integrity of existing masonry structures, as these buildings were never designed to withstand seismic loading. A strengthening measure was deemed necessary, to reduce damage due to seismic loading. Among others, an intervention method that was considered was retrofitting with bed joint reinforced repointing, often done in combination with foundation strengthening. This is an attractive solution, as it is already often used in strengthening of masonry structures against settlement-induced damage, especially for heritage structures, as it does not affect the aesthetics of the structure. Furthermore, since this reinforcing technique is already applied to limit damage due to ground settlements, it is an attractive potential solution to counter damage due to seismic loading, as it does not require additional funding. However, not much research is available on the performance of existing masonry structures retrofitted with bed joint reinforced repointing, considering both the effect of ground settlements and seismic loading conditions.

To investigate the added benefit of bed joint reinforcement, used to counteract seismic-induced damage, nonlinear finite element analyses, of a case study of a typical masonry farmhouse in the Groningen region, were performed. In this research, an orthotropic continuum model called the engineering masonry model (EMM) was adopted. The used numerical modelling approach was first validated against in-plane experimental tests of unstrengthened and strengthened masonry walls, performed at TU Delft (Licciardello, Esposito, 2019). A sensitivity study on the head-joint failure type, analysis procedure settings, iterative method and interpolation scheme was performed, to see which analysis settings provided optimal results in terms of initial stiffness, peak load, crack patterns and crack widths. These results were used in analysis of the masonry farmhouse. Considering that the type of strengthening measure applied acts mainly on the in-plane resistance of the structural elements, only the farmhouse façade was modelled, meaning it was assumed no out-of-plane failure could occur. The façade of the masonry farmhouse, subject to settlement and seismic loading was modelled leveraging on a previous study (Korswagen et al., 2019). A long façade was considered, where the wall and foundation were assigned the same masonry material properties. Soil-structure interaction was implemented by means of a series of vertically and horizontally distributed springs and dashpots. Ground settlements were simulated by applying a differential settlement profile along the length of the façade. Transient dynamic nonlinear finite element analyses were performed, using a ground motion recorded in the Groningen region in 2018, where time shift and spatial amplification were considered. Various cases were analysed: an unstrengthened façade, strengthened façades, using various peak ground velocities (namely the expected load and two models including an amplified seismic load by a factor of 1.5 and 2), where bed joint reinforced repointing was applied *after* the settlement loading phase, and a partially reinforced masonry façade, where the bed joint reinforcement was applied *before* the settlement loading phase. The results were analysed in terms of crack widths, crack patterns and a damage values (ψ_D). The damage value parameter was previously developed by others for analysing progressive damage in masonry (Korswagen et al., 2019). This chapter provides the final conclusions and recommendations following the research outlined in this report.

6.1 Conclusions

The main research question of this thesis was formulated as:

What is the added benefit of bed joint reinforced repointing, used as a repair method against settlement, for masonry farmhouses subjected to seismic loading?

Answering the sub-questions will provide more insight into answering this main research question. Below a detailed explanation for each sub-question is provided.

1. Which modelling approach is most appropriate to simulate progressive damage in masonry strengthened with bed joint reinforced repointing?

   Validation of the modelling approach was done through numerical modelling of an unstrengthened and strengthened wall retrofitted with bed joint reinforcement, which were experimentally tested at TU Delft (Licciardello, Esposito, 2019). Here, the engineering masonry model was implemented, instead of other common smeared failure models, as it is known that it performs especially well under cyclic loading conditions, such as seismic loading. Previous studies already found that the engineering masonry model was able to correctly capture the observed experimental behaviour (Lee, 2022; Mahmoudimotlagh, 2019). When using the engineering masonry model, the numerical analyses have shown there is good agreement, in terms of initial stiffness, peak loading, crack patterns and crack withs, between the numerical and experimental results. A sensitivity study with respect to the head-joint failure type of the engineering masonry model, analysis procedure settings, iterative method and interpolation scheme, was carried out. It was found that optimal results, in terms of the above-mentioned quantities, were obtained when using the head-joint failure type ‘tensile strength head-joint defined by friction’, the secant method with BFGS and quadratic elements. Therefore it was opted to use these analysis settings in numerical analysis of the façade.

2. What is the contribution of bed joint reinforced repointing on the performance of a farmhouse in the Groningen region, subjected to settlement and seismic loading?

   When comparing the numerical results of the unstrengthened façade with the façade that has been retrofitted with bed joint reinforced repointing, a few things quickly become clear. Like for the masonry walls, no significant increase in the force capacity of the façade is found due to application of the steel reinforcement. Furthermore, a reduction in the relative displacements between the top and bottom of the façade is found, meaning the in-plane stiffness of the façade increased. A reduction in crack formation and propagation is observed, resulting in lower crack widths and damage values during peaks of seismic loading, compared to the unstrengthened façade. When the maximum total damage value, during seismic loading, is reached, a reduction of -4.7% in the maximum crack width is observed, as well as a reduction in the maximum total damage value of -5.5%, compared to the unstrengthened façade. However, the steel reinforcement does not only restrict the opening of cracks, but also the closing of cracks. This results in larger crack widths at certain locations at the end of analysis, compared to the unstrengthened façade. In fact, the maximum crack width at the end of analysis is +7.5% higher for the strengthened façade, compared to the unstrengthened one. However, due to more extensive cracking of the unstrengthened façade at the end of analysis, compared to the strengthened one, the total damage values do in fact decrease, namely by -2.0%. Due to the limited damage caused by an earthquake with the expected seismic load (PGV of 64mm/s), application of bed joint reinforced repointing does, not greatly increase the structural performance of this type of farmhouse façade. It was evident that damage of the façade was mainly governed by the ground settlement and less so by seismic loading. Amplification of the seismic load by a factor 1.5 shows that the increase in crack widths and damage values, at any point during seismic loading, is minor compared to the numerical models where the expected seismic load has been used, while the reinforcement is significantly more activated, compared to the numerical model using the expected seismic load. However, damage quickly ramps up when the seismic load in amplified by a factor 2. In this numerical model, failure is even observed. Although quite some time steps are non-converged, for the numerical models using an amplified load, the results can still be considered decently trustworthy, since the number and magnitude of exceedance of the force norm is minimal.

3. What is the contribution of bed joint reinforced repointing in partially reinforced masonry on the performance of a farmhouse in the Groningen region, subjected to settlement and seismic loading?

   The results of the numerical model with partially reinforced masonry show that application of bed joint reinforcement before the settlement loading phase is initiated, has a major impact on the performance of the façade. Due to application of the bed joint reinforcement before the settlement loading phase is initiated, only very minor cracking is observed at the end of this loading phase. During seismic loading, once again, a minor increase in the force capacity of the façade is found due to combined application of these strengthening techniques, as well a reduction in the relative displacements. Furthermore, a sharp reduction in crack widths and damage values is found at every point, compared to the unstrengthened façade. For the maximum crack widths, during seismic loading, a reduction of -58.1% was observed, as well as a reduction in the maximum total damage value of -23.6%, compared to the unstrengthened façade. At the end of analysis, a reduction in the maximum crack width of -60.3% was found, compared to the unstrengthened façade. For the total damage value this was -23.7%. Therefore it can be concluded that for the partially reinforced masonry façade a significant increases the structural performance was observed.

The damage found in the façade is mainly governed by ground settlements, and less so by seismic loading. In fact, the magnitude of settlement loading is one of the most sensitive parameters of the considered façade. When retrofitting with bed joint reinforcement after the ground settlement has occurred, large damage values are already present in the façade. Due to the limited damage caused by seismic loading, when using the expected seismic load, application of bed joint reinforcement after settlement has occurred, results in only a minor decrease in damage values at the end of analysis, compared to the unstrengthened façade. Since the damage due to seismic loading is so small, it is therefore not recommended to strengthen this type of façade with bed joint reinforcement purely against seismic-induced damage, as the added benefit is small. However, since this strengthening technique is often applied already for strengthening against only ground settlements, it could provide a minor benefit during seismic loading, as a side effect. When looking at the results of the partially reinforced façade, a sharp reduction in crack widths and damage values is observed at the end of analysis, compared to the unstrengthened façade, since the steel reinforcement now also resists the ground settlements (most sensitive parameter). Thus, when this type of façade is subjected to combined settlement and seismic loading, the added benefit of bed joint reinforced repointing in partially reinforced masonry is very significant. Since this numerical model simulates the case in which the bed joint reinforcement is applied during the construction phase, use of bed joint reinforcement would be beneficial for future masonry constructions. To make conclusive statements on the benefit of existing masonry structures, more in-depth numerical modelling of foundation strengthening measures is necessary, since this numerical model can be seen as a slimmed down form of foundation strengthening.

According to Eurocode 6 (NEN-EN 1996, 2005) the minimum required area of reinforcement should not be less than 0.05% of the effective cross-sectional area of the member. In case of the masonry façade, this minimum reinforcement area criterium is not met, and is therefore considered slightly under-reinforced. It is important to remark what the consequences, of failure to meet this criterium, are. First, not meeting the minimum reinforcement area could lead to more cracking, allowing moisture and other agents to penetrate the masonry, resulting in corrosion of the masonry and steel reinforcement, affecting its long-term (structural) performance. Furthermore, under-reinforcing of the masonry might lead to increased displacements of the structural elements, during seismic loading, which might affect the serviceability (and performance) of the structure. Finally, application of steel reinforcement increases the ductility of the masonry structure. When the specified minimum reinforcement area is not met, failure of the structure will occur in a more brittle manner. This means that failure will occur with less, or even no warning, compared to a properly reinforced masonry façade. This could result in dangerous situations that might lead to injuries or, in extreme cases, even fatalities.

Due to the nature of the retrofitting technique, the bed joint reinforcement is placed eccentrically in the masonry. Even though the masonry farmhouse is modelled as a façade, meaning out-of-plane effects are not considered, it is important to note the consequences of eccentric steel reinforcement configurations. Previous research, on eccentrically placed reinforcement bars in concrete (Elrakib, Arafa, 2012), has shown that eccentric reinforcement can lead to a reduction in the capacity and ductility of the structure. It is important to take this into account when considering retrofitting with bed joint reinforced repointing.

6.2 Recommendations

Based on the outcomes of this thesis, several recommendations for further research can be formulated. These are:

1. For the considered façade with a small height to length (H/L) ratio, the settlement-induced damage is prominent with respect to the seismic-induced one; consequently, the benefit of bed joint reinforced repointing is minor. It is advised to consider also other types of façades with a higher H/L ratio, to extend the validity of the conclusions.
2. Only one hogging settlement profile has been considered in this research. However, it could well be that another type of settlement profile is critical for this type of façade. Investigating this further would be a big improvement on the work done here. Additionally, the amplitude of the settlement profile could be decreased and increased, to investigate more in depth the sensitivity of the façade to settlement loading.
3. Since the considered façade is very sensitive to damage due to settlement, the impact of further foundation strengthening measures should be investigated. For example, after settlement, the soil-structure interactions parameters (springs and dashpots) can be adjusted such that a numerical model is created where these parameters are equivalent to the result of a certain foundation strengthening measure.
4. Different seismic loads can be considered. In this research a low frequency seismic load has been considered. The effect of seismic loads with a higher frequency has not been considered. Research has shown that for certain types of façades, high frequency motions can be critical and might significantly affect the structural response of a given façade (Korswagen et al., 2019).
5. Modification of the bed joint reinforcement layout and amount can be extended further. Different configurations, where the minimum reinforcement area is reached, can be considered. This would be especially interesting when loading up to near collapse, since the reinforcement is significantly more activated here.
6. Extension of the model to include the out-of-plane dimension. The seismic load obviously does not only act in-plane of the considered façade. A detailed 3D model of the farmhouse can be made, which includes seismic loading in *both* horizontal directions, as well as the vertical direction.
7. In this research a simplification of the soil-structure interaction has been used. Modelling of this interaction by means of distributed springs and dashpots is not a completely correct way of representing reality. In further research the soil itself, and its properties, can be modelled, to more realistically predict the structural response of the façade under earthquake loading.
8. For the masonry walls a sensitivity analysis with respect to the material properties of the masonry was performed. The results of this investigation give an indication of how a change in masonry material properties could potentially impact the obtained numerical results of the façade. However, a one-on-one comparison, between the masonry walls and façade, cannot be made, and therefore it is recommended that a more in-depth sensitivity analysis (for the masonry façade), with respect to the masonry material properties, is performed.

Bibliography

Front page figures: from https://www.helifix.com.au/applications/crack-stitching/ taken on 9 July 2024

British Standards Institution. (1996). Eurocode 6: Rules for reinforced and unreinforced masonry (together with United Kingdom national application document). London, British Standards Institution. https://doi.org/10.1680/cien.2001.144.6.44

Bruneau, M. (1994). State-of-the-Art Report on Seismic Performance of Unreinforced Masonry Buildings. Journal of Structural Engineering, 120(1), 230–251. https://doi.org/10.1061/(asce)0733-9445(1994)120:1(230)

D'Ayala, D., & Speranza, E. (2003). Definition of Collapse Mechanisms and Seismic Vulnerability of Historic Masonry Buildings. Earthquake Spectra, 19(3), 479–509. https://doi.org/10.1193/1.1599896

DIANA FEA. (2020). DIANA 10.4 user's manual. https://dianafea.com/diana-manuals

Drougkas, A., Licciardello, L., Rots, J. G., & Esposito, R. (2020). In-plane seismic behaviour of retrofitted masonry walls subjected to subsidence-induced damage. Engineering Structures, 223, 111192. https://doi.org/10.1016/j.engstruct.2020.111192

El Gawady, M., Lestuzzi, P., & Badoux, M. (2006). Retrofitting of masonry walls using shotcrete. Proceedings of NZSEE Conference, 45, 45–54. http://db.nzsee.org.nz/2006/Paper45.pdf

Elrakib, T., & Arafa, A. I. (2012). Experimental evaluation of the common defects in the execution of reinforced concrete beams under flexural loading. HBRC Journal/HBRC Journal, 8(1), 47–57. https://doi.org/10.1016/j.hbrcj.2012.08.006

Giardina, G. (2013). Modelling of settlement induced building damage (Delft University of Technology). https://doi.org/10.4233/UUID:8523BCA8-91D3-4DA5-ABD2-2FF2CFDDF9A0

Jafari, S. (2021). Material characterisation of existing masonry: a strategy to determine strength, stiffness and toughness properties for structural analysis (Delft University of Technology). https://pure.tudelft.nl/ws/portalfiles/portal/97634525/Thesis_SamiraJafari.pdf

Jafari, S., Esposito, R. (2017). Material tests for the characterisation of replicated solid clay brick masonry (Delft University of Technology). http://resolver.tudelft.nl/uuid:65f9775c-b50a-4b32-ae58-b628a65a6f04

Jendele L., Červenka, J., Saouma, V., & R. Pukl (2001). On the choice between discrete or smeared approach in practical structural FE analyses of concrete structures. Proceedings of ICADD-4. https://www.cervenka.cz/assets/files/papers/Glasgow_ICADD4_2001_v2.pdf

Korswagen, P. A., Longo, M., Meulman, E., & Rots, J. G. (2019). Crack initiation and propagation in unreinforced masonry specimens subjected to repeated in-plane loading during light damage. Bulletin of Earthquake Engineering, 17(8), 4651–4687. https://doi.org/10.1007/s10518-018-00553-5

Korswagen, P., Longo, M., Meulman, E. (2019). Damage sensitivity of Groningen masonry structures – Experimental and computational studies. Report number C31B69WP0-14-2, Report, version 1.0, Appendix L1 of December 2019, Unpublished.

Korswagen, P.A., Longo, M., Meulman, E., van Hoogdalem, C. (2017). Damage sensitivity of Groningen masonry structures – experimental and computational studies (Delft University of Technology). http://resolver.tudelft.nl/uuid:b59d4678-3228-4bf9-adad-d2ffe063acf0

Lee, K.H. (2022). A comparison study of numerical modelling approaches for simulating the in-plane seismic response of masonry walls. (Delft University of Technology). https://repository.tudelft.nl/record/uuid:48343e5e-7d70-45cb-9163-3d05026bea30

Licciardello, L. and Esposito, R. (2019). Experimental study on unreinforced masonry strengthened with bed joint reinforcement (Delft University of Technology). Unpublished.

Lourenco, P. (1996). Computational strategies for masonry structures". Delft University of Technology (Delft University of Technology). http://resolver.tudelft.nl/uuid:b59d4678-3228-4bf9-adad-d2ffe063acf0

Mahmoudimotlagh, S. (2020). Numerical modelling of the in-plane seismic behaviour of unreinforced masonry wall retrofitted with bed joint reinforcement. (Delft University of Technology). http://resolver.tudelft.nl/uuid:c1edb4f5-582a-4723-8217-bb05c55ad409

Moreira, Susana, Ramos, Luís, F., Csikai, Barna, Bastos. (2014). Bond behaviour of twisted stainless steel bars in mortar joints. 9th International Masonry conference. http://repositorium.sdum.uminho.pt/handle/1822/30900?mode=full

Najam, F.A. (2017). Nonlinear Static Analysis Procedures for Seismic Performance Evaluation of Existing Buildings – Evolution and Issues. In Facing the Challenges in Structural Engineering (pp. 180–198). Springer International Publishing. https://doi.org/10.1007/978-3-319-61914-9_15

NEHRP Consultants Joint Venture. (2012). Soil-structure interaction for building structures. https://www.nehrp.gov/pdf/nistgcr12-917-21.pdf

Vlek, C. (2019). Rise and reduction of induced earthquakes in the Groningen gas field, 1991–2018: statistical trends, social impacts, and policy change. Environmental Earth Sciences, 78(3). https://doi.org/10.1007/s12665-019-8051-4

Appendix A

For the numerical models of the masonry façade subjected to an amplified seismic load (factor 1.5 or 2) a reduced number of maximum iterations has been used. In all other numerical models of the façade, a maximum of 500 iterations was used, while for these two specific models, a maximum of 100 iterations was used. This was done to reduce the computational effort required, since in these models extensive cracking was encountered, which resulted in a significant number of time-steps to encounter non-convergence. In this appendix it is shown that this reduction in the maximum number of iterations is warranted, by comparing the crack patterns, and crack widths, at two points, namely when the total damage value is at its maximum ($\psi_{total,max}$) and after the peak of the motion has passed, namely at xx.

In figure A.1 the crack patterns found when using a maximum of 100 and 500 iterations is shown, when the maximum total damage value is found. Here, the crack widths are basically the same, and also the two crack patterns are nearly indistinguishable from one another. The only difference here is that the cracked area at the bottom most-left side of the façade is slightly larger, when using a maximum of 500 iterations.

In figure A.2 the crack pattern found when using a maximum of 100 and 500 iterations is shown when the maximum total damage value is found. Once again, the crack width are basically the same, as well as the crack patterns. From the above it can be concluded that a reduction of the maximum number of iterations, of 500 to a 100, is warranted.

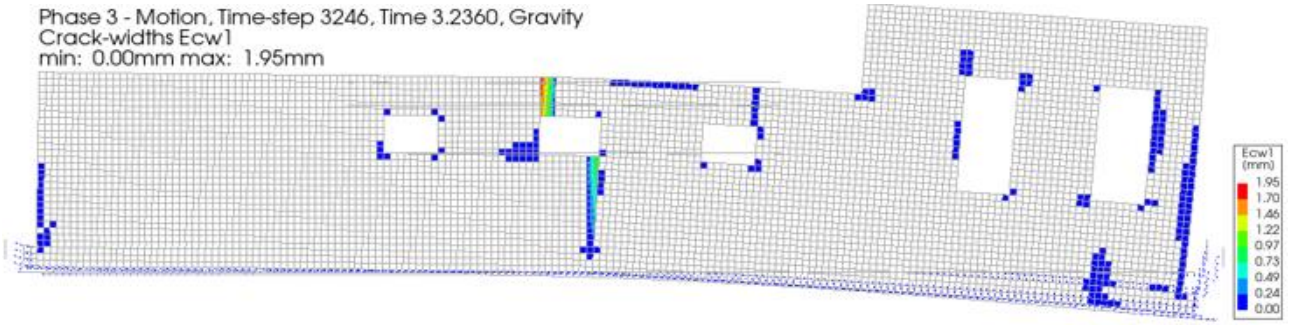

(a) maximum 100 iterations (scale factor 0.05)

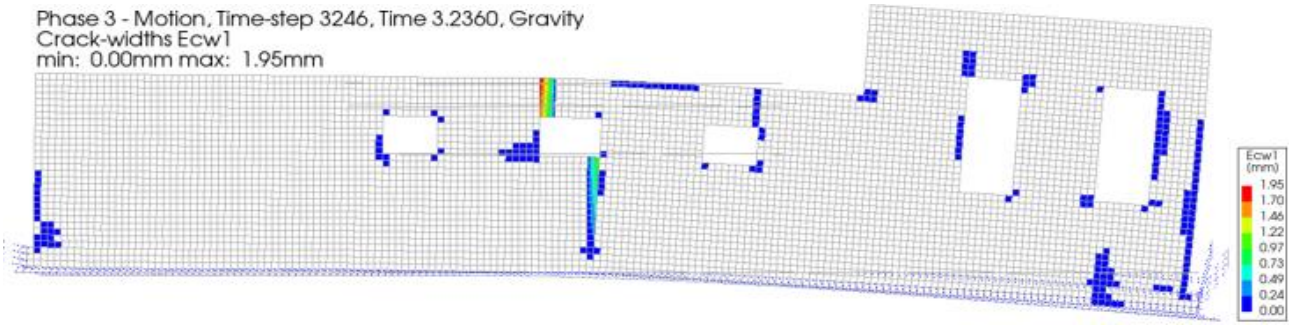

(b) maximum 500 iterations (scale factor 0.05)

Figure A.1 crack pattern at $\psi_{total,max}$ for a maximum of (a) 100 iterations and (b) 500 iterations

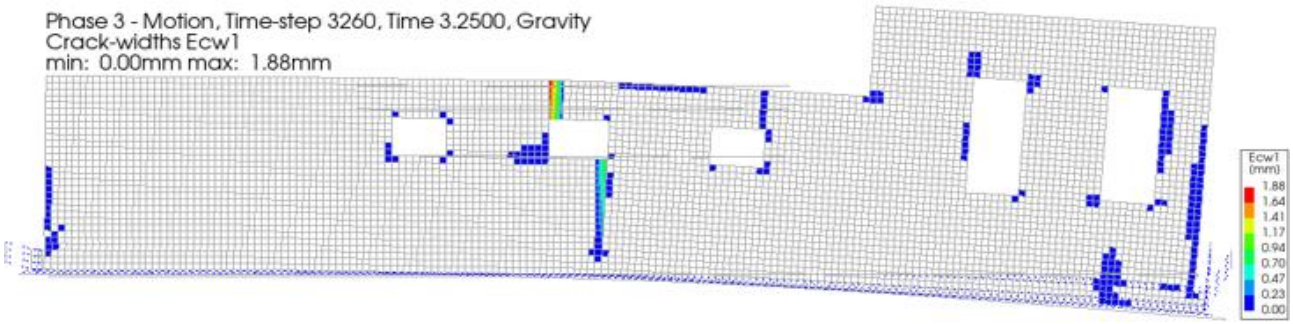

(a) maximum 100 iterations (scale factor 0.05)

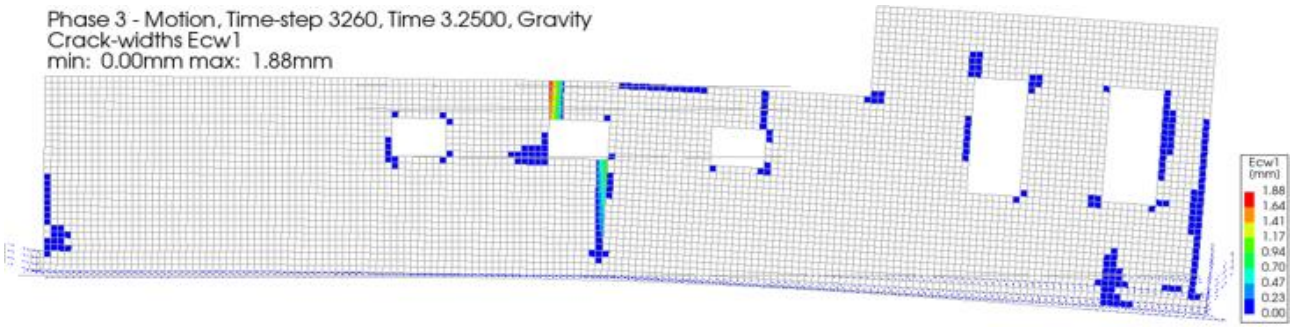

(b) maximum 500 iterations (scale factor 0.05)

Figure A.2 crack pattern at t = 3.250s for a maximum of (a) 100 iterations and (b) 500 iterations